Spin dynamics in the central spin model: Application to graphene quantum dots

Dissertation
zur Erlangung des naturwissenschaftlichen Doktorgrades
der Bayerischen Julius-Maximilians-Universität Würzburg

vorgelegt von
Moritz Jakob Fuchs
aus Vilsbiburg

Würzburg 2016

Eingereicht am: 02.02.2016 .....
bei der Fakultät für Physik und Astronomie

1. Gutachter: Prof. Dr. Björn Trauzettel .....

2. Gutachter: Prof. Dr. Haye Hinrichsen .....

der Dissertation

1. Prüfer: Prof. Dr. Björn Trauzettel .....

2. Prüfer: Prof. Dr. Haye Hinrichsen .....

3. Prüfer: Prof. Dr. Jens Pflaum .....

im Promotionskolloqium

Tag des Promotionskolloqiums: 03.06.2016 .....

Doktorurkunde ausgehändigt am: .....

Zusammenfassung

Auf Grund ihres Potentials hinsichtlich der Realisierung eines Quantencomputers wurde Quantenpunkten im Laufe der letzten Jahre große Aufmerksamkeit zuteil. In diesen Halbleiterstrukturen können einzelne Elektronen kontrolliert eingeschlossen werden, deren Spin wiederum als Basis eines Quantenbits zu Speicherung von Informationen verwendet werden kann. Allerdings unterliegt das Elektron vielvältigen Wechselwirkungen mit seiner Umgebung, was oftmals zu einem sehr schnellen Verlust dieser Information führt. Eine der wichtigsten Ursachen stellt dabei die Hyperfeinwechselwirkung der Kernspins der Halbleiteratome mit dem Elektronspin dar. Eine vielversprechende Möglichkeit diesen Effekt zu minimieren besteht daher in der Verringerung der Anzahl an Kernspins durch Anreicherung spinfreier Isotope. Diese Strategie kann auf Bauteile, bestehend aus Elementen der IV. Gruppe des Periodensystems wie beispielsweise Kohlenstoff, angewendet werden. Ausgehend von dieser Möglichkeit, wird in der vorliegenden Arbeit das Verhalten des Elektronspins in (kohlenstoffbasierten) Graphenquantenpunkten im Rahmen des zentralen Spinmodells analysiert. Besonderes Augenmerk wird dabei auf die Abhängigkeit der Dekohärenzphänomene von der Kernspinzahl gelegt.

Da sich die Modelle, auf denen diese Untersuchung basiert, an experimentellen Gegebenheiten orientieren, wird zunächst ein Überblick über die wichtigsten experimentellen Errungenschaften präsentiert. Neben einer allgemeinen Behandlung der Spinwechselwirkungen in Halbleitern wird dabei auch speziell auf die Eigenschaften von GaAs- und Graphenquantenpunkten eingegangen, die beide als Musterbeispiele angesehen werden können. Des Weiteren wird erläutert, wie sich das zentrale Spinmodell als offenes bzw. geschlossenes Quantensystem beschreiben lässt und mit welchen theoretischen Methoden sich diese untersuchen lassen.

Aufbauend auf diesen Erkenntnissen, wird dann das Verhalten des Elektronspins mit Hilfe analytischer und numerischer Methoden erforscht. Im Rahmen der statistischen Physik findet sich ein thermisch induzierter Wechsel der Spinorientierung. Überdies wird die Zeitentwicklung des Elektronspins für unterschiedliche Kernspinzahlen analysiert. Der Limes großer Kernspinzahlen wird mit Hilfe der Nakajima-Zwanzig Mastergleichung untersucht, wobei sich für den zeitlichen Verlauf der Dekohärenz des Elektronspins ein Potenzgesetz findet. Die Details dieses Potenzgesetzes hängen dabei von der Orientierung eines äußeren Magnetfeldes ab. Eine Beschränkung auf sehr kleine Spinsysteme ermöglicht die Anwendung von exakter Diagonalisierung, welche zusätzliche Erkenntnisse über die mikroskopischen Vorgänge, die zu Dekohärenz führen, liefert. Insbesondere ist ein schneller Übergang zu einem quasi-statischen Verhalten beobachtbar, das durch kleine Fluktuationen um einen Langzeitmittelwert gekennzeichnet ist. Für diese Fluktuationen konnten im Rahmen der Quantenthermodynamik zusätzlich analytische Obergrenzen gefunden werden.

Summary

Due to their potential application for quantum computation, quantum dots have attracted a lot of interest in recent years. In these devices single electrons can be captured, whose spin can be used to define a quantum bit (qubit). However, the information stored in these quantum bits is fragile due to the interaction of the electron spin with its environment. While many of the resulting problems have already been solved, even on the experimental side, the hyperfine interaction between the nuclear spins of the host material and the electron spin in their center remains as one of the major obstacles. As a consequence, the reduction of the number of nuclear spins is a promising way to minimize this effect. However, most quantum dots have a fixed number of nuclear spins due to the presence of group III and V elements of the periodic table in the host material. In contrast, group IV elements such as carbon allow for a variable size of the nuclear spin environment through isotopic purification. Motivated by this possibility, we theoretically investigate the physics of the central spin model in carbon based quantum dots. In particular, we focus on the consequences of a variable number of nuclear spins on the decoherence of the electron spin in graphene quantum dots.

Since our models are, in many aspects, based upon actual experimental setups, we provide an overview of the most important achievements of spin qubits in quantum dots in the first part of this Thesis. To this end, we discuss the spin interactions in semiconductors on a rather general ground. Subsequently, we elaborate on their effect in GaAs and graphene, which can be considered as prototype materials. Moreover, we also explain how the central spin model can be described in terms of open and closed quantum systems and which theoretical tools are suited to analyze such models.

Based on these prerequisites, we then investigate the physics of the electron spin using analytical and numerical methods. We find an intriguing thermal flip of the electron spin using standard statistical physics. Subsequently, we analyze the dynamics of the electron spin under influence of a variable number of nuclear spins. The limit of a large nuclear spin environment is investigated using the Nakajima-Zwanzig quantum master equation, which reveals a decoherence of the electron spin with a power-law decay on short timescales. Interestingly, we find a dependence of the details of this decay on the orientation of an external magnetic field with respect to the graphene plane. By restricting to a small number of nuclear spins, we are able to analyze the dynamics of the electron spin by exact diagonalization, which provides us with more insight into the microscopic details of the decoherence. In particular, we find a fast initial decay of the electron spin, which asymptotically reaches a regime governed by small fluctuations around a finite long-time average value. Finally, we analytically predict upper bounds on the size of these fluctuations in the framework of quantum thermodynamics.

Contents

Introduction

> "If I have seen further it is by standing on ye shoulders of giants."
>
> *Isaac Newton [1]*

In his letter to Robert Hooke, Isaac Newton refers to an old metaphor attributed to Bernard of Chartres. The original metaphor of dwarfs sitting on the shoulders of giants expresses the relation between new discoveries and previous achievements [2]. Naturally, this Thesis rests upon many giants. But rather than the giants themselves, let us name two of their footsteps guiding us to the physics described in this Thesis. Much of modern physics roots in the formulation of quantum mechanics in the mid-twenties of the 20^{th} century. Having originally been developed to describe the physics of microscopic objects such as the hydrogen atom, it has been shown in the course of more than eighty years, that its laws extend to much larger objects of mesoscopic or even macroscopic size [3]. One possibility to prove this extensive validity is the detection of a coherent superposition of states, a hallmark of quantum mechanics. Such coherences have, for instance, been successfully demonstrated by interference experiments on molecules [4] containing hundreds of atoms. Another important step towards the physics relevant for this Thesis, has been the realization of the transistor in the 1940s [5, 6]. Quite reverse to quantum mechanics, the transistor, since then, took a route from the macroscopic world down towards the mesoscopic realm following the predictions of Moore's law [7] in remarkable agreement.

At the end of this development, we find single electron transistors. These extraordinary devices are small boxes made of semiconducting materials, which contain only few electrons [8, 9]. With regard to their small spatial extension, these transistors are also referred to as quantum dots (QDs). The fact that objects like single electron transistors can be designed and manipulated on very small lengthscales gives rise to exciting possibilities for new types of quantum devices. One of the most prominent examples is the quantum computer. As its name already suggests, quantum mechanics is at the heart of this computer. While a classical bit of information is encoded in either of the two states "0" and "1", a quantum computer processes information stored in a qubit [10], which is any coherent superposition of these two states. Using specific algorithms [11, 12], the quantum computer allows for a fundamental new way of processing the data stored in arrays of such qubits [10], which allows to solve certain problems much more efficient. It was in 1998, when Loss and DiVincenzo finally suggested to do "quantum computation with quantum dots" [13]. In their seminal work, they have proposed the spin of an electron in a QD to realize a qubit. Moreover, Loss and DiVincenzo have demonstrated the feasibility of quantum algorithms in coupled QDs in terms of universal quantum operations. Much progress has been achieved since then, but the path towards a working quantum computer

seems still long and challenging. One reason is that quantum systems are not isolated. Instead quantum systems, like the qubits, are rather fragile with respect to interactions with their environment, leading to a very fast loss of their coherence. In the case of electron spin qubits, the interaction with the nuclear spins of the QD is one of the reasons for decoherence.[1] However, as we will see, it is more our limited capabilities than quantum mechanics itself, which gives rise to this (apparent) loss of coherence.

Besides this rather practical issues of how to construct and operate quantum devices, the advance of technology down to the mesoscopic and microscopic regime highlights even more fundamental questions concerning the coexistence of the quantum and the classical world. First attempts to explain the appearance of a classical world in a quantum universe by decoherence have been pioneered by H. D. Zeh [14] in 1970. However, it was not until the mid of the 1980s that decoherence attracted the attention of a broader community by the seminal work of Zurek [15, 16] and Joos and Zeh [17].[2] In 1991, this development culminated in Zurek's article in Physics today [19], which finally introduced decoherence to a broad audience. In the years that followed, decoherence has been studied in various models, many of which can now be actually investigated in numerous physical systems with QDs being only one of them.

It is a fascinating observation that decoherence links both fundamental questions scrutinizing the foundations of quantum mechanics and practical difficulties in the development of new devices such as the quantum computer. Schlosshauer [18] summarizes this intriguing circumstance in the preface to his book "Decoherence and the quantum-to-classical transition": "Decoherence makes a fantastic subject of research, as it touches upon many different facets of physics, from philosophically inclined questions of interpretation all the way to down-to-earth problems in experimental settings and engineering applications."

In view of these words, this Thesis is mostly concerned with the down-to-earth part of physics. In particular, we will investigate the dynamics of an electron spin in a QD interacting with the surrounding nuclear spins. While the number of nuclear spins is typically high for many materials such as the widely used GaAs heterostructures, devices realized with group IV elements like graphene allow for the realization of nuclear spin environments of variable size. Consequently, we will analyze the dynamics of the electron spin surrounded by many and very few nuclear spins. Besides external magnetic fields, the most important driving force for this dynamics is the hyperfine interaction (HI) between the electron spin and the nuclear spins. The limit of large environments is analytically investigated by means of a quantum master equation. More specifically, we will exploit the Nakajima-Zwanzig equation, which is applicable to systems exhibiting so-called non-Markovian dynamics. Subsequently, turning to very small nuclear spin environments will allow us to analyze the dynamics using exact diagonalization. This approach will enable us to better understand the microscopic processes being relevant for the decoherence of the electron spin. Moreover, we will explore the importance of the size of the environment by slowly increasing the number of nuclear spins. Based on these investigations, we will then turn to the generic problem of equilibration in closed, mesoscopic quantum systems.

[1] The decoherence time gives the timescale on which coherent superpositions of states are lost. We clarify the meaning of decoherence in Chapter 2.

[2] More details on the development of the "decoherence program" can be found in the introduction of Ref. [18].

To this end, we will derive certain analytic bounds on the fluctuations of the electron spin, which we will then compare to its dynamics obtained before. Besides this dynamics, we will also analyze the properties of the electron spin and the nuclear spins in thermal equilibrium. Surprisingly, we will encounter a thermally induced flip of the electron spin upon increasing temperature for certain materials. In total, these chapters constitute the second part of this Thesis.

Since not all readers will be familiar with the physics of quantum dots, which is necessary to follow the presentation of our findings, we give a summary of the most important properties of quantum dots and some techniques to investigate them in the first part of this Thesis. To this end, we review the physics of solid state QDs with a focus on GaAs and graphene based setups. Subsequently, we will recapitulate how quantum systems like the spin system in QDs can be modeled in terms of closed and open quantum systems. In this context, we will also explain the physical reasons for the non-Markovian behavior of our model. Furthermore, we will also discuss different theoretical tools to investigate this model such as the Nakajima-Zwanzig equation and the method of exact diagonalization.

While we will give specific conclusions about our findings at the end of each chapter, we will draw a more complete picture at the end of this Thesis. In this Conclusion we will also suggest how the work presented in this Thesis can be continued in future projects. Let us finally return once again to the giants of this Thesis. Regarding its limitations in view of the previous achievements of so many physicists, let us cite a slightly different version of Newton's words.

> "If I have not seen as far as others, it is because giants were standing on my shoulders."
>
> *attributed to Hal Anderson, Prof. at the MIT [2]*

Part I.

Physical background of quantum dots

1. Physical properties of quantum dots

In this chapter, we give an overview on the physics of solid state quantum dots (QDs).[1] To this end, we first discuss how QDs can be realized in solid state systems by means of a brief overview of commonly used materials. Subsequently, we discuss the spin physics of QDs by introducing the particles present in these nanostructures and the interactions among them. Based on this background, we review two important experimental realizations of QDs in GaAs heterostructures and in graphene in more detail. Finally, we review, how the states of the involved particles can be manipulated using the specific properties of these QDs. This chapter as a whole is intended to provide the physical background for the subsequent chapters. However, information relevant to understand the main ideas is given in each chapter, such that this chapter can be likewise skipped upon first reading.

The interest in solid state QDs and the investigation of non-equilibrium spin physics of an excess electron has been strongly promoted by the seminal work of Loss and DiVincenzo [13], in which the spin of a confined electron has been proposed as a realization of a qubit for quantum computation. Considering the DiVincenzo criteria [20] for a quantum computer with respect to this specific qubit, the authors have presented an (at that time) ambitious, yet promising way towards the realization of a quantum computer. Pushed by this proposal, the quest for realizing qubits and, consequently, a quantum computer by means of solid state QDs has become a prospering branch of physics.

So far, we have omitted a strict definition of what a QD is. QDs can be considered as structures in which an electron is confined in each spatial dimension on length scales comparable to its wavelength [21, 22]. For semiconductors, this wavelength is typically given by the Fermi-wavelength of the electron [21]. In fact, typical diameters of QDs range between tens and hundreds of nanometers [9, 23, 24] in agreement with the above statement. According to the discrete spacing of their energy levels, these zero-dimensional structures are also often referred to as artificial atoms.

Due to the capabilities of semiconductor nanostructuring, solid state QDs can be quite intuitively considered as "a scalable physical system with well characterized qubits" [20]. In addition, the spin of the electron is less prone to environmental noise [13] than its charge, which potentially gives rise to "long relevant decoherence times ..." [20]. However, as we will show in Section 1.2, also the spin of the electron is not totally isolated from its environment leading to a loss of information stored in the spin qubit. In particular, we will see that the rate of loss strongly depends on the material used to built the QD. Moreover, a meaningful quantum computer must provide "the ability to initialize the state of the qubits ... ", "a 'universal' set of quantum gates", and "a qubit specific measurement capability" [20]. Below, we illustrate these so-called DiVincenzo criteria in more detail by virtue of a specific example.

[1] All acronyms used in this Thesis are also listed on p. 141 for convenience.

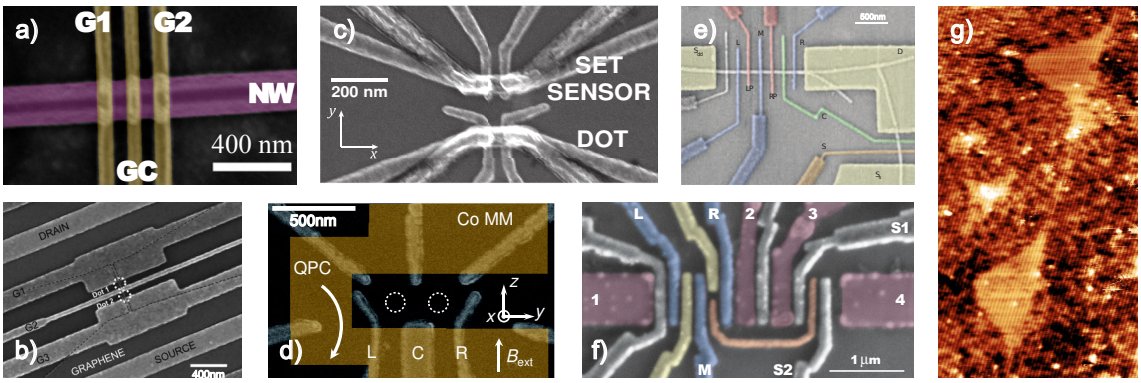

Figure 1.1. QDs realized in different materials. **a)-f)**: scanning electron microscopy images, **g)**: scanning tunneling microscopy topographic image. **a)**: InAs nanowire double QD, **b)**: gated graphene double QD, **c)**: Si-MOS QD, **d)**: GaAs double QD with a micro-magnet (yellow), **e)**: Ge/Si nanowire double QD, **f)**: CNT double QD (CNT underneath the gate electrodes) **g)**: two self assembled InAs QDs. *Figure **a)** reprinted from [25], ©2008, with permission from Elsevier, figure **b)** reprinted with permission from [26], ©2010 American Chemical Society, figure **c)** reprinted from [27], used in accordance with the Creative Commons Attribution (CC BY) license, figure **d)** adapted with permission from [28], ©2014 American Physical Society, figure **e)** reprinted by permission from Macmillan Publishers Ltd: [29], ©2007, figure **f)** reprinted by permission from Macmillan Publishers Ltd: [30], ©2009, figure **g)** reprinted with permission from [31], ©2010 AIP Publishing LLC.*

1.1. Materials

As the DiVincenzo criteria and our definition of a QD suggest, there is a plethora of methods [22, 32][2] to realize qubits in solid state systems. A collection of qubits formed in various materials is shown in Fig. 1.1

Among the experimentally most successful systems over the past decade, one finds QDs based on a two-dimensional electron gas (2DEG) formed in III-V heterostructures [9] such as AlGaAs/GaAs. While the confinement in one dimension is achieved by a difference in the band gaps, the remaining spatial degrees of freedom of the electron are usually limited by electrostatic potentials built on top of the heterostructure, cf. Fig. 1.1 d). By exploiting the specific properties of these QDs, these so-called gates also allow for a fast and precise electric control of the electron spin. We elaborate on this type of QDs in Section 1.3.1 below. Very similar physics can be achieved if the spin of a hole—a missing electron in the valence band—is considered. Since electron and holes can not coexist in these QDs due to the specific properties of the band edges, the respective spins cannot be addressed by optical means. However, this is possible in so-called self-assembled quantum dots [24] also made from group III and V elements, where electrons and holes form excitons. The most prominent example is probably an InAs QD formed in an AlAs or GaAs host material shown in Fig. 1.1 g). By applying laser light, precise control of the spins has been demonstrated in many groundbreaking experiments [24]. Alternatively, QDs from III-V

[2] These and most of the following references of this section are mainly detailed review articles or textbooks, which should enable the interested reader to explore this wide area of physics.

materials can be also formed by means of nanowires [22], where two spatial dimensions are already confined by the geometry, cf. Fig. 1.1 a). The remaining spatial degree of freedom can again be limited by either electrostatic gates or again by a difference in the energy gaps in heterostructures. The major advantage of these III-V systems is an overall high quality of the QD samples and a high degree of control of the spin forming the qubit. However, this comes with the price of a huge nuclear spin environment introduced by the group III and V elements. Thus, the electron spin typically interacts with up to 10^6 nuclear spins via the HI leading to a comparably fast decay of its initial state.

One way to overcome this issue is to use group IV elements instead, in which the abundance of spin carrying isotopes is typically low on the order of few percent. By isotopic purification [33, 34, 35, 36] even spin free environments have been realized [37]. A prominent example is a QD formed in graphene [38, 39], in which the carbon atoms are ordered in a two-dimensional honeycomb lattice. The confinement of the electron in this plane can for instance be achieved by etching the desired structure out of single-layer graphene or by electrostatic gates in bilayer graphene [23] as shown in Fig. 1.1 b). More details on graphene based QDs are presented in Section 1.3.1. Besides graphene, carbon nanotubes (CNTs) [40] form the second class of carbon systems used to realize quantum dots, cf. Fig. 1.1 f). Since a CNT can be considered as a graphene sheet rolled up along some direction, these QDs share many properties with graphene QDs, among which a very weak hyperfine interaction is the most important one. Moreover, in both systems, the electron exhibits another degree of freedom, the so-called valley degree of freedom, which makes the spin physics more complex. We discuss its implications on the spin physics in more detail below. The confinement of the electrons in CNTs is usually achieved by top gates placed upon the CNT, which locally change the chemical potential. Finally, qubits can be also found in so-called NV color centers of diamond [41], which show remarkable properties regarding the spin physics with very long spin decoherence times even at room temperature [34]. However, since the electron spin is bound to the color center in insulating diamond, the construction of linked multi-qubit arrays seems much more challenging.

Besides carbon, also silicon and germanium are interesting for forming QDs [42]. Two examples of this type of QDs are presented in Fig. 1.1 c) and e). Due to advanced fabrication technologies, a wide variety of different quantum dot designs has been developed, where geometrical and electrostatical confinement complement each other. Electrons bound to dopants in Si crystals and self-assembled silicon nanocrystals constitute intrinsically zero-dimensional QDs. One dimensional nanowires can be grown from either pure silicon or germanium and from heterostructures of both elements. For instance, in Si/Ge core/shell nanowires, a one dimensional hole gas is established at the interface. The confinement of the particles in these one-dimensional nanostructures can again be obtained by gate electrodes. Finally, also 2DEGs can be formed in Ge/Si heterostructures or in silicon MOSFETs. Similar to the case of group III-V QDs, this electron gas is then locally depleted by means of additional electrostatic potentials. However, as in the case of carbon, also silicon features a valley degree of freedom, which makes the spin physics more complicated for certain applications [42].

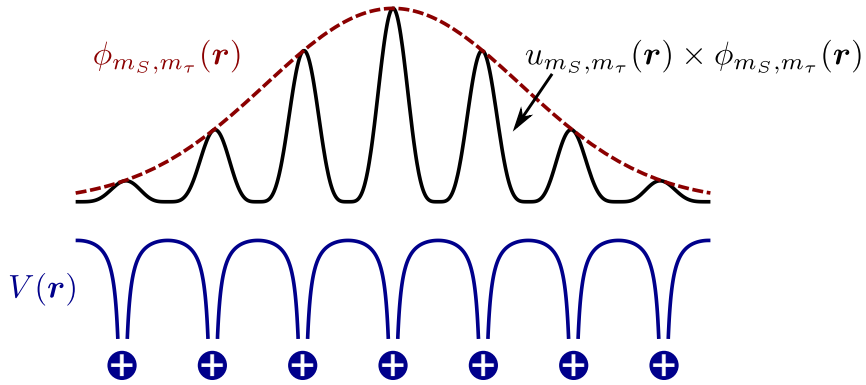

Figure 1.2. Schematic diagram illustrating the periodic potential landscape $V(\boldsymbol{r})$ created by the positively charged nuclear cores. This periodicity is taken into account by the lattice periodic Bloch function $u_{m_S,m_\tau}(\boldsymbol{r})$, which is modulated by the envelope function $\phi_{m_S,m_\tau}(\boldsymbol{r})$. *Figure adapted from Ref. [43], ©2009 WILEY-VCH Verlag GmbH & Co. KGaA, Weinheim.*

1.2. Particles and interactions in solid state quantum dots

Despite the fact that QDs are constructed in many different shapes, the relevant particles in these devices are overall the same. Electrons and, likewise, holes are in the focus of research, since they can be manipulated directly due to a strong coupling to external fields. In contrast to this, the nuclear spins have been mainly treated as an obstacle towards the realization of long-lived qubits in the past, since they interact with both electrons and holes. Yet recently, a change of paradigm can be observed, where these nuclear spins are rather considered as a resource for interesting physics. Moreover, the unavoidable presence of phonons in solid state systems potentially gives rise to relaxation processes of the spins, which have to be taken into account. In addition, certain QD setups feature cavities, in which a photon bath is established. Since the physics, which we describe in the second part of this Thesis, is not concerned with these systems, we give no further information about photons here.

1.2.1. Electrons and holes

Depending on the details of the respective QD and the strength of the applied electrostatic potentials, QDs can hold an arbitrary[3] number of electrons and (or) holes. Within the envelope-function approximation [44], the state of a single electron is described by

$$|\psi\rangle = \sum_{j,m_S,m_\tau} c^j_{m_S,m_\tau} |\Phi^j_{m_S,m_\tau}\rangle \otimes |m_S\rangle \otimes |m_\tau\rangle \,, \tag{1.1}$$

where $|\Phi^j_{m_S,m_\tau}\rangle$ is the orbital degree of freedom of an electron in band j and $|m_S\rangle$ describes its spin. The complex coefficients $c^j_{m_S,m_\tau}$ obey $\sum_{j,m_S,m_\tau} |c^j_{m_S,m_\tau}|^2 = 1$. In Eq. (1.1), we have also considered the so-called valley pseudo-spin $|m_\tau\rangle$ for completeness. This

[3] Of course, this number shows an upper limit. However, the experimentally relevant regime is found for only few particles in the dot, such that the exact size of this limit is not important.

additional degree of freedom is only present in certain materials such as carbon or silicon and results from certain symmetries of the atomic lattice. The orbital part of the state $|\Phi_{m_S^j,m_\tau}\rangle = |\phi^j_{m_S,m_\tau}\rangle \otimes |u^j_{m_S,m_\tau}\rangle$ is described by a product of a lattice periodic Bloch function $u^j_{m_S,m_\tau}(\boldsymbol{r}) = \langle \boldsymbol{r} \,|\, u^j_{m_S,m_\tau}\rangle$ and the envelope function $\phi^j_{m_S,m_\tau}(\boldsymbol{r}) = \langle \boldsymbol{r} \,|\, \phi^j_{m_S,m_\tau}\rangle$ originating from the confining potential. In contrast to the Bloch part, this envelope function varies only slowly over the extent of the QD as is illustrated in Fig. 1.2. The single particle state given in Eq. (1.1) also forms the basis for the calculation of effective Hamiltonians, where typically expectation values with respect to the Bloch function are calculated. As an example, we will calculate the effective spin Hamiltonian of the HI in Section 1.2.3. As a consequence, the position $\boldsymbol{r}$ of the particle within the dot only enters via the envelope function $\phi_{m_S,m_\tau}(\boldsymbol{r})$. Since most experiments are carried out at very low temperatures usually only the envelope function of the ground state and potentially energetically low-lying excited states are taken into account for further investigations.

The state of the spin of an electron is described by eigenstates of the z-component of the spin operator $\hat{\boldsymbol{S}}$

$$\hat{S}_z|m_S\rangle = m_S|m_S\rangle \qquad m_S \in \{-\frac{1}{2},+\frac{1}{2}\} \;\hat{=}\; \{\Downarrow,\Uparrow\}\,. \tag{1.2}$$

In our notation, this spin operator is defined dimensionless ($\hbar = 1$). This definition is extended to all other operators describing angular momentum in this Thesis. In the final results, we will reintroduce the factor $\hbar$ in all expressions in order to obtain physical dimensions. Moreover, we likewise use $\Uparrow$ for $m_S = +\frac{1}{2}$ and $\Downarrow$ for $m_S = +\frac{1}{2}$, since this notation is often more intuitive. Interestingly, in many semiconductors, the spin of a heavy hole can be described identically. The splitting of heavy-hole and light-hole subbands [44] with total angular momentum $j = \frac{3}{2}$ causes a well defined two-level system formed by the two total spin eigenstates $m_J = \pm\frac{3}{2}$, which allows for an effective description in the form of Eq. (1.2). Finally, the valley degree of freedom, if relevant, can be described in terms of eigenstates $|m_\tau\rangle$ of the $\hat{\tau}_z$ Pauli-matrix, where

$$\hat{\tau}_z|m_\tau\rangle = m_\tau|m_\tau\rangle \qquad m_\tau \in \{-1,+1\}\,. \tag{1.3}$$

In many cases, however, this valley degree of freedom is irrelevant [38, 42, 45, 46, 47]. First, if only the spin dynamics of a single particle is considered, the respective spin Hamiltonians do not couple to the valley pseudo spin and, hence, we do not have to take it into account in the effective theory. Moreover, often, the presence of boundaries and substrates within the QD structures induces a valley splitting, which lifts the valley degeneracy. As a consequence, the electron stays within one valley subspace during its dynamics and, thus, the valley degree of freedom can be also neglected. We will give more information on this mechanism when we discuss the realization of graphene QDs in Section 1.3.1.

At last, we would like to set the basis for the discussion of the interactions the electron spin is subjected to. For spin physics in semiconductors, the most important interactions are the Zeeman coupling of the electron spin to external fields, the spin-orbit interaction (SOI) which couples both spin and angular momentum, and the HI of the electron spin and the nuclear spins. All these interactions can be rigorously derived from the relativistic

Dirac equation

$$\mathrm{i}\hbar\frac{\partial|\Psi\rangle}{\partial t} = [c\,\hat{\boldsymbol{\alpha}}\cdot(\hat{\boldsymbol{p}}+e\boldsymbol{A}) + m_0c^2\hat{\beta} - e\Phi\mathbb{1}]|\Psi\rangle = \hat{H}_{\mathrm{D}}|\Psi\rangle\,, \tag{1.4}$$

where Ψ denotes a four-component spinor describing the spin states of the electron and the positron and $\hat{\alpha}_1$, $\hat{\alpha}_2$, $\hat{\alpha}_2$, and $\hat{\beta}$ are the Dirac matrices [48, 49]. Moreover, this equation takes into account the coupling of the electron to the electromagnetic potentials $\boldsymbol{A}$ and Φ as well as the relativistic rest energy m_0c^2, where e is the elementary charge, m_0 is the mass of the free electron, and c is the speed of light. An expansion of the Dirac-Hamiltonian in powers of $\frac{1}{m_0c^2}$ can be obtained by means of subsequent Foldy-Wouthuysen-transformations [48, 49] of the Dirac Hamiltonian $\hat{H}_{\mathrm{D}}$.[4] Expanding to third order in $\frac{1}{m_0c^2}$ results in the effective Hamiltonian, in which the first two components of the four spinor decouple from the second pair of components. The differential equation for the first pair of components describes the dynamics of the electron and is explicitly given by

$$\mathrm{i}\hbar\frac{\partial|\psi\rangle}{\partial t} = \Bigg\{ \Big[m_0c^2 + \overbrace{\frac{1}{2m_0}(\hat{\boldsymbol{p}}+e\boldsymbol{A})^2}^{=\hat{H}_{\mathrm{kin}}} - \frac{p^4}{8m_0^3c^2}\Big] - e\Phi \;+\; \frac{e\hbar^2}{8m_0^2c^2}\,\boldsymbol{\nabla}\cdot(\boldsymbol{\nabla}\Phi) \tag{1.5}$$

$$\underbrace{+\,g\frac{e\hbar}{2m_0}\,\hat{\boldsymbol{S}}\cdot(\boldsymbol{\nabla}\times\boldsymbol{A})}_{=\hat{H}^S_{\mathrm{ZE}}} \underbrace{+\,\frac{e\hbar}{2m_0^2c^2}\,\hat{\boldsymbol{S}}\cdot\Big[(\boldsymbol{\nabla}\Phi)\times(\hat{\boldsymbol{p}}\;+\;e\boldsymbol{A})\Big]}_{=\hat{H}_{\mathrm{SOI}}} \Bigg\}|\psi\rangle\,, \tag{1.6}$$

where $|\psi\rangle$ now describes the state of the electron. Moreover, we assumed that the magnetic field $\boldsymbol{B} = \boldsymbol{\nabla}\times\boldsymbol{A}$ is constant over time resulting in $\boldsymbol{\nabla}\times\boldsymbol{E} = 0$, such that the electric field $\boldsymbol{E} = \boldsymbol{\nabla}\Phi$ originates solely from the Coulomb potential. In this form, Eq. (1.6) corresponds to the Pauli equation [52] with additional relativistic corrections. The terms in the rectangular bracket in the first line correspond to relativistic corrections to the kinetic energy. The following term describes the coupling of the electron charge to the Coulomb potential Φ. The last term in the first line of Eq. (1.6) is the Darwin term, which is related to the so-called Zitterbewegung [50] of the electron. The terms, which are of particular interest for this Thesis, are the kinetic term $\hat{H}_{\mathrm{kin}}$, the electron Zeeman term $\hat{H}^S_{\mathrm{ZE}}$ and the spin-orbit interaction described by $\hat{H}_{\mathrm{SOI}}$. As we will show below, the HI arises from all of these terms. We will discuss the Zeeman interaction and the HI in more detail below and focus on the SOI

$$\hat{H}_{\mathrm{SOI}} = \frac{e\hbar}{2m_0^2c^2}\hat{\boldsymbol{S}}\cdot\Big[(\boldsymbol{\nabla}\Phi)\times(\hat{\boldsymbol{p}}\;+\;e\boldsymbol{A})\Big] \tag{1.7}$$

now. For a central potential $\Phi = \Phi(r = |\boldsymbol{r}|)$ and $\boldsymbol{A} = 0$, this interaction takes the familiar form $\hat{H}_{\mathrm{SOI}} \propto \hat{\boldsymbol{S}}\cdot\hat{\boldsymbol{L}}$, since $\boldsymbol{\nabla}\Phi(r) = \frac{1}{r}(\frac{\partial\Phi(r)}{\partial r})\,\boldsymbol{r}$ and $\hbar\hat{\boldsymbol{L}} = \hat{\boldsymbol{r}}\times\hat{\boldsymbol{p}}$ is the orbital angular momentum. For $\boldsymbol{A}\neq 0$, additional contributions arise, which are, for instance, responsible for the so-called contact HI caused by the magnetic moment of the nucleus.

[4] An alternative approach to obtain such an expansion based on an elimination of the second pair of spinors, can be found in [50]. This approach is also used by Stoneham [51] in order to derive the HI in solid state systems.

The confinement of the electron motion in quasi one- or two-dimensional electron gases and the structure of the lattice influence the specific form of the SOI for a given quantum dot. Following different approaches to calculate the SOI in semiconductors relying on an analysis of symmetries [44] yields more specific results for the SOI Hamiltonian. We refer to work of Winkler [44] and to the discussion of the SOI in GaAs and graphene below for more details.

1.2.2. Nuclear spins

Depending on the respective host material, there will be K nuclear spins being spread over the N_{sites} atoms within the dot. If not all isotopes of the elements forming the QD carry a spin, the natural abundance $n_I = \frac{K}{N_{\text{sites}}}$ fulfills $0 < n_I < 1$, which allows to change the number of nuclear spins from $K = 0$ to $K = N_{sites}$ by isotopic purification. In carbon and silicon systems such a purification was already successfully applied [33, 34, 35, 36]. For typical graphene QDs, the diameters vary in the range of 10 nm to 100 nm and, hence, the number of carbon atoms is on the order of 10^3 to 10^5. Recently, dots with diameters on the order of 1 nm were realized [53]. Thus, nuclear spin numbers K which range from less than ten to 10^5 for a pure ^{13}C QD seem feasible. In contrast to this, the widely used III-V semiconductors have $n_I = 1$ and, thus, do not allow to exploit isotopic purification. Consequently, these QDs contain typically on the order of 10^5 to 10^6 nuclear spins [9, 24].

In parts of the theoretical work on spin dynamics in QDs, these nuclear spins are described as spin one-half particles for simplicity, despite the fact that many are actually of higher spin number [43, 54]. This strategy allows us to identify the important mechanisms determining the spin dynamics of the electron spin. Moreover, often the properties of different isotopes are not distinguished, but average values weighted by the abundance of the respective isotope or atom are considered. If x_j is some property of the atomic species j like the nuclear g-factor or the HI coupling constant and n_j is its abundance, then the average value of this property is given by $x = \sum_j n_j x_j$. If not stated otherwise, we also adopt these simplifications in order to identify the important spin physics, which could otherwise be concealed by the microscopic details. For graphene, which is mainly considered in this Thesis, however, these difficulties do not arise anyway, since all nuclear spins are carried by the ^{13}C isotope, which are true spin one-half particles. In summary, if not stated otherwise, we describe all nuclear spins by

$$\hat{I}_{k,z}|m_k\rangle = m_k|m_k\rangle \qquad m_k \in \{-\frac{1}{2}, +\frac{1}{2}\} \;\hat{=}\; \{\downarrow, \uparrow\}\,, \tag{1.8}$$

where $k \in \{1, \ldots, K\}$. Similar to the electron spin states, we also use the alternative notation $\uparrow$ and $\downarrow$ for $m_k = +\frac{1}{2}$ and $m_k = -\frac{1}{2}$, respectively.

1.2.3. Direct spin interactions

Zeeman interaction

The coupling of the electron spin to external magnetic fields $\boldsymbol{B}$ is of great importance for the realization of spin qubits in semiconductors, since it allows for a direct manipulation of its state. As we discussed above, this interaction is a consequence of the relativistic

Material	GaAs	Graphene
A^S_{ZE}	10^1	10^2
A^I_{ZE}	10^{-2}	10^{-2}
$A^{\mathrm{p}}_{\mathrm{HI}}$	10^2	10^{-2}
$A^{\mathrm{f}}_{\mathrm{HI}}$	10^{-2}	10^{-4}
$A^{\mathrm{s}}_{\mathrm{HI}}$	10^{-4}	10^{-6}
A_{DD}	10^{-6}	10^{-5}
$A^{\mathrm{e}}_{\mathrm{DD}}$	10^{-6}	10^{-8}

Table 1.1. Energy scales of different direct spin interactions, where all energies are measured in μeV: The electron and nuclear Zeeman energies A^S_{ZE} and A^I_{ZE} are calculated for an external magnetic field of $B_z = 1$ T. We give the energy scale of the HI for a fully polarized ($A^{\mathrm{p}}_{\mathrm{HI}} = n_I A_{\mathrm{HI}}$), a randomly fluctuating nuclear spin bath ($A^{\mathrm{f}}_{\mathrm{HI}} = n_I A_{\mathrm{HI}}/\sqrt{K}$), and for a single nuclear spin ($A^{\mathrm{s}}_{\mathrm{HI}} = n_I A_{\mathrm{HI}}/K$) in the center of the QD. We have chosen $N_{\mathrm{sites}} = 10^6$ and $n_I = K/N_{\mathrm{sites}} = 0.01$ ($n_I = 1$) for graphene (GaAs). The nuclear dipole-dipole energy scale A_{DD} is effectively reduced to $A^e_{\mathrm{DD}} = A_{\mathrm{DD}}\, n_I^{3/2}$ by the abundance $n_I = K/N_{\mathrm{sites}}$ of spin carrying isotopes.

nature of the electron. According to Eq. (1.6), the Zeeman coupling is given by $\hat{H}^S_{\mathrm{ZE}} = g\mu_B\, \boldsymbol{B}\cdot\hat{\boldsymbol{S}} = \hbar\gamma_S\, \boldsymbol{B}\cdot\hat{\boldsymbol{S}}$, where $g = 2$ is the bare g-factor of the electron and $\mu_B = \frac{|e|\hbar}{2m_0}$ is Bohr's magneton. Often, the Zeeman interaction is expressed in terms of the gyromagnetic ratio $\gamma_S = \frac{g\mu_B}{\hbar}$. In many semiconductors, however, this coupling is modified due to a comparably strong SOI, which can be taken into account by replacing g with an effective electron g-factor g^*. It was first shown by Roth et al. [55], that SOI gives rise to effective g-factors, which can differ significantly from the bare g-factor. Later, an even more elaborate theory [44] has been used to include subtleties such as the anisotropy of the valence bands, which give rise to an anisotropic effective g-factor. However, typically, this anisotropy is not taken into account leading to the following Zeeman Hamiltonian for an electron in a semiconductor

$$\hat{H}^S_{\mathrm{ZE}} = g^*\mu_B\, \boldsymbol{B}\cdot\hat{\boldsymbol{S}}\,. \tag{1.9}$$

Important exceptions of this are QDs realized in carbon and silicon nanostructures, where the SOI is too weak to renormalize the bare g-factor of the electron. If we choose $\boldsymbol{B} = (0,0,B_z)^T$ without loss of generality, we can define the energy associated with the Zeeman interaction by $A^S_{\mathrm{ZE}} = g^*\mu_B B_z$.

Similar to the electron, also the magnetic moments of the nuclear spins couple to external magnetic fields. In contrast to the negatively charged electron, however, their magnetic moment is parallel to the nuclear spin $\hat{\boldsymbol{I}}$ resulting in a relative sign difference in the respective Zeeman Hamiltonian:

$$\hat{H}^I_{\mathrm{ZE}} = -g_N\mu_N\, \boldsymbol{B}\cdot\hat{\boldsymbol{I}} \tag{1.10}$$

where g_N is the nuclear g-factor [54] and $\mu_N = \frac{e\hbar}{2m_p}$ is the nuclear magneton. For $\boldsymbol{B} =$

$(0, 0, B_z)$, the associated energy of the Zeeman interaction is given by $A^I_{\mathrm{ZE}} = g_N \mu_N B_z$. Alternatively to the product of g-factor and nuclear magnetic moment, the gyromagnetic ratio $\gamma_N = \frac{g_N \mu_N}{\hbar}$ is used to describe the Zeeman coupling of the nuclear spins. Extensive lists of either g_N or γ_N for many elements of semiconducting materials can be found in Refs. [43] and [54]. Due to the large mass m_p of the proton, the nuclear magnetic moment is about three orders of magnitude smaller than Bohr's magneton, which renders the nuclear Zeeman coupling negligible in many cases. This fact is illustrated in Tab. 1.1, where we compare different spin interactions for the most important materials.

Hyperfine interaction

Besides the Zeeman couplings of the spins to external fields, the HI is another important spin interaction, which mediates between the electron spin and the nuclear spins. The HI in solid state structures can be directly related to the atomic HI, which itself can be derived from the Dirac equation in Eq. (1.4) and its non-relativistic expansion given in Eq. (1.6). The effect of a nucleus and its spin can be taken into account by means of its Coulomb potential and the magnetic field induced by the magnetic dipole. The charge of the nucleus gives rise to a point like Coulomb potential $\Phi = \frac{Z_{\mathrm{eff}} e}{4\pi\varepsilon_0} \frac{1}{r}$ depending on the absolute value r of the position $\boldsymbol{r}$, where $Z_{\mathrm{eff}} e$ is the effective charge of the nucleus and ε_0 is the electric constant. The vector potential caused by the magnetic moment of the nuclear spin is given by $\boldsymbol{A} = \frac{\mu_0}{4\pi} g_N \mu_N \boldsymbol{\nabla} \times \hat{\boldsymbol{I}} \, \frac{1}{r} = \frac{\mu_0}{4\pi} g_N \mu_N \hat{\boldsymbol{I}} \times \frac{\boldsymbol{r}}{r^3}$, where μ_0 is the vacuum permeability. Note, that we have assumed a point like source for both potentials. Hence, these two potentials are only good approximations to the exact potentials as long as the distance r is larger than some length d, which is on the order of atomic core diameters. As a consequence, one has to take care whenever expectation values of the interactions arising from these potentials are calculated.

Inserting both potentials in the expanded Dirac equation in Eq. (1.6) yields three major contributions to the HI [51]. The first contribution $\hat{h}_1$ is the so-called contact hyperfine interaction, which stems from the coupling of the electron spin to the vector potential in the SOI term $\hat{H}_{\mathrm{SOI}} \propto \hat{\boldsymbol{S}} \cdot \Big[(\boldsymbol{\nabla}\Phi) \times \boldsymbol{A} \Big)\Big]$. Inserting the definitions of Φ and $\boldsymbol{A}$ from above finally yields

$$\hat{h}_1 = \frac{\mu_0}{4\pi} g_N \mu_N g \mu_B \frac{d}{2} \frac{1}{r^6} \left[r^2 \, \hat{\boldsymbol{S}} \cdot \hat{\boldsymbol{I}} - (\boldsymbol{r} \cdot \hat{\boldsymbol{S}})(\boldsymbol{r} \cdot \hat{\boldsymbol{I}}) \right], \tag{1.11}$$

where $d = \frac{Z_{\mathrm{eff}} e^2}{4\pi\varepsilon_0} \frac{1}{m_0 c^2} \approx 1.5 \times 10^{-15}$ m $\cdot Z_{\mathrm{eff}}$ is a length on the order of atomic core diameters.[5]

At this point, two comments seem necessary: The interaction in Eq. (1.11) shows a divergence at $r = 0$, which arises from the approximation of the nucleus as a point like charge and dipole. This unphysical behavior can be corrected by the introduction of an additional factor $(1 + \frac{d}{r})^{-1}$ [51], which cancels the divergence for $r < d \approx 10^{-15}$ m.[6] In

[5] Interestingly, this is half of the classical electron radius for $Z_{\mathrm{eff}} = 1$.

[6] This factor is derived by Stoneham [51] by virtue of an exact solution of the Dirac equation for the electron two-spinor. Comparing this with a similar approach presented in [50], however, lets us believe that the derivation of Stoneham [51] is questionable, since it misses some subtleties mentioned in [50] such as the appearance of a non-hermitian operator and the fact that the resulting equation is not

addition, the point like approximation of the dipole moment even leads to an ill-defined definition of the contact HI. As pointed out by Soliverez [56], the well known result for the contact HI is restored if a spherical volume for the magnetic moment is considered.

Typically, the contact HI is not presented in this form, but rather a simpler, effective Hamiltonian $\hat{h}_1^{\text{eff}}$ is considered, which, however, gives the same expectation values with respect to the electron wave functions. This effective Hamiltonian can be found considering two aspects. First, $\hat{h}_1$ is clearly dominated by the contributions at small $r \sim d$. Second, the typical length scale of the wave function $\Psi(\boldsymbol{r}) = \langle \boldsymbol{r} \,|\, \Psi \rangle$is much larger than the cutoff d. For instance, often the orbitals of semiconducting elements are approximated by hydrogen orbitals [57, 58], still using an effective charge Z_{eff}, which vary on length scales on the order of Bohr's radius $a_0 = 5.29 \times 10^{-11}$ m $\gg d$. Thus, only the value of the wave function at $r \approx 0$ is relevant for expectation values of $\hat{h}_1$. Since these orbitals are additionally either spherically symmetric around the atomic core or vanish as $r \to 0$, the expectation value of the second term in Eq. (1.11) vanishes, which finally yields:

$$\langle \Psi | \hat{h}_1 | \Psi \rangle = \frac{\mu_0}{4\pi} \frac{8\pi}{3} g_N \mu_N g \mu_B |\Psi(0)|^2 \,. \tag{1.12}$$

The effective Hamiltonian giving rise to the same expectation value is, thus, given by

$$\hat{h}_1^{\text{eff}} = \frac{\mu_0}{4\pi} \frac{8\pi}{3} g_N \mu_N g \mu_B \; \delta(\boldsymbol{r}) \; \hat{\boldsymbol{S}} \cdot \hat{\boldsymbol{I}} \,, \tag{1.13}$$

where $\delta(\boldsymbol{r})$ is the Dirac delta function. This effective Hamiltonian is then considered to calculate the actual contact HI in a specific material, where usually the envelope function approximation is applied. Hence, the energy scale A_{HI} of the HI is obtained by

$$A_{\text{HI}} = \frac{\mu_0}{4\pi} \frac{8\pi}{3} g_N \mu_N g \mu_B |u^j_{m_S, m_\tau}(0)|^2 \,, \tag{1.14}$$

which is typically on the order of μeV. In contrast to the Zeeman Hamiltonian, the bare g-factor of the electron enters the HI, since this interaction is strongly localized around the core, such that the renormalization caused by the SOI is irrelevant [59].

The second contribution $\hat{h}_2$ to the HI is anisotropic and results from inserting the vector potential $\boldsymbol{A}$ into the Zeeman term $g\mu_B \hat{\boldsymbol{S}} \cdot [\nabla \times \boldsymbol{A}]$ of the expanded Dirac equation in Eq. (1.6):

$$\hat{h}_2 = \frac{\mu_0}{4\pi} g_N \mu_N g \mu_B \hat{\boldsymbol{S}} \cdot [\nabla \times (\nabla \times \hat{\boldsymbol{I}} \, \frac{1}{r})] \approx \frac{\mu_0}{4\pi} g_N \mu_N g \mu_B \frac{3(\boldsymbol{e}_r \cdot \hat{\boldsymbol{S}})(\boldsymbol{e}_r \cdot \hat{\boldsymbol{I}}) - \hat{\boldsymbol{S}} \cdot \hat{\boldsymbol{I}}}{r^3 (1 + \frac{d}{r})} \tag{1.15}$$

where $\boldsymbol{e}_r$ is a unit vector parallel to $\boldsymbol{r}$ and the additional factor $(1 + \frac{d}{r})^{-1}$ has been introduced to avoid unphysical behavior. According to its specific form, it is clear, why

an exact eigenvalue equation. Moreover, if we solved the Dirac equation itself, the problem of the divergence at $r \to 0$ would still exist without the additional factor correcting it. In summary, it seems somewhat inadequate to take d, which is half the classical electron radius, rather than the size of the nuclear core as a cutoff. Nevertheless, the classical electron radius gives the right length scale and the resulting-factor is physically reasonable. In addition, this factor is also considered in the literature and, consequently, we also choose this factor, but consider it rather as a phenomenological approach to recover the correct physics.

this interaction can be also considered as the interaction of two magnetic dipoles from a (more) classical point of view. The expectation value of $\hat{h}_2$ vanishes identically for spherical symmetric states like the s-states. Finally, the last contribution to the HI arises from the mixed term $\frac{e}{m}\,\hat{\boldsymbol{p}}\cdot\boldsymbol{A}$ in the kinetic part $(\hat{\boldsymbol{p}}+e\boldsymbol{A})^2$:

$$\hat{h}_3 = \frac{e}{m_0}\boldsymbol{A}\cdot\hat{\boldsymbol{p}} \approx \frac{\mu_0}{4\pi} g_N \mu_N g \mu_B \,\frac{1}{r^3(1+\frac{d}{r})}\,\hat{\boldsymbol{I}}\cdot\hat{\boldsymbol{L}}\,. \tag{1.16}$$

Since both terms $\hat{h}_2$ and $\hat{h}_3$ scale with r^{-3}, also these contributions are strongly localized around the core and, therefore, only the bare g-factor of the electron enters. The energy of these terms is given by

$$A_{\mathrm{HI}} = \frac{\mu_0}{4\pi} g_N \mu_N g \mu_B \langle u^j_{m_S,m_\tau} | \frac{1}{r^3} | u^j_{m_S,m_\tau} \rangle\,, \tag{1.17}$$

where the expectation value is calculated with respect to the Bloch part of the electron wave function.

We will discuss the relevance and the exact form of the HI contributions $\hat{h}_{1,2,3}$ in more detail in Section 1.3.1, where we elaborately analyze the properties of GaAs and graphene based quantum dots.

Additional direct spin interactions

In the previous section, we have identified an interaction between the nuclear magnetic moment and the magnetic moment of the electron. Obviously, two nuclear magnetic moments $\hat{\boldsymbol{I}}_i$ and $\hat{\boldsymbol{I}}_j$ also interact with each other via the dipole-dipole interaction:

$$\hat{H}_{\mathrm{DD}} = -\frac{\mu_0}{4\pi}\frac{\mu_N^2 g_i g_j}{a_{\mathrm{NN}}^3}\frac{3(\hat{\boldsymbol{I}}_i\cdot\mathbf{e}_{i,j})(\hat{\boldsymbol{I}}_j\cdot\mathbf{e}_{i,j}) - \hat{\boldsymbol{I}}_i\cdot\hat{\boldsymbol{I}}_j}{r_{i,j}^3}\,, \tag{1.18}$$

where g_i is the g-factor of the nuclear spin $\hat{\boldsymbol{I}}_i$. For convenience, we measure the absolute distance between two nuclei $r_{i,j} = |\boldsymbol{r}_i - \boldsymbol{r}_j|/a_{\mathrm{NN}}$ in units of the nearest-neighbor distance a_{NN} and we have defined the unit vector $\mathbf{e}_{i,j} = |\boldsymbol{r}_i - \boldsymbol{r}_j|/(a_{\mathrm{NN}}\, r_{i,j})$. Since this interaction is generally anisotropic, it does not preserve spin. However, the energy scale

$$A_{\mathrm{DD}} = \frac{\mu_0}{4\pi}\frac{\mu_N^2 g_i g_j}{a_{\mathrm{NN}}^3} \tag{1.19}$$

is typically several orders of magnitude smaller than the Zeeman energy and the energy associated with the HI as can be seen from Tab. 1.1. Hence, these non-spin-conserving processes become already irrelevant in moderate magnetic fields. The remaining part of this interaction

$$\hat{H}_{\mathrm{DD}}^{\mathrm{sec}} = -A_{\mathrm{DD}}\,\frac{[3\cos(\theta_{i,j})^2 - 1][\hat{I}_{i,z}\hat{I}_{j,z} - \hat{I}_{i,x}\hat{I}_{j,x} - \hat{I}_{i,y}\hat{I}_{j,y})]}{r_{i,j}^3} \tag{1.20}$$

still leads to a spin diffusion, which gives rise to an exchange with nuclear spins in the bulk around the QD. However, in the presence of a sufficiently large gradient of Zeeman energies,

this diffusion is strongly quenched [60]. In a QD, such a gradient is naturally present due to the Knight-field induced by the HI [60, 61]. Such an energy difference suppressing this dipolar interaction can be also caused by the quadrupole interaction [43, 60], which is present for nuclear spins with quantum numbers $I > \frac{1}{2}$. This interaction couples the nuclear spin to gradients of electric fields at the position of the nuclear spin [62, 63] and is particularly relevant in systems with strain such as optically active QDs [24]. Since the energy scales related to the quadrupole interaction are very small compared to the Zeeman coupling and the HI, we will not take this interaction into account for the remainder of this Thesis. The suppression of the nuclear dipole-dipole interaction is also known as the frozen core or diffusion barrier effect.

Further, the dipole-dipole interaction is on average reduced in systems with a low natural abundance n_I of spin carrying isotopes such as carbon. If we consider, for instance, graphene and randomly place nuclear spins with equal probability for each site, the average distance in units of a_{NN} is given by $\tilde{r} = \sqrt{n_I} \cdot r_0$, where $r_0 = O(1)$. Hence, the dipole-dipole interaction is reduced by a factor $n_I^{3/2}$, which gives three orders of magnitude for the natural abundance of ^{13}C.

In summary, the nuclear dipole-dipole interaction is only relevant if there is no HI or on very long timescales, when the total spin in the system changes due to the non-spin-conserving contributions for small external magnetic fields. In addition to that, systems with a low abundance of spin carrying isotopes such as carbon or silicon exhibit large inter-nuclear distances $r_{i,j}$, which renders this interaction even less important. Hence, we will neglect this interaction for the rest of this Thesis as long as the HI is present.

1.2.4. Indirect spin interactions with phonons

As mentioned in the beginning of this chapter, the spins do not only interact with each other, but they are also affected by the unavoidable presence of phonons. Yet due to their lack of a spin degree of freedom, the phonons cannot couple directly to the spins of the electron and to the nuclear spins. However, as we will discuss in more detail below, by means of additional interactions such as electron spin-orbit interaction and nuclear dipole-dipole interaction, the phonons can couple indirectly to these spins.

Although the phonons cannot couple to the electron spin, they can well interact with its charge via electric fields. Keeping the SOI in mind, electric fields can influence the electron spin indirectly. In general, fluctuating electric fields can arise from many sources, including fluctuations in the gate potentials, background charge fluctuations or other electrical noise. However, these sources can be minimized by a careful design of an experimental setup [9], such that phonons become the most important source of an electric field. First, so-called deformation potential phonons inhomogeneously deform the crystal lattice, which leads to a spatially altering band gap and effectively to fluctuating electric fields [9, 42]. This effect is present in all semiconductors. Second, in polar crystals such as GaAs the piezoelectric effect leads to electric fields in the presence of homogeneous strain [9, 42]. These two effects are typically subsumed as electron-phonon coupling (EPC).

Thus, the electron spin can be coupled to phonons by the combined interaction of SOI and EPC [64, 65]. There are two ways to interpret the effect of this combined interaction. First, a sequential view: The spin-orbit interaction perturbs the pure spin states and

creates states, which consist of admixtures of spin and orbital states. These states are then coupled by the electron phonon coupling. Second, one can apply perturbation theory directly to the combined Hamiltonian $\hat{H}_{\mathrm{SOI}} + \hat{H}_{\mathrm{EPC}}$. In both cases, the perturbation leads to a relaxation of the electron spin induced by the phonon bath. Usually, only acoustic phonons are taken into account, since their energy spectrum matches the other relevant energy scales in the QD. Since the phonons pick up the spin flip energy difference, the relaxation rate depends on the Zeeman energy and, hence, on the strength of the external magnetic field. Moreover, it depends on the (material specific) strength of the SOI and the EPC. Finally, also the number of phonons is relevant. This number is typically small at mK temperatures, at which the experiments are carried out. As a consequence, the relevance of the electron spin phonon coupling has to be considered for each QD setup individually. We will discuss the importance of this spin interaction in more detail for GaAs and graphene QDs in the next section.

The interaction of nuclear magnetic moments with phonons is a well studied phenomenon. In the field of nuclear magnetic resonance research it is known as spin lattice relaxation. The corresponding timescales are typically quite long and can reach minutes (GaAs, carbon) [66, 67]. Since this exceeds the relevant times scale of the electron spin dynamics by several orders of magnitude [22], this interaction is normally not taken into account for investigations of the electron spin dynamics. However, it can be relevant if one is interested in the thermal equilibrium of the nuclear spins as discussed in Chapter 3.

1.3. Experimental properties of solid state quantum dots

In the previous section, we have discussed the microscopic details of spin interactions in QDs in general. In this section, we will discuss different experimental realizations of QDs, in which this spin physics are important and can be investigated. Our focus lies on QDs in which the electron spin can be controlled by means of electrostatic potentials also known as gates. In comparison with optically controlled electron spins, scalability is more promising in gated QDs. Moreover, having silicon based QDs in mind, a combination of a quantum computer with conventional computer technology within one device seems feasible. Finally, many groundbreaking experiments on electron spin qubits have been carried out using electrical control.

QDs in GaAs can be considered as the prime example of a whole family of "gated" QDs due to the large number of groundbreaking experiments realized in this material during the past decade. In particular, we will elaborately explain the properties of double QDs due to their importance for these experiments. In this specific setup many techniques to manipulate both the electron spin and the nuclear spins have been developed, some of which we will discuss at the end of this section in more detail. Many of these ideas can be directly transferred to graphene based QDs, once the difficulty of confining an electron, due to Klein-Tunneling, has been overcome. The most important difference of graphene is, however, its low abundance of spin carrying isotopes, which severely changes the spin physics in these QDs. With respect to this last property, graphene can be considered as a prototype of group IV element based QDs.

1.3.1. Quantum dots in specific materials

Quantum dots in AlGaAs/GaAs heterostructures

GaAs QDs are among the technologically most advanced QD realizations, where the fabrication of multi QDs [68] and QDs with additional features such as micro-magnets [69] has been demonstrated. Based on these exceptional experimental prerequisites, many important steps towards the realization of a solid state quantum computer have been taken, such as single electron occupation of the QDs as well as single- and two-(spin) qubit operations. Moreover, even control over the nuclear spin environment has been demonstrated, which we will review in Section 1.3.3 below.

GaAs QDs are formed in a 2DEG emerging at the interface of AlGaAs and GaAs, where free electrons are introduced by doping the AlGaAs layer with Si, cf. Fig. 1.3. By means of electron beam lithography, electrostatic gates are grown on top of these heterostructures, which are used to deplete the 2DEG locally via electrostatic potentials, as illustrated in Fig. 1.3 c). These potentials also function as electrostatic gates, which allow to manipulate the electron spin as described in the previous section.

The electron spin can be further controlled through external magnetic fields, where the effective g-factor $g^* = -0.44$ in the Zeeman Hamiltonian in Eq. (1.9) is negative. Moreover, electron spins in a double QDs experience an effective spin-spin interaction. If the energy scale associated with the hopping of the electrons is much smaller than the charging energy of the respective QDs, than this effective interaction is of the Heisenberg form

$$\hat{H}_J = J(\{V_i\})\, \hat{\boldsymbol{S}}_1 \cdot \hat{\boldsymbol{S}}_2\,, \tag{1.21}$$

whose strength can be changed via the electrostatic potentials $\{V_i\}$ of the gates. The physics of this effective interaction will be explained in more detail in Section 1.3.2.

The most important intrinsic spin interaction is provided by the HI. In order to find the effective HI for GaAs, its band structure has to be considered, which is described within the envelope function approximation (EFA). For an electron in the conduction band, the Bloch part of the orbital wave function in Eq. (1.1) is of s-type and, thus, only the contact HI given in Eq. (1.13) contributes [43]. The anisotropic HI $\hat{h}_2$ given in Eq. (1.15) vanishes due the symmetry of the s-orbital and the third contribution $\hat{h}_3$ is zero due to the missing angular momentum $L = 0$ for an s-state. Calculating the expectation value of the HI within the EFA, thus, yields [43, 54]

$$\hat{H}_{\mathrm{HI}} = \sum_{k=1}^{K} \underbrace{A_{\mathrm{HI}}\, v_0\, |\phi(\boldsymbol{r}_k)|^2}_{\equiv A_k}\, \hat{\boldsymbol{S}} \cdot \hat{\boldsymbol{I}}_k = \sum_{k=1}^{K} A_k [\hat{S}_z \hat{I}_{k,z} + \frac{1}{2}(\hat{S}_+ \hat{I}_{k,-} + \hat{S}_- \hat{I}_{k,+})]\,, \tag{1.22}$$

where we sum over the contributions of all nuclear spins in the QD. Since in GaAs different atoms and isotopes are involved, the HI coupling constant A_{HI} depends on the species of the k-th atom. In most theoretical studies of the HI in QDs, however, this dependence is neglected and an average value A_{HI} is used as described in Section 1.2.2. We will also adopt this scheme and we will use this average value, henceforth. The product of the envelope function $|\phi(\boldsymbol{r}_k)|^2$ with the atomic volume v_0, which is half the volume of the unit cell, gives the probability to find the electron at the site $\boldsymbol{r}_k$ of the atom. We

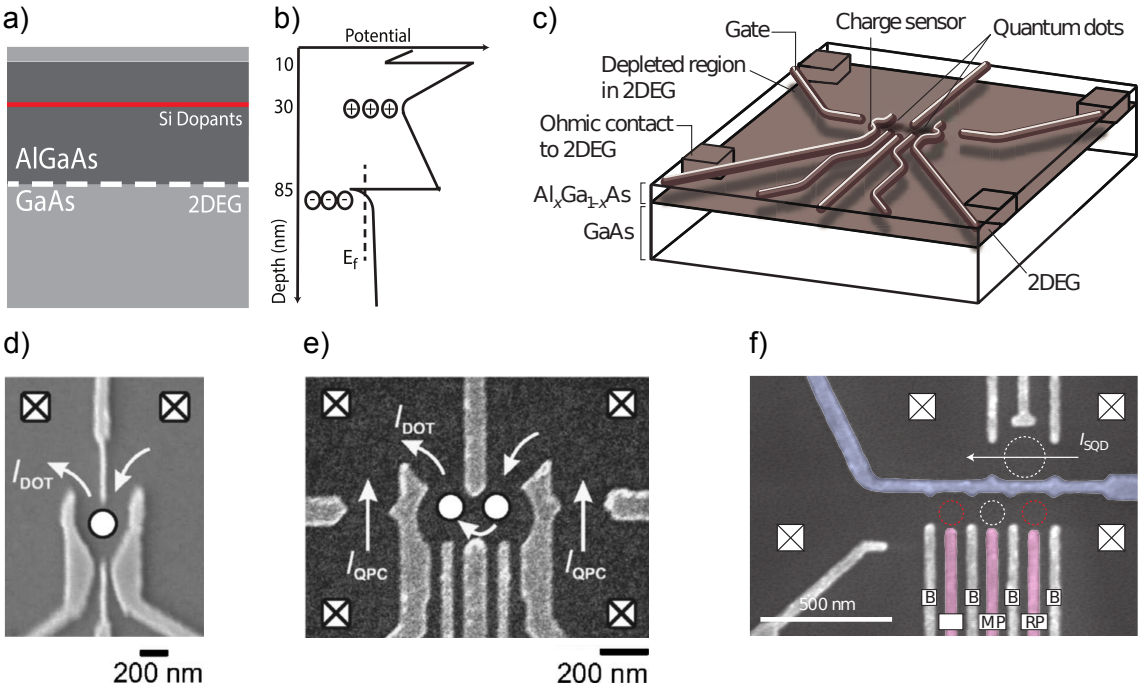

Figure 1.3. **a)**: An AlGaAs/GaAs heterostructure exhibiting a 2DEG at the interface. **b)**: The specific form of the conduction bands of AlGaAs and GaAs cause the additional electrons of the Si dopants to accumulate at their interface. **c)**: By means of electrostatic gates on top, this 2DEG can be locally depleted forming a quantum dot. By this procedure, single **d)**, double **e)**, and multiple **f)** QDs can be realized. (Scanning electron micrographs.) *Figures **a)** and **b)** reprinted from [68], ©2013 WILEY-VCH Verlag GmbH & Co. KGaA, Weinheim, figure **c)** adapted by permission from Macmillan Publishers Ltd: [70], ©2013, figures **d)** and **e)** reprinted with permission from [9], ©2007 American Physical Society, figure **f)** reprinted by permission from Macmillan Publishers Ltd: [71], ©2013.*

have defined the usual raising and lowering operators $\hat{S}_\pm = \hat{S}_x \pm \mathrm{i}\hat{S}_y$ and $\hat{I}_\pm = \hat{I}_x \pm \mathrm{i}\hat{I}_y$, respectively, and the HI coupling constant is given by $A_{\mathrm{HI}} = 85\mu\mathrm{eV}$, cf. Tab. 1.1. Obviously, this interaction strongly depends on the probability $|\phi(\boldsymbol{r}_k)|^2$ to find the electron at the position of the respective nuclear spin. Typically, the experiments are carried out using dilution refrigerators, which cool the system down to the mK regime [24, 39, 40, 72]. The corresponding thermal energies are on the order of μeV and, thus, well below the orbital energies of the electron, which are on the order of 1 mK [9, 23, 24, 72]. Hence, only the ground state and low lying excited states have to be considered. The envelope function of the ground state is typically approximated by a Gaussian [73, 74, 75, 76]

$$\phi(\boldsymbol{r}_k) = \phi_0 \exp\Big[-\frac{1}{2}\Big(\frac{r_k}{R_D}\Big)^2\Big], \tag{1.23}$$

where a circular QD with radius R_D is assumed and $r_k = |\boldsymbol{r}_k|$. Consequently, the normalization factor is given by $\phi_0 = \frac{1}{\sqrt{\pi}R_D}$. This envelope function is not the exact electron wave function, but should give a good approximation to the precise solution. The most important aspects, which are captured by this specific choice are the absence of nodes in the ground-state, a peak of the wave function in the center as well as a strong decay inside the barriers.

As a consequence of this choice, the probability $v_0|\phi(\boldsymbol{r}_k)|^2$ to find the electron at a site with a distance r_k from the center is only of considerably magnitude within the radius R_D, which defines the number of atoms within the dot: $N_{\mathrm{sites}} = \frac{\pi R_D^2}{v_0}$. Evidently, the number of atoms is equal to the number of nuclear spins $K = n_I N_{\mathrm{sites}}$, since the abundance of spin carrying isotopes is $n_I = 1$ in GaAs. However, in the next section, we consider graphene, in which only the ^{13}C-isotopes carry a spin with $n_I \approx 0.01$. According to Eq. (1.23), the probability distribution of the electron $v_0|\phi(\boldsymbol{r}_k)|^2$ and, consequently, also the coupling constants of the HI

$$A_k = A_{\mathrm{HI}}\, v_0\, |\phi(r_k)|^2 = \frac{A_{\mathrm{HI}}}{N_{\mathrm{sites}}} \exp\Big[-(\frac{r_k}{R_D})^2\Big] = \frac{n_I A_{\mathrm{HI}}}{K} \exp\Big[-(\frac{r_k}{R_D})^2\Big] \tag{1.24}$$

scale with the inverse of the number of atoms. Thus, the typical energy scale of the HI between the electron and a single nuclear spin in the center of the QD is given by $A^s_{\mathrm{HI}} = n_I A_{\mathrm{HI}}/K$. This energy scale also defines a typical timescale $\tau^s_{\mathrm{HI}} = 2\hbar/A^s_{\mathrm{HI}}$, which is on the order of $\tau^s_{\mathrm{HI}} = 1\,\mu$s for GaAs. The restriction to atoms with a sufficiently large probability density of the electron effectively corresponds to the introduction of a constant cutoff C, where the following relation holds

$$\frac{|\phi(\boldsymbol{r}_k)|^2}{|\phi_0|^2} > C\,. \tag{1.25}$$

This point of view is especially convenient for a numerical simulation of the spin dynamics in a QD as employed in Chapter 5, where we choose $C = 10^{-6}$. An illustrative example of such a cutoff is shown in Fig. 1.5 b).

The typical diameters of GaAs QDs are in the range of 10 nm to 100 nm [9], for which the number of atoms in the QD is on the order of $K \sim 10^4$ to 10^6 [22]. Since all atoms in GaAs carry a nuclear spin, the number of nuclear spins K is equal to this number. In

many cases, it is convenient not to take each nuclear spin individually into account, but to consider the collective effect of all spins by an effective magnetic field operator

$$\hat{\boldsymbol{h}} = \sum_{k=1}^{K} A_k \hat{\boldsymbol{I}}_k \approx g^* \mu_B \hat{\boldsymbol{B}}_{\mathrm{nuc}} \,. \tag{1.26}$$

Many experimental results can be understood in terms of the quantity [72] $B_{\mathrm{nuc}} = \sqrt{\langle \hat{\boldsymbol{B}}_{\mathrm{nuc}}^2 \rangle}/\sqrt{3}$, where the expectation value $\langle \ldots \rangle$ is taken with respect to the nuclear spin states. This effective field is known as the Overhauser field, whose size is $B_{\mathrm{nuc}} = \frac{A_{\mathrm{HI}}}{g^* \mu_B} \approx 5$ T for a fully polarized spin bath in GaAs.

However, in typical experiments, the nuclear spins exhibit a random distribution of their spins. Since the number K of nuclear spins is large, the effective nuclear magnetic field being a sum of these magnetic moments can be calculated using the central limit theorem. According to this theorem, we find a Gaussian distribution for the values of the nuclear magnetic field with a vanishing average value and a root mean square value of its fluctuations proportional to $\sqrt{K}$. Since the dynamics of the nuclear spins is much slower than the electron spin dynamics, these fluctuations are quasi constant and the typical nuclear magnetic field seen by the electron is on the order of $B_{\mathrm{nuc}} = \sqrt{K} \frac{A_{\mathrm{HI}}}{K g^* \mu_B} \approx 1$ mT for $K = 10^6$ nuclear spins. Due to this statistical nature of the nuclear magnetic field, the local nuclear magnetic fields of two neighboring QDs are different, which leads to different spin dynamics in each dot. We will present a scheme to manipulate electron spins by means of such a difference in Section 1.3.3 below.

Besides the HI also SOI mediated spin relaxation with the phonon bath could be relevant for GaAs QDs as explained in Section 1.2.4. However, the SOI is strongly suppressed due to the reduced dimensionality of the QDs leading to unusually low spin flip rates [64, 65]. As a result, the related timescales τ_{SOI} of these effects are at least on the order of ms [77] for experimentally realistic parameters, which is well above the timescales of the HI induced electron spin dynamics [43, 61, 73, 74, 75, 76, 78]. As a consequence, the SOI has been neglected for most investigations on the electron spin dynamics in GaAs QDs.

Graphene quantum dots

Although GaAs QDs have proved to be an outstanding system for the realization of quantum dots, there are reasons to consider other materials like graphene [84]. The most important advantage of graphene QDs over GaAs is the low natural abundance of spin carrying isotopes, which carbon shares with silicon and germanium. Among the group IV elements, carbon additionally exhibits the smallest HI coupling constant, which is about one order of magnitude smaller than in silicon and about two orders of magnitude smaller than in GaAs, cf. Tab. 1.2. Moreover, graphene is considered to have a comparably weak SOI in contrast to CNTs. Finally, graphene is a truly two-dimensional condensed matter system with strong confinement of the electrons perpendicular to the plane of the graphene sheet. Due to the honeycomb structure of its atomic lattice, graphene features very interesting electronic properties [85, 86], which allow the implementation of efficient electric circuits to run future quantum devices due to a high mobility of the charge carriers. Finally, additional degrees of freedom give rise to interesting possibilities to construct

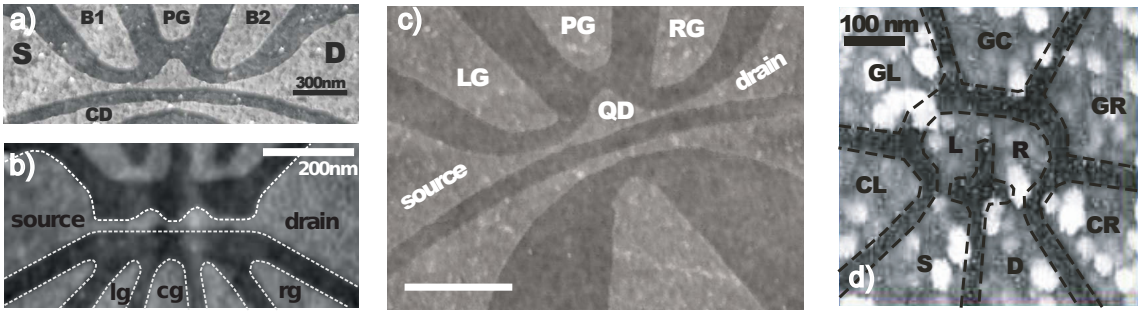

Figure 1.4. Atomic force micrographs of single and double graphene QDs realized on a silicon substrate. **a)** and **c)**: QDs made from single-layer graphene. Nearby the QDs additional electrostatic gates (B1,B1,Lg,Pg,RG) have been created, which allow to tune the devices. Below the QDs a graphene nanoribbon serves as a charge detector (CD). The QDs are contacted by source and drain also formed in graphene. Scale bar in c) denotes 500 nm. **b)**: A double QD realized in bilayer graphene. **d)**: A double QD formed in single-layer graphene. *Figure **a)** reprinted with permission from [79], ©2008 AIP Publishing LLC, figure **b)** reprinted from [80], ©2012 WILEY-VCH Verlag GmbH & Co. KGaA, Weinheim, figure **c)** reprinted with permission from [81], ©2010 American Physical Society, figure **d)** reprinted with permission from [82].*

		GaAs	Graphene
N_{sites}		10^6	10^5
n_I		1	0.01
$K = n_I\, N_{\text{sites}}$		10^6	10^3
A_{HI}	[μeV]	85	0.6
$B_{\text{nuc}} = n_I A_{\text{HI}}/g^*\mu_B$	[T]	3.5	2.6×10^{-3}
$\tau^s_{\text{HI}} = 2\hbar K/n_I A_{\text{HI}}$	[μs]	1	100

Table 1.2. Comparison of the most important parameters of GaAs and graphene. The total number of nuclei N_{sites} is estimated for a QD of typical size $R_D = 50$ nm. While all nuclei in GaAs carry spin, the abundance n_I of ^{13}C can in principle be modified, where the natural abundance is only $n_I = 0.01$. The HI constant A in GaAs is about two orders of magnitude higher than in graphene (with $n_I = 1$) demanding lower external magnetic fields $B_0 \gg B_{\text{nuc}}$ and leading to a prolonged typical hyperfine timescale τ^s_{HI}. *Table adapted with permission from [83], ©2012 American Physical Society. All rights reserved.*

quantum devices. For instance, there is an interesting proposal of a tunable Heisenberg interaction similar to Eq. (1.21) [23, 46, 87] between arbitrary electron spins in arrays of graphene QDs.

However, these electronic properties also make the realization of QDs in graphene more challenging. The low energy physics in graphene is dominated by electronic states around two inequivalent K-points $\boldsymbol{K}$ and $\boldsymbol{K}'$ in the Brillioun zone known as valleys [86]. Near these valleys, the spectrum is linear resembling the one of massless Dirac fermions. As a consequence of this effective relativistic behavior, Klein tunneling [88] through potential barriers occurs, which makes it impossible to confine electrons in graphene just by using electrostatic potentials as done in GaAs heterostructures. Moreover, the occurrence of the additional valley degree of freedom of the orbital part of the electron wave function can have serious implications on the spin physics in graphene double QDs [89].

One way to construct QDs by means of electrostatic potentials similar to GaAs, is to create a finite energy gap in the spectrum [23, 47, 90, 91], which can, for instance, be induced in single-layer graphene by the substrate [92, 93] or in bilayer graphene by applying different potentials to the layers [94, 95, 96, 97]. Other proposals involve quasi-bound states and magnetic confinement of the electrons [23]. For more information on the realization of graphene nanostructures and the confinement of electrons within them, we also refer to the review articles by Recher and Trauzettel [23] and Rozhkov et al. [38]. Finally, graphene QDs can be carved out of graphene flakes by a chemical or mechanical treatment, which is the experimentally most applied approach [39, 98, 99, 100, 101, 102, 103], cf. Fig. 1.4. However, so far the resulting QDs typically suffer from rough edges and and defects stemming from vacancies, adatoms and irregularly shaped substrates, which severely reduce the functionality of the QDs [39]. In particular, the few electron regime and the Pauli blockade regime have not yet been reached, which are both essential for effective characterization and operation of QDs as explained in Section 1.3.2.

Typical diameters of graphene QDs are on the order of tens to hundreds of nanometers resulting in 10^3 to 10^5 carbon atoms within the QD. Assuming a natural abundance of spin carrying ^{13}C of 1%, there are $K = 15$ to $K = 1500$ nuclear spins present in the QD. Thus reducing the abundance of ^{13}C by only two orders of magnitude leads to very small spin baths even in the case of rather large QDs. Recently, ultra small graphene QDs with diameters in the 1 nm range were fabricated using electroburning [53], which should also host only very few nuclear spins. In contrast, a complete enrichment with ^{13}C will lead to large nuclear spin baths with $K = 10^5$ nuclear spins. Altogether, these considerations show that graphene quantum dots allow to study both the spin physics in very small and very large nuclear spin baths and to possibly identify a crossover of both regimes. In the second part of this Thesis, we will explore both regimes in Chapters 4 and 5, respectively.

The peculiarities of graphene also have direct consequences on the relevant spin interactions. The effective Hamiltonian of the HI in graphene can be obtained within the EFA [58] analogously to GaAs. In graphene, the conduction band is mainly formed by the p_{2z} orbital, which is used to describe the electron wave function at an arbitrary ^{13}C atom. Thus, the Bloch part of the wave function $|u_{m_S}\rangle$ can be described by a hydrogenic orbital with an effective central potential of charge $Z_{^{13}C} = 3.16$, whose angular part is given by the spherical harmonic $|Y_1^0\rangle$. This choice implicitly assumes a tight binding of the electron around the carbon atoms, whose validity has been verified by Fischer et al. [58].

Since the radial part of this orbital vanishes at the origin, the contact HI in Eq. (1.11) does not contribute. Further, the coupling of the nuclear spins to the orbital angular momentum vanishes as described in Eq. (1.16) identically, since the expectation value of $\hat{h}_3$ with respect to the orbital part of the wave function is zero. Thus, the only contribution to the HI in graphene stems from the anisotropic part $\hat{h}_2$ in Eq. (1.15), which yields an anisotropic effective HI

$$\hat{H}_{\mathrm{HI}} = \sum_{k=1}^{K} A_k \sum_{\mu,\nu} \overleftrightarrow{A}_{\mu\nu} \hat{S}_\mu \hat{I}_{k,\nu} \,, \tag{1.27}$$

where the indices μ and ν run over spatial coordinates x, y, z and the coupling constants $A_k \propto A_{\mathrm{HI}}$ are defined in Eq. (1.24). The energy scale of this interaction is given by $A_{HI} = 0.6\,\mu$eV [58]. The Hamiltonian in Eq. (1.27) forms a spherical tensor [104] of rank 2, where the matrix $\overleftrightarrow{A}$ takes into account the anisotropy of the HI in graphene [58]. Due to the symmetry of the p_{2z} orbital, the Hamiltonian takes its simplest form if we choose the z-component of the spins to be perpendicular to the graphene plane as illustrated in Fig. 1.5:

$$\hat{H}_{\mathrm{HI}} = \sum_{k=1}^{K} A_k \, [\hat{S}_z \hat{I}_{k,z} - \frac{1}{4}(\hat{S}_+ \hat{I}_{k,-} + \hat{S}_- \hat{I}_{k,+})] \,. \tag{1.28}$$

Physically, this means that the spin components in x- and y-direction are not conserved. If we consider a coordinate system, which is tilted by an angle β around the y-axis[7] with respect to the graphene plane, the matrix $\overleftrightarrow{A}$ is given by

$$\overleftrightarrow{A} = \overleftrightarrow{A}(\beta) = \begin{pmatrix} \frac{1}{4}[1 - 3\cos(2\beta)] & 0 & -\frac{3}{4}\sin(2\beta) \\ 0 & -\frac{1}{2} & 0 \\ -\frac{3}{4}\sin(2\beta) & 0 & \frac{1}{4}[1 + 3\cos(2\beta)] \end{pmatrix} . \tag{1.29}$$

We will see, that this anisotropy has profound consequences on the spin dynamics in Chapters 4 and 5.

If the temperature is very low, the electron occupies only the orbital ground-state of the QD, whose envelope function is again approximated by the Gaussian function in Eq. (1.23), since the same requirements as for the ground-state of a GaAs QD apply. This assumption is also in agreement with a recent experiment investigating the wave function of a graphene QD with soft confinement [106]. As a consequence, the HI coupling constants are given by Eq. (1.24) as in the case of GaAs. However, since only a small portion of the carbon atoms carries a nuclear spin, these coupling constants are effectively diminished by the abundance $n_I < 1$ according to Eq. (4.8) if we express them in terms of the number of nuclear spins $K = n_I N_{\mathrm{sites}}$. Aside from this additional reduction, the HI constant A_{HI} in graphene is already two orders of magnitude smaller than in GaAs. Since the typical timescale of the electron spin dynamics is set by $\tau^s_{\mathrm{HI}} = \frac{2\hbar K}{n_I A_{\mathrm{HI}}}$, appreciable decoherence will set in on longer timescales. Moreover, typically magnetic fields $B_0 \gg B_{\mathrm{nuc}} = \frac{n_I A_{\mathrm{HI}}}{g^* \mu_B} = 2.6$ mT well

[7] Since we consider circular shaped QDs, any axis in the graphene plane can be considered.

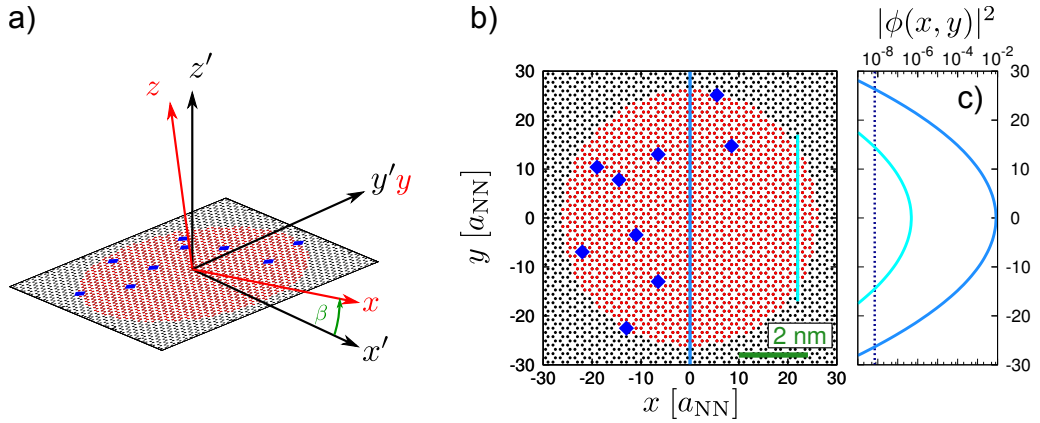

Figure 1.5. **a)**: The HI Hamiltonian takes its simplest form in the reference frame defined by the geometry of the graphene plane (black axes). The consequences of its anisotropy are apparent in the rotated coordinate system (red axes), in which we represent all operators. **b)**: A graphene QD (red sites) for a Gaussian envelope function with $K = 10$ uniformly random distributed ^{13}C atoms (blue squares). The QD is defined via the cut-off relation in Eq. (1.25) with $C = 10^{-6}$. All spatial coordinates are measured in units of the nearest-neighbor distance a_{NN}. **c)**: The envelope function for fixed $x = 0$ and $x = 22\, a_{\mathrm{NN}}$, respectively. The dashed line indicates the cut-off. *Figure adapted with permission from [105], ©2013 American Physical Society. All rights reserved.*

above the nuclear magnetic field are used to stabilize the electron spin. Hence, graphene allows to use significantly smaller external fields. A comparison of important properties of graphene and GaAs QDs is presented in Tab. 1.2.

So far, we have only considered the effect of the HI on the electron spin. The HI in graphene gives also rise to a valley scattering, which is caused by the short range nature of the r^{-3} potential in Eq. (1.15). We have investigated the resulting momentum dependence of the coupling constant $A_{\mathrm{HI}} = A_{\mathrm{HI}}(\mathbf{Q})$, where $\mathbf{Q}$ is the difference between incoming and outgoing momentum. Assuming, that the most important contributions arise from on-site terms [58], we estimate, that the valley mixing $\mathbf{Q} = \Delta\mathbf{K} = \mathbf{K} - \mathbf{K}'$ and valley conserving $\mathbf{Q} = 0$ processes are of comparable strength, which agrees with the analysis by Pályi and Burkard [89]. Hence, the valley scattering is irrelevant only if it is forbidden due to energy conservation. From Eq. (4.8) and Tab. 1.1, we know that the energy scale of a single scattering processes between the electron and a nuclear spin is on average of order $10^{-6}\,\mu$eV. In typical graphene QDs, we expect a non-zero valley splitting $\Delta_{\mathbf{K},\mathbf{K}'}$ because of several mechanisms. First, every experimental setup will have deviations from an "ideal" setup, e.g., roughness of the boundaries or adatoms, which couple the valleys. But even in an ideal experiment, one can expect a valley-splitting due to the presence of an external magnetic-field in combination with a finite mass term induced by the substrate [47]. Furthermore, if we assume a QD made of a semi-conducting graphene ribbon with armchair boundaries, the valley degeneracy is also lifted by $\Delta_{\mathbf{K},\mathbf{K}'} \sim 10$ meV [23]. Thus, the valley degeneracy should be lifted for many experimentally relevant setups. Finally, as mentioned in Section 1.2.1, the valley degree of freedom is irrelevant if only one electron spin in a single QD is considered. As a consequence, the valley degree of freedom will be neglected henceforth.

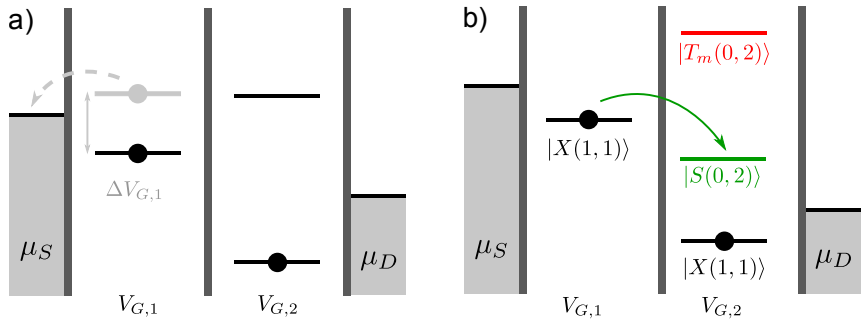

Figure 1.6. Orbital energy levels of double QDs. **a)**: The gate potentials $V_{G,1}$ and $V_{G,2}$ of each QD allow to control the position of the energy levels with respect to the chemical potentials μ_S and μ_D of source and drain, respectively. Hence, shifting these energy levels allows to change the number of electrons (circles) in the double QDs. A current from source to drain is prohibited due to the Coulomb interaction between the electrons, which raises the second energy level of the right QD. **b)**: The gate potentials $V_{G,1}$ and $V_{G,2}$ allow to bring the system in the Pauli blockade regime. In the $(1,1)$ charge configuration, the singlet and triplet states ($X = S, T_m$) are (almost) degenerate. The electron in the left QD can only tunnel if the two electrons form a singlet $|S(1,1)\rangle$. If they are in a triplet state $|T_m(1,1)\rangle$, an orbital of higher energy has to be occupied in the final state $|T_m(0,2)\rangle$ due to the Pauli exclusion principle and, hence, the tunneling is suppressed.

Besides the HI, also the SOI can affect the dynamics of the electron spin. A figure of merit to estimate the relevance of SOI is the spin life-time T_1, over which the electron spin relaxes due to the SOI mediated interaction with the phonon bath. This lifetime is only well defined if this relaxation follows an exponential decay. Considering graphene nanoribbons [107, 108] and QDs [109], this timescale has been found to exceed milliseconds for external magnetic fields below $B_0 \lesssim 1$ T. Since the scattering rate strongly depends on the matching of the electron Zeeman energy with the phonon energy, this timescale is even larger for smaller fields. Additionally, also the decoherence time T_2 has been investigated for graphene QDs [109], which is predicted to be on the same order of magnitude. Besides more specific factors such as the geometry of the graphene structure and time reversal symmetry, these remarkably long times are traced back to the weak SOI in (flat) graphene. As we will see, the effects investigated in this Thesis have typical timescales well below milliseconds, such that neglecting the SOI is justified. Finally, the weakness of SOI in graphene is also reflected by the fact that the electron g-factor is not renormalized. Thus, the bare g-factor of the electron $g = 2$ enters the Zeeman Hamiltonian in Eq. (1.9), which is also in agreement with recent transport experiments [110].

1.3.2. Properties of gated quantum dots

As stated above, the most important examples of gated single and double QDs are based on GaAs heterostructures. Accordingly, most of the ideas described below have been developed and tested in these systems. Nevertheless, most of these techniques are readily transferred to other QDs realized in graphene, CNT, nanowires, and silicon. The common feature of all of these setups is the possibility to control the chemical potentials of the QDs by surrounding electrostatic potentials, as shown in Figs. 1.1, 1.3 and 1.4. Adjusting

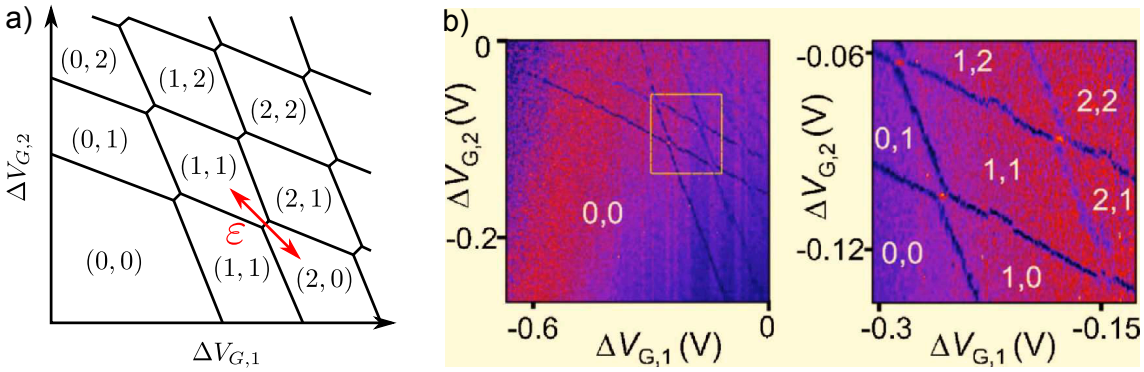

Figure 1.7. A charge stability diagram (n_L, n_R) shows the number of electrons on the left (n_L) and right (n_R) QD, respectively, as a function of the voltages $\Delta V_{G,1}$ and $\Delta V_{G,2}$ applied on the respective gates. **b)**: Differential conductance $\frac{\mathrm{d}I_{\mathrm{QPC}}}{\mathrm{d}V_{G,1}}$ through a QPC as a function of the voltages $\Delta V_{G,1}$ and $\Delta V_{G,2}$ for double QD in AlGaAs/GaAs [111]. *Figures **b)** reprinted with permission from [9], ©2007, American Physical Society. All rights reserved.*

the voltages of the central gate, the source and the drain, respectively, allows to control the flow of electrons through the QD and, consequently, to manipulate the number of electrons on the dot, as illustrated in Fig. 1.6. If additionally an external magnetic field is applied, the degenerate electron spin states split up by their difference in the Zeeman energy. In addition to the QD itself, oftentimes quantum point contacts (QPC) are defined nearby. Since the current through a QPC is very sensitive to changes of the local Coulomb potentials [112], they function as very sensitive electrometers measuring the charge and, thus, the number of electrons on the QD non-invasively. A scanning electron micrograph of such a QPC is, for instance, shown in Fig. 1.3 e). Besides the charge, also a measurement of the spin of the electrons is needed according to the DiVincenzo criteria. However, the magnetic field originating from the electron spin is on the order of $B_S \sim 10^{-12}$ T at a distance of 1 μm away from the electron spin. Since the magnetic moment of the electron spin is, therefore, too small to be measured directly, a so-called spin-to-charge conversion is needed, which allows to determine the spin state indirectly via charge measurements. Indeed, various methods for such a spin-to-charge conversion have been proposed [9, 113] such as a technique developed by Elzerman et al. [114], where the energy difference of the spin states is used to achieve single-shot readout in single QDs. Another important method is to tune the energy levels of two coupled QDs into the so-called spin- or Pauli blockade regime, in which the tunneling of the electrons from one QD to the other is spin-dependent as we discuss below.

However, the interest in these double QDs is not only based on the existence of Pauli blockade. In addition, these systems are the smallest possible realization of a qubit array, in which two-spin operations can be investigated. Further, the extension of the double dot setup to lines of several QDs is, in principle, straightforward.[8] These facts make the double QDs a very interesting setup, whose most important properties are summarized in

[8] Since source and drain couple only to the outer QDs, the loading of a desired number of electrons, however, becomes more and more difficult for longer chains of QDs. Yet, these difficulties may be overcome for more advanced designs of multi dot setups [22].

the following.

A double QD can be realized by putting two QDs next to each other and connecting them via a tunable tunnel barrier as shown in Fig. 1.3 e). By changing the height of this potential barrier, the tunneling coupling t_c of the two electrons can be tuned during the experiment as suggested by Loss and DiVincenzo [13] and experimentally realized by Bertrand et al. [115]. In most experiments, however, the tunnel coupling is kept at a fixed value, while the levels of the two dots are shifted with respect to each other via electrostatic gates. If in addition the chemical potentials of source and drain are fixed, a variation of the electrostatic gates $\Delta V_{G,1}$ and $\Delta V_{G,2}$ of the dots allows to control the number of electrons in the double QD system as shown in Fig. 1.6 a). This setup also allows to control the current through the double dot by means of the so-called Coulomb blockade. In this regime, the strong Coulomb interaction between the electrons within a QD prohibits a transition of the electron from one dot to the other one as illustrated in Fig. 1.6 a).

If the charge configuration (n_L, n_R) consisting of the number of electrons on the left (n_L) and right (n_L) QD, respectively, is plotted as a function of these gate voltages a charge stability diagram is obtained as shown in Fig. 1.7. The theoretical diagram in Fig. 1.7 a) obtained by means of the constant interaction model [9, 116] shows a remarkable agreement with experimentally measured charge configurations presented in Fig. 1.7 b). The absence of charge transition lines in a comparably large region allows to experimentally identify the region in which the QDs are completely depleted. The number of electrons in different configurations can then be reached with certainty by counting the number of charge transitions lines. Once a desired number of electrons in the setup is reached, the two voltages $V_{G,1}$ and $V_{G,2}$ can be tuned with respect to each other such that the total number of electrons is constant as illustrated in Fig. 1.7 a). This (de)tuning is usually described by the detuning parameter $\varepsilon = \varepsilon(\Delta V_{G,1}, \Delta V_{G,2})$.

The most relevant case is the two electron configuration. For the $(1,1)$ charge state, the two electrons can be described in the basis of singlet

$$|S(1,1)\rangle = (|\Downarrow\Uparrow\rangle - |\Uparrow\Downarrow\rangle)/\sqrt{2} \tag{1.30}$$

and triplet spin states

$$|T_+(1,1)\rangle = |\Uparrow\Uparrow\rangle \tag{1.31}$$

$$|T_0(1,1)\rangle = (|\Downarrow\Uparrow\rangle + |\Uparrow\Downarrow\rangle)/\sqrt{2} \tag{1.32}$$

$$|T_-(1,1)\rangle = |\Downarrow\Downarrow\rangle\,, \tag{1.33}$$

which are degenerate for zero magnetic field and a vanishing tunnel coupling between the dots. However, this degeneracy is generally lifted. First, in most experiments, an external magnetic field $\boldsymbol{B}_0$ is applied, which splits off the $|T_\pm\rangle$ triplets from the remaining triplet state $|T_0\rangle$ and the singlet $|S\rangle$. Second, also the singlet and triplet states exhibit different energies. For a finite tunnel coupling $t_c > 0$ between the QDs, the singlet and triplet states are separated in energy by an exchange energy $J = 4\frac{t_c^2}{E_C}$ if $t_c \ll E_C$, where E_C is the charging energy of the QDs. However, another mechanism is typically more important. Imagine that the electrons in the two quantum dots feel magnetic fields of

different strength B_L and B_R with $g^*\mu_B|B_{L,R}| \gg J$. In this case, the eigenstates of the corresponding Hamiltonian are no longer the singlet $|S\rangle$ and triplet $|T_0\rangle$ states, but the bare product states $|\Uparrow\Downarrow\rangle$ and $|\Downarrow\Uparrow\rangle$. As we will discuss below, such different magnetic fields $\boldsymbol{B}_L$ and $\boldsymbol{B}_R$ are typically generated by the nuclear spins residing in both QDs. Another possibility to create such a field difference is to build a ferromagnet with an inhomogeneous stray field close to the QDs [69].

For the $(0,2)$ charge state, the situation is different. The ground state is given by the singlet state $|S(0,2)\rangle$ with both electrons in the lowest orbital level of the (right) QD. If the energy levels in both dots are equal, its energy, however, is above the energy of the $|S(1,1)\rangle$ singlet due to the Coulomb repulsion of the two electrons. Also, the triplet states are affected by this additional energy. Moreover, the $(0,2)$ triplet states exhibit even higher energies than the singlet state, because one of the electrons has to occupy an excited orbital state due to the Pauli exclusion principle, which gives rise to a singlet-triplet splitting E_{ST}. This splitting is very important for the hybridization of the charge states $(1,1)$ and $(0,2)$ due to the finite tunnel coupling t_c between the QDs. Since the tunneling processes conserve spin, $(1,1)$ singlet (triplet) states can only couple to $(0,2)$ singlet (triplet) states. For a specific value of the detuning, the energies of $|S(1,1)\rangle$ and $|S(0,2)\rangle$ cross without a coupling of the dots as is illustrated in Fig. 1.8 a). However, for finite $t_c > 0$, this crossing is avoided due to a tunnel splitting of $2\sqrt{2}t_c$, cf. Fig. 1.8 b). The same is true for the triplet states, but due to the singlet-triplet splitting E_{ST} this happens at much larger detuning ε. This observation has two important consequences [9]: First, the charge distribution of the singlet and triplet states is different over a wide range of detunings, where the triplet stays in the $(1,1)$ while the singlet changes from $(1,1)$ to $(0,2)$. This property in fact allows to map these spin states to different charge states. Second, the size of the energy splitting $J = J(\varepsilon)$ between the singlet and the triplet states becomes effectively a function of the detuning ε, which allows for an electrical control of an effective Heisenberg interaction between the two electron spins $\hat{\boldsymbol{S}}_1$ and $\hat{\boldsymbol{S}}_2$:

$$\hat{H}_J = J(\varepsilon)\ \hat{\boldsymbol{S}}_1 \cdot \hat{\boldsymbol{S}}_2\,. \tag{1.34}$$

An important consequence of the conservation of spin in tunneling processes is the phenomenon of a current blockade known as Pauli blockade. Let us assume a specific choice of the chemical potential as depicted in Fig. 1.6 b) and a $(1,1)$ charge configuration. Due to the specific arrangement of the energy levels, the only reachable state with a $(0,2)$ charge configuration is the singlet state $|S(0,2)\rangle$. If the two electrons form a singlet $|S(1,1)\rangle$ in the beginning, the transition to the $(0,2)$ charge state is allowed and a current from left to right is possible. However, if the initial state is a triplet $|T_0(1,1)\rangle$, the Pauli exclusion principle forbids the electron in the left QD to tunnel to the right. Thus, the current from left to right is blocked until the left electron spin has been changed relative to the other spin due to an interaction, for instance, with the nuclear spins. As a consequence, this spin-to-charge conversion can be utilized to measure the spin state of the left electron. A typical experiment to study the spin dynamics of an electron on the left dot would, thus, exhibit the following scheme: 1) Prepare a $(0,2)$ singlet state. 2) Move one electron to the left to obtain $(1,1)$. 3) Let the system evolve for some time. 4) Change the potentials, such that the Pauli blockade regime is fulfilled and measure if the electron tunnels from left to right. Thus, the right electron spin serves as a reference for the left electron spin,

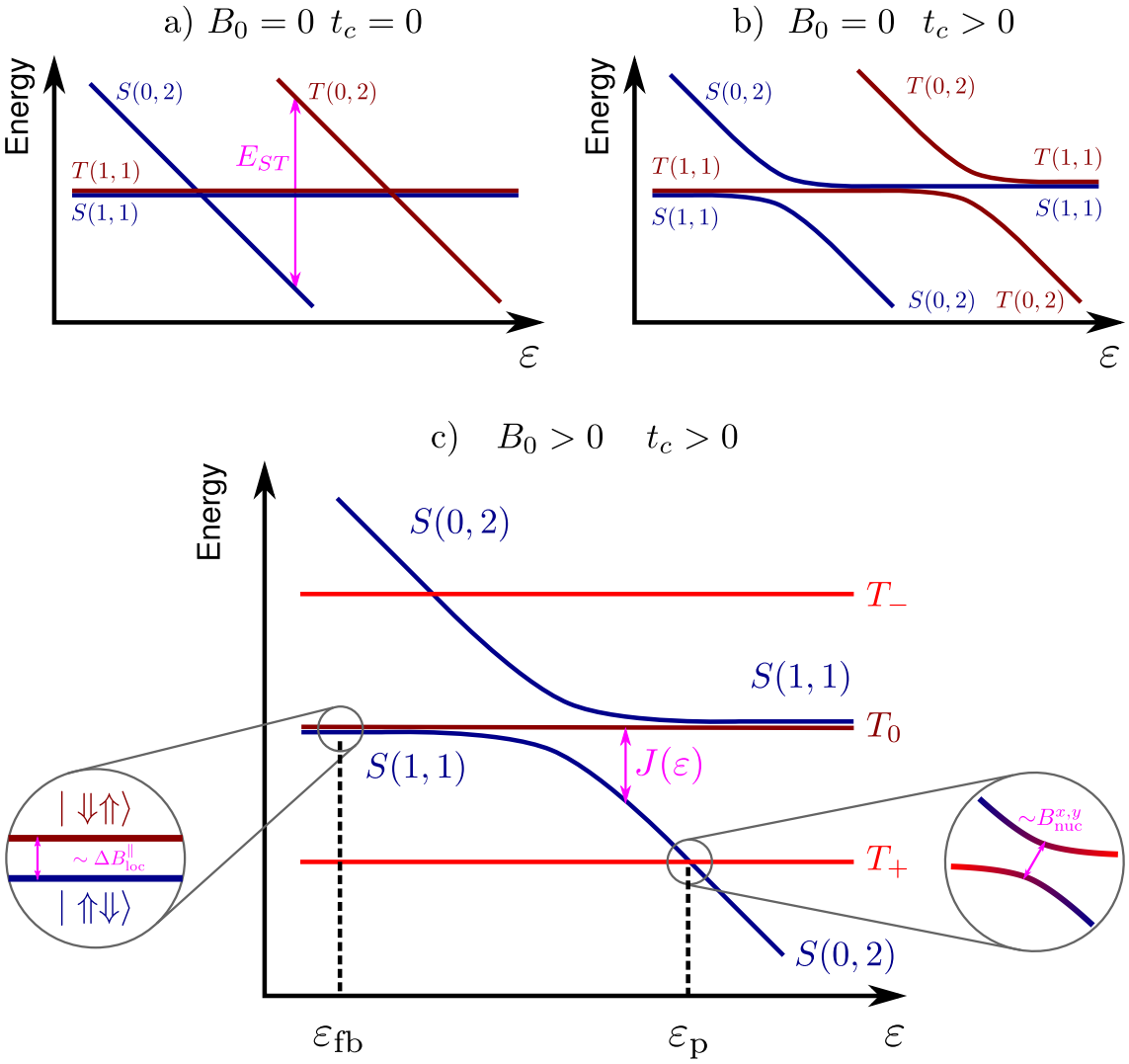

Figure 1.8. **a)**: Energies of the triplet and singlet state without an external magnetic field and no coupling between the dots. The energies are presented as a function of the detuning ε between the levels of the left and right dot. In this case, the detuning is chosen such that the average of the left and right levels is constant explaining the constant energy of $(1,1)$ states. Due to the singlet-triplet splitting E_{ST} the energies of the singlet and the triplets for different charge configurations cross at different values of ε. **b)**: If tunneling between the dots is allowed, this crossing is avoided due to a hybridization of the charge states. **c)**: In presence of a magnetic field B_0, the degeneracy of the triplet states is lifted, where $g^* < 0$ is assumed. *Figure adapted from [9] and [70].*

such that the measurement will reveal the relative change of both spins. Experimentally, this Pauli blockade measurement scheme has turned out to be the most successful electron spin measurement, which enabled many groundbreaking results.

1.3.3. Manipulating spins in quantum dots

Gated double QDs built in the way described above exhibit very interesting possibilities to manipulate the spin of the residing electrons necessary for quantum computation. We will discuss these methods in more detail by reviewing exemplary experiments. Additionally, we will also provide a survey of electron spin control in other systems. Based on the full control of the electron spin, these QDs setups further allow for very powerful schemes to prepare the nuclear spins in a desired state, which include dynamical nuclear polarization, state narrowing and nuclear magnetic resonance. The implementation of tailored nuclear states has originally been motivated by its importance to prolong the electron coherence times. However, as we will show in Chapter 6, precise control of both the electron spin and the nuclear spins also provides an excellent experimental playground to investigate predictions of recent theoretical investigations of closed quantum systems.

Electron spin control

The experiment carried out by Brunner et al. [69] was not the first experiment realizing single electron spin control and two-spin operations, but it is remarkable for several reasons. First, single electron spin manipulation has been achieved by solely using electrostatic gates, which has been possible due to a magnetic field gradient of an attached micro-magnet. Before, time-dependent magnetic fields have usually been employed, which are, however, more challenging to control. Moreover, this magnetic field gradient allows to address electrons in different QDs individually, because electric fields can be sufficiently localized in contrast to magnetic fields. Finally, also two-spin operations have been realized in the very same experimental setup, which allow for the realization of universal quantum gates.

Single electron spin operations are conveniently described in the Bloch sphere representation of the electron spin states

$$|\Psi_S\rangle = \cos\left(\frac{\theta}{2}\right)|\Downarrow\rangle + \sin\left(\frac{\theta}{2}\right)\mathrm{e}^{\mathrm{i}\phi}|\Uparrow\rangle\,, \tag{1.35}$$

where the parameters θ and ϕ can be interpreted as the polar, $0 \leq \theta \leq \pi$, and the azimuthal angle, $0 \leq \phi \leq 2\pi$, describing a point on the unit sphere in $\mathbb{R}^3$ [10] as depicted in Fig. 1.9 a). In order to reach an arbitrary point on the surface of this so-called Bloch-sphere, rotations around two different axes are necessary. Since experiments are typically carried out in the presence of a strong static magnetic field $\boldsymbol{B}_0 = B_0\boldsymbol{e}_z$, the first rotation is simply achieved by a precession of the electron spin around this magnetic field with the Larmor frequency $\omega_0 = \frac{g^*\mu_B B_0}{\hbar}$. A rotation around a second axis can be realized by additionally coupling the electron spin to a time-dependent magnetic field $\boldsymbol{B}_1(t) = B_1(\cos(\omega t)\boldsymbol{e}_x + \sin(\omega t)\boldsymbol{e}_y)$ perpendicular to $\boldsymbol{B}_0$.[9] This interaction induces transitions between $|\Downarrow\rangle$ and $|\Uparrow\rangle$ known as

[9] In a reference frame rotating with the Larmor frequency ω_0, this magnetic field induces a rotation around

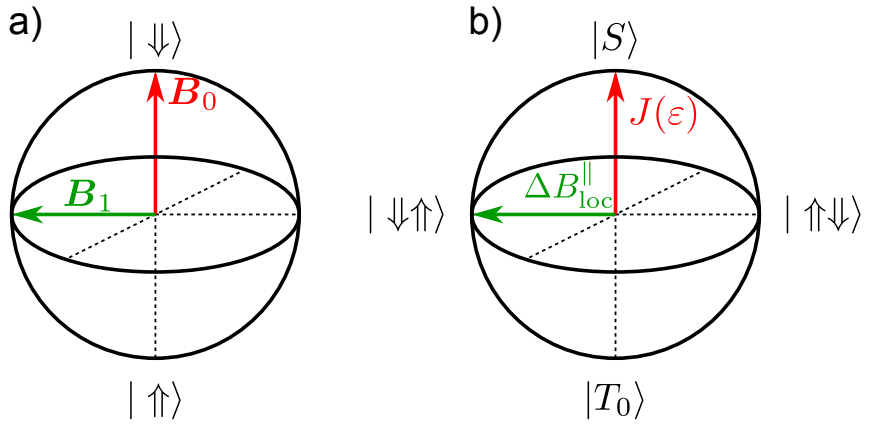

Figure 1.9. **a)**: Bloch sphere representation of a single electron spin. Rotations around the z-axis are achieved by the Larmor precession around the static magnetic field $\boldsymbol{B}_0 = B_0\boldsymbol{e}_z$. Rotations around another axis are obtained by means of Rabi oscillations induced by the time-dependent magnetic field $\boldsymbol{B}_1(t)$. In a reference frame rotating with the Larmor frequency, these oscillations correspond to rotations around the fixed direction of $\boldsymbol{B}_1(t)$. **b)**: Bloch sphere representation of two-spin states. Rotations between the bare product states $|\Downarrow\Uparrow\rangle$ and $|\Uparrow\Downarrow\rangle$ are driven by a finite singlet-triplet exchange energy $J(\varepsilon) > 0$. If the system is tuned towards $J(\varepsilon_{\mathrm{fb}}) \ll g^*\mu_B\Delta B^{\parallel}_{\mathrm{loc}}$, the difference in the nuclear magnetic field $\Delta B^{\parallel}_{\mathrm{loc}}$ allows to induce rotations in the plane of the singlet and triplet states.

Rabi oscillations [104]. Assuming the initial electron spin state to be $|\Uparrow\rangle$, the probability to find it in $|\Downarrow\rangle$ at time t is given by

$$P_{\Uparrow\to\Downarrow}(\omega, t) = \frac{\omega_1^2}{\omega_1^2 + (\omega - \omega_0)^2} \sin^2\left(\sqrt{\omega_1^2 + (\omega - \omega_0)^2}\,\frac{t}{2}\right) \tag{1.36}$$

where we have defined $\omega_1 = \frac{g^*\mu_B B_1}{\hbar}$. If the time-dependent magnetic field is in resonance with the Larmor frequency of the static field, $\omega = \omega_0$, this probability is maximal. In this case, the frequency of the Rabi oscillations $\omega_1 \propto B_1$ is solely determined by the strength of the time-dependent field. The first observation of single electron spin resonance (ESR) has been achieved by directly using the magnetic field of a narrow wire located near a double QD [117]. Since this approach has certain disadvantages as discussed above, it is beneficial to realize ESR by other means. In the experiment by Brunner et al. [69], such a time-dependent magnetic field is created by means of an micro-magnet attached to a double QD. The resulting setup is similar to the one shown in Fig. 1.1 d), where the underlying shape of the electrostatic gates is equivalent to the arrangement depicted in Fig. 1.3. In the presence of the spatially non-uniform magnetic field $\boldsymbol{B}^{\mathrm{M}}(\boldsymbol{r})$ of the micro-magnet, a time-dependent magnetic field can be realized by a spatial displacement of the electron spin induced by microwave pulses applied to the electrostatic gates.[10] Since the local, static magnetic field $B_{\mathrm{loc}} = B_0 + B_z^{\mathrm{M}}(\boldsymbol{r})$ is varying over the extent of the double

a fixed axis, whereas in the laboratory frame, the trajectory of the electron spin along the Bloch sphere is a spiral.

[10] In experiments, typically, only magnetic fields oscillating in one direction can be achieved. Yet, this magnetic field $B_1\cos(\omega t)\boldsymbol{e}_x = \frac{1}{2}[\boldsymbol{B}_1(t) + \tilde{\boldsymbol{B}}_1(t)]$ can be considered as a sum of two magnetic fields

QD, the resonance occurs at different Larmor frequencies $\omega_{\mathrm{loc}} \propto B_{\mathrm{loc}}$ allowing for an individual addressing of electron spins in the left and the right QD, respectively. Besides the magnetic field gradient of a micro-magnet, also SOI [118] and a spatially varying g-factor can be exploited to generate time-depend magnetic fields via microwave pulses. Another interesting approach is to create an effective time-dependent HI [119] by taking advantage of its spatial dependence described in Eq. (1.22). Since, in this case, a flip of the electron is accompanied by a flip of a nuclear spin, this method can be also applied to manipulate the nuclear spins. All these techniques relying on a spatial variation of the electron by electric fields in combination with another interaction are known as electron-dipole spin resonance (EDSR).

While single-spin operations are already a powerful experimental tool to investigate the spin dynamics in QDs, also two-spin operations are necessary for the realization of quantum computation. These operations can be described similar to single-spin operations if we consider the singlet $|S\rangle$ and triplet states $|T_0\rangle$ as a logical qubit. In a Bloch sphere representation, these two states then form the poles, while the bare product states $|\Uparrow\Downarrow\rangle$ and $|\Downarrow\Uparrow\rangle$ lie on opposite sides of the equatorial plane, as illustrated in Fig. 1.9 b). The energy difference of this singlet-triplet two-level system is given by the exchange splitting $J(\varepsilon)$, whose strength can be tuned electrically, as illustrated in Fig. 1.8. A detailed theoretical analysis of the parameters determining this splitting, we refer the reader to Ref. [120]. For a finite $J(\varepsilon) > 0$, the eigenstates[11] for two-spins are the singlet and triplet states. As a consequence, this exchange splitting drives rotations around to the singlet-triplet axis [72]. If we start in the product state $|\Uparrow\Downarrow\rangle$ and wait for a time $\tau_J = \frac{\pi\hbar}{J(\varepsilon)}$, this state is rotated by an angle π to $|\Downarrow\Uparrow\rangle$, which corresponds to a swap of both spins. If we rotate just by half the angle a $\sqrt{\mathrm{swap}}$ gate is achieved, which in combination with the single-spin rotations constitutes a universal set of quantum gates [9, 10].

For completeness, we also mention a second rotation around a different axis, which is provided by the difference $\Delta B^{\parallel}_{\mathrm{loc}}$ of the magnetic fields components parallel to $\boldsymbol{B}_0$ in the left and right QD, respectively. Interestingly, this rotation is also part of an efficient feedback scheme, which allows to manipulate the state of the nuclear spins as we explain below. If the exchange energy is tuned to $J(\varepsilon_{\mathrm{fb}}) \ll g^*\mu_B \Delta B^{\parallel}_{\mathrm{loc}}$, cf. Fig. 1.8, the eigenstates of the corresponding Hamiltonian are no longer the singlet and the triplet state[11], but the bare product states $|\Downarrow\Uparrow\rangle$ and $|\Uparrow\Downarrow\rangle$, respectively. Due to the magnetic field difference between the left and the right QD, the resulting Larmor frequencies cause a relative rotation of the spins with respect to each other, which in turn gives rise to a rotation of the two-spin states around the $|\Uparrow\Downarrow\rangle$-$|\Downarrow\Uparrow\rangle$ axis. Even without a micro-magnet, such rotations can be realized due to the presence of the nuclear spins. The statistical nature of the nuclear magnetic field originating from the HI gives rise to two different magnetic fields $\boldsymbol{B}_{\mathrm{nuc},L}$ and $\boldsymbol{B}_{\mathrm{nuc},R}$ in the left and right QD[12], which have been used for the first experimental

$\boldsymbol{B}_1(t) = B_1\cos(\omega t)\boldsymbol{e}_x + B_1\sin(\omega t)\boldsymbol{e}_y$ and $\tilde{\boldsymbol{B}}_1(t) = B_1\cos(\omega t)\boldsymbol{e}_x - B_1\sin(\omega t)\boldsymbol{e}_y$ with frequencies ω and $-\omega$, respectively [104]. But, if $\boldsymbol{B_1}(t)$ is resonant at ω_0, the other part of the magnetic field $\tilde{\boldsymbol{B}}_1(t)$ is off resonance by $2\omega_0$ and can, thus, be neglected according to Eq. (1.36).

[11] In the strict sense, these states are only approximate eigenstates due to the presence of the local magnetic field B_{loc}. The exact eigenstates take into account both the exchange splitting as well as the local magnetic fields.

[12] These are the root mean square values $\boldsymbol{B}_{\mathrm{nuc},L}, \boldsymbol{B}_{\mathrm{nuc},R} \propto \sqrt{K}$ of the random fields, please see the

realization of two-spin operations [112].

Of course, coherent control of single and multiple electron spin states is not limited to gated GaAs QDs. In fact, there is a huge variety of materials in which equivalent methods have been developed. An extensive review on optical control of electron spins in III-V and II-VI QDs is given by Liu et al. [121]. Gate controlled experiments on group IV element QDs include CNTs [40] and silicon devices [42, 122]. Further, Kloeffel and Loss [22] present a broad overview including additional systems such as nanowires.

Dynamical nuclear polarization and state narrowing

Although nuclear spins are generally much more difficult to manipulate due to their weak coupling to external fields, many efforts have been undertaken to accomplish this task all the same. Once control over the nuclear spin states is established, they can serve as long-lived quantum memories [70, 123], in which, for instance, information processed by electron spin quantum computation could be stored. Moreover, strongly polarized nuclear spin baths or baths with a narrowed distribution of contributing states significantly reduce the effect of the HI according to Eqs. (1.22) and (1.28) and, hence, result in longer coherence times of the electron spin. Ironically, such a dynamical nuclear polarization (DNP) or state narrowing (SN) can be accomplished by means of the very same interaction as we show by reviewing an experiment carried out in a GaAs double QD.

All techniques to control the nuclear spin bath by means of the HI rely on the presence of flip-flop terms $\hat{S}_+\hat{I}_{k,-} + \hat{S}_-\hat{I}_{k,+}$ terms. In terms of the nuclear Overhauser field $\boldsymbol{B}_{\mathrm{nuc}}$, this is expressed by the coupling of the electron to $B_{\mathrm{nuc}}^{x,y}$ as indicated in Fig. 1.8 c). Hence, the nuclear spins are polarized by a two step process. First, the electron spin is prepared in a state with defined angular momentum. This momentum is then transferred to the nuclear spins via the HI. If this procedure is repeated many times, an accumulation of angular momentum in the nuclear spin bath is achieved, as long as the pumping rate exceeds the relaxation rate of the nuclear spins. Given the slow dynamics of the nuclear spins in absence of the HI as discussed in Section 1.2.3, large polarizations seem possible both in gated and optically controlled QDs.

However, the involved spin flips are suppressed in finite magnetic fields B_0 due to the large Zeeman splitting of the electron spin unless energy is provided from another source. As mentioned above one possibility is to apply microwave pulses on the electrostatic gates, which generates an effective time-dependent HI [119, 124]. Alternatively, the specific properties of double QDs can be exploited [125], which we discuss in more detail below. By tuning the energy levels of the left and right dot, the detuning can be chosen, such that the singlet state $|S(0,2)\rangle$ of the electrons becomes degenerate with the triplet state $|T_+(1,1)\rangle$ at $\varepsilon = \varepsilon_{\mathrm{p}}$ as illustrated in Fig. 1.8.

Typically the system is initialized with $\varepsilon \gg \varepsilon_{\mathrm{p}}$, for which the singlet $|S(0,2)\rangle$ is the ground-state. Then, the gate voltages are tuned to ε_{p}, where the electron spin and one nuclear spin flip with probability $(1 - P_S)$. Subsequently, the system is tuned to the Pauli blockade regime with $\varepsilon \gg \varepsilon_{\mathrm{p}}$ for readout. Since the left electron can only tunnel back if its spin has not been flipped, a measurement of the charge on the right QD allows to determine

discussion after Eq. (1.26) for more details

the singlet probability P_S, which has, for instance, been estimated to be $P_S \sim 0.7$ for a specific experiment [125]. Finally, one electron is removed from the dot and the next sequence begins with the initialization of the singlet state $|S(0,2)\rangle$ with a new electron from the leads. Alternatively to this probabilistic approach, another deterministic pulse sequence has been investigated [125]. Starting from the initial $(0,2)$ singlet with $\varepsilon \gg \varepsilon_\mathrm{p}$, the detuning can be rapidly changed to $\varepsilon \ll \varepsilon_\mathrm{p}$. Since the time spent at the degeneracy $\varepsilon \approx \varepsilon_\mathrm{p}$ is then comparably short, the singlet is preserved in the $(1,1)$ configuration. If the detuning is subsequently adiabatically increased up to $\varepsilon \gg \varepsilon_\mathrm{p}$, this singlet will be transformed to the $|T_+(1,1)\rangle$ triplet state due to the avoided crossing at ε_p and a nuclear spin is flipped. This sequence is also completed by pushing out one of the electrons. In summary, both S pumping cycles [125] increase the total nuclear momentum by $\Delta I = +1$ such that a polarization parallel to the external magnetic field $\boldsymbol{B}_0$ is built up. Conversely, the system can be also initialized in the triplet state $|T_+(1,1)\rangle$. With the remainder of the detuning cycles unchanged a T_+ pumping cycle is realized, which allows to change the total nuclear angular momentum by $\Delta I = -1$ resulting in an anti-parallel polarization of the nuclear spins [126]. By many repetitions of these cycles, a finite nuclear polarization can be established due to the comparably slow spin dynamics of the nuclear spins in absence of the HI as explained in Section 1.2.3. A theoretical investigation of this nuclear state preparation is provided in Ref. [127]. Once the pumping rate exceeds the spin diffusion rate, a finite polarization on the order of few percent is established [43]. However, also a polarization up to 40 % has been reported [128].

Similarly to the electrically operated DNP, also DNP induced by optical excitation relies on fast control of the electron spin, spin transfer by means of the HI, and slow relaxation rates of the nuclear spins. For more details, we refer to the extensive review by Urbaszek et al. [24]. Nuclear spin polarizations achieved by optical preparation are typically higher than in gate controlled systems, where values of up to 60 % are now routinely obtained [70]. Such high degrees of polarization are possible because of strong quadrupolar effects in strained, optically active QDs, which strongly suppress spin diffusion in the environment.

Although, this is a quite remarkable degree of polarization, it is still far from the polarizations p necessary in order to significantly prolong the coherence times of the electron spin. For a polarized nuclear spin bath with a Gaussian distribution of states, a Gaussian decay of the coherences on a timescale $\tau_c \propto \sqrt{1-p^2}$ has been found [76], which demands a polarization above $p > 0.99$ in order to prolong this timescale by one order of magnitude. However, it turns out that the effect of the HI can be strongly suppressed even at small polarizations by changing the distribution of the nuclear spin states [61, 76, 78, 129, 130, 131]. By reducing the statistical fluctuations, the nuclear spin state is driven towards an eigenstate $|n\rangle$ of the nuclear magnetic field operator $\hat{h}_z$ defined in Eq. (1.26)

$$\hat{h}_z|n\rangle = \langle \hat{h}_z \rangle_n |n\rangle \,. \tag{1.37}$$

We will consider this nuclear initial state in Chapter 4, where we will investigate the electron spin dynamics in presence of a large number of nuclear spins and a strong external magnetic field for a graphene QD.

In gated QDs, such a state preparation can be achieved by a slight modification of the experiment discussed above. After initializing the electron spin state in the singlet

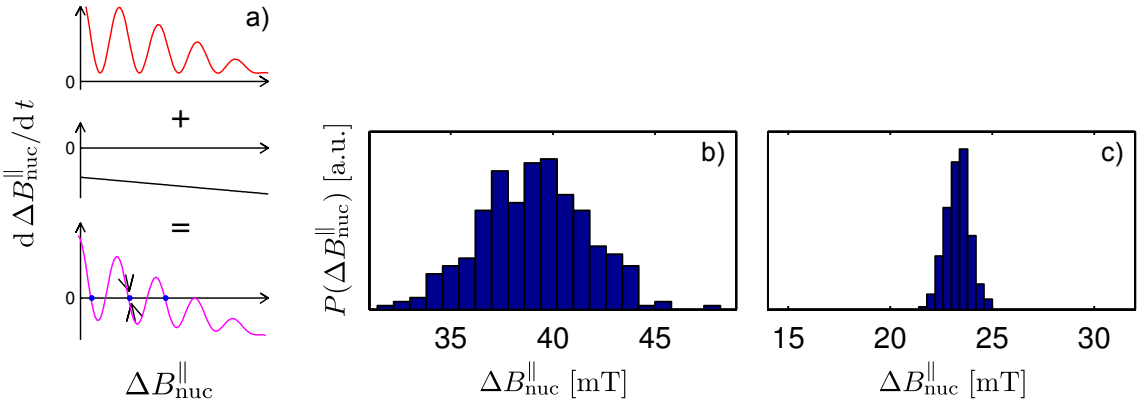

Figure 1.10. DNP and SN of nuclear spin states in QDs. Experimentally, the distribution of the states is determined by the distribution of the hyperfine field gradient $\Delta B^{\parallel}_{\mathrm{nuc}}$ between the two QDs. This gradient is a function of the polarization according to Eq. (1.26), where $\Delta B^{\parallel}_{\mathrm{nuc}} \propto p$ if only one nuclear spin species would be present and uniform HI couplings $A_k = A$ are assumed.) **a)**: A feedback loop can be achieved by combining a positive oscillating S pumping rate with a negative T_+ pumping rate. By this procedure, stable fixed points emerge, which lock the nuclear magnetic field to a specific value. Measured nuclear magnetic field gradient without **b)** and with feedback **c)**. *All figures adapted with permission from [132], ©2010 American Physical Society. All rights reserved.*

$|S(0,2)\rangle$, the system can be tuned to the $(1,1)$ charge configuration at $\varepsilon \ll \varepsilon_{\mathrm{fb}}$, where oscillations between the singlet $|S(1,1)\rangle$ and the triplet $|T_0(1,1)\rangle$ are induced by the nuclear magnetic field gradient as discussed in the previous section and illustrated in Fig. 1.8. The probability of finding the singlet after a time τ_{fb} is given by [132]

$$P_S = \frac{1 + \cos(g^* \mu_B \Delta B^{\parallel}_{\mathrm{nuc}} \tau_{\mathrm{fb}/\hbar})}{2}\,. \tag{1.38}$$

If the system is then swept back to ε_{p}, only the singlet part of the electron state allows for an exchange of angular momentum. Hence, if this cycle is repeated many times, the pump rate $\frac{\mathrm{d}\Delta\, B^{\parallel}_{\mathrm{nuc}}}{\mathrm{d}t}$ of this feedback pulse is proportional to P_S [132] and, thus, oscillates as a function of $\Delta B^{\parallel}_{\mathrm{nuc}}$. If this positive pump rate is combined with the negative pump rate of the T_+ cycle, a stable fixed point of $\Delta B^{\parallel}_{\mathrm{nuc}}$ can be established whenever the total $\frac{\mathrm{d}\Delta\, B^{\parallel}_{\mathrm{nuc}}}{\mathrm{d}t}$ crosses zero with a negative slope as depicted in Fig. 1.10 a). By applying such a feedback scheme, indeed a narrowed nuclear magnetic field has been measured [132] in contrast to a broader distribution if only DNP is applied as shown Fig. 1.10 b) and c). The effect of this SN has been tested measuring the dephasing time T_2^* of the electron spin, where an enhancement from 14 ns to 94 ns has been observed [132] after the preparation of a narrowed state.

Similar effects have also been achieved by optical means [24, 70], where a stabilization of the nuclear polarization has been realized by resonant continuous-wave and pulsed laser excitation. By reversing any changes of the nuclear magnetic field via feedback, narrowed distributions around low polarization have been obtained

Besides DNP and SN, also nuclear magnetic resonance (NMR) has been successfully

used to manipulate the nuclear spins. By applying radio frequency pulse schemes, the authors of [133] were able to show fast redirection on the microsecond timescale of the Overhauser field on the order of 0.5 T. This was achieved using coherent control of an ensemble of 10^5 optically polarized nuclear spins.

Finally, the nuclear spins can be also driven towards an ordered state if the system is sufficiently cooled [43]. Due to their interaction with electrons spin via the HI [134, 135] and the RKKY interaction [136, 137], the nuclear spins are supposed to undergo a phase transition to an ordered magnetic state below a Curie temperature in the mK regime. Although a recent experiment has possibly detected a nuclear spin ordering in a GaAs nanowire, a clear experimental evidence for these phase transitions is still missing. In Chapter 3, we will analyze a single electron spin coupled to the nuclear spin via the HI by means of statistical physics similar to the work of Fröhlich and Nabarro [134]. In contrast to them, we also investigate the properties of the electron spin, where we find an intriguing thermal spin flip together with an ferromagnetic state of the nuclear spins.

2. Systems, environments and decoherence

2.1. Introduction to decoherence

If a physicist was given the task to give an idea about quantum mechanics in a single word, a good choice might be "superposition". The coherent superposition of states

$$|\psi\rangle = \sum_n c_n |\psi_n\rangle \tag{2.1}$$

forming a new state $|\psi\rangle$ is one of the fundamental differences between quantum mechanics and classical physics [18]. In the resulting state, all states $|\psi_n\rangle$ are simultaneously realized with complex coefficients c_n determining their weight and the coherent phase relation between them. This property is in contrast to a classical ensemble, where (classical) probabilities describe our lack of knowledge about in which single state the system is currently prepared. Due to the importance of the superposition principle, decoherence describing the disappearance of coherence is a very important mechanism, which touches various fields such as the foundations of quantum mechanics [3, 18, 138, 139] or rather "applied" topics like quantum error correction for quantum computation [10, 140].

Let us, for instance, consider the superposition $|\psi\rangle = (|\psi_1\rangle + \mathrm{e}^{\mathrm{i}\phi}|\psi_2\rangle)/\sqrt{2}$ of two states $|\psi_1\rangle$ and $|\psi_2\rangle$. The resulting state is called coherent with respect to $|\psi_1\rangle$ and $|\psi_2\rangle$ if they have a constant relative phase ϕ. In fact, this phase and, thus, coherence is experimentally measurable. An illustrative example for such experiments is the Ramsey interferometry [18, 141], which is, for instance, used to measure the relative phase of electron spin states by observing interference patterns. As we describe in Section 1.3.3, the spin of an electron in a quantum dot can be manipulated such that any superposition of its states $|\Uparrow\rangle$ and $|\Downarrow\rangle$ can be created. This is typically achieved by a Larmor precession around a static external magnetic field B_z in combination with Rabi oscillations, which are induced by an oscillating magnetic field $B_\perp$ or by laser light. Both operations are mathematically expressed by unitary transformations, where $\hat{U}_z(\phi(t)) = \mathrm{e}^{-\mathrm{i}\phi(t)\hat{S}_z}$ and $\hat{U}_y(\phi(t)) = \mathrm{e}^{-\mathrm{i}\phi(t)\hat{S}_y}$ correspond to the Larmor precession and the Rabi oscillations, respectively. In both cases, the amount of the acquired phase $\phi(t)$ can be controlled by the time t we allow these processes to act. Given these tools, the Ramsey experiment can be carried out by the following scheme.

If we start in $|\Uparrow\rangle$ and apply $\hat{U}_y(\frac{\pi}{2})$ to this state, we obtain a superposition $\frac{1}{\sqrt{2}}(|\Uparrow\rangle + |\Downarrow\rangle)$. Due to the external magnetic field, both states $|\Uparrow\rangle$ and $|\Downarrow\rangle$ start to precess in opposite directions according to $\hat{U}_z(\phi(t))$, which results in a superposition

$$|\psi_L\rangle = \hat{U}_z(\phi_L)\hat{U}_y(\tfrac{\pi}{2})|\Uparrow\rangle = \tfrac{1}{\sqrt{2}}(\mathrm{e}^{-\mathrm{i}\phi_L/2}|\Uparrow\rangle + \mathrm{e}^{\mathrm{i}\phi_L/2}|\Downarrow\rangle) \tag{2.2}$$

exhibiting a relative phase difference of $\phi_L = \phi(t_L)$. The experiment is finished by applying another rotation $\hat{U}_y(\frac{\pi}{2})$ and measuring $\hat{S}_z$, which is equivalent to a measurement

of $\hat{U}_y^\dagger(\frac{\pi}{2})\hat{S}_z\hat{U}_y(\frac{\pi}{2}) = -\hat{S}_x$ in the first place. With this, we find the following expectation value

$$\langle\hat{S}_z\rangle = \langle\psi_L|\hat{U}_y^\dagger(\tfrac{\pi}{2})\hat{S}_z\hat{U}_y(\tfrac{\pi}{2})|\psi_L\rangle = \langle\psi_L|(-\hat{S}_x)|\psi_L\rangle = -\frac{1}{2}\cos(\phi_L)\,. \tag{2.3}$$

Hence, the relative phase ϕ_L acquired by the Larmor precession during the time t_L leads to interference patterns, which are actually measurable. While it is not particularly surprising for a non-classical degree of freedom such as the spin to show non-classical behavior, interference experiments on molecules containing hundreds of atoms [4] have also demonstrated the existence of interference and, therefore, the relevance of coherence even for large objects.

However, in most cases, the assumption of an isolated quantum system is unrealistic. So, what do we, for instance, expect for an electron spin coupled to an environment? Let us illustrate this by considering an electron spin in a QD, which is in contact with the nuclear spins of the host material via the HI interaction as described in Chapter 1 [18, 141]. In order to prevent our example from being overcomplicated, we impose two simplifications. First, we assume that the HI interaction is switched on after we have acquired the relative phase of ϕ_L. Second, we neglect the (off-diagonal) flip-flop terms in Eq. (1.22), which leads to the following effective interaction

$$\hat{H}_{\mathrm{HI}}^{\mathrm{eff}} = \hat{S}_z\sum_{k=1}^{K} A_k\hat{I}_{k,z}\,, \tag{2.4}$$

where K is the number of nuclear spins. Since the electron spin and the nuclear spins have not interacted with each other, they are initially uncorrelated yielding a product state for the combined system

$$|\Psi_L\rangle = \frac{1}{\sqrt{2}}(\mathrm{e}^{-\mathrm{i}\phi_L/2}|\Uparrow\rangle + \mathrm{e}^{\mathrm{i}\phi_L/2}|\Downarrow\rangle)\otimes|\Psi_{\mathrm{nuc}}\rangle\,. \tag{2.5}$$

The initial state of the nuclear spins $|\Psi_{\mathrm{nuc}}\rangle = \sum_n c_n|n\rangle$ can be expressed in terms of complex coefficients $c_n \in \mathbb{C}$ and product states $|n\rangle = \bigotimes_{k=1}^{K}|m_k^n\rangle$ with $\hat{I}_{k,z}|m_k^n\rangle = m_k^n|m_k^n\rangle$. The resulting basis states $\{|m_S\rangle\otimes|n\rangle\}$ are already eigenstates of the HI Hamiltonian with

$$\hat{H}_{\mathrm{HI}}^{\mathrm{eff}}|m_S\rangle\otimes|n\rangle = m_s E_n|m_S\rangle\otimes|n\rangle\,, \tag{2.6}$$

where $E_n = \sum_{k=1}^{K} A_k m_k^n$. Calculating the time evolution $\hat{U}_{\mathrm{HI}}(t) = \mathrm{e}^{-\mathrm{i}\hbar^{-1}\hat{H}_{\mathrm{HI}}^{\mathrm{eff}}t}$ caused by the HI, this procedure then yields

$$|\Psi_L(t)\rangle = \hat{U}_{\mathrm{HI}}(t)|\Psi_L\rangle = \frac{1}{\sqrt{2}}(\mathrm{e}^{-\mathrm{i}\phi_L/2}|\Uparrow\rangle\otimes|\Psi_{\mathrm{nuc}}^{\Uparrow}(t)\rangle + \mathrm{e}^{\mathrm{i}\phi_L/2}|\Downarrow\rangle\otimes|\Psi_{\mathrm{nuc}}^{\Downarrow}(t)\rangle)\,, \tag{2.7}$$

where $|\Psi_{\mathrm{nuc}}^{m_S}(t)\rangle) = \sum_n c_n\,\mathrm{e}^{-\mathrm{i}\hbar^{-1}m_S E_n t}$. Finally, we apply again a $\frac{\pi}{2}$-rotation around the y-axis and calculate the expectation value of $\hat{S}_z$, which results in

$$\begin{aligned}\langle\hat{S}_z\rangle &= \langle\Psi_L(t)|\hat{U}_y^\dagger(\tfrac{\pi}{2})\hat{S}_z\hat{U}_y(\tfrac{\pi}{2})|\Psi_L(t)\rangle = \langle\Psi_L(t)|(-\hat{S}_x)|\Psi_L(t)\rangle\\ &= -\frac{1}{2}(\mathrm{e}^{-\mathrm{i}\phi_L}\langle\Psi_{\mathrm{nuc}}^{\Downarrow}(t)\,|\,\Psi_{\mathrm{nuc}}^{\Uparrow}(t)\rangle\langle\Downarrow|\hat{S}_x|\Uparrow\rangle + \mathrm{e}^{\mathrm{i}\phi_L}\langle\Psi_{\mathrm{nuc}}^{\Uparrow}(t)\,|\,\Psi_{\mathrm{nuc}}^{\Downarrow}(t)\rangle\langle\Uparrow|\hat{S}_x|\Downarrow\rangle)\\ &= -\frac{1}{2}\mathrm{Re}[\mathrm{e}^{\mathrm{i}\phi_L}\langle\Psi_{\mathrm{nuc}}^{\Uparrow}(t)\,|\,\Psi_{\mathrm{nuc}}^{\Downarrow}(t)\rangle]\,.\end{aligned} \tag{2.8}$$

Due to the interaction of the electron spin with the nuclear spins, its expectation value is modified by the overlap of the two nuclear spin states $|\Psi^{\Uparrow}_{\mathrm{nuc}}(t)\rangle$ and $|\Psi^{\Downarrow}_{\mathrm{nuc}}(t)\rangle$. The physical mechanism behind this phenomenon is the generation of entanglement[1] between system and environment, which spreads the coherence over the total system. If no HI interaction was present, the two nuclear spin states would be equal and we would recover our previous result in Eq. (2.3), since no entanglement would have been established. With the HI being active, we find for the overlap

$$r(t) = \langle \Psi^{\Uparrow}_{\mathrm{nuc}}(t) \,|\, \Psi^{\Downarrow}_{\mathrm{nuc}}(t) \rangle = \sum_{n=0}^{2^K-1} |c_n|^2 \, \mathrm{e}^{-\mathrm{i}\hbar^{-1}E_n t} = \sum_{n=0}^{2^K-1} |c_n|^2 \prod_{k=1}^{K} \mathrm{e}^{-\mathrm{i}\hbar^{-1}A_k m_k^n t} \; . \tag{2.9}$$

In a first attempt to analyze the behavior of this function, it can be considered as a vector in the complex plane, which results from the addition of 2^K vectors, whose length and direction are determined by $|c_n|^2$ and $\hbar^{-1}E_n t$, respectively. If there are no special relations between the different coupling constants, the directions will be approximately random at any time t larger than the decoherence timescale τ_{d}. Therefore, the decoherence function $r(t)$ can be considered as a result of a random walk in a two-dimensional plane [16, 18]. Assuming the initial nuclear spin state to be close to a uniform distribution over the whole Hilbert space, the average step size $\langle |c_n|^2 \rangle$ is equal to 2^{-K} due to the normalization condition $\sum_n |c_n|^2 = 1$ of the nuclear states. The average distance traveled in a random walk after K steps is given by the root mean square distance $\sigma_r \simeq 2^{K/2}$, see, for instance, Ref. [142]. Consequently, the average value of the decoherence function scales with

$$\langle r(t) \rangle \simeq \langle |c_n|^2 \rangle \sigma_r = 2^{-K} \, 2^{\frac{K}{2}} = 2^{-\frac{K}{2}} \tag{2.10}$$

Thus, even comparably small environments can lead to a suppression of the signal $\langle S_z \rangle(t) \propto r(t)$ below any experimentally feasible resolution. Clearly, the exact behavior of this decoherence factor $r(t)$ [18] depends on the specific choice of the coefficients c_n and on the distribution of the coupling constants. Investigating this and similar toy models, a Gaussian decay of the decoherence function on very short timescales τ_d has been observed for a wide range of distributions of the couplings A_k [16, 18, 143]. Yet, for any limited number of nuclear spins, the decoherence function will return to 1 at the recurrence time τ_R. However, it has been shown, that this recurrence time is typically very large and even exceeding the age of the universe for comparably small environments [16, 144]. Thus, from a practical point of view decoherence is irreversible. Yet there are ways to circumvent decoherence by a careful choice of the nuclear initial state as can be seen from the decoherence function. If we, for instance, choose one of the product states $|m\rangle$, we have $c_m = 1$ and $c_{n \neq m} = 0$ and, therefore, $r(t) = \mathrm{e}^{-\mathrm{i}\hbar E_m t}$, for which the interference patterns are restored.

Since a precise knowledge of decoherence is essential for any meaningful quantum error correction, the decoherence of electrons in QDs has been under intensive research over the past decade due to their potential as qubits. We review some important findings at

[1] Two systems S_1 and S_2 are called entangled if the state of the composite system S cannot be written as a tensor product $|\Psi\rangle = |\Psi_1\rangle \otimes |\Psi_2\rangle$, where $|\Psi_1\rangle$ and $|\Psi_2\rangle$ represent the state of system S_1 and S_2, respectively. Please also see, e.g., Ref. [18].

the beginning of Chapter 4, in which we analyze the decoherence of an electron spin in a graphene quantum dot interacting with the surrounding nuclear spins. In this review, we encounter a large variety of decoherence functions exhibiting exponential, Gaussian or power-law decay. Also these studies suggest very short decoherence times τ_d if no further efforts are undertaken.

For clarity, let us illustrate decoherence on the basis of our simple example: First, we have considered an isolated electron spin starting in a particular state. An experiment revealing the coherence of quantum states via interference has been described by a set of unitary transformations, which in the end resulted in the interference pattern of the electron spin expectation value in Eq. (2.3). In our second example, we have introduced a nuclear spin environment with which the electron is interacting. Starting from a specific initial state, we have again been able to calculate the final state by another set of unitary transformations. However, this time, the expectation value of $\hat{S}_z$ has shown decoherence. So why do we find decoherence in the second case although again only unitary transformations have been applied. As it turns out, the answer to this questions is the fact that we have the wrong "tool" to find interference patterns. When calculating the expectation value of the electron spin we have been imprecise, since we have not explicitly stated that this operator acts only on a subspace of the whole Hilbert space. Thus in more obvious notation, we have to determine the expectation value of $\hat{S}_x = \hat{S}'_x \otimes \mathbb{1}_{\mathrm{nuc}}$, where the local measurement $\hat{S}'_x$ acts only on the electron spin subspace and $\mathbb{1}_{\mathrm{nuc}}$ is the identity operation on the nuclear spin subspace. However, we have seen that the coherence is spread over the total system due to the establishment of entanglement between the electron spin and the nuclear spins. Thus, the apparent decoherence of the electron spin states is an effect caused by the locality of our measurement. The total state of the system is coherent for all times and given a proper measurement we could find interference patterns. However, given the large size of typical environments, such a global measurement cannot be found in general. Thus, a theory is needed, which is capable of dealing with such a limitation to local observables.

In the following sections, we show how these findings can be formalized in terms of closed and open quantum systems. By using the density matrix formalism, we demonstrate how effective equations of motion of the electron spin can be obtained, which take into account the interaction with an environment. Equipped with these equations, we are then able to analyze decoherence in the context of QDs. A general description of decoherence and its implications is beyond the scope of this Thesis and, therefore, we refer the interested reader to the books of Joos et al. [138] and Schlosshauer [18] for a broad and in-depth discussion of this exciting topic.

2.2. Modeling quantum systems

From the examples above, we have already seen two different notions of quantum systems, whose properties we want to discuss in more detail. The first example constitutes a closed system, where in principle all degrees of freedom are accessible to the observer. Thus, there is no contact to any kind of environment except for external fields. The time evolution of a closed system is determined by a Hamiltonian, which is in general time-dependent. If

the Hamiltonian is time-independent, the system is called isolated [145]. In any case, the time evolution of the system is deterministic and can be calculated by means of a unitary time evolution operator.

However, a closed quantum system is in general unrealistic, since perfect isolation of a system is not possible. Moreover, as our first example illustrates, this model is also not capable of describing decoherence. Thus, a more realistic description of a quantum system is needed. In our second example, we have seen that both issues are resolved if we limit our perspective to a (sub)system, which is in contact with an environment, for instance, the other part of the system.

If we limit our point of view to observables of the subsystem and follow its dynamics by its genuine Hamiltonian and the interaction with the environment, we will generally encounter a non-unitary time evolution due to system-environment correlations [145]. Nevertheless, the combination of this system and its environment again constitutes a closed quantum system with unitary time evolution.[2] Thus, typically this total system is chosen as a starting point, from which the effective dynamics of the (sub)system can be obtained. According to this scheme, the (sub)system is also called the reduced system. For simplicity, we use the expression "system" for both the total system and the (sub)system as long as the correct meaning is guaranteed by the context.

So far, we have not imposed any restrictions on the environment such as a minimum size. In fact, we will encounter particularly small environments consisting of less than ten nuclear spins in Chapters 5 and 6. There, we demonstrate, that already very few nuclear spins can suffice in order to equilibrate the electron spin. Although it is difficult to define a strict border, there is certainly a (finite) number of environmental degrees of freedom for every model, above which the environment effectively acts as if it were infinite. Typically, its energy spectrum is then (quasi-)continuous and its state is hardly changed due to the interaction with the system. Such environments are usually referred to as reservoirs. We consider such a reservoir in Chapter 4, in which we follow the dynamics of an electron spin in contact with many nuclear spins. If in addition a reservoir is in thermal equilibrium, we speak of a heat bath or bath [145]. This is the typical setting, in which standard statistical mechanics is applicable [146]. We follow this approach in Chapter 3, where we assume that a system consisting of both the electron spin and the nuclear spins is in contact with a heat bath.

2.2.1. Closed quantum systems

Although not stated explicitly, the examples in the introduction have been described in terms of the familiar quantum state vectors $|\Psi\rangle$. The dynamics of these elements of a Hilbert space $\mathcal{H}$ is determined by the Hamiltonian $\hat{H}$ of the system via the well known Schrödinger equation

$$\frac{\partial}{\partial t}|\Psi(t)\rangle = -\mathrm{i}\hbar^{-1}\hat{H}(t)|\Psi(t)\rangle \tag{2.11}$$

[2] Of course, there may again be an environment interacting with this total system, which makes this an unrealistic approximation to nature in the strict sense. However, since this interaction is generally even much weaker, the combined system-environment is in general a much better approximation than considering the system alone. Thus, the typical timescales related to this coupling to another environment is much longer than the timescale on which the dynamics of the subsystem occurs.

This differential equation is solved by the introduction of the time-evolution operator

$$\hat{U}(t,t_0) = \exp[-\mathrm{i}\hbar^{-1}\int_{t_0}^{t} \mathrm{d}t'\ \hat{H}(t')]\,, \tag{2.12}$$

which maps the initial state $|\Psi(t_0)\rangle$ to the final state $|\Psi(t)\rangle = \hat{U}(t,t_0)|\Psi(t_0)\rangle$ at time t. With this time-dependent state at hand, we are then able to calculate the expectation values of any observable $\hat{O}$. Using the spectral decomposition of the operator $\hat{O} = \sum_i O_i|O_i\rangle\langle O_i|$, we find

$$\langle\hat{O}\rangle(t) = \langle\Psi(t)|\hat{O}|\Psi(t)\rangle = \sum_i O_i|\langle O_i\,|\,\Psi(t)\rangle|^2\,, \tag{2.13}$$

where O_i is a eigenvalue and $|O_i\rangle$ is the corresponding state. A equivalent description of this physics can be obtained by defining a projector $\hat{\rho}(t) = |\Psi(t)\rangle\langle\Psi(t)|$, which is called density operator or density matrix.[3] This projector allows us to calculate the expectation value of an operator $\hat{O}$ by performing the trace operation[4]

$$\langle\hat{O}\rangle(t) = \mathrm{Tr}[\hat{O}\hat{\rho}(t)] = \mathrm{Tr}[\hat{O}\hat{U}(t,t_0)\hat{\rho}(t_0)\hat{U}^\dagger(t,t_0)]\,. \tag{2.14}$$

Since the eigenstates $|O_i\rangle$ constitute a basis[5] of the Hilbert space, we explicitly find

$$\langle\hat{O}\rangle(t) = \sum_i \langle O_i|\hat{O}\hat{\rho}(t)|O_i\rangle = O_i|\langle O_i\,|\,\Psi(t)\rangle|^2\,, \tag{2.15}$$

which is the same result as in Eq. (2.13) above. This is not particularly surprising, since both the state vector $|\Psi\rangle(t)$ and the corresponding density matrix $\hat{\rho}(t)$ contain the maximum knowledge we have about the state of the physical system [18]. If we express the state vector $|\Psi(t)\rangle = \sum_i c_i(t)|\Psi_i\rangle$ in a particular basis $|\Psi_i\rangle$ by means of complex coefficients $c_i(t)$, we find for the density matrix

$$\hat{\rho}(t) = \sum_i |c_i(t)|^2|\Psi_i\rangle\langle\Psi_i| + \sum_{i\neq j} c_i c_j^*|\Psi_i\rangle\langle\Psi_j|\,, \tag{2.16}$$

where the off-diagonal terms $i \neq j$ encode the coherence between the states $|\Psi_i\rangle$ and $|\Psi_j\rangle$. If we reconsider our first example of an isolated electron spin, we find for its density matrix

$$\hat{\rho}_S = |\Psi_L\rangle\langle\Psi_L| = \frac{1}{2}(|\Uparrow\rangle\langle\Uparrow| + |\Downarrow\rangle\langle\Downarrow|) + \frac{1}{2}(\mathrm{e}^{-\mathrm{i}\phi_L}|\Uparrow\rangle\langle\Downarrow| + \mathrm{e}^{\mathrm{i}\phi_L}|\Downarrow\rangle\langle\Uparrow|)\,, \tag{2.17}$$

in which the coherences are found in the off-diagonal elements. However, the density matrix is a Hermitian operator and, therefore, we can find a basis $|\tilde{\Psi}_i\rangle$ in which it is

[3] Strictly speaking, this is not the matrix representation with respect to a particular basis, but a basis independent operator. However, the expression density matrix for this operator is established in the literature.

[4] If the set of states $\{|\Psi_i\rangle\}_{i=1}^d$ forms a basis of a Hilbert space $\mathcal{H}$ with dimension $d = \dim(\mathcal{H})$, then the trace of an arbitrary operator $\hat{O}$ is defined by $\mathrm{Tr}[\hat{O}] = \sum_i \langle\Psi_i|\hat{O}|\Psi_i\rangle$.

[5] In the case of degenerate eigenvalues, a basis for the degenerate subspace may be found using the Gram-Schmidt procedure.

diagonal and the coherences seem to be absent. Thus, the exact form of the coherences and the interferences is in general depending on our choice of the basis in which the density matrix is represented. Since the basis $|O_i\rangle$ defined by our observable typically does not coincide with the eigenstates of the density matrix, this ostensible loss of coherence is not present in an experiment.

Nevertheless, there are situations in which we clearly have insufficient knowledge of the state of the system, which, for instance, arises from probabilistic elements in the initialization of the system [18]. Within the density matrix formalism, also a lack of knowledge of the state of a system can be easily incorporated by means of a so-called mixed density matrix $\hat{\rho} = \sum_i p_i |\Psi_i\rangle\langle\Psi_i|$ with $p_i \in \mathbb{R}$ and $\sum_i p_i = 1$. Hence, the physical system is always in one of the pure states $\hat{\rho}_i = |\Psi_i\rangle\langle\Psi_i|$, but we do not know in which. The only knowledge the observer can gain by measurement is the classical probability p_i [18] to find a specific pure state. By inserting this mixed density matrix in Eq. (2.15), we can readily show, that the resulting expectation value $\langle\hat{O}\rangle$ of any observable $\hat{O}$ exhibits the correct average over the probability distribution $\{p_i\}$.

Similar to the density matrix being the equivalent to the state vectors, the Schrödinger equation in Eq. (2.11) has its counterpart, too, the (Liouville-) von Neumann equation [145]

$$\frac{\mathrm{d}}{\mathrm{d}t}\hat{\rho}(t) = -\mathrm{i}\hbar^{-1}[\hat{H}(t), \hat{\rho}(t)]\,. \tag{2.18}$$

Using the time-evolution operator defined in Eq. (2.12), the density matrix at time t can be obtained from its initial state by

$$\hat{\rho}(t) = \hat{U}(t, t_0)\hat{\rho}(t_0)\hat{U}^\dagger(t, t_0)\,. \tag{2.19}$$

If we have a closer look at our findings in Eqs. (2.14), (2.15) and (2.19), we see that the role, which the state vectors of the Hilbert space play in the density matrix formalism, is rather small. Their only remaining purpose is to provide a basis necessary to calculate the final trace. Hence, this formalism is mainly based on the operators acting on elements of the Hilbert space such as $\hat{H}(t)$, $\hat{O}$, and $\hat{\rho}(t)$. These operators themselves are elements of another vector space known as the Liouville space $\mathcal{F}$ [147]. Similar to these operators acting on elements of the Hilbert space, there exist so-called superoperators acting on the elements of the Liouville space. We have already encountered one example of such a superoperator above. Since the commutator of the density matrix with the Hamiltonian creates another element of the Liouville space, we can rewrite the above equation by

$$\frac{\mathrm{d}}{\mathrm{d}t}\hat{\rho}(t) = -\mathrm{i}\mathcal{L}(t)\,\hat{\rho}(t) \tag{2.20}$$

where the Liouville (super)operator [147] is given by $\mathcal{L}(t)\hat{O} = \hbar^{-1}[\hat{H}(t), \hat{O}]$ for an arbitrary operator $\hat{O} \in \mathcal{F}$.[6] For the remainder of this section, we assume a time-independent Hamiltonian for simplicity and refer to the books by Fick and Sauermann [147] and Breuer and Petruccione [145] for a detailed discussion including time-dependent Hamiltonians. The Liouville superoperator acts by definition on everything to its right such that powers

[6] This definition follows the convention of Ref. [147], whereas in Ref. [145] the factor of $-\mathrm{i}$ is absorbed in $\mathcal{L}$.

of it result in nested commutators according to $\mathcal{L}^n\hat{O} = \mathcal{L}^{n-1}[\hat{H},\hat{O}] = \mathcal{L}^{n-2}[\hat{H}[\hat{H},\hat{O}]] = \ldots$. The von Neumann equation is formally solved by

$$\hat{\rho}(t) = \mathcal{U}(t,t_0)\hat{\rho}(t_0)\,, \tag{2.21}$$

where we have introduced another superoperator $\mathcal{U}(t,t_0)$. If we insert this equation in the differential equation Eq. (2.20), we obtain a differential equation for this superoperator

$$\frac{\mathrm{d}}{\mathrm{d}t}\mathcal{U}(t,t_0) = -\mathrm{i}\mathcal{L}\,\mathcal{U}(t,t_0) \qquad \text{with} \qquad \mathcal{U}(t_0,t_0) = \mathbb{1}\,, \tag{2.22}$$

which finally yields

$$\mathcal{U}(t,t_0) = \mathrm{e}^{-\mathrm{i}\mathcal{L}(t-t_0)}\,. \tag{2.23}$$

Hence the time evolution of the density matrix is completely determined according to Eqs. (2.21) and (2.22). The formulation of the time-evolution of a closed system in terms of superoperators is equivalent to the usual description using standard operators acting on states of the corresponding Hilbert space. Comparing, for instance, Eqs. (2.19) and (2.21), we find

$$\hat{\rho}(t) = \mathcal{U}(t,t_0)\hat{\rho}(t) = \hat{U}(t,t_0)\hat{\rho}(t_0)\hat{U}^\dagger(t,t_0)\,, \tag{2.24}$$

Thus, so far the introduction of the Liouville space has not provided any advantage. However, physically relevant systems are in general too complicated to be solved analytically. There are two possibilities to circumvent this difficulty: approximate solutions of so-called open systems and exact diagonalization of sufficiently small systems. As we will show below, these approximate solutions for the former case are conveniently expressed in terms of Liouville superoperators.

If we are in contrast confronted with a small system, it is always possible to represent the Hamiltonian in some basis $|n\rangle$ of the Hilbert space $\mathcal{H}$ and to diagonalize the resulting matrix H_{nm} exactly by numerical means. This technique known as "exact diagonalization" has been successfully applied to investigate the spin dynamics in QDs before [74, 148, 149, 150]. This procedure provides all eigenvalues $\{E_\nu\}_{\nu=1}^d$ with $d = \dim(\mathcal{H})$ and the corresponding eigenstates $|\Psi_\nu\rangle$ of the Hamiltonian matrix. Defining the matrix M through its elements $M_{\nu n}$, the n-th element of eigenstate $|\Psi_\nu\rangle$, we can rewrite the time-evolution operator $U_{nm}(t-t_0) = \langle n|\hat{U}(t-t_0)|m\rangle$ in diagonal form

$$V(t,t_0) = MU(t,t_0)M^\dagger = \begin{pmatrix} \mathrm{e}^{-\mathrm{i}\hbar^{-1}E_1(t-t_0)} & & & \\ & \mathrm{e}^{-\mathrm{i}\hbar^{-1}E_2(t-t_0)} & & \\ & & \ddots & \\ & & & \mathrm{e}^{-\mathrm{i}\hbar^{-1}E_d(t-t_0)} \end{pmatrix}. \tag{2.25}$$

With this form, the expectation value of an observable $\hat{O}$ is then given by

$$\langle\hat{O}\rangle(t) = \mathrm{Tr}[\hat{O}\hat{\rho}(t)] = \sum_{\substack{n,m,p,q\\ \nu,\mu}} O_{nm}M^*_{m\nu}V_{\nu\nu}(t,t_0)M_{\nu p}\,\rho_{pq}(t_0)\,M^*_{q\mu}V^*_{\mu\mu}(t,t_0)M_{\mu n} \tag{2.26}$$

with the matrix representations $O_{nm} = \langle n|\hat{O}|m\rangle$ and $\rho_{pq}(t_0) = \langle p|\hat{\rho}(t_0)|q\rangle$. In Chapters 5 and 6, we use exact diagonalization in order to investigate the dynamics of an electron

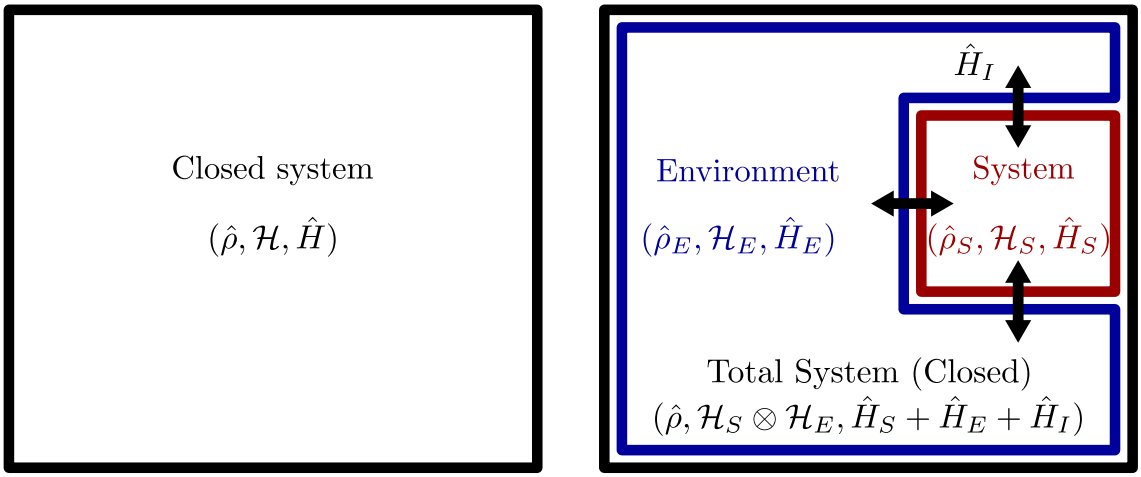

Figure 2.1. Illustration of different perspectives on quantum systems. If a system of interest is not interacting with another system it is called closed. However, since perfect isolation is not possible, more sophisticated models consider a system in contact with an environment. The combined system itself is again a closed quantum system.

spin coupled to less than ten nuclear spins. This spin model is also very illustrative to demonstrate the limitations of this procedure. Since each spin has a two dimensional Hilbert space, the dimension of the total Hilbert space is given by $d = 2^{K+1}$, where K is the number of nuclear spins. This exponential growth quickly outruns the capacity of even the most powerful computers. Therefore, the notion of open quantum systems has been introduced, which allows to treat large environments.

2.2.2. Open quantum systems

If we combine a system S with an environment E, the Hilbert space of the total system is given by the tensor product $\mathcal{H} = \mathcal{H}_S \otimes \mathcal{H}_E$ of the Hilbert spaces of the system $\mathcal{H}_S$ and the environment $\mathcal{H}_E$. The total Hamiltonian is then given by

$$\hat{H} = \hat{H}_S' \otimes \mathbb{1}_E + \mathbb{1}_S \otimes \hat{H}_E' + \hat{H}_I \equiv \hat{H}_S + \hat{H}_E + \hat{H}_I \,, \tag{2.27}$$

where $\hat{H}_S'$ is the Hamiltonian of the system, $\hat{H}_E'$ is the Hamiltonian of the environment, and $\mathbb{1}_x$ is the identity operation on the respective subspaces $x \in \{S, E\}$. The Hamiltonian $\hat{H}_I$ describes the interaction between them. A schematic of this combination is shown in Fig. 2.1. Since the total system is closed, we already know the time-evolution of its density matrix $\hat{\rho}$ according to Eq. (2.24). However, as we have seen in our second example above, often only a certain subspace of the whole Hilbert space is relevant for the calculation of expectation values of observables $\hat{O}_S \otimes \mathbb{1}_E$, where $\mathbb{1}_E$ is the identity operation on the environment. Hence, there should be a density matrix $\hat{\rho}_S(t)$ in this subspace, which gives rise to the same expectation values as the full density matrix:

$$\mathrm{Tr}[\hat{O}_S \otimes \mathbb{1}_E \; \hat{\rho}(t)] \equiv \mathrm{Tr}[\hat{O}_S \hat{\rho}_S(t)] \,, \tag{2.28}$$

where the second trace operation is solely carried out in the subspace of the system. Indeed, there is a unique operation known as partial trace [10, 18], which allows to calculate the

density matrix $\hat{\rho}_S(t)$ of the subsystem from the total density matrix $\hat{\rho}(t)$. If the states $\{|\Psi_{E,i}\rangle\}$ form a basis in $\mathcal{H}_E$, the partial trace with respect to the environment is defined by

$$\mathrm{Tr}_E[\hat{\rho}(t)] = \sum_i \langle\Psi_{E,i}|\hat{\rho}(t)|\Psi_{E,i}\rangle = \sum_{k,l} \hat{\rho}'_{k,l}(t)|\Psi_{S,k}\rangle\langle\Psi_{S,l}| \equiv \hat{\rho}_S(t)\,, \tag{2.29}$$

where the states $\{|\Psi_{S,k}\rangle\}$ form a basis of the Hilbert space $\mathcal{H}_S$ and the coefficients are given by $\hat{\rho}'_{k,l}(t) = \sum_i \langle\Psi_{S,k}|\langle\Psi_{E,i}|\hat{\rho}(t)|\Psi_{E,i}\rangle|\Psi_{S,l}\rangle$. Since the resulting density matrix $\hat{\rho}_S(t)$ acts only on a subspace of the total Hilbert space, it is often referred to as reduced density matrix. As an example, let us calculate the reduced density matrix of our second example above, in which the electron spin interacts with the nuclear spins via the HI. Given the time evolution of its state $|\Psi_L(t)\rangle$ in Eq. (2.7), we can calculate its total density matrix $\hat{\rho}(t)$ on which we apply a partial trace over the nuclear spins:

$$\hat{\rho}_S(t) = \mathrm{Tr}_{\mathrm{nuc}}[\hat{\rho}(t)] = \frac{1}{2}(|\Uparrow\rangle\langle\Uparrow| + |\Downarrow\rangle\langle\Downarrow|) + \frac{1}{2}(\mathrm{e}^{-\mathrm{i}\phi_L}\, r^*(t)|\Uparrow\rangle\langle\Downarrow| + \mathrm{e}^{\mathrm{i}\phi_L}\, r(t)|\Downarrow\rangle\langle\Uparrow|)\,, \tag{2.30}$$

where the decoherence function $r(t) = \langle\Psi^{\Uparrow}_{\mathrm{nuc}}(t)\,|\,\Psi^{\Downarrow}_{\mathrm{nuc}}(t)\rangle$ has been discussed above. If we compare this result to the density matrix of an isolated electron spin in Eq. (2.17), we see that the off-diagonal elements encoding the coherences are reduced by the decoherence factor $r(t)$. Despite of this factor, however, both density matrices are formally equal.

By means of the partial trace, we also obtain a differential equation for the reduced density matrix $\hat{\rho}_S(t)$ from the Liouville equation of the total system in Eq. (2.20)

$$\frac{\mathrm{d}}{\mathrm{d}t}\hat{\rho}_S(t) = -\mathrm{i}\,\mathrm{Tr}_E[\mathcal{L}\,\hat{\rho}(t)]\,. \tag{2.31}$$

However, so far we have not gained anything by the fact that we are only interested in the subsystem, since we have to calculate the time-evolution of the total system before we are able to obtain the dynamics of the reduced system. Thus, in order to profit from the distinction between system and environment, another approach is preferable, which directly yields an effective differential equation for $\hat{\rho}_S(t)$ without the need to solve the total system in the first place. Due to its importance and the generality of this problem, various schemes have been developed such as the projection operator techniques leading to the Nakajima-Zwanzig [145, 147] equation, which we will discuss in the subsequent section.

In the course of this discussion, we will encounter situations in which a superoperator can be divided into two parts. For such superoperators, we generalize the findings in Eqs. (2.22) and (2.23) for later convenience. Let us define $\frac{\mathrm{d}}{\mathrm{d}t}\mathcal{U}_{\mathcal{O}}(t,t_0) = -\mathrm{i}\mathcal{O}\mathcal{U}_{\mathcal{O}}(t,t_0)$ and $\mathcal{U}_{\mathcal{O}}(t_0,t_0) = \mathbb{1}$ for an arbitrary superoperator $\mathcal{O}$, which is solved by

$$\mathcal{U}_{\mathcal{O}}(t,t_0) = \mathrm{e}^{-\mathrm{i}\mathcal{O}(t-t_0)}\,. \tag{2.32}$$

In the case of a separable superoperator in the form $\mathcal{O} = \mathcal{O}_1 + \mathcal{O}_2$, there exists a relation between the full superoperator $\mathcal{U}_{\mathcal{O}}(t,t_0)$ and an partial superoperator $\mathcal{U}_{\mathcal{O}_1}(t,t_0)$

$$\mathcal{U}_{\mathcal{O}}(t,t_0) = \mathcal{U}_{\mathcal{O}_1}(t,t_0) - \mathrm{i}\int_{t_0}^{t} \mathrm{d}t'\;\mathcal{U}_{\mathcal{O}_1}(t,t')\,\mathcal{O}_2\,\mathcal{U}_{\mathcal{O}}(t',t_0)\,, \tag{2.33}$$

where a proof of this relation is presented in Ref. [147]. This relation is even valid for time-dependent superoperators $\mathcal{O}_1(t)$ and $\mathcal{O}_2(t)$, where the exponents are given by time-ordered integrals over these superoperators. In the time-independent case, we can insert the explicit form of $\mathcal{U}_{\mathcal{O}}(t-t_0)$ and $\mathcal{U}_{\mathcal{O}_1}(t-t_0)$ in Eq. (2.23) yielding

$$\mathrm{e}^{-\mathrm{i}\mathcal{O}(t-t_0)} = \mathrm{e}^{-\mathrm{i}\mathcal{O}_1(t-t_0)} - \mathrm{i}\int_{t_0}^{t} \mathrm{d}t' \;\; \mathrm{e}^{-\mathrm{i}\mathcal{O}_1(t-t')}\,\mathcal{O}_2\,\mathrm{e}^{-\mathrm{i}\mathcal{O}(t'-t_0)} \;. \tag{2.34}$$

2.3. The Nakajima-Zwanzig generalized master equation

Typically, open quantum systems as described above are analyzed in the framework of quantum master equations, which are effective equations of motion of the subsystem only and allow the investigation of non-unitary effects in open quantum systems. The interaction with the environment is taken into account in an indirect manner. Depending on the ability of the environment to keep track of earlier events, these quantum master equations are divided into two groups. If the environment loses its memory quickly, the resulting dynamics are called Markovian, which are consequently described in terms of so-called Markovian master equations [18, 145]. In contrast, if the internal dynamics of the environment are slow, the environment preserves its memory, which typically gives rise to more complicated dynamics. Thus, we need so-called non-Markovian master equations for this particular situation, which are, however, in general mathematically more demanding. We will make more quantitative arguments for this distinction in the course of this section. The most prominent examples for a non-Markovian master equation are the Nakajima-Zwanzig equation and the time convolutionless master equation [145]. The applicability of both equations strongly depends on the specific properties of the microscopic model to study [145, 151]. Typically, the unitary time-evolution of the total system consisting of the actual system of interest and its environment is taken as a starting point to obtain an equation of motion of the system alone. In this Thesis, we focus on the Nakajima-Zwanzig equation, which has been successfully applied to the central spin model as described in the previous chapter. The mathematical formulation of the Nakajima-Zwanzig equation closely follows the book of Fick and Sauermann [147], whereas we additionally refer to the books of Breuer and Petruccione [145] and Schlosshauer [18] for a physical interpretation of various important steps within this derivation.

2.3.1. Relevant and irrelevant parts of the density matrix

By considering an open quantum system instead of a closed one, we have drastically enlarged the Hilbert space $\mathcal{H}$ and the associated Liouville space $\mathcal{F}$, respectively, in order to capture the effects of the environment. At the same time, however, certainly only a limited set of observables $\{\hat{O}_n\} \subset \mathcal{F}$ is of interest, since we have at most only limited knowledge about the environment.[7] Since the associated operators do not constitute a

[7] This set of observables does not have to be limited to observables of the system. In fact, these observables can be more complicated objects, which for instance also take into account certain correlations between the system and its environment.

complete basis of the Liouville space, only certain parts of the density matrix $\hat{\rho}(t)$ are relevant for the calculation of expectation values $\langle \hat{O}_n \rangle = \mathrm{Tr}[\hat{O}_n \hat{\rho}(t)]$ of the operators [147]. Thus, we can split the density matrix

$$\hat{\rho}(t) = \hat{\rho}_{\mathrm{rel}}(t) + \hat{\rho}_{\mathrm{irr}}(t) \tag{2.35}$$

in a relevant part $\hat{\rho}_{\mathrm{rel}}(t)$ and an irrelevant part $\hat{\rho}_{\mathrm{irr}}(t)$, such that

$$\mathrm{Tr}[\hat{O}_n \hat{\rho}(t)] = \mathrm{Tr}[\hat{O}_n \hat{\rho}_{\mathrm{rel}}(t)] \tag{2.36}$$

and

$$\mathrm{Tr}[\hat{O}_n \hat{\rho}_{\mathrm{irr}}(t)] = 0 \tag{2.37}$$

hold. The relevant part of the density matrix obviously shows a strong analogy to the reduced density matrix $\hat{\rho}_S$ of the subsystem. However, the relevant part of the density matrix is more general and acts on the total Hilbert space rather than the Hilbert space of the system. The specific form of the relevant part of the density matrix depends on the set of operators $\{\hat{O}_n\}$, but Eqs. (2.35) to (2.37) do not define it uniquely leaving freedom in the choice of the mapping

$$\hat{\rho}(t) \mapsto \hat{\rho}_{\mathrm{rel}}(t) = f(t, \hat{\rho}(t)) \tag{2.38}$$

The simplest choice for this mapping is a time-independent linear function, which we will discuss in the following. For a treatment of non-linear dependencies and an explicit time-dependence of f, we refer the interested reader to the book of Fick and Sauermann [147]. Our specific choice of the mapping allows us to re-express Eq. (2.38) by

$$\hat{\rho}_{\mathrm{rel}}(t) = \mathcal{P}\hat{\rho}(t)\,, \tag{2.39}$$

where we have introduced a linear superoperator $\mathcal{P}$. Once the density matrix only contains the relevant part $\hat{\rho}_{\mathrm{rel}}(t)$, this operator should give exactly the same density matrix $\mathcal{P}\hat{\rho}_{\mathrm{rel}}(t) = \hat{\rho}_{\mathrm{rel}}(t)$. Hence this superoperator is idempotent,

$$\mathcal{P}^2 = \mathcal{P}\,. \tag{2.40}$$

and, consequently, $\mathcal{P}$ is a projector on the relevant part of the density matrix. Moreover, this superoperator has to preserve the expectation values of our observables of interest according to

$$\mathrm{Tr}[\hat{O}_n \hat{\rho}(t)] = \mathrm{Tr}[\hat{O}_n \hat{\rho}_{\mathrm{rel}}(t)] = \mathrm{Tr}[\hat{O}_n \mathcal{P}\hat{\rho}(t)]\,. \tag{2.41}$$

The above assumptions regarding the projector also imply certain constraints on the initial state of the system. In general, physical experiments include a (willful) preparation of the initial state of the system. Owing to our definition of the relevant part of the density matrix by means of measurable observables, it is reasonable to assume, that we are able to prepare the system initially in a state with no irrelevant part, which results in

$$\mathcal{P}\hat{\rho}(t_0) = \hat{\rho}(t_0)\,. \tag{2.42}$$

2.3.2. Derivation of the Nakajima-Zwanzig equation

With the definitions of the relevant part of the density matrix and the corresponding projector $\mathcal{P}$, we proceed with the derivation of an effective differential equation of the relevant part from the Liouville equation of the total system. To this end, we define the complementary operator $\mathcal{Q}$ via $\mathcal{Q}\hat{\rho} = \hat{\rho} - \mathcal{P}\hat{\rho}$, which has the following defining properties

$$\mathcal{P} + \mathcal{Q} = \mathbb{1} \tag{2.43}$$

$$\mathcal{Q}^2 = \mathcal{Q} \tag{2.44}$$

$$\mathcal{P}\mathcal{Q} = \mathcal{Q}\mathcal{P} = 0\,. \tag{2.45}$$

We start with the Liouville equation of the total system given in Eq. (2.20) to which we apply the projector $\mathcal{P}$ yielding

$$\frac{\mathrm{d}}{\mathrm{d}t}\mathcal{P}\hat{\rho}(t) = -\mathrm{i}\mathcal{P}\mathcal{L}\,\hat{\rho}(t) = -\mathrm{i}\mathcal{P}\mathcal{L}\mathcal{P}\,\hat{\rho}(t) - \mathrm{i}\mathcal{P}\mathcal{L}\mathcal{Q}\,\hat{\rho}(t)\,. \tag{2.46}$$

The first term on the right hand side is already of the desired form containing only the relevant part $\mathcal{P}\hat{\rho}(t) = \hat{\rho}_{\mathrm{rel}}(t)$. The irrelevant part $\mathcal{Q}\hat{\rho} = \hat{\rho}_{\mathrm{irr}}$ can be eliminated by applying Eq. (2.34) to the time-evolution of the total density matrix in Eq. (2.21), where we choose $\mathcal{O}_1 = \mathcal{L}\mathcal{Q}$ and $\mathcal{O}_2 = \mathcal{L}\mathcal{P}$ such that $\mathcal{O}_1 + \mathcal{O}_2 = \mathcal{L}\mathcal{Q} + \mathcal{L}\mathcal{P} = \mathcal{L}$. Applying $\mathcal{Q}$ from left then yields

$$\begin{aligned}\mathcal{Q}\hat{\rho}(t) &= \mathcal{Q}\,\mathrm{e}^{-\mathrm{i}\mathcal{L}(t-t_0)}\,\hat{\rho}(t_0) \\ &= \mathcal{Q}\,\mathrm{e}^{-\mathrm{i}\mathcal{L}\mathcal{Q}(t-t_0)}\,\hat{\rho}(t_0) - \mathrm{i}\int_{t_0}^{t}\mathrm{d}t'\;\; \mathcal{Q}\,\mathrm{e}^{-\mathrm{i}\mathcal{L}\mathcal{Q}(t-t')}\,\mathcal{L}\mathcal{P}\underbrace{\mathrm{e}^{-\mathrm{i}\mathcal{L}(t'-t_0)}\,\hat{\rho}(t_0)}_{=\hat{\rho}(t')}\end{aligned} \tag{2.47}$$

The exponential functions of this equation can be rewritten using the idempotence of the projector $\mathcal{Q}$ in the form

$$\mathcal{Q}\,\mathrm{e}^{-\mathrm{i}\mathcal{L}\mathcal{Q}(t-t_0)} = \mathrm{e}^{-\mathrm{i}\mathcal{Q}\mathcal{L}\mathcal{Q}(t-t_0)} = \mathcal{Q}\,\mathrm{e}^{-\mathrm{i}\mathcal{Q}\mathcal{L}\mathcal{Q}(t-t_0)}\,\mathcal{Q} = \mathrm{e}^{-\mathrm{i}\mathcal{Q}\mathcal{L}(t-t_0)}\,\mathcal{Q}\,. \tag{2.48}$$

Thus, we finally obtain the Nakajima-Zwanzig equation

$$\begin{aligned}\frac{\mathrm{d}}{\mathrm{d}t}\mathcal{P}\hat{\rho}(t) =& -\mathrm{i}\mathcal{P}\mathcal{L}\mathcal{P}\,\hat{\rho}(t) - \int_{t_0}^{t}\mathrm{d}t'\;\; \mathcal{P}\mathcal{L}\mathcal{Q}\,\mathrm{e}^{-\mathrm{i}\mathcal{Q}\mathcal{L}\mathcal{Q}(t-t')}\,\mathcal{Q}\mathcal{L}\mathcal{P}\hat{\rho}(t') \\ &- \mathrm{i}\mathcal{P}\mathcal{L}\mathcal{Q}\,\mathrm{e}^{-\mathrm{i}\mathcal{Q}\mathcal{L}\mathcal{Q}(t-t_0)}\,\mathcal{Q}\hat{\rho}(t_0)\,,\end{aligned} \tag{2.49}$$

which is an exact integro-differential equation. No approximation has been applied so far to obtain this equation. If the system exhibits only a relevant part at the beginning as described in Eq. (2.42), the last term vanishes according to $\mathcal{Q}\hat{\rho}(t_0) = \hat{\rho}_{\mathrm{irr}}(t_0) = 0$. In this case, the Nakajima-Zwanzig equation can be reformulated in compact form by

$$\frac{\mathrm{d}}{\mathrm{d}t}\hat{\rho}_{\mathrm{rel}}(t) = -\mathrm{i}\mathcal{L}_{\mathrm{rel}}\,\hat{\rho}_{\mathrm{rel}}(t) - \mathrm{i}\int_{t_0}^{t}\mathrm{d}t'\;\; \mathcal{K}(t-t')\hat{\rho}_{\mathrm{rel}}(t')\,, \tag{2.50}$$

where we have defined $\mathcal{L}_{\mathrm{rel}} = \mathcal{P}\mathcal{L}\mathcal{P}$ and the memory kernel

$$\mathcal{K}(t-t') = -\mathrm{i}\mathcal{P}\mathcal{L}\mathcal{Q}\,\mathrm{e}^{-\mathrm{i}\mathcal{Q}\mathcal{L}\mathcal{Q}(t-t')}\,\mathcal{Q}\mathcal{L}\mathcal{P}\,. \tag{2.51}$$

This memory kernel is also often referred to as the self-energy superoperator. According to Eq. (2.50), the Nakajima-Zwanzig equation contains both a unitary part and a non-unitary part. The unitary contribution $-\mathrm{i}\mathcal{L}_{\mathrm{rel}}\,\hat{\rho}_{\mathrm{rel}}(t)$ has the same form as the Liouville equation of a closed system, but the dynamics originate from an effective Hamiltonian $\hat{H}_{\mathrm{rel}}$ ($\mathcal{L}_{\mathrm{rel}}\hat{O} = [\hat{H}_{\mathrm{rel}}, \hat{O}]$). The non-unitary part takes into account the whole history of events from time t_0 to time t, where the influence of the irrelevant part of the system on the relevant part is expressed by the memory kernel $\mathcal{K}(t-t_0)$.

In summary, we have first split the density matrix of the total system into a relevant and an irrelevant part by realizing, that we do not need the full density matrix in order to calculate the expectation values of a finite number of observables. Based on this separation, we have then obtained the Nakajima-Zwanzig equation, which is an exact integro-differential equation for the relevant part only. So far, we have not applied any approximations, but the price for this is a rather abstract result with little use for actual calculations. In particular, the memory kernel still contains the full Liouville superoperator, which makes the actual calculation of the convolution in Eq. (2.50) challenging. The first step towards a more applicable equation of motion is to make a physically meaningful assignment of relevant and irrelevant parts. Once this is done, we will be able to define the projection operators $\mathcal{P}$ and $\mathcal{Q}$, where we will encounter the need of certain approximations, which are subsumed in the so-called Born approximation.

Born approximation

With the previous sections in mind, we consider an open system consisting of the system of interest S and an environment E, where the relevant part is identified with a product state of the system S with a certain environmental state. The Liouville superoperator of the combined system is then given by the commutator

$$\mathcal{L}\hat{O} = [\hat{H}, \hat{O}] = [\hat{H}_S + \hat{H}_E + \hat{H}_I, \hat{O}] \tag{2.52}$$

of an arbitrary operator $\hat{O}$ with the total Hamiltonian given in Eq. (2.27). Due to the linearity of the commutator we can split the total Liouville operator

$$\mathcal{L} = \mathcal{L}_S + \mathcal{L}_E + \mathcal{L}_I\,, \tag{2.53}$$

where the individual Liouville operators are defined by $\mathcal{L}_i\hat{O} = [\hat{H}_i, \hat{O}]$ with $i = S, E, I$. While these superoperators are fixed by the respective Hamiltonians, we have some freedom of choice for the projection operator $\mathcal{P}$ defining the relevant part of the density matrix. Keeping in mind the physical situation, which we want to describe, this task can be guided by the following aspects:

1. Since we are able to measure and control the system, it is reasonable to assume, that the system and the environment are not correlated at the beginning of the experiment, which results in a tensor product state $\hat{\rho}(t_0) = \hat{\rho}_S(t_0) \otimes \hat{\rho}_E(t_0)$.

2. Typically, the dimension of the system is much smaller than the dimension of the environment, which is formally expressed by $\dim(\mathcal{H}_S) \ll \dim(\mathcal{H}_E)$.

3. The interaction between the system and its environment should be weak compared to the internal interactions of system and environment, which can be quantified by the respective spectral norms[8] fulfilling $\|\hat{H}_I\| \ll \|\hat{H}_S\|$. Elsewise, we should modify our separation of system and environment, such that this condition is fulfilled.

Considering the last argument, the interaction between system and environment is sufficiently weak, such that almost no correlations between both subspaces are built up during the duration of the experiment. As a consequence, the initial product form of the total density matrix will approximately be preserved yielding $\hat{\rho}(t) = \hat{\rho}_S(t) \otimes \hat{\rho}_E(t)$. However, as we will see below, this assumption does not imply the disappearance of all correlations within the system or within the environment. If we further assume the environment to be sufficiently large, the interaction with the system will only slightly change its state, which effectively leads to a constant density matrix $\hat{\rho}_E(t) \approx \hat{\rho}_E(t_0) \equiv \hat{\rho}_E$. These two approximations together form the well known Born approximation. Since we additionally consider an initial product state, a possible choice for the projector, which fulfills all requirements described in Eqs. (2.40) to (2.42) is given by

$$\mathcal{P}\hat{O} = \mathrm{Tr}_E[\hat{O}] \otimes \hat{\rho}_E \,, \tag{2.54}$$

where $\hat{O}$ is an arbitrary operator in $\mathcal{F}$. However, this rather simple form of the operator comes not without a price. It has been shown [151, 152] that this approach only gives rise to a good approximation deep in the Born regime $\|\hat{H}_I\| \ll \|\hat{H}_S\|$, where correlations between the system and the environment are small. However, if these correlations become stronger, another projector, which explicitly takes into account these correlations, can be chosen [151, 152]. In this Thesis, however, we apply this master equation approach on models well satisfying the Born approximation and, hence, the above choice of $\mathcal{P}$ is sufficient.

Due to this specific form of the projector, several useful relations with respect to the Liouville operators $\mathcal{L}$, $\mathcal{L}_S$, $\mathcal{L}_E$, and $\mathcal{L}_I$ can be obtained. Using the definition of $\mathcal{P}$ and writing the superoperators $\mathcal{L}$ explicitly in the commutator form yields:

$$\mathcal{P}\mathcal{L}_S\hat{O} = \mathcal{L}_S\mathcal{P}\hat{O} \tag{2.55}$$

as well as

$$\begin{aligned} \mathcal{P}\mathcal{L}_E\hat{O} &= \mathrm{Tr}_E\Big[[\hat{H}_E, \hat{O}]\Big] \otimes \hat{\rho}_E = \mathrm{Tr}_E\Big[[\mathbb{1}_S \otimes \hat{H}'_E, \hat{O}_S \otimes \hat{O}_E]\Big] \otimes \hat{\rho}_E = 0 \,, \\ \mathcal{L}_E\mathcal{P}\hat{O} &= [\hat{H}'_E, \mathrm{Tr}_E[\hat{O}] \otimes \hat{\rho}_E] = \hat{O}_S \,\mathrm{Tr}[\hat{O}_E]\, [\mathcal{H}'_E, \hat{\rho}_E] = 0 \,, \end{aligned} \tag{2.56}$$

where we have assumed the state of the environment to be stationary in the last line. With these results, we additionally find

$$\mathcal{P}\mathcal{L}\mathcal{P} = \mathcal{P}(\mathcal{L}_S + \mathcal{L}_I)\mathcal{P} \,, \tag{2.57}$$

$$\mathcal{P}\mathcal{L}\mathcal{Q} = \mathcal{P}\mathcal{L}_I\mathcal{Q} \,, \tag{2.58}$$

$$\mathcal{Q}\mathcal{L}\mathcal{P} = \mathcal{Q}\mathcal{L}_I\mathcal{P} \,. \tag{2.59}$$

[8] For a Hermitian operator such as the Hamiltonian $\hat{H}$, the spectral norm $\|\hat{H}\| = \max_j(|E_j|)$ is equal to the largest absolute value of its eigenvalues E_i.

Since all of these combined superoperators appear in the Nakajima-Zwanzig equation in Eq. (2.50) and Eq. (2.51), we will analyze their effect on an arbitrary operator $\hat{O}$ in more detail. Applying the first superoperator in Eq. (2.57) on $\hat{O}$ yields

$$\mathcal{P}\mathcal{L}\mathcal{P}\hat{O} = \mathcal{P}(\mathcal{L}_S + \mathcal{L}_I)\mathcal{P}\hat{O} = \mathcal{P}[\hat{H}_S + \langle \hat{H}_I \rangle_{\hat{\rho}_E}, \hat{O}]\,, \tag{2.60}$$

where $\langle \hat{H}_I \rangle_{\hat{\rho}_E} = \mathrm{Tr}_E[\hat{H}_I \ \mathbb{1}_S \otimes \hat{\rho}_E] \otimes \mathbb{1}_E \equiv \langle \hat{H}_I \rangle'_{\hat{\rho}_E} \otimes \hat{\rho}_E$ is the expectation value of the interaction with respect to the environment [147]. In the Nakajima-Zwanzig equation this superoperator acts on the total density matrix $\hat{\rho}$, which leads to

$$\mathcal{P}(\mathcal{L}_S + \mathcal{L}_I)\mathcal{P}\ \hat{\rho}_S(t) \otimes \hat{\rho}_E = \mathcal{P}[\hat{H}'_S + \langle \hat{H}_I \rangle'_{\hat{\rho}_E}, \hat{\rho}_S(t)] \otimes \hat{\rho}_E \equiv \mathcal{P}(\tilde{\mathcal{L}}_S \hat{\rho}_S(t)) \otimes \hat{\rho}_E\,. \tag{2.61}$$

Both Hamiltonians and, consequently, also the effective Liouville superoperator $\tilde{\mathcal{L}}_S$ act only on the subspace of the system S and, hence, this term leads to a unitary time-evolution of the system driven by the effective Hamiltonian $\hat{H}'_S + \langle \hat{H}_I \rangle'_{\hat{\rho}_E}$. Thus, the interaction with the environment leads to a renormalization of the energy levels of the unperturbed system S, which is known as Lamb-shift contribution [18]. Similarly, we find the action of the superoperators in Eqs. (2.58) and (2.59) on an arbitrary operator

$$\mathcal{P}\mathcal{L}_I\mathcal{Q}\hat{O} = \mathcal{P}[\hat{H}_I - \langle \hat{H}_I \rangle_{\hat{\rho}_E}, \hat{O}] \tag{2.62}$$

$$\mathcal{Q}\mathcal{L}_I\mathcal{P}\hat{O} = [\hat{H}_I - \langle \hat{H}_I \rangle_{\hat{\rho}_E}, \mathcal{P}\hat{O}]\,, \tag{2.63}$$

where commutators of the operator with the "fluctuations" $\hat{H}_I - \langle \hat{H}_I \rangle_{\hat{\rho}_E}$ of the system-environment interaction appear [147]. Both superoperators enter the memory kernel defined in Eq. (2.51) and, thus, the non-unitary behavior can be related to these "fluctuations". Using the relations in Eqs. (2.57) to (2.63) and performing a trace over the environment, we finally find the Nakajima-Zwanzig equation for the density matrix of the system S to be of the comparably simple form

$$\frac{\mathrm{d}}{\mathrm{d}t}\hat{\rho}_S(t) = -\mathrm{i}\tilde{\mathcal{L}}_S\,\hat{\rho}_S(t) - \mathrm{i}\int_{t_0}^{t} \mathrm{d}t'\ \mathcal{K}_S(t-t')\hat{\rho}_S(t')\,, \tag{2.64}$$

where

$$\mathcal{K}_S(t-t')\hat{\rho}_S(t') = -\mathrm{i}\,\mathrm{Tr}_E[\mathcal{P}\mathcal{L}_I\mathcal{Q}\,\mathrm{e}^{-\mathrm{i}\mathcal{Q}\mathcal{L}\mathcal{Q}(t-t')}\,\mathcal{P}\mathcal{L}_I\mathcal{Q}\ \hat{\rho}_S(t') \otimes \hat{\rho}_E]\,. \tag{2.65}$$

Although, we have already gained some physical insight in the structure of the Nakajima-Zwanzig equation, it remains complicated to be solved even with these approximations. The reason for this is its complex non-unitary part, which involves a convolution of the memory kernel with the reduced density matrix $\hat{\rho}_S(t)$.

In principle, there are two different schemes to simplify this non-unitary part. The first scheme pursues the same path, which we have already taken by the Born approximation. Due the weakness of the system-environment interaction the kernel can be expanded in powers of $\mathcal{L}_I$. In order to obtain such an expansion, we use Eq. (2.34), where we set $\mathcal{O} = \mathcal{Q}\mathcal{L}\mathcal{Q}$ and split it into $\mathcal{O}_1 = \mathcal{Q}(\mathcal{L}_S + \mathcal{L}_E)\mathcal{Q}$ and $\mathcal{O}_2 = \mathcal{Q}\mathcal{L}_I\mathcal{Q}$. Since $\mathcal{L}_S$ and $\mathcal{L}_E$

commute with the projector $\mathcal{Q}$ due to Eqs. (2.55) and (2.56), we can use its idempotence given in Eq. (2.44) to find

$$\mathrm{e}^{-\mathrm{i}\mathcal{Q}\mathcal{L}\mathcal{Q}(t-t')} = \mathrm{e}^{-\mathrm{i}(\mathcal{L}_S+\mathcal{L}_E)(t-t')}\,\mathcal{Q} - \mathrm{i}\int_{t'}^{t}\mathrm{d}t''\;\; \mathrm{e}^{-\mathrm{i}(\mathcal{L}_S+\mathcal{L}_E)(t-t'')}\,\mathcal{Q}\mathcal{L}_I\mathcal{Q}\,\mathrm{e}^{-\mathrm{i}\mathcal{Q}\mathcal{L}\mathcal{Q}(t''-t')}\;. \quad (2.66)$$

Inserting this relation into Eq. (2.65) then yields $\mathcal{K}_S(t-t') = \mathcal{K}_S^{(2)}(t-t')+\mathcal{K}_S^{(3)}(t-t')+\ldots$, where the superscript indicates the number of $\mathcal{L}_I$ superoperators. Thus, in lowest order Born-approximation, the memory kernel is given by

$$\mathcal{K}_S^{(2)}(t-t')\hat{\rho}_S(t') = -\mathrm{i}\,\mathrm{Tr}_E[\mathcal{P}\mathcal{L}_I\mathcal{Q}\,\mathrm{e}^{-\mathrm{i}(\mathcal{L}_S+\mathcal{L}_E)(t-t')}\,\mathcal{Q}\mathcal{L}_I\mathcal{P}\;\hat{\rho}_S(t')\otimes\hat{\rho}_E]\,. \quad (2.67)$$

Evidently, truncating this series at second or any higher order yields only a reasonable approximation if the contributions with higher powers of the interaction are suppressed. Indeed, this is intimately related to the discussion about a suitable choice of the projector $\mathcal{P}$ above. It has been shown [151, 152], that an analysis including all orders is needed in the case of a comparably strong system-environment interaction in order to obtain the correct physical behavior. In these situations, a different choice of $\mathcal{P}$ allows to restrict the maximally needed order to a feasible number.

Unfortunately, testing whether a specific choice of $\mathcal{P}$ is suitable is generally a difficult task with such an abstract version of the Nakajima-Zwanzig equation. Rather, we have to prove its validity for a specific model as we do in Chapter 4. However, this approach does not dissolve the convolution and in many cases even the expanded version of the memory kernel is still too complicated to solve. Fortunately, there is another scheme to get rid of this convolution known as Markov approximation.

Markov approximation

The Markov approximation is based on an analysis of the lifetime of correlations within the environment. In general, an environmental correlation originating from the interaction between system and environment does not persist forever, but decays on a timescale τ_{corr}. If this timescale is much shorter than the typical timescale τ_S over which the system changes noticeably, the interaction of the system with its environment does not depend on events which have happened at earlier times $t' < t$, since it has effectively lost its memory. This assumption is known as Markov approximation. As this "loss of memory" already indicates, this separation of timescales allows us to simplify the convolution of the memory kernel $\mathcal{K}_S(t-t')$ with the density matrix $\hat{\rho}_S(t')$, in which the history of events is encoded.

The dependence of the dynamics on the lifetime of correlations within the environment can be made explicit by rewriting the memory kernel given in Eq. (2.65), where we analyze the lowest order Born approximation $K_S^{(2)}(t-t')$ for simplicity. This analysis follows a similar investigation in Ref. [18], in which, however, another master equation is considered. Higher order contributions to the kernel can be reformulated analogously, where the calculus is just as simple but tedious. According to Eqs. (2.62) and (2.63), this memory kernel contains two commutators with the interaction Hamiltonian $\hat{H}_I = \sum_n \hat{S}_n \otimes \hat{E}_n$, which can

be expressed in terms of system and environment operators $\hat{S}_n$ and $\hat{E}_n$, respectively [18]. With this form, we find

$$\hat{H}_I - \langle \hat{H}_I \rangle_{\hat{\rho}_E} = \sum_n \hat{S}_n \otimes (\hat{E}_n - \mathrm{Tr}[\hat{E}_n \hat{\rho}_E]) \equiv \sum_n \hat{S}_n \otimes \Delta\hat{E}_n \tag{2.68}$$

Inserting this formula in the definition of the second order memory kernel and expressing the time evolution operator in terms of ordinary operator according to Eq. (2.19) finally yields

$$\begin{aligned}\mathcal{K}_S^{(2)}(t-t')\hat{\rho}_S(t') = -\mathrm{i}\sum_{n,m} &[\hat{S}_n, \mathrm{e}^{-\mathrm{i}\hat{H}'_S(t-t')}\,\hat{S}_m\hat{\rho}_S(t')\,\mathrm{e}^{-\mathrm{i}\hat{H}'_S(t-t')}]\,\langle \Delta\hat{E}_n(t-t')\Delta\hat{E}_m\rangle_{\hat{\rho}_E} \\ &-[\hat{S}_n, \mathrm{e}^{-\mathrm{i}\hat{H}'_S(t-t')}\,\hat{\rho}_S\hat{S}_m(t')\,\mathrm{e}^{-\mathrm{i}\hat{H}'_S(t-t')}]\,\langle \Delta\hat{E}_m\Delta\hat{E}_n(t-t')\rangle_{\hat{\rho}_E}\,,\end{aligned} \tag{2.69}$$

where we have introduced the correlation functions

$$\langle \Delta\hat{E}_n(t-t')\Delta\hat{E}_m\rangle_{\hat{\rho}_E} = \mathrm{Tr}[\mathrm{e}^{i\hat{H}'_E(t-t')}\,\Delta\hat{E}_n\,\mathrm{e}^{-i\hat{H}'_E(t-t')}\,\Delta\hat{E}_m\,\hat{\rho}_E] \tag{2.70}$$

and

$$\langle \Delta\hat{E}_m\Delta\hat{E}_n(t-t')\rangle_{\hat{\rho}_E} = \mathrm{Tr}[\Delta\hat{E}_m\,\mathrm{e}^{i\hat{H}'_E(t-t')}\,\Delta\hat{E}_n\,\mathrm{e}^{-i\hat{H}'_E(t-t')}\,\hat{\rho}_E]\,. \tag{2.71}$$

Hence, the timescale $\tau_{\mathrm{corr}} \propto \|\hat{H}'_E\|^{-1}$ on which the correlations decay is determined by the internal interaction $\hat{H}'_E$ of the environment. This fact becomes clear if we carry out the trace using the eigenstates of $\hat{H}'_E$, where we find a similar mathematical structure as for the decoherence function in Eq. (2.9). According to Eq. (2.64), the (short-time) dynamics of the system is predominantly caused by the effective system Hamiltonian $\hat{H}'_S + \langle \hat{H}'_I \rangle_{\hat{\rho}_E}$ and, hence, the timescale on which the system changes significantly is given by $\tau_S \propto \|\hat{H}'_S + \langle \hat{H}'_I \rangle_{\hat{\rho}_E}\|^{-1}$. Thus, the Markov approximation is valid as long as

$$\frac{\tau_{\mathrm{corr}}}{\tau_S} = \frac{\|\hat{H}'_S + \langle \hat{H}'_I \rangle_{\hat{\rho}_E}\|}{\|\hat{H}'_E\|} \ll 1\,. \tag{2.72}$$

In this case, the correlation functions are sharply peaked[9] at $t - t' \approx 0$ enabling several convenient simplifications. Since these environmental correlations decay quickly, the density matrix of the system $\hat{\rho}_S(t')$ does not change appreciably and, consequently, we can replace it by $\hat{\rho}_S(t)$. Due to this modification, the convolution in Eq. (2.64) is dissolved and the integro-differential equation becomes time-local. In this form, it is known as the Redfield equation [18]. In addition to its fast loss of memory, the recurrence time of the environment is in general large[9], which enables the extension of the lower bound of the integral t_0 to $-\infty$ without changing the integral. Substituting $t' \to \tau = t - t'$, Eq. (2.64)

[9] At first glance, the correlation functions undergo periodic oscillations, which ultimately lead to their recurrence at some time. Since the environment is large, these recurrences are, however, typically much longer than the age of the universe [144]. We will encounter this argument again in Chapter 6, where we analyze the recurrence time of the central spin model for less than ten nuclear spins.

finally becomes

$$\frac{\mathrm{d}}{\mathrm{d}t}\hat{\rho}_S(t) = -\mathrm{i}\tilde{\mathcal{L}}_S\,\hat{\rho}_S(t) - \sum_{n,m}\int_0^\infty \mathrm{d}\tau\ \Big\{[\hat{S}_n, \mathrm{e}^{-\mathrm{i}\hat{H}'_S\tau}\,\hat{S}_m\hat{\rho}_S(t)\,\mathrm{e}^{-\mathrm{i}\hat{H}'_S\tau}]\,\langle\Delta\hat{E}_n(\tau)\Delta\hat{E}_m\rangle_{\hat{\rho}_E} - [\hat{S}_n, \mathrm{e}^{-\mathrm{i}\hat{H}'_S\tau}\,\hat{\rho}_S\hat{S}_m(t)\,\mathrm{e}^{-\mathrm{i}\hat{H}'_S\tau}]\,\langle\Delta\hat{E}_m\Delta\hat{E}_n(\tau)\rangle_{\hat{\rho}_E}\Big\}. \tag{2.73}$$

However, in many situations of physical interest, the requirement for the Markov approximation in Eq. (2.72) is not fulfilled due to low temperatures of the environment leading to longer τ_{corr} or comparably weak interactions within the environment. An example for this, which is relevant for this Thesis, is the central spin model with the electron spin interacting with the nuclear spins via HI. Neglecting external magnetic fields, the typical timescale τ_S of the electron spin is determined by the effective nuclear magnetic field originating from a random distribution of the nuclear spin states: $\tau_S \propto A^{\mathrm{f}}_{\mathrm{HI}} = n_I A_{\mathrm{HI}}/\sqrt{K}$. The internal dynamics of the nuclear spins is driven by either the nuclear dipole-dipole interaction or by the Knight-field due to the HI depending on which mechanism is stronger. In QDs, the dipole-dipole interaction is typically very weak, cf. Tab. 1.1 and, hence, correlations are lost over a time $\tau_{\mathrm{corr}} \propto A^{\mathrm{s}}_{\mathrm{HI}}$, where $A^{\mathrm{s}}_{\mathrm{HI}} = n_I A_{\mathrm{HI}}/K$ is the energy involved with the Knight-field. Using the values for $A^{\mathrm{f}}_{\mathrm{HI}}$ and $A^{\mathrm{s}}_{\mathrm{HI}}$ given in Tab. 1.1, we find for the ratio of the respective timescales $\frac{\tau_{\mathrm{corr}}}{\tau_S} = \frac{A^{\mathrm{f}}_{\mathrm{HI}}}{A^{\mathrm{s}}_{\mathrm{HI}}} \sim 10^2$ for GaAs and graphene. As a consequence, the nuclear spins keep track of their past and, thus, the dynamics of the electron spin become non-Markovian [76].

Part II.

The central spin model in quantum dots

3. Thermal electron spin flip in quantum dots

In this chapter, we are interested in the thermal properties of the electron spin, which we investigate in terms of statistical physics. The most important interactions determining the properties of the electron spin involve the HI between the electron spin and the nuclear spins and the Zeeman coupling of these spins to an external magnetic field as discussed in Chapter 1. Besides these interactions, there is a comparably weak interaction between the spins and the phonons present in the QD. As a consequence of this weakness, it is justified to consider the electron spin and the nuclear spins as one system, which is in contact with the phonon environment. Hence, it is possible to study the equilibrium physics of the electron spin and the nuclear spins in terms of the canonical ensemble of statistical physics, where the coupling to the phonon environment defines the temperature of the system. Using this approach, we find an intriguing flip of the electron spin, which is triggered by an increasing temperature.

Due to these properties, the present chapter is particular with respect to the subsequent chapters for several reasons. While in the following chapters the nuclear spins are considered as the environment interacting with the electron spin, they are a part of the system of interest here. Moreover, we are interested in equilibrium states rather than in spin dynamics investigated in the subsequent chapters. Finally, the results obtained in the present chapter are most relevant for QDs built from group III and V or II and VI elements of the periodic table, whereas the rest of this Thesis focuses on (group IV based) graphene QDs.

This chapter closely follows our publication in Ref. [153].[1] In order to improve the readability of the text, some derivation of results discussed in this chapter are presented in detail in Appendix A.

3.1. Introductory considerations

Our analysis of the thermal behavior of the combined system is based on a minimal model for the spin dynamics in a QD. It incorporates an external magnetic field to which the electron and the nuclear spins couple and the HI which links the electron spin to all nuclear spins. The effect of an external magnetic field on the electron spin $\hat{S}_z$ is described by the Zeeman Hamiltonian in Eq. (1.9), where we choose the external magnetic field to point in z-direction,

$$\hat{H}^S_{\mathrm{ZE}} = g^* \mu_B B_z \hat{S}_z \,. \tag{3.1}$$

[1]

Likewise, the nuclear spins $\hat{I}_{k,z}$ also align with respect to the external magnetic field by means of another Zeeman term

$$\hat{H}^I_{\mathrm{ZE}} = -\sum_{k=1}^{K} g_N \mu_N B_z \hat{I}_{k,z} \,. \tag{3.2}$$

The relative sign difference between Eq. (3.1) and Eq. (3.2) resembles the negative sign of the electron charge.

By writing the nuclear Zeeman Hamiltonian in the form of Eq. (3.2), we already assume that there is only one spin species present in the dot. This assumption simplifies our reasoning and, thus, allows us to better identify the main physics being relevant for our results. Distinguishing different spin species would not change our findings significantly as we discuss at the end of this chapter. As a consequence of this simplification, we use average values of the nuclear g-factors, where we refer to Section 1.2.2 for more details of this average over different spin species. Our assumption of a single spin species also simplifies the HI Hamiltonian in Eq. (1.22)

$$\hat{H}_{\mathrm{HI}} = \sum_{k=1}^{K} A_k \Big[\hat{S}_z \hat{I}_{k,z} + \frac{1}{2} (\hat{S}_+ \hat{I}_{k,-} + \hat{S}_- \hat{I}_{k,+}) \Big] \,, \tag{3.3}$$

where the coupling constants

$$A_k = A_{HI}\, v_0 |\phi(\boldsymbol{r}_k)|^2 \tag{3.4}$$

are defined in Eq. (1.24). From our discussion of the HI in Section 1.2.3, we know that the constant

$$A_{\mathrm{HI}} \propto g\, g_N \tag{3.5}$$

is proportional to the nuclear g-factor g_N and the bare electron g-factor g in contrast to the effective g-factor g^* entering the Zeeman Hamiltonian in Eq. (3.1). Since g is positive, the sign of the HI is determined by the sign of the nuclear g-factor g_N. This sign, however, plays an important role, since it determines the form of the ground state of the HI.

If the coupling constant A_{HI} is positive (negative), the ground state of the bare HI will favor an anti-parallel (parallel) alignment of the electron spin with respect to all nuclear spins. Both ground states are twice degenerate, since a flip of all spins results in the same energy. Similarly, the two Zeeman terms also show the same two types of spin ordering depending on the signs of the respective g-factors g^* and g_N. In contrast to the HI, these ground states are unique. If, for instance, $g^* < 0$ and $g_N > 0$, the Zeeman terms would force both the electron spin and all nuclear spins to be parallel to the external magnetic field at zero temperature. Thus, when both the HI and the Zeeman interaction are present, there can arise an interesting competition of spin ordering with the electron spin being parallel or anti-parallel with respect to the nuclear spins. In particular, if the external magnetic field is sufficiently small, the HI is still strong enough to maintain the anti-parallel alignment of the electron spin with respect to the nuclear spins. If then additionally the signs of the g-factors are given by $g^* < 0$ and $g_N > 0$, the electron spin will be anti-parallel to the external magnetic field, whenever its Zeeman energy is below the total Zeeman energy of all nuclear spins. Starting from this particular ground state, we will show that a sudden flip of all spins can happen at a finite temperature $T_0 > 0$.

To this end, we will first argue in Section 3.2.1 how the HI Hamiltonian can be simplified based on physical arguments. We will then apply standard statistical physics to the Hamiltonian $\hat{H} = \hat{H}^S_{\mathrm{ZE}} + \hat{H}^I_{\mathrm{ZE}} + \hat{H}_{\mathrm{HI}}$ in Section 3.2.2, where we neglect the off-diagonal parts of the HI. Doing so, we calculate the thermal expectation value of the electron spin, whose properties are studied both analytically and numerically in Sections. 3.2.3 and 3.2.4, respectively. In Section 3.2.4, we also present the results for the thermal expectation values for an extended HI Hamiltonian including its off-diagonal part, i.e., the flip-flop terms. The corresponding calculations are carried out in Appendix A. After this mathematical analysis, we will then explain the physical mechanism being responsible for this spin flip in Section 3.2.5. We finally review our initial simplifications of the HI and discuss in which real systems our findings should be observable in Section 3.3.

3.2. Thermal electron spin flip

3.2.1. Simplified Hamiltonian

As mentioned above, we will first introduce certain simplifications to the HI Hamiltonian, which allow for an analytical calculation of thermal expectation values:

1. We assume that all nuclear spins are spin one-half, where the number of nuclear spins is K.

2. We will use the so-called box-model, where the couplings $A_k = \frac{A_{\mathrm{HI}}}{K}$ are all the same. By this, we assume that every nucleus in the dot carries a spin and that the envelope function $\phi(\boldsymbol{r}_k)$ of the electron does not change much inside the QD.

With these two assumptions and $g^* < 0$ as explained in the introduction, the total Hamiltonian is given by

$$\begin{aligned}\hat{H}_\alpha &= \hat{H}^S_{\mathrm{ZE}} + \hat{H}^I_{\mathrm{ZE}} + \hat{H}_{\mathrm{HI}} \\ &= -|g^*|\mu_B B_z \hat{S}_z - g_N \mu_N B_z \hat{J}_z + \frac{A_{\mathrm{HI}}}{K}\left[\hat{S}_z\hat{J}_z + \frac{\alpha}{2}(\hat{S}_+\hat{J}_- + \hat{S}_-\hat{J}_+)\right], \end{aligned} \tag{3.6}$$

where we have introduced the total nuclear spin $\hat{\boldsymbol{J}} = \sum_{k=1}^{K} \hat{\boldsymbol{I}}_k$ for convenience. The usual raising and lowering operators $\hat{S}_\pm = \hat{S}_x \pm \mathrm{i}\hat{S}_y$ and $\hat{J}_\pm = \hat{J}_x \pm \mathrm{i}\hat{J}_y$ form the flip-flop terms. By means of the parameter α, we distinguish between an extended Hamiltonian $\hat{H}_1$ and a simplified Hamiltonian $\hat{H}_0$, which allows us to present the basic physics of the electron spin flip more easily.

Before we proceed with the calculation of thermal expectation values, we introduce dimensionless parameters by measuring all energies in units of $\frac{A_{\mathrm{HI}}}{2K}$. The total Hamiltonian then reads

$$\hat{H}_\alpha = -\sigma\hat{S}_z - \nu\hat{J}_z + 2\hat{S}_z\hat{J}_z + \alpha\left(\hat{S}_+\hat{J}_- + \hat{S}_-\hat{J}_+\right), \tag{3.7}$$

where the parameters are given by $\sigma = |g^*|\mu_B B_z/\frac{A_{\mathrm{HI}}}{2K}$ and $\nu = g_N\mu_N B_z/\frac{A_{\mathrm{HI}}}{2K}$. These two quantities are obviously not independent of each other since both are proportional to the external magnetic field B_z. Thus, we choose $\sigma = K\rho\nu$, where $\rho = |g^*|\mu_B B_z/(K\, g_N\mu_N B_z)$ is the ratio of the Zeeman energies of the electron and all nuclear spins, respectively. This

ratio can be also characterized by the critical number of nuclear spins $\kappa = \rho K$, which is constant for a given material. If the number of nuclear spins present in the QD is below this critical number, there is no electron spin flip, because the electron is parallel to the external magnetic field for all temperatures.

In the following, we will first analyze the thermal expectation value of the electron spin for the simplified Hamiltonian $\hat{H}_0$. Since this Hamiltonian is already diagonal in the basis of products states of the individual spin states, all calculations are much easier and, hence, the physics causing the spin flip becomes more apparent. However, it is not clear in the first place, if the neglected flip-flop terms give rise to quantum fluctuations, which destroy the electron spin flip. Thus, we have also calculated the thermal expectation value of the electron spin for an extended Hamiltonian $\hat{H}_1$ including the flip-flop terms in Appendix A. Interestingly, many findings are unchanged with respect to the simpler case or restored in the limit of large system sizes, where the flip-flop terms are shown to be irrelevant.

3.2.2. Thermal expectation values

Without the flip-flop terms, the simplified Hamiltonian is already diagonal in the product basis $|m_S\rangle \otimes \bigotimes_{k=1}^{K} |m_k\rangle$, where $|m_S\rangle$ is an eigenstate of $\hat{S}_z$ with $m_S \in \{-\frac{1}{2}, \frac{1}{2}\}$. Similarly, the state $|m_k\rangle$ is an eigenstate of the k-th nuclear spin operator $\hat{I}_{k,z}$ with $m_k \in \{-\frac{1}{2}, \frac{1}{2}\}$. In this basis, the partition function for this Hamiltonian then reads

$$Z = \mathrm{Tr}[e^{-\hat{H}_0/k_B T}] = \sum_{m_S} \sum_{\{m_k\}_{k=1}^{K}} e^{-\langle m_S, m_K, m_{K-1}, \ldots | \hat{H}_0 | m_S, m_K, m_{K-1}, \ldots \rangle / k_B T}, \tag{3.8}$$

where the diagonal matrix elements are given by

$$\begin{aligned} &\langle m_S, m_K, m_{K-1}, \ldots | \hat{H}_0 | m_S, m_K, m_{K-1}, \ldots \rangle / k_B T \\ &= -\frac{2}{\tau} \Big[\rho \nu K \, m_S + \sum_{k=1}^{K} \left(\nu \, m_k - 2 \, m_S m_k \right) \Big] \end{aligned} \tag{3.9}$$

with the dimensionless temperature $\tau = k_B T / \frac{A_{\mathrm{HI}}}{2K}$. Exploiting the fact that sums in the exponential functions factorize finally yields

$$Z = \sum_{m_S} \prod_{k=1}^{K} \sum_{m_k} e_{m_S, m_k} = (e_{\frac{1}{2},\frac{1}{2}} + e_{\frac{1}{2},-\frac{1}{2}})^K + (e_{-\frac{1}{2},\frac{1}{2}} + e_{-\frac{1}{2},-\frac{1}{2}})^K, \tag{3.10}$$

where

$$e_{m_S, m_k} = \exp\left[\frac{2}{\tau} \left(\rho \nu \, m_S + \nu \, m_k - 2 \, m_S m_k \right) \right]. \tag{3.11}$$

With the partition function at hand, the calculation of the thermal expectation value of the electron spin is readily obtained

$$\langle \hat{S}_z \rangle_\tau = \frac{\tau}{2} \frac{\partial}{\partial \sigma} \ln[Z] = \frac{\tau}{2K\nu} \frac{\partial}{\partial \rho} \ln[Z] = \frac{1}{2} \left(\frac{1}{1 - \Pi} - \frac{1}{1 - \Pi^{-1}} \right), \tag{3.12}$$

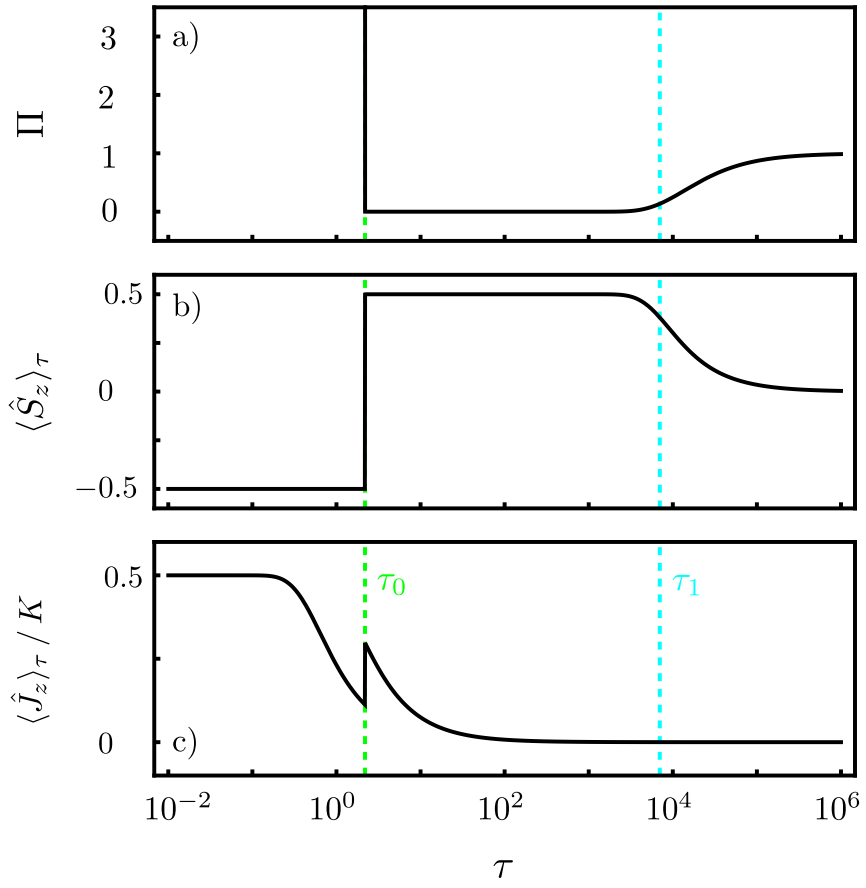

Figure 3.1. **a)**: $\Pi(\tau, \nu, \rho, K)$ as a function of the dimensionless temperature τ for $\nu = 2$, $\rho = 0.35$ and $K = 10^4$. As we show in the text and in Fig. 3.2, this choice of parameters fulfills the necessary conditions for the spin flip. At a temperature τ_0, the function suddenly drops from very large values to zero. At temperatures $\tau \gtrsim \tau_1$ the function rises again and saturates at $\Pi = 1$ for large temperatures. **b)**: The thermal expectation value of the electron spin $\langle \hat{S}_z \rangle_\tau$ exhibits a sudden flip at τ_0. For temperatures above τ_1 the electron spin is thermally equilibrated. **c)**: The thermal expectation value of the total nuclear spin $\langle \hat{J}_z \rangle_\tau = \frac{\tau}{2} \frac{\partial}{\partial \nu} \ln[Z]$ decreases before the electron spin flip. At τ_0, it is suddenly increased again. For $\nu < 1$ instead, the total nuclear spin would exhibit a flip similar to the electron spin. *Figure reprinted with permission from [153].*

where the function

$$\Pi = \Pi(\tau, \nu, \rho, K) = \left[\frac{e_{-\frac{1}{2},\frac{1}{2}} + e_{-\frac{1}{2},-\frac{1}{2}}}{e_{\frac{1}{2},\frac{1}{2}} + e_{\frac{1}{2},-\frac{1}{2}}} \right]^K \tag{3.13}$$

controls the behavior of $\langle \hat{S}_z \rangle_\tau$. If $\Pi \to \infty$, we find $\langle \hat{S}_z \rangle_\tau \to -\frac{1}{2}$, $\Pi = 0$ results in $\langle \hat{S}_z \rangle_\tau = \frac{1}{2}$ and, finally, $\Pi = 1$ yields $\langle \hat{S}_z \rangle_\tau = 0$. As it turns out, the electron spin has to go through exactly these steps for the thermal spin flip to occur as illustrated in Fig. 3.1. In the following, we will first explore the parameter space of $\Pi(\tau, \nu, \rho, K)$ to mathematically find the conditions necessary for the spin flip to occur. Afterwards, we calculate at which temperatures Π and, consequently, $\langle \hat{S}_z \rangle_\tau$ undergo their characteristic changes. To this end, we will analyze Π analytically and compare the findings with numerical calculations of $\langle \hat{S}_z \rangle_\tau$. Finally, we will interpret these results in order to understand when and why this effect appears in a physical system.

3.2.3. Analysis of the spin flip

By inserting the definition of the exponential functions in Eq. (3.11) into Eq. (3.13) and rearranging factors, we find

$$\Pi(\tau, \nu, \rho, K) = \left\{ \exp\left[-\frac{2\rho\nu}{\tau} \right] \frac{\exp\left[\frac{1}{\tau}(-\nu - 1)\right] + \exp\left[\frac{1}{\tau}(\nu + 1)\right]}{\exp\left[\frac{1}{\tau}(-\nu + 1)\right] + \exp\left[\frac{1}{\tau}(\nu - 1)\right]} \right\}^K \equiv \pi^K \,. \tag{3.14}$$

By further rearrangements of factors in Eq. (3.14), we identify that $\rho < 1$ and $0 < \nu < \rho^{-1}$ are necessary conditions for Π to diverge at $\tau \to 0$ and, consequently, for the spin flip to occur. Within this parameter regime, we want to identify the temperature τ_0, at which Π drops from infinity to zero, and the temperature τ_1 at which Π rises to 1 as indicated in Fig. 3.1.

The latter temperature can be directly read off from Eq. (3.14), since $\Pi = 1$ for all temperatures τ well above

$$\tau_1 = 2\rho\nu K \,. \tag{3.15}$$

At a specific temperature τ the function π defined in Eq. (3.14) changes from $\pi > 1$ to $\pi < 1$. Since one has to take it to the power of $K \gg 1$, this marks the temperature, at which the sudden drop from $\Pi \gg 1$ to $\Pi \ll 1$, and, hence, the spin flip occurs. Thus, the transcendental equation defining τ_0 reads

$$\rho = -\frac{\tau_0}{2\nu} \ln \left\{ \frac{\exp\left[\frac{1}{\tau_0}(-\nu - 1)\right] + \exp\left[\frac{1}{\tau_0}(\nu + 1)\right]}{\exp\left[\frac{1}{\tau_0}(-\nu + 1)\right] + \exp\left[\frac{1}{\tau_0}(\nu - 1)\right]} \right\}. \tag{3.16}$$

This equation can be expanded in powers of $\frac{1}{\tau_0} \ll 1$,

$$\rho \approx \frac{1}{\tau_0} + \mathrm{O}\Big(\frac{1}{\tau_0^3}\Big) \,. \tag{3.17}$$

As a consequence, the temperature $\tau_0 \approx \rho^{-1}$ is independent of ν for $\rho \ll 1$. Since $\rho = \kappa/K$ is a constant for a given QD, this is a rather intriguing result. This constant being $\rho \ll 1$

corresponds to a situation, where the total nuclear Zeeman energy is much larger than the electron Zeeman energy.

Before we give a detailed physical interpretation of our results, let us compare these analytical results for the simplified Hamiltonian $\hat{H}_0$ with a numerical analysis of Eqs. (3.12) and (3.13), respectively, and the behavior of the electron spin for the extended Hamiltonian $\hat{H}_1$ as calculated in Appendix A.

3.2.4. Numerical results and the spin flip for the extended Hamiltonian

In order to verify our analytical results for $\hat{H}_0$, we show density plots of the expectation value of the electron spin $\langle \hat{S}_z \rangle_\tau = \langle \hat{S}_z \rangle_\tau (\tau, \nu, \rho, K)$, where we choose the number of nuclear spins to be $K = 10^4$. With K being fixed, τ, ρ, and ν remain as parameters. In Fig. 3.2 a), we show $\langle \hat{S}_z \rangle_\tau$ as a function of τ and ρ with $\nu = 2$. As we will show below, for this choice of ν, the electron Zeeman energy competes with the total HI energy. If $\rho\nu > 1$ the Zeeman energy exceeds the HI energy and the electron spin is up for all τ, which is clearly shown in Fig. 3.2 a). Additionally, we plotted Eqs. (3.15) and (3.16) in order to demonstrate the behavior of τ_1 and τ_0, respectively. Both analytical results show a remarkable agreement with the numerical findings. In Fig. 3.2 b), we show the same plot for $\nu = 0.09$. For this choice of ν, the electron Zeeman energy is always smaller than the total HI energy. However, if $\rho > 1$, the electron Zeeman energy is larger than the total nuclear Zeeman energy and, consequently, the electron spin flip is up for all τ as can be seen from Fig. 3.2 b).

As indicated above, in a real system, ρ is rather a fixed parameter than a real variable. Hence, we also calculated $\langle \hat{S}_z \rangle_\tau$ as a function of temperature τ and the Zeeman energy of a single nucleus ν, which is proportional to the magnetic field B_z. The result is shown in Fig. 3.2 c), where we have chosen $\rho = \frac{\kappa}{K} = 0.09$. This is a realistic value considering the values of the critical number κ in Tab. 3.1 and the typical number of nuclear spins on the order of $K \simeq 10^5$ to 10^6. In this figure, the behavior of $\tau_0 = \rho^{-1}$ is most prominent. Moreover, it is obvious that $\rho\nu < 1$ is indeed a necessary condition for the spin flip.

Finally, we have to confirm that the influence of the flip-flop terms, which are present in the extended Hamiltonian $\hat{H}_1$ does not destroy the electron spin flip. As we show in Appendices A.2 and A.3, the thermal expectation value of the electron spin can be exactly solved for the box-model [154, 155, 156, 157]. By investigating the temperature dependence of $\langle \hat{S}_z \rangle_\tau$ for up to $K = 60$ nuclear spins, we find that both temperature scales τ_0 and τ_1 are unchanged. For small numbers of nuclear spins, however, we find that the additional interaction alters the behavior of $\langle \hat{S}_z \rangle_\tau$. To be more specific, the minimum of the thermal expectation value $\langle \hat{S}_z \rangle_0$ at zero temperature is larger than $-\frac{1}{2}$ for few nuclear spins as can be seen from Fig. 3.3 a). For larger system sizes, the original value of $\langle \hat{S}_z \rangle_0 = -\frac{1}{2}$ seems to be restored. Identifying the ground state of the system in Appendix A.4, we are indeed able to show that $\langle \hat{S}_z \rangle_0 = -\frac{1}{2}$ is exactly reached in the limit of large K. Moreover, the maximum of the electron expectation value at approximately $\tau = \frac{2}{\rho}$ is altered by the flip-flop terms as is obvious from Fig. 3.3 b). Again, their effect is most pronounced for small K, while the results for $\hat{H}_0$ are reproduced for large system sizes. Thus, the quantum fluctuations do not destroy the spin flip. Physically, it seems very likely, that the nuclear Zeeman energy additionally stabilizes the spin system against the flip-flop terms. In the limit of large system sizes, the physics of the simplified Hamiltonian is restored, which can

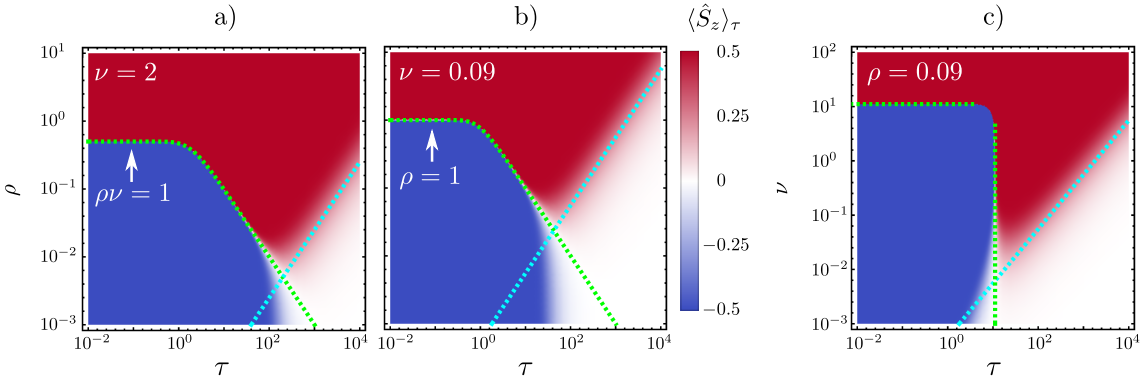

Figure 3.2. **a)**: The thermal expectation value of the electron spin as a function of temperature τ and ρ for $\nu = 2$. The green dashed line shows the defining Eq. (3.16) of τ_0. For small ρ, one finds $\tau_0 = \rho^{-1}$ in agreement with the plot. The light blue line is given by τ_1 in Eq. (3.15). For $\rho\nu \geq 1$ the spin flip is absent. For temperatures above τ_1, the electron is thermally equilibrated and, hence, $\langle \hat{S}_z \rangle_\tau = 0$. **b)**: The thermal expectation value of the electron spin as a function of temperature τ and ρ for $\nu = 0.09$. Clearly, the spin flip is absent for $\rho \geq 1$. **c)**: The thermal expectation value of the electron spin as a function of temperature τ and ν for $\rho = 0.09$. The light blue line is given by τ_1 in Eq. (3.15). The horizontal green line corresponds to $\nu = \rho^{-1}$ and the vertical green line to $\tau = \rho^{-1}$. For $\rho\nu \geq 1$ the spin flip is absent. For temperatures above τ_1, the electron is again thermally equilibrated. *Figure reprinted with permission from [153]. ©2015 American Physical Society. All rights reserved.*

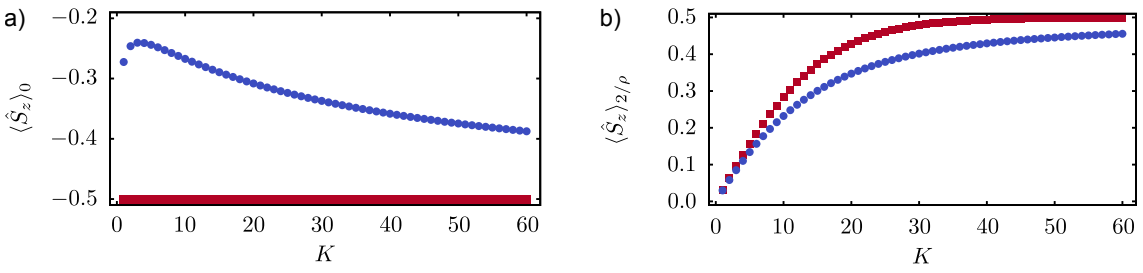

Figure 3.3. Dependence of the thermal expectation value of the electron spin $\langle \hat{S}_z \rangle_\tau$ on the number of nuclear spin for the simplified Hamiltonian $\hat{H}_0$ (red squares) and the extended Hamiltonian $\hat{H}_1$ (blue circles) containing the flip-flop terms. We have chosen $\rho = 0.35$, $\nu = 2$, and $\sigma = K\rho\nu$. **a)**: At $\tau = 0$, the electron spin $\langle \hat{S}_z \rangle_0$ is in its ground state, which depends on K in the case of $\hat{H}_1$. **b)**: The electron spin $\langle \hat{S}_z \rangle_{2/\rho}$ reaches its maximum at approximately $\tau = 2/\rho$. This maximum is in any case a function of K. *Figure reprinted with permission from [153]. ©2015 American Physical Society. All rights reserved.*

be understood by analyzing how different states are affected by the flip-flop terms. The states being most efficient for this interaction are of the form $|-\frac{1}{2},\frac{1}{2},\ldots,\frac{1}{2}\rangle$ and vice versa, since the electron spin can flip with every nuclear spin. The states $|-\frac{1}{2},\frac{1}{2},-\frac{1}{2},\frac{1}{2},-\frac{1}{2},\ldots\rangle$ (and all permutations of the nuclear spins) are the less affected ones. For large system sizes, however, the statistical weight of the latter states is much higher than for the former states, explaining the vanishing influence of the flip-flop terms for increasing K.

3.2.5. Physical interpretation of the results

So far, we have mathematically clarified for which parameters one finds the spin flip. In the following, we want to explain why this spin flip occurs and how the conditions found above can be interpreted physically. Therefore, we will have a closer look on the energies of the Hamiltonian $\hat{H}_0$ given in Eq. (3.7). Since the Hamiltonian is invariant under the exchange of two nuclear spins, only the total nuclear angular momentum $M_J = \sum_k m_k$ is relevant resulting in

$$N_{M_J}^K = \binom{K}{\frac{K}{2} - M_J} \tag{3.18}$$

equal energies

$$E_{m_S}^{M_J} = -K\rho\nu m_S - M_J\nu + 2m_S M_J\,. \tag{3.19}$$

A plot of $E_{1/2}^{M_J}$ and $E_{-1/2}^{M_J}$ is presented in Fig. 3.4, where a small system size of $K = 10$ nuclear spins has been chosen for practical reasons. Although the spin flip is not perfect for such a small number of nuclear spins as is obvious from Fig. 3.3 b), the physics of the spin flip still becomes clear. The ground state is given by $m_S = -\frac{1}{2}$ and $M_J = \frac{K}{2}$, whose energy eigenvalue $E_{-1/2}^{K/2}$ is not degenerate. Hence, the electron spin is anti-parallel to the external magnetic field, whereas all nuclear spins are parallel. If one follows the energies $E_{-1/2}^{M_J}$ and $E_{1/2}^{M_J}$ starting from $M_J = \frac{K}{2}$, one finds that $E_{-1/2}^{M_J}$ increases much faster than $E_{1/2}^{M_J}$, which is also obvious from Eq. (3.19). Since the degeneracy of the corresponding energy levels $N_{M_J}^K$ defined in Eq. (3.18) is strongly increasing, many states with $m_S = \frac{1}{2}$ become thermally available for finite temperatures. Once the temperature reaches τ_0, there is a strong imbalance between the number of states with $m_S = -\frac{1}{2}$ and the number of states with $m_S = \frac{1}{2}$, which finally causes the sudden spin flip. If the temperature is further increased above τ_1, almost all states are reached and, hence, one finds $\langle \hat{S}_z \rangle_\tau = 0$.

Finally, we would like to interpret the mathematical conditions on the parameters physically. Let us start with the constraints on ρ and $\rho\nu$. Since the parameter $\rho = |g^*|\mu_B B_z / K g_N \mu_N B_z$ is given by the ratio of the electron Zeeman and the total nuclear Zeeman energy, the ratio being $\rho < 1$ implies that the Zeeman energy of all nuclear spins exceeds the electron Zeeman energy. Similarly, the product $\rho\nu = 2|g^*|\mu_B B_z / A_{\mathrm{HI}} < 1$ tells us that the Zeeman energy of the electron has to be smaller than the total HI energy. This imposes an upper bound on the external magnetic field

$$B_z < B_{\max} = \frac{A_{\mathrm{HI}}}{2|g^*|\mu_B}\,. \tag{3.20}$$

Yet, the magnetic field has additionally to be large enough in order to separate the two temperatures τ_0 and τ_1. For small magnetic fields, the former temperature is given by

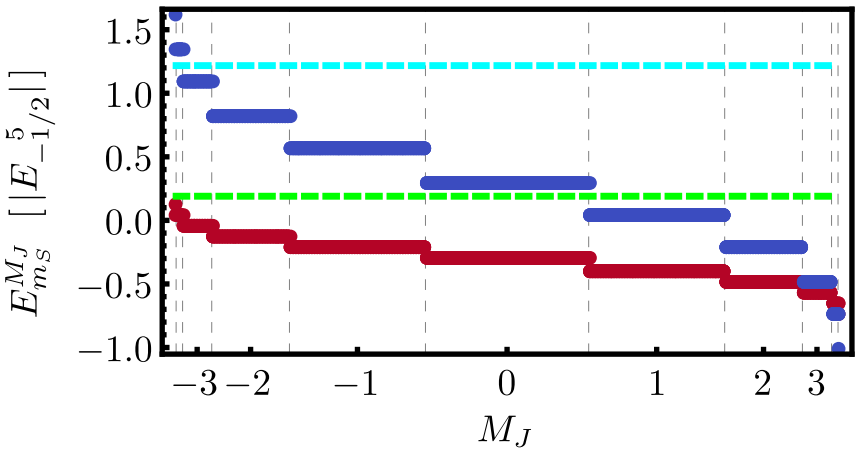

Figure 3.4. Energies of the Hamiltonian as a function of the total nuclear angular momentum $M_J = \sum_k m_k$ for an electron spin parallel ($m_S = \frac{1}{2}$, red) and anti-parallel ($m_S = -\frac{1}{2}$, blue) to the external magnetic field. The other parameters are $\nu = 2$, $\rho = 0.35$, and $K = 10$. The width of a column is proportional to the degeneracy of the respective energy level given by $N_{M_J}^K$ in Eq. (3.18). The green and light blue line show the temperatures τ_0 and τ_1, respectively. *Figure reprinted with permission from [153]. ©2015 American Physical Society. All rights reserved.*

$\tau_0 = \rho^{-1}$, which corresponds to an absolute temperature

$$T_0 = k_B^{-1} \frac{A_{\mathrm{HI}}}{2} \frac{g_N \mu_N}{|g^*| \mu_B} \,. \tag{3.21}$$

The latter temperature τ_1 corresponds to the Zeeman splitting of the electron, since

$$T_1 = k_B^{-1} |g^*| \mu_B B_z \,. \tag{3.22}$$

For $T_0 < T_1$ the spin flip is present, which is the case if the magnetic field obeys

$$B_z > B_{\mathrm{min}} = \frac{g_N \mu_N}{|g^*| \mu_B} \frac{A_{\mathrm{HI}}}{2|g^*| \mu_B} = \frac{1}{\kappa} B_{\mathrm{max}} \,. \tag{3.23}$$

3.3. Discussion and conclusion

All of the above results were obtained applying certain approximations, which are in general not fulfilled by real systems. In the following, we will discuss all approximations one by one and analyze, how a more realistic model would change our results.

First of all, we have assumed that all nuclear spins are of the same species. This is a commonly made approximation [43], where root-mean-square averages of the Zeeman and HI coupling constants can be used to mimic the situation of only one spin species being present as described in Section 1.2.2. As long as the individual constants are not too different and if the sign of the nuclear magnetic moment is the same for all nuclear spins, we do not expect qualitative changes of our findings. Additionally, we have chosen all nuclear spins to be one-half. If one allows for larger nuclear spin quantum numbers $I = \frac{1}{2}, \frac{3}{2}, \ldots$, the model can still be solved analytically. Since the thermal relaxation of the

Material	g^*	g_N	κ [10^3]	A_{HI} [μeV]	$B_{\max}$ [mT]	$I_{\min}$	T_0 [mK]	T_1 [mK]
GaAs	-0.4	1.2	0.66	84	1700	$\frac{3}{2}$	3.7	49
CdTe	-1.8	-1.3	2.4	-34	170	$\frac{1}{2}$	0.008	20
$Ga_{0.47}In_{0.53}As$	-4.4	1.2	6.6	93	180	$\frac{3}{2}$	0.41	54
InAs	-15	1.1	2.5	98	57	$\frac{3}{2}$	0.11	57

Table 3.1. Relevant materials and their parameters. The values of g^* are taken from Ref. [44]. The magnetic moment g_N and the HI constant A_{HI} are averaged by $g_N = \sum_i n_i g_N^i$ and $A_{\mathrm{HI}} = \sum_i n_i A_{\mathrm{HI}}^i$, where n_i is the natural abundance of isotope i. The values are taken from Refs. [43, 54, 158]. The temperatures T_1 and T_0 are calculated at $B_z = 0.1\,B_{\max}$, at which $T_0 = k_B^{-1}\,[4I(I+1)/3]\,\kappa^{-1}\frac{A_{\mathrm{HI}}}{2}$ is valid. By this choice, we also take into account that larger nuclear spin quantum numbers I increase T_0. For simplicity, we took the smallest quantum number $I_{\min}$ of different isotopes present in the dot. Please note the difference of the data presented here and in our publication [153], in which wrong values of the nuclear g-factors have been used. *Table adapted with permission from [153]. ©2015 American Physical Society. All rights reserved.*

electron spin does only depend on its Zeeman energy, the temperature τ_1 is unchanged. In contrast to this, the spin flip temperature $\tau_0 = \rho^{-1} 4\,I(I+1)/3$ increases by an I-dependent factor. Finally, we have also implicitly assumed that all nuclei carry a spin. Yet, this is not the case for all materials. If K out of N nuclei carry a spin, the probability to find the electron at the site of a nuclear spin is given by $v_0|\phi(\boldsymbol{r}_k)|^2 = N^{-1} = K^{-1}\,(K/N) \equiv K^{-1}\,n_I$, where $0 \leq n_I \leq 1$ is the abundance of spin carrying nuclei [58]. Hence, our results still hold if the HI constant A_{HI} is replaced by $n_I\,A_{\mathrm{HI}}$ according to Eq. (3.4).

Besides approximations concerning the nuclear spins, we simplified the physics of the electron spin by using the box model for its envelope function: $|\phi(\boldsymbol{r}_k)|^2 = K^{-1}\,n_I$. In reality, the probability to find the electron, should strongly decrease with the distance from the center of the QD. As we discuss in Section 1.3.1, this envelope function is often described by a Gaussian envelope function $|\phi(\boldsymbol{r}_k)|^2 \propto K^{-1}\exp[-(r_k/R)^2]$, where we again assume that all nuclei carry a spin. Our results should be modified in this case by two aspects: Nuclear spins with $|\phi(\boldsymbol{r}_k)|^2 \ll K^{-1}$ couple only very weakly to the electron and can, thus, be neglected. Effectively, this reduces the number of involved nuclear spins from K to $K_{\mathrm{eff}} < K$. For nuclear spins in the center, one finds $\mathcal{O}(|\phi(\boldsymbol{r}_k)|^2) = K^{-1}$. As a consequence, the non-uniform HI will (slightly) lift the degeneracy of the energies in Eq. (3.19) and Fig. 3.4, but it will not change the energy spectrum in principle. Therefore, the main physical mechanism stays the same and our results still hold.

Finally, we have investigated the behavior of the electron spin expectation value for the extended Hamiltonian including the HI flip-flop terms in Appendices. A.2 to A.4. Doing so, we have confirmed, that the relevant temperature scales are essentially the same and that the physics of the simplified Hamiltonian is reproduced in the limit of a large number of nuclear spins.

Having convinced ourselves, that the results obtained within the simplified model should

be reasonable for real systems, we finally want to give several examples, where we expect the spin flip to occur. The most severe constraint is the negative sign of g^*. As can be seen from Tab. 3.1, this is realized, for instance, in III-V heterostructures, where the electron experiences a strong spin-orbit interaction. Most promising among the considered materials is GaAs, since its spin flip temperature is on the order of mK. The other materials having a smaller T_0 suffer mostly from a large g^* factor. Beside a small g^* factor, potential materials would also benefit from a strong HI and from heavy nuclei with large g_N factors and large spin quantum numbers I. Among them, also systems with a negative g_N such as CdTe can be considered, since this sign changes both the nuclear Zeeman coupling and the sign of the HI. Redefining the nuclear spin operator by $\hat{I}_z \to -\hat{I}_z$ then yields the same results.

Finally, let us briefly discuss the nature of the spin flip. If one leaves the equilibrium state while heating up the system (non-adiabatically), it will take some time for the system to reach the equilibrium at its new temperature. Especially for crossing T_0, the system is not only forced to flip the electron spin, but also approximately up to $\kappa \gg 1$ nuclear spins. Thus, depending, for instance, on the microscopic details of the coupling of the spins to one or several baths, the time needed to equilibrate could be comparably long.

4. Spin decoherence in graphene quantum dots due to hyperfine interaction

The investigation of spin decoherence in QDs has attracted a lot of interest over the past decade due to its importance for the future realization of quantum computers using QDs. Due to the experimental success of GaAs based QDs, these systems are also in the focus of most of the theoretical works. We give a brief overview on theoretical investigations of the decoherence of the electron spin at the beginning of this chapter. Among other techniques, these studies have been carried out applying quantum master equations such as the Nakajima-Zwanzig equation, cf. Section 2.3. We also use this formalism, but we consider graphene based QDs instead of GaAs QD, which show several graphene related peculiarities as we have discussed in Section 1.3.1. We repeat these properties, when we discuss our model below in more detail. Moreover, we briefly explain how the Nakajima-Zwanzig equation has to be adapted in order to apply it to our problem. The results presented in this chapter have been published in Ref. [83].[1]

4.1. Overview on spin decoherence in QDs

Successful quantum computation requires a coherent manipulation of qubits over a sufficiently long time interval. Although, the coherence of spin qubits is in general preserved over longer times than in other qubits like charge qubits, it is still prone to interactions with the environment, which sooner or later leads to a loss of coherence. The most important source for the decoherence of spin qubits is given by the HI with the nuclear spins of the host material, as pointed out in Section 1.3.1.

Evidently, a promising approach is to use materials, which allow to reduce the number of nuclear spins. Indeed, isotopic purification of group IV element based QDs allows, in principle, for spin free environments. We will investigate systems with very few nuclear spins in Chapters 5 and 6. However, often this strategy is not applicable. In consequence, decoherence is, at least to some degree, an unavoidable phenomenon, and, hence, strategies to cope with it are necessary.

Since decoherence is not an instantaneous effect, a simple strategy is to speed up the quantum computation, such that it finishes before the coherence of the electron spin states is lost. However, there is a limit to the fastness of quantum operations due to finite switching times and a limited strength of the applied fields, cf. Section 1.3.3. Since typical quantum algorithms involve a large number of quantum gates, the total operation time often exceeds the decoherence time. In this case, more sophisticated strategies known as quantum error correction [10, 140] are needed, which allow fault tolerant quantum

computation. A figure of merit if this strategy is applicable is given by ratio of the decoherence time and the longest operation time [22]. This ratio estimates the number of operations, which can be performed before information is lost. If this number exceeds the threshold of a specific error correction code, fault tolerant quantum computation is possible. For standard codes, this threshold is on the order of 10^4 operations [22], whereas for specific surface codes [159] already 10^2 suffices. Such codes allow to (partially) undo the effect of decoherence, where, however, precise knowledge of decoherence is necessary. In particular, the specific dependence of the decoherence function on time is of high relevance. Therefore, the details of the electron spin decoherence have been in the focus of theoretical research revealing a great variety of different types of decay.

While different publications certainly (slightly) differ in the models used to obtain these results, we can nonetheless define a "canonical" model incorporating the most important aspects needed to investigate decoherence in spin based QDs. We have already mentioned the HI as the main source of decoherence. The number of nuclear spins is typically assumed to be large and the envelope function of the electron is considered to be of Gaussian form as described in Section 1.3.1. Basically, there are two ways to reduce the effect of the HI. First, a strong external magnetic field can be applied, which stabilizes the electron spin, as we will show below. Second, we have argued in Section 1.3.3, that certain nuclear spin states drastically reduce the action of the HI. To be more specific, we will consider a so-called narrowed state, which is an eigenstate of the effective nuclear magnetic field originating from the HI. In summary, our "canonical" model consists of the Zeeman interaction of the spins with an external magnetic field, the HI between the electron spin and the nuclear spins, and a narrowed nuclear spin state. This model, with some variations, has been used to investigate the effect of decoherence in numerous works [57, 73, 75, 76, 78, 152, 160, 161, 162, 163, 164, 165, 166]. We also adopt it for this chapter. In all of these works, the physics of a free induction decay (FID) has been investigated. For a FID experiment, the electron is initially prepared in some reference state and its current state is measured after some time t. By repeating the experiment and varying t, the whole dynamics of the electron spin can be monitored.

If we follow the time evolution of the electron spin by regarding its expectation values $\langle \hat{S}_z \rangle(t)$ and $\langle S_+ \rangle(t) = \langle S_x \rangle(t) + \mathrm{i}\langle S_y \rangle(t)$, we encounter three relevant timescales [22]. First, the relaxation timescale T_1 characterizes the time, over which the electron relaxes from the excited state $|\Uparrow\rangle$ to its ground state $|\Downarrow\rangle$ due to the interaction with the environment. This time is typically sufficiently long, such that it does not limit quantum computations [22]. Second, investigating $\langle S_+ \rangle(t)$ allows to determine the decoherence timescale T_2, which is the characteristic time over which the amplitude of oscillations of $\langle \hat{S}_+ \rangle(t)$ decay. As we discuss in Chapter 2, the physical mechanism of this behavior is the apparent loss of coherence between the electron spin states due to the entanglement with the environment. However, in practice, measuring the time evolution of the electron spin involves many repetitions of the experiment in order to determine the quantum mechanical expectation value. Due to the limited precision of any experiment, these runs slightly differ from each other leading effectively to an ensemble average of the observable, which leads to additional damping. Thus, the decay of $\langle S_+ \rangle(t)$ is seemingly faster on a timescale T_2^* known as dephasing time. In the strict sense, these timescales are only well defined if the corresponding decay is exponential. In the literature, however, this notation is occasionally

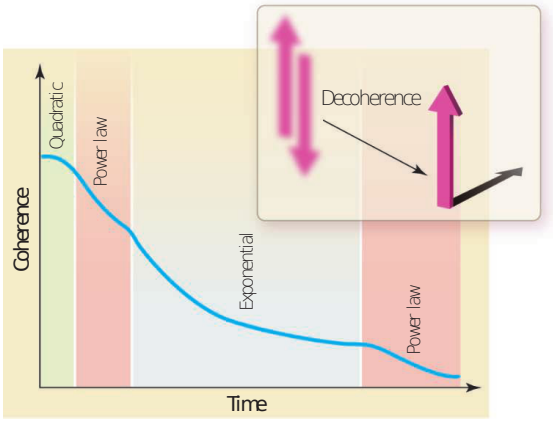

Figure 4.1. Schematic decay of $|\langle \hat{S}_+ \rangle(t)|$, which is a measure for the coherence of the electron spin states $|\Uparrow\rangle$ and $|\Downarrow\rangle$. The loss of their coherent superposition is illustrated in the inset. The presented behavior is typical for an electron spin experiencing a large Zeeman splitting, which stabilizes it against the HI with the nuclear spins. These spins are assumed to be in a narrowed state. The nature of the decay changes with time and includes quadratic, power-law and exponential decay. *Figure from [167]. Reprinted with permission from AAAS*

used to characterize other, non-exponential forms of decay [22]. Typically, the three timescales are related to each other by $T_2^* < T_2 \ll T_1$ [22]. Hence, quantum computation is mainly limited by decoherence and, therefore, we focus on the time evolution of $\langle S_+ \rangle(t)$ in the following.

Before we analyze the time evolution of the electron spin in a graphene QD, let us briefly review the time evolution for an electron confined in GaAs QDs. Intensive research on this model has revealed that the expectation value $\langle \hat{S}_+ \rangle(t)$ undergoes several regimes with very different types of decay as illustrated in Fig. 4.1. In the beginning, a very short quadratic decay has been observed, which is followed by a partial power-law decay. Via a quadratic shoulder, the signal than enters an exponential regime lasting over a rather long time. At long times finally, it experiences again a power-law decay. Note that these results are, in general, specific to two-dimensional QDs exhibiting a Gaussian envelope function [22, 76]. The origin of this variety is the non-Markovian conditions arising from the slow dynamics of the nuclear spins as discussed at the end of Section 2.3. While these findings have been obtained using many different approaches [57, 73, 75, 76, 78, 161, 162, 163, 168], all of them have been recovered in one unified method by Coish et al. [61], which is based on the Nakajima-Zwanzig method described in Section 2.3. In their work, the authors also provide a detailed discussion of the different stages of the decay, which is beyond the scope of this Thesis.

Most of the results reported above have been obtained considering an isotropic HI. Motivated by the anisotropic HI in graphene, we consider a more general form of the HI to investigate the decoherence of an electron spin. Based on the background on the physics of QDs in Chapter 1, we will first discuss the initial states of the electron spin and the nuclear spins and the Hamiltonian of our problem. We will then adjust the Nakajima-Zwanzig equation discussed in Section 2.3 to our specific model. With this equation of

motion of the electron spin at hand, we will be able to investigate the non-Markovian dynamics of the electron spin.

4.2. Hamiltonian and initial conditions

4.2.1. Initial conditions

A reasonable initial state of the total system consisting of the electron spin and the nuclear spins can be obtained from the following considerations. First, the nuclear spin state is prepared in a narrowed state by means of dynamical nuclear polarization (DNP) and state narrowing (SN) as described in Section 1.3.3. Then, a new electron is loaded into the QD and its state is prepared in a specific state. As we discuss in Section 1.3.3, in principle the whole Bloch sphere is experimentally accessible. Due to this preparation scheme, the electron spin and the nuclear spins are initially uncorrelated giving rise to a product state

$$\hat{\rho}(0) = \hat{\rho}_S(0) \otimes \hat{\rho}_I \,, \tag{4.1}$$

where the density matrix of the electron spin may be written as

$$\hat{\rho}_S(0) = \frac{1}{2}\Big(\mathbb{1} + \langle \hat{S}_x \rangle_0 \, \sigma_x + \langle \hat{S}_y \rangle_0 \, \sigma_y + \langle \hat{S}_z \rangle_0 \, \sigma_z \Big) \,. \tag{4.2}$$

The matrices $\{\hat{\sigma}_i\}_{i=x,y,z}$ are the 2×2-Pauli-matrices and $\mathbb{1}$ is the identity operator. Defining $\sigma_{\Uparrow,\Downarrow} = \frac{1}{2}(\mathbb{1} \pm \sigma_z)$ and $\sigma_\pm = \frac{1}{2}(\sigma_x \pm \sigma_y)$, this density matrix can be rewritten by

$$\hat{\rho}_S(0) = \langle \hat{S}_\Uparrow \rangle_0 \sigma_\Uparrow + \langle \hat{S}_\Downarrow \rangle_0 \sigma_\Downarrow + \langle \hat{S}_+ \rangle_0 \sigma_+ + \langle \hat{S}_- \rangle_0 \sigma_- \,. \tag{4.3}$$

where the components of the electron spin are given by $\langle \hat{S}_{\Uparrow,\Downarrow} \rangle_0 = \frac{1}{2} \pm \langle \hat{S}_z \rangle_0$ and $\langle \hat{S}_\pm \rangle_0 = \langle \hat{S}_x \rangle_0 \pm \mathrm{i} \langle \hat{S}_y \rangle_0$.

The density matrix of the nuclear spins is assumed to be $\hat{\rho}_I = |n\rangle\langle n|$, where the narrowed state $|n\rangle$ defined in Eq. (1.37) is an eigenstate of the nuclear magnetic field $\hat{h}_z$. For a large number of nuclear spins, this narrowed state is, in general, a superposition of g_n degenerate eigenstates $|n_j\rangle$:

$$|n\rangle = \sum_{j=1}^{g_n} \alpha_j |n_j\rangle \qquad \text{with} \qquad \hat{h}_z |n_j\rangle = \langle \hat{h}_z \rangle_n |n_j\rangle \,. \tag{4.4}$$

The corresponding eigenvalue of the nuclear field operator $\hat{h}_z$ is then given by [76]:

$$\langle \hat{h}_z \rangle_n = \sum_k A_k \sum_{j=1}^{g_n} \langle n_j | \hat{I}_{k,z} | n_j \rangle = \sum_k A_k \sum_{j=1}^{g_n} m_k^{n_j} \,, \tag{4.5}$$

The sum over the degenerate eigenstates $|n_j\rangle$ on the right hand-side of Eq. (4.5) corresponds to an average of the z-component of the k-th nuclear spin. Assuming a uniform polarization p of the nuclear spins, its value $\sum_{j=1}^{g_n} m_k^{n_j} = pI$ is the same for all nuclear spins. Since $\sum_k A_k$ equals $n_I A_{\mathrm{HI}}$ by definition, we find

$$\langle \hat{h}_z \rangle_n = p \, I \, n_I A_{\mathrm{HI}} \,. \tag{4.6}$$

4.2.2. Hamiltonian

The Zeeman interaction of the electron spin and the nuclear spins as well as the HI forming the total interaction of our "canonical" model have been discussed in detail in Chapter 1. We assume the external magnetic field to point in z-direction and rewrite the Zeeman Hamiltonians for the electron spin and the nuclear spins given in Eqs. (1.9) and (1.10), respectively, in terms of the Zeeman energies A^S_{ZE} and A^I_{ZE}. This formulation yields the simple Hamiltonians $\hat{H}^S_{\mathrm{ZE}} = A^S_{\mathrm{ZE}}\hat{S}_z$ and $\hat{H}^k_{\mathrm{ZE}} = A^I_{\mathrm{ZE}}\hat{I}_{k,z}$. Moreover, we express the HI in terms of the effective nuclear magnetic field defined in Eq. (1.26) and split it into $\hat{h}_z = \sum_k A_k\hat{I}_{k,z}$ and $\hat{h}_{x,y} = \sum_k A_k\hat{I}_{k,x} + A_k\hat{I}_{k,y}$. If we relate the radial position $r_k < R_D$ of an arbitrary nuclear spin to the number of nuclear spins k within this radius r_k [76, 83] by

$$\left(\frac{r_k}{R_D}\right)^2 = \frac{k}{K}\,, \tag{4.7}$$

we can rewrite the expression for the coupling constants

$$A_k = \frac{n_I A_{\mathrm{HI}}}{K}\exp\Big[-(\frac{r_k}{R_D})^2\Big] = \frac{n_I\, A_{\mathrm{HI}}}{K}\exp\left[-\frac{k}{K}\right]\,, \tag{4.8}$$

for a QD containing $K = n_I N_{\mathrm{sites}}$ nuclear spins. With the splitting of the HI interaction, we can define an unperturbed Hamiltonian

$$\hat{H}_0 = A^S_{\mathrm{ZE}}\hat{S}_z + \sum_{k=1}^{K} A^I_{\mathrm{ZE}}\hat{I}_{k,z} + \lambda_z\hat{h}_z\hat{S}_z \tag{4.9}$$

and a perturbative Hamiltonian

$$\hat{H}_V = \lambda_x\hat{h}_x\hat{S}_x + \lambda_y\hat{h}_y\hat{S}_y\,, \tag{4.10}$$

where the constants λ_x, λ_y, and λ_z take into account a potential (directional) anisotropy of the HI. For the isotropic contact HI present in GaAs QDs, we simply have $\lambda_x = \lambda_y = \lambda_z = 1$, whereas the anisotropic HI in graphene leads to different values of these constants depending on the direction of the external magnetic field $\boldsymbol{B} = (0, 0, B_z)^T$ with respect to the graphene plane. The tilt of the graphene sheet with respect to the magnetic field can be parametrized by an angle β as depicted in Fig. 1.5. The resulting values for the constants λ_i can be calculated using Eq. (1.29). We find $\lambda_x = \lambda_y = -\frac{1}{2}$ and $\lambda_z = 1$ for $\beta = 0$ and $\lambda_y = \lambda_z = -\frac{1}{2}$ and $\lambda_x = 1$ for $\beta = \frac{\pi}{2}$. For other values of β, additional terms like $\hat{S}_x\hat{I}_z$ or $\hat{S}_z\hat{I}_x$ arise, which are, however, not captured by our Hamiltonian in Eq. (4.10). It is convenient to rewrite the perturbative Hamiltonian in terms of raising and lowering operators

$$H_V = \frac{1}{2}\Big(\hat{g}_+\hat{S}_- + \hat{g}_-\hat{S}_+\Big)\,, \tag{4.11}$$

where we have introduced generalized nuclear operators

$$\hat{g}_\pm = \frac{1}{2}\left[(\lambda_x \pm \lambda_y)\,\hat{h}_+ + (\lambda_x \mp \lambda_y)\,\hat{h}_-\right] \equiv \frac{1}{2}\left[\lambda_\pm\hat{h}_+ + \lambda_\mp\hat{h}_-\right]\,. \tag{4.12}$$

The bare nuclear magnetic field operators $\hat{h}_\pm = \hat{h}_x \pm \mathrm{i}\hat{h}_y$ can also be considered in terms of single nuclear spin raising and lowering operators: $\hat{h}_\pm = \sum_k A_k\hat{I}_{k,\pm}$. If $\lambda_x = \lambda_y$, the generalized operators $\hat{g}_\pm = \lambda_x\hat{h}_\pm$ reduce to simple multiples of the bare nuclear operators.

4.3. Method

4.3.1. Nakajima-Zwanzig-equation

Since the nuclear spins have comparably slow dynamics, as explained in detail in Sections 1.2, 1.3, and 2.3, the whole spin system is in a non-Markovian regime, which we want to analyze by means of the Nakajima-Zwanzig equation. To this end, we identity the electron spin with the subsystem S and the nuclear spins form the environment E. Assuming a large external magnetic field, the electron Zeeman energy is much larger than the HI interaction and, hence, the Born approximation is justified. We have already seen in Section 2.3, that the initial state of the environment is approximately preserved within the Born approximation. Thus, we have for the nuclear spin state

$$\hat{\rho}_I(t) \approx \hat{\rho}_I(0) = |n\rangle\langle n| \,. \tag{4.13}$$

With the state of the environment known, the projector $\mathcal{P}$ onto the relevant part of the density matrix is given by

$$\mathcal{P}\hat{O} = \mathrm{Tr}_I[\hat{O}] \otimes \hat{\rho}_I \,. \tag{4.14}$$

With this definition, we are able to start our analysis of the non-Markovian spin dynamics with Eq. (2.64), which we slightly rewrite to find

$$\frac{\mathrm{d}}{\mathrm{d}t}\hat{\rho}_S(t) = -\mathrm{i}\mathcal{L}_0^n\hat{\rho}_S(t) - \mathrm{i}\int_0^t \mathrm{d}t' \;\; \Sigma_S(t-t')\,\hat{\rho}_S(t') \,. \tag{4.15}$$

The unitary part of this equation is determined by the effective Liouville operator $\mathcal{L}_0^n\hat{O}_S = [\omega_n \hat{S}_z, \hat{O}_S]_-$.[2] The action of this superoperator on an arbitrary operator in the Hilbert space of the electron spin is given by its commutator with the effective Hamiltonian

$$\hat{H}_0^n = (A_{\mathrm{ZE}}^S + \langle \hat{h}_z \rangle_n)\hat{S}_z \equiv \omega_n \hat{S}_z \,. \tag{4.16}$$

The self-energy $\Sigma_S(t-t')$ is equal to the memory kernel $K_S(t-t')$ defined in Eq. (2.65). In order to dissolve the convolution between the self-energy $\Sigma_S(t)$ and the spin density matrix, we perform a Laplace transform to obtain a much simpler algebraic form

$$s\hat{\rho}_S(s) - \hat{\rho}_S(0) = -\mathrm{i}\,\mathcal{L}_0^n\hat{\rho}_S(s) - \mathrm{i}\,\Sigma_S(s)\,\hat{\rho}_S(s) \,, \tag{4.17}$$

$$\Sigma_S(s) = -\mathrm{i}\;\mathrm{Tr}_I\left[\mathcal{L}_V\left\{\sum_{l=0}^{\infty}\frac{1}{s+\mathrm{i}\mathcal{Q}\mathcal{L}_0}\left(-\mathrm{i}\mathcal{Q}\mathcal{L}_V\frac{1}{s+\mathrm{i}\mathcal{Q}\mathcal{L}_0}\right)^l\right\}\mathcal{L}_V\hat{\rho}_I\right] \equiv \sum_{j=2}^{\infty}\Sigma_S^{(j)}(s) \,. \tag{4.18}$$

The series for the self-energy $\Sigma_S(s)$ in powers of the interaction Liouvillian $\mathcal{L}_V$ is obtained by applying the Laplace-transform to Eq. (2.66).

For the explicit calculation of these self-energy terms, it is convenient to express the density matrix $\hat{\rho}_S(s)$ according to Eq. (4.3) and to consider the matrices $\sigma_{\Uparrow,\Downarrow}$ and $\sigma_{\pm}$ as

[2] Since we will also encounter anti-commutators, we have introduced the notation $[\ldots]_{\pm}$ for clarity, where $-$ $(+)$ denotes the (anti-)commutator.

basis vectors in an abstract vector space. The electron spin density matrix then forms a 4-component vector

$$\begin{aligned}\hat{\rho}_S(s) &= \langle\hat{S}_{\Uparrow}\rangle(s)\,\sigma_{\Uparrow} + \langle\hat{S}_{\Downarrow}\rangle(s)\,\sigma_{\Downarrow} + \langle\hat{S}_{+}\rangle(s)\,\sigma_{-} + \langle\hat{S}_{-}\rangle(s)\,\sigma_{+} \\ &= \Big(\langle\hat{S}_{\Uparrow}\rangle(s), \langle\hat{S}_{\Uparrow}\rangle(s), \langle\hat{S}_{+}\rangle(s), \langle\hat{S}_{-}\rangle(s)\Big)^{T}. \end{aligned} \tag{4.19}$$

In this particular basis, the unperturbed Liouvillian is given by a diagonal matrix $\mathcal{L}_0 = \frac{1}{2}\,\mathrm{diag}\,(\mathcal{L}_-, -\mathcal{L}_-, -\mathcal{L}_+, \mathcal{L}_+)$, where the operators

$$\mathcal{L}_{\pm}\hat{O}_I = [\hat{H}_0, \hat{O}_I]_{\pm} \tag{4.20}$$

are defined by their action on an arbitrary nuclear spin operator $\hat{O}_I$. The perturbative Liouvillian $\mathcal{L}_V$ has a 4×4 off-diagonal form containing the generalized nuclear magnetic field operators $\hat{g}_{\pm}$. For further details of this calculation, we refer to Appendix A of Ref. [76] and note that the bare nuclear magnetic field operators $\hat{h}_{\pm}$ there correspond to the generalized operators $\hat{g}_{\pm}$ of our model. In general, all contributions $\Sigma^{(2j+1)}(s)$ to the self-energy containing odd powers of $\mathcal{L}_V$ vanish, since only virtual flip-flop processes are allowed due to the large Zeeman splitting of the electron spin. Each even summand $\Sigma^{(2j+2)}(s)$ is associated with a small parameter [76] Δ^j, where Δ is given by

$$\Delta = \frac{n_I A_{\mathrm{HI}}}{2\omega_n}\,, \tag{4.21}$$

which is small for a large Zeeman splitting of the electron spin. In this parameter regime, all orders higher than second order are strongly suppressed and, thus, can be neglected. As we show below, neglecting terms of order $O(\Delta)$ limits the range of validity of our analysis to times of order $t \ll \Delta^{-1}$. In order to extent to longer times, it would be necessary to include higher orders of the self-energy [61], which is, however, beyond the scope of this article.

The self-energy exhibits to all orders of $\mathcal{L}_V$ a 4×4 structure

$$\Sigma_S(s) = \begin{pmatrix} \Sigma_{\uparrow\uparrow}(s) & \Sigma_{\uparrow\downarrow}(s) & 0 & 0 \\ \Sigma_{\downarrow\uparrow}(s) & \Sigma_{\downarrow\downarrow}(s) & 0 & 0 \\ 0 & 0 & \Sigma_{++}(s) & \Sigma_{+-}(s) \\ 0 & 0 & \Sigma_{-+}(s) & \Sigma_{--}(s) \end{pmatrix}, \tag{4.22}$$

which shows a block-diagonal form indicating, that the $\hat{S}_z$ and $\hat{S}_{\pm}$ subspaces are decoupled. This fact becomes more obvious, if we calculate the expectation values of these observables according to

$$\langle\hat{S}_i\rangle(s) = \mathrm{Tr}_S\left(\hat{S}_i\hat{\rho}_S(s)\right), \tag{4.23}$$

where $i = z, \pm$. Using this equation, we find

$$\langle\hat{S}_z\rangle(s) = \frac{\langle S_z\rangle_0 - \frac{\mathrm{i}}{2\,s}\left[\Sigma_{\uparrow\uparrow}(s) + \Sigma_{\uparrow\downarrow}(s)\right]}{s + \mathrm{i}\Big[\Sigma_{\uparrow\uparrow}(s) - \Sigma_{\uparrow\downarrow}(s)\Big]} \tag{4.24}$$

and

$$\langle\hat{S}_{\pm}\rangle(s) = \frac{\langle\hat{S}_{\pm}\rangle_0}{D_{\pm}(s)} + \frac{\mathrm{i}\Sigma_{\pm\mp}(s)\,\langle\hat{S}_{\mp}\rangle_0}{D_{\pm}(s)\,D_{\mp}(s)}\,, \tag{4.25}$$

where the denominator functions are given by

$$D_{\pm}(s) = s \mp \mathrm{i}\omega_n + \mathrm{i}\Sigma_{\pm\pm}(s) \ . \tag{4.26}$$

With these results, we are then able to calculate time-dependent expectation values by means of an inverse Laplace transform

$$\langle \hat{S}_i \rangle(t) = \frac{1}{2\pi\mathrm{i}} \int\limits_{\gamma-\mathrm{i}\infty}^{\gamma+\mathrm{i}\infty} \mathrm{d}s \ \ \mathrm{e}^{st} \langle \hat{S}_i \rangle(s) \,, \tag{4.27}$$

where the integral is evaluated along the Bromwich contour, as illustrated in Fig. 4.2 below. The constant $\gamma \in \mathbb{R}$ is chosen, such that all singularities of $\langle \hat{S}_i \rangle(s)$ have a real part smaller than γ. Since the mathematics involved with this integration is quite involved, we will only present the results of $\langle \hat{S}_+ \rangle(t)$, which are the relevant ones for decoherence. For the calculation of $\langle \hat{S}_z \rangle(t)$, we refer to our publication [83]. There, we show that the calculation of this observable is connected with the solution of $\langle \hat{S}_+ \rangle(t)$ by a shift of the variable s. Hence, the main mathematical steps presented in the following are also relevant for $\langle \hat{S}_z \rangle(t)$. Evaluating the self-energy in second order according to Eq. (4.18), we find

$$\Sigma^{(2)}_{++}(s) = -\frac{\mathrm{i}}{4} \mathrm{Tr}_I \left(\hat{g}_+ \mathcal{G}_\uparrow \hat{g}_- \hat{\rho}_I + \hat{g}_- \hat{g}_+ \mathcal{G}_\downarrow \hat{\rho}_I \right) \ , \tag{4.28}$$

$$\Sigma^{(2)}_{+-}(s) = \ \ \frac{\mathrm{i}}{4} \mathrm{Tr}_I \left(\hat{g}_+ \mathcal{G}_\downarrow \hat{g}_+ \hat{\rho}_I + \hat{g}_+ \hat{g}_+ \mathcal{G}_\uparrow \hat{\rho}_I \right) \ , \tag{4.29}$$

$$\Sigma^{(2)}_{-+}(s) = \ \ \frac{\mathrm{i}}{4} \mathrm{Tr}_I \left(\hat{g}_- \mathcal{G}_\uparrow \hat{g}_- \hat{\rho}_I + \hat{g}_- \hat{g}_- \mathcal{G}_\downarrow \hat{\rho}_I \right) \ , \tag{4.30}$$

$$\Sigma^{(2)}_{--}(s) = -\frac{\mathrm{i}}{4} \mathrm{Tr}_I \left(\hat{g}_- \mathcal{G}_\downarrow \hat{g}_+ \hat{\rho}_I + \hat{g}_+ \hat{g}_- \mathcal{G}_\uparrow \hat{\rho}_I \right) \ , \tag{4.31}$$

where

$$\mathcal{G}_{\uparrow,\downarrow}(\mathcal{L}_-) = \left(s + \frac{\mathrm{i}}{2} \alpha_{\uparrow,\downarrow} \mathcal{Q} \mathcal{L}_- \right)^{-1} \qquad \text{with} \qquad \alpha_{\uparrow,\downarrow} = \pm 1 \tag{4.32}$$

Using Eq. (4.12), these elements can be explicitly calculated as shown in Appendix B. In order to simplify the resulting contributions to the self-energy, we additionally assume, that the nuclear Zeeman energy $A^I_{\mathrm{ZE}} = g_N \mu_N B_z$ is much smaller than the energy involved with the HI interaction. The relevant HI energy is given by $A^s_{\mathrm{HI}} = n_I A_{\mathrm{HI}}/K$, which is the energy scale involved with a single spin flip. Thus, the external magnetic field should be chosen sufficiently weak. However, we have to keep in mind that the Zeeman energy $A^S_{\mathrm{ZE}} = g^* \mu_B B_z$ of the electron spin has to be much larger than the total HI in order to satisfy $\Delta \sim \frac{n_I A_{\mathrm{HI}}}{A^S_{\mathrm{ZE}}} \ll 1$, which demands a sufficiently strong magnetic field. Combining both requirements and inserting the specific forms of the Zeeman energies, we find

$$\frac{K}{\kappa} B_z \ll B_{\mathrm{nuc}} \ll B_z \,, \tag{4.33}$$

where $\kappa = \frac{g_N \mu_N}{g^* \mu_B}$ and $B_{\mathrm{nuc}} = \frac{n_I A_{HI}}{g^* \mu_B}$ are material dependent constants. In graphene, these constants are given by $\kappa \approx 2.5 \times 10^3$ and $B_{\mathrm{nuc}} \approx 2.6$ mT and, hence, we can adjust both K and B_z such that this inequality is fulfilled. In this case, we can neglect A^I_{ZE} to obtain a

more tractable form of the self-energy, but this assumption also limits the range of validity of our predictions to times smaller than $\tau_{\mathrm{ZE}}^{I} = \hbar/A_{\mathrm{ZE}}^{I}$. With this simplification, the second order matrix elements of the self-energy contributing to $\langle \hat{S}_{+} \rangle (s)$ are given by

$$\Sigma_{++}^{(2)}(s) = -\mathrm{i}K \frac{\lambda_{-}^{2} + \lambda_{+}^{2}}{4\,\lambda_{z}^{2}} \left[c_{+} I_{-}(s) + c_{-} I_{+}(s) \right] , \tag{4.34}$$

$$\Sigma_{--}^{(2)}(s) = -\mathrm{i}K \frac{\lambda_{-}^{2} + \lambda_{+}^{2}}{4\,\lambda_{z}^{2}} \left[c_{-} I_{-}(s) + c_{+} I_{+}(s) \right] , \tag{4.35}$$

$$\Sigma_{-+}^{(2)}(s) = -\frac{2\lambda_{-}\lambda_{+}}{\lambda_{-}^{2} + \lambda_{+}^{2}} \Sigma_{++}^{(2)}(s) , \tag{4.36}$$

$$\Sigma_{+-}^{(2)}(s) = -\frac{2\lambda_{-}\lambda_{+}}{\lambda_{-}^{2} + \lambda_{+}^{2}} \Sigma_{--}^{(2)}(s) \tag{4.37}$$

where the coefficients $c_{\pm}$ originate from the action of the perturbation $\mathcal{L}_{V}$ on the nuclear spin state $\hat{\rho}_{I}$ [152]. For a spin $\frac{1}{2}$ system like graphene with a uniform polarization, these coefficients $c_{\pm}$ are explicitly given by $c_{\pm} = [1 \mp p]/2$ depending on the polarization p. The action of the superoperator $\mathcal{G}_{\uparrow,\downarrow}(\mathcal{L}_{-})$ on nuclear magnetic field eigenstates $|q\rangle$,$|n\rangle$ gives rise to the functions

$$I_{\pm}(s) = s \left[\log(s \mp i) - \log(s) \right] \pm i , \tag{4.38}$$

which are calculated applying the same continuum limit as used to obtain Eq. (4.6). Analyzing the above Eqs. (4.34) to (4.37) in more detail, one finds that the diagonal parts $\Sigma_{++}^{(2)}$ and $\Sigma_{--}^{(2)}$ are always finite, whereas the off-diagonal parts $\Sigma_{\pm\mp}(s)$ vanish for $\lambda_x = \lambda_y$.

In the following, we introduce dimensionless quantities by measuring energies in units of $\tilde{A}_{\mathrm{HI}}^{s} = \frac{|\lambda_z|}{2} A_{\mathrm{HI}}^{s}$, where $A_{\mathrm{HI}}^{s} = n_I \frac{A_{\mathrm{HI}}}{K}$ is the energy involved with a single HI flip. This energy scale also defines the timescale $\tilde{\tau}_{HI}^{s} = \hbar/\tilde{A}_{\mathrm{HI}}^{s} = \tau_{\mathrm{HI}}^{s}/|\lambda_z|$, which serves as a measure for times henceforth. As a consequence, the small parameter expressed in dimensionless units reads $\Delta = \frac{K}{\omega_n}$. For clarity, we give a summarizing list of the most important symbols in Tab. 4.1.

4.3.2. Inverse Laplace transform

With the explicit form of the self-energy in second order given in Eqs. (4.34) to (4.37), we are able to proceed with the inverse Laplace transform. The components of the electron spin perpendicular to the external magnetic field can be split into two parts

$$\langle \hat{S}_{+} \rangle (s) = \frac{\langle \hat{S}_{+} \rangle_{0}}{D_{+}(s)} + \frac{\mathrm{i}\Sigma_{+-}^{(2)}(s) \langle \hat{S}_{-} \rangle_{0}}{D_{+}(s)\, D_{-}(s)} . \tag{4.39}$$

With the introduction of the effective nuclear spin number $\tilde{K} = K(\lambda_x^2 + \lambda_y^2)/2\lambda_z^2$, these functions are formally equal for an arbitrary choice of the constants $\{\lambda_i\}$. Using Eqs. (4.36) and (4.37), one can rewrite the spin component $\langle \hat{S}_{+} \rangle (s)$ in terms of two generalized functions:

$$\langle \hat{S}_{+} \rangle (s) = \langle S_{+,1} \rangle (s) + \langle S_{+,2} \rangle (s) = \frac{\langle S_{+,1} \rangle_{0}}{D_{+}(s)} + \frac{\langle S_{+,2} \rangle_{0} (s + \mathrm{i}\omega_n)}{D_{+}(s)\, D_{-}(s)} , \tag{4.40}$$

Symbol	Definition	Symbol	Definition
A^s_{HI}	$n_I A_{\mathrm{HI}} \,/\, K$	$\tilde{A}^s_{\mathrm{HI}}$	$\lvert\lambda_z\rvert A^s_{\mathrm{HI}} \,/\, 2$
τ^s_{HI}	$2\hbar \,/\, A^s_{\mathrm{HI}}$	$\tilde{\tau}^s_{\mathrm{HI}}$	$\tau^s_{\mathrm{HI}} \,/\, \lvert\lambda_z\rvert$
Δ	$n_I A_{\mathrm{HI}} \,/\, 2\omega_n$	$\tilde{\Delta}$	$\Delta\,(\lambda_x^2+\lambda_y^2) \,/\, 2\lvert\lambda_z\rvert$
δ	$\Delta^2 \,/\, K$	$\tilde{\delta}$	$\delta\,(\lambda_x^2+\lambda_y^2) \,/\, 2$
$c_\pm$	$[1 \mp p] \,/\, 2$	$\tilde{K}$	$K(\lambda_x^2+\lambda_y^2) \,/\, 2\lambda_z^2$

Table 4.1. Index of recurring symbols in the text. The parameters $c_\pm$ originate from expectation values of the nuclear spin operators $\hat{h}_\pm$ depending on the polarization p. The total Zeeman energy is given by $\omega_n = b_S + \lambda_z \langle \hat{h}_z \rangle_n$. The small parameter $\Delta \ll 1$ determines the perturbative regime, while the second small parameter δ quantifies the non-Markovian corrections. The shorthands $\tilde{K}$, $\tilde{\Delta}$, and $\tilde{\delta}$ allow a compact notation of our results. *Table adapted with permission from [83].*

Symbol	$\perp$	$\parallel$	$(\lambda_x, \lambda_y, \lambda_z)$
$\langle S_{+,1} \rangle_0$	$\langle \hat{S}_+ \rangle_0$	$\langle \hat{S}_+ \rangle_0 - \frac{3}{5}\langle \hat{S}_- \rangle_0$	$\langle \hat{S}_+ \rangle_0 - \frac{\lambda_x^2-\lambda_y^2}{\lambda_x^2+\lambda_y^2}\langle S_- \rangle_0$
$\langle S_{+,2} \rangle_0$	0	$\frac{3}{5}\langle \hat{S}_- \rangle_0$	$\frac{\lambda_x^2-\lambda_y^2}{\lambda_x^2+\lambda_y^2}\langle \hat{S}_- \rangle_0$

Table 4.2. Prefactors defined in Eq. (4.40) for graphene in a magnetic field perpendicular ($\perp$) or parallel ($\parallel$) to the graphene plane. In the first case ($\perp$), we find $\lambda_x = \lambda_y = -\frac{1}{2}$ and $\lambda_z = 1$, whereas a parallel magnetic field leads to $\lambda_z = \lambda_y = -\frac{1}{2}$ and $\lambda_x = 1$. For completeness, we also consider a general anisotropy with $\{\lambda_i\}$. Note that there is no special choice of the initial values $\langle S_{+,i} \rangle_0$ of the electron spin. *Table adapted with permission from [83].*

where the prefactors for different cases are listed in Tab. 4.2. In our publication [83], we have shown that these generalized functions are invariant under a change of sign of both $\lambda_z \to -\lambda_z$ and the external magnetic field $B_z \to -B_z$. Hence, we consider only positive λ_z in the following.

Since the Laplace transform is a linear operation, its inverse can be carried out independently for each summand by evaluating integrals of the form

$$\langle \hat{S}_{+,i} \rangle (t) = \frac{1}{2\pi \mathrm{i}} \int\limits_{\gamma - \mathrm{i}\infty}^{\gamma + \mathrm{i}\infty} \mathrm{e}^{st} \langle \hat{S}_{+,i} \rangle (s) \, \mathrm{d}s \ . \tag{4.41}$$

The singularities of $\langle \hat{S}_{+,i} \rangle (s)$ are generated by the denominators $D_\pm (s)$ each possessing zeros at $s_{j,\pm}$ $(j = 1, 2, 3)$, which come in complex-conjugated pairs $s_{j,+} = s_{j,-}^*$. Furthermore, there are three branch cuts from $s = 0, \pm\mathrm{i}$ to $-\infty$, whose position in the complex plane is illustrated in Fig. 4.2.

In order to evaluate the integral in Eq. (4.41), one can close the contour as depicted in Fig. 4.2, where the integral over the great circle vanishes according to Jordan's lemma. Note that the poles with finite real part $s_{2,\pm}$ are outside of this contour and, hence, do not contribute to the integral. Therefore, the solution of Eq. (4.41) generally consists of residues arising from the remaining poles, $s_{1,\pm}$ and $s_{3,\pm}$, the integrals $B_i^\alpha (t)$ along the upper and lower branch-cut as well as an integral $I_i (t)$ along the imaginary axis:

$$\langle \hat{S}_{+,i} \rangle (t) = \sum_{s = s_{j,\pm}} \mathrm{Res} \left[\mathrm{e}^{st} \langle \hat{S}_{+,i} \rangle (s) \right] - \frac{1}{2\pi \mathrm{i}} \underbrace{\Big\{ \sum_\alpha B_i^\alpha (t) + I_i (t) \Big\}}_{= P_{+,i}(t)} , \tag{4.42}$$

where the integrals are explicitly given by

$$B_i^\alpha (t) = \lim_{\eta \to 0} \mathrm{e}^{\mathrm{i}\alpha t} \int\limits_{-\infty}^{0} \mathrm{d}x \ \ \mathrm{e}^{xt} \langle \hat{S}_{+,i} \rangle \Big(x + \mathrm{i}\alpha (1 + \eta) \Big) \tag{4.43}$$

with $\alpha = \pm 1$ and

$$I_i (t) = \mathrm{i} \int\limits_{-1}^{1} \mathrm{d}y \ \ \mathrm{e}^{\mathrm{i}yt} \ \langle \hat{S}_{+,i} \rangle (\mathrm{i}y) \, . \tag{4.44}$$

In order to simplify the notation of the results and to make their interpretation easier, we use the short hands $\tilde{K}$, Δ, $\tilde{\Delta} = \Delta \left(\lambda_x^2 + \lambda_y^2 \right) / 2\lambda_z^2$, δ, and $\tilde{\delta} = \delta \left(\lambda_x^2 + \lambda_y^2 \right) / 2$ listed in Table 4.1 as well as the relations $c_- + c_+ = 1$ and $c_- - c_+ = p$, which are fulfilled for nuclei with spin $I = 1/2$ [76, 152] as considered here.

4.4. Results

4.4.1. Inverse Laplace transform of the first spin contribution

We begin the inverse transform back into the time domain with the first part of the spin component $\langle S_{+,1} \rangle (s)$, which is exemplary for the calculation of all other expectation values.

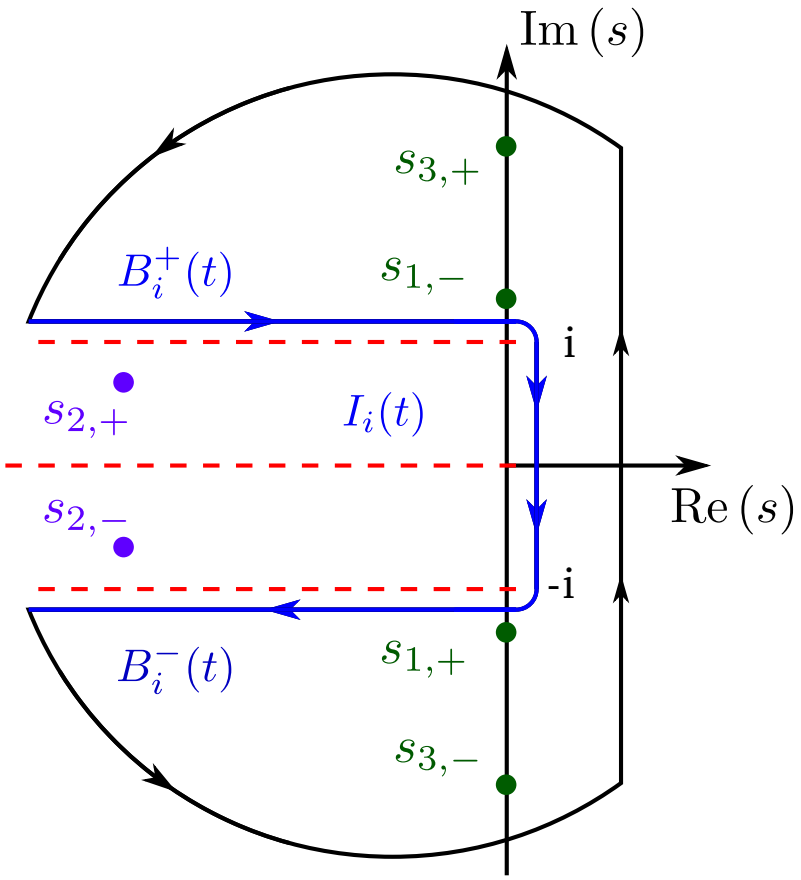

Figure 4.2. Illustration of the Bromwich contour integral in the complex plane with the analytic features of the denominator functions $D_+(s)$ and $D_-(s)$ consisting of branch-cuts (red dashed lines) and poles (blue and green disks). The integral in Eq. (4.41) is completed to a closed contour by an exponentially vanishing integral over the great circle, integrals along the upper and lower branch-cuts, $B_i^\alpha(t)$, and an integral along the imaginary axis $I_i(t)$. Within this closed contour lie the poles $s_{j,\pm}$, $j = 1, 3$, whereas the poles $s_{2,\pm}$ are not encircled and, thus, do not contribute to the integral. Note that the poles $s_{j,-}$ are relevant only for the calculation of $\langle S_{2,+}\rangle(t)$. *Figure adapted with permission from [83].*

$s_{j,+}$	$\mathrm{Res}\left[\mathrm{e}^{st}\left\langle S_{+,1}\right\rangle(s)\right]_{s=s_{j,+}}$
$s_{1,+} = -\mathrm{i}\left[1 + 2^{-\frac{c_-}{c_+}}\,\mathrm{e}^{-\frac{1}{\Delta\, c_+}}\right]$	$\langle S_{+,1}\rangle_0\left[\tilde{K} c_+ 2^{\frac{c_-}{c_+}}\right]^{-1}\mathrm{e}^{-\frac{1}{\Delta\, c_+}-\mathrm{i}t}$
$s_{3,+} = \mathrm{i}\omega_n$	$\langle S_{+,1}\rangle_0\left[1+\frac{1}{2}\tilde{\delta}\right]^{-1}\mathrm{e}^{\mathrm{i}\omega_n t}$

Table 4.3. Zeros of the denominator $D_+(s)$ and the corresponding residues for $\langle S_{+,1}\rangle(t)$. The purely imaginary pole $s_{3,+}$ gives rise to an undamped oscillation around the effective magnetic-field ω_n. *Table adapted with permission from [83].*

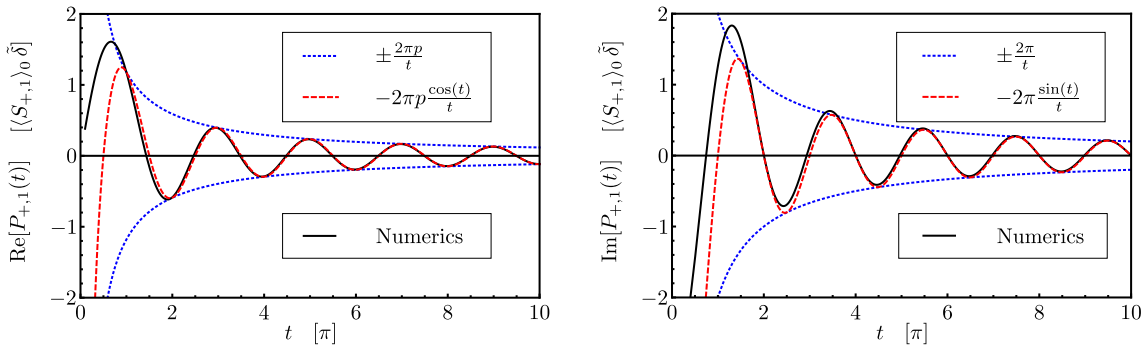

Figure 4.3. Real and imaginary part of $P_{+,1}(t)$ (solid, black) as a function of time obtained by numerical integration. For times $t > \pi$ ($\tilde{\tau}^s_{\mathrm{HI}} = 1$), the real part approximately described by an oscillating function (dashed, red), whose amplitude decays with $\sim t^{-1}$ (dotted, blue), where the amplitude is proportional to the polarization p. The oscillations show a period of 2π determined by the HI. The imaginary part of $P_{+,1}(t)$ (solid, black) exhibits a similar behavior as the real part. In contrast to the real part, the amplitude of the imaginary part does not depend on the polarization. The parameters used to create these plots are $\tilde{K} = 100$, $\Delta = 0.003$, and $p = 0.59$. *Figure adapted with permission from [83]. ©2012 American Physical Society. All rights reserved.*

First, we analyze the residues arising from the poles $s_{j,+}$, which are summarized in Tab. 4.3. The pole $s_{3,+}$ located on the imaginary axis gives rise to a purely oscillating term, where the frequency is given by the effective magnetic field ω_n. This oscillating part corresponds to a simple precession of the electron spin around this magnetic field. The calculation of this residue also nicely illustrates in which sense the disregard of the fourth order contribution $\Sigma^{(4)}(s) \propto \Delta$ of the self-energy sets an upper time limit. For simplicity, we assume that this contribution can be described by a complex valued constant $\Sigma^{(4)}(s) \approx \xi\Delta$ of order $O(\Delta)$, where we neglect any dependence on s. According to Eq. (4.26), this constant shift can be formally treated as a modification of the effective magnetic field $\mathrm{i}\omega_n \to \mathrm{i}\omega_n - \xi\Delta$ giving rise to an additional exponential factor $\exp(-\xi\Delta t)$. Hence, our predictions are valid only for times $t \ll \Delta^{-1}\tilde{\tau}^s_{\mathrm{HI}}$, for which this factor is irrelevant. In order to extend this limit, one would have to take the fourth order contribution with its full s-dependence into account. This line of arguing is, however, not directly applicable to the oscillating portion originating from the pole $s_{1,+}$, since this pole has a more complicated structure. It is located near the lower branching point at $-\mathrm{i}$, as is illustrated in Fig. 4.2. This residue generates an amplitude, which is exponentially small $\exp[-(c_+\Delta)^{-1}] \ll 1$ in a large magnetic field. As a consequence of its small size, we will neglect this contribution in the following for simplicity. Finally, the pole $s_{2,+}$ does not contribute, because it is outside of the contour.

Since the integral over the great circle vanishes due to Jordan's lemma, the only remaining, unknown expressions arise from the integrals along the branch-cuts and along the imaginary axis. The calculation of these integrals is, however, mathematically very challenging due to the fact that three different scaling behaviors are involved. The inverse Laplace transform itself gives rise to an exponential factor $\exp(st)$, while the denominators contain both logarithmic and power-law terms hampering analytical solutions to these integrals. Nevertheless, analytical considerations give valuable insights to the structure

of the results. First, we checked, that there are no contributions present in $P_i(t)$, which diverge for longer times and, thus, would lead to unphysical results. Moreover, one can testify, that the leading order contributions arising from the branch cut integrals $B_i^{\pm}(t)$ and from the imaginary integrals $I_i(t)$ cancel each other leaving terms of order $\delta = \Delta^2/K$. While it is easy to show that the contributions of this order stemming from the branch cut integrals are oscillating with a frequency proportional to $1/\tilde{\tau}_{\mathrm{HI}}^s$ determined by the HI, this is not evident for the imaginary integral. Furthermore, there is no obvious way to analytically extract more information on the time dependence of the amplitudes such as the form of a possible decay. Hence, we use numerical methods to find the results for all integrals, which are subsequently summed up in order to give the functions $P_i(t)$ defined in Eq. (4.42) above.

The function being relevant for $\langle S_{+,1}\rangle(t)$ is given by $P_{+,1}(t)$, whose real and imaginary part is plotted in Figs. 4.3 a) and 4.3 b), respectively. For times $t > \pi$ ($\tilde{\tau}_{\mathrm{HI}}^s = 1$), we find that the sum of the branch-cut contributions is approximately described by an oscillating term, whose amplitude is decaying with a power law:

$$P_{+,1}(t) = \langle S_{+,1}\rangle_0 \left\{ -2\pi \mathrm{i}\,\tilde{\delta}\left[\frac{\sin(t)}{t} - \mathrm{i}p\frac{\cos(t)}{t}\right]\right\}. \tag{4.45}$$

The final result for $\langle S_{+,1}\rangle(t)$ is obtained by summing up the residues and power-law contributions according to Eq. (4.42):

$$\langle S_{+,1}\rangle(t) = \langle S_{+,1}\rangle_0 \left\{ \left[1 + (\lambda_x^2+\lambda_y^2)\frac{\delta}{4}\right]^{-1} \mathrm{e}^{\mathrm{i}\omega_n t} + \frac{\lambda_x^2+\lambda_y^2}{2}\,\delta\left[\frac{\sin(t)}{t} - \mathrm{i}p\frac{\cos(t)}{t}\right]\right\}, \tag{4.46}$$

where we reintroduced the explicit dependence on the anisotropy of the HI using the relations summarized in Tab. 4.1.

For the special case of $\lambda_x = \lambda_y$, Eq. (4.40) readily gives $\langle S_{+,2}\rangle = 0$. Thus, the above equation already allows us to interpret the dynamics of such a system, which is, for instance, realized in GaAs or graphene subjected to a perpendicular magnetic field. According to Eq. (4.46) only a small fraction of order $\delta = \Delta^2/K$ of the initial spin decays and does so in a power law, while most of the spin is preserved and oscillates with a frequency determined by the effective magnetic field ω_n.

4.4.2. Inverse Laplace transform of the second spin contribution

So far, we have calculated the time-dependence of the first spin part $\langle S_{+,1}\rangle(t)$, which fully describes the behavior of a system with rotational symmetry in the transverse x-y-plane. For a system having a broken rotational symmetry with $\lambda_x \neq \lambda_y$, one has additionally to calculate the second spin function $\langle S_{+,2}\rangle(t)$, which contains two denominator functions $D_+(s)$ and $D_-(s)$ instead of one.

Turning first to the residues, we can take advantage of the fact, that the zeros of these denominators come in complex conjugated pairs $s_{j,+} = s_{j,-}^*$ because of the relation $D_+^*(s) = D_-(s^*)$. Therefore, the calculation of the residues is straightforward, resulting in the contributions listed in Tab. 4.4. The poles $s_{1,\pm}$ generate exponentially suppressed terms, which are equivalent to the $s_{1,+}$-residue of $\langle S_{+,1}\rangle(t)$. This means in particular,

s_j	$\mathrm{Res}\left[\mathrm{e}^{st}\langle S_{+,2}\rangle(s)\right]_{s=s_{j,+}}$	$\mathrm{Res}\left[\mathrm{e}^{st}\langle S_{+,2}\rangle(s)\right]_{s=s_{j,-}=s_{j,+}^*}$
$s_{1,+}$	$\frac{\langle S_{2,+}\rangle_0}{\tilde{K}c_+ 2\frac{c_-}{c_+}}\ \mathrm{e}^{-\mathrm{i}t}\ \mathrm{e}^{-\frac{1}{\tilde{\Delta}c_+}}$	$-\frac{\langle S_{2,+}\rangle_0}{\tilde{K}c_+ 2\frac{c_-}{c_+}}\ \mathrm{e}^{\mathrm{i}t}\ \mathrm{e}^{-\frac{1}{\tilde{\Delta}c_+}}$
$s_{3,+}$	$\langle S_{+,2}\rangle_0 \left[1+\frac{1}{2}\tilde{\delta}\right]^{-1} \mathrm{e}^{\mathrm{i}\omega_n t}$	0

Table 4.4. Residues of the second spin part $\langle S_{2,+}\rangle(t)$. The poles $s_{j,+}$ are listed in Tab. 4.3. Here, the $s_{3,\pm}$-poles produce inequivalent residues due to the rewritten form of $\langle S_{2,+}\rangle(s)$ in Eq. (4.40). *Table adapted with permission from [83].*

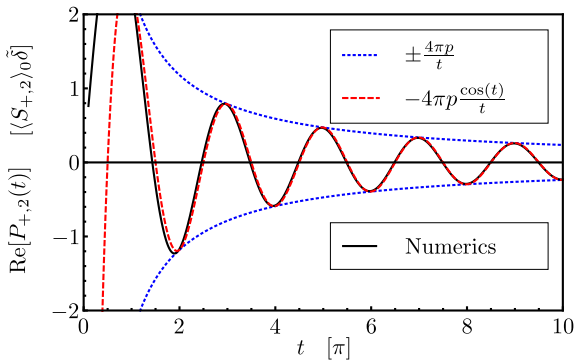

Figure 4.4. Real part of $P_{+,2}(t)$ (solid, black) as a function of time obtained by numerical integration. For times $t > \pi$ ($\tilde{\tau}^s_{\mathrm{HI}} = 1$), it is approximately described by an oscillating power-law decay (dashed, red; dotted, blue) $\sim t^{-1}$, where the amplitude is proportional to the polarization p and the period is given by 2π. The same parameters as in Fig. 4.3 have been used. *Figure adapted with permission from [83].*

that these residues are also negligible for large magnetic fields. In contrast to these paired terms, the pole $s_{3,+}$ creates a purely oscillating component, while the residue of pole $s_{3,-}$ vanishes identically.

The calculation of the sum of the branch-cut integrals, $P_{+,2}(t)$, is again obtained by numerical integration accompanied by analytical considerations. We find, that only the real part of $P_{+,2}(t)$ has a relevant contribution of order $O(\delta)$, while the imaginary part is much smaller, namely of order $O(\delta/\omega_n)$ and, thus, neglected. The time evolution of this real part is, up to a factor of two, analogous to the real part of $P_{+,1}(t)$, which can be read off from Fig. 4.4.

We find, that the branch-cut contribution can be approximately described by

$$P_{+,2}(t) = \langle S_{+,2}\rangle_0 \left\{ -2\pi \mathrm{i}\, \tilde{\delta}\Big[-\mathrm{i}2p\frac{\cos(t)}{t}\Big] \right\} \tag{4.47}$$

for times $t > \pi$. In order to obtain the full $\langle S_{+,2}\rangle(t)$ term, we sum up the residues and power-law contributions yielding:

$$\langle S_{+,2}\rangle(t) = \langle S_{+,2}\rangle_0 \left\{ \Big[1 + (\lambda_x^2+\lambda_y^2)\frac{\delta}{4}\Big]^{-1} \mathrm{e}^{\mathrm{i}\omega_n t} + \frac{\lambda_x^2+\lambda_y^2}{2}\,\delta\Big[-\mathrm{i}2p\frac{\cos(t)}{t}\Big] \right\}. \tag{4.48}$$

In combination with the result for $\langle S_{+,1}\rangle(t)$ given in Eq. (4.46), we are now able to formulate the time dependence of the electron spin component $\langle S_+\rangle(t)$ for arbitrary constants λ_x, λ_y, λ_z, and a general initial condition $\langle S_\pm\rangle_0 = \langle S_x\rangle_0 \pm \mathrm{i}\langle S_y\rangle_0$:

$$\begin{aligned}\langle S_+\rangle(t) = {} & \Big(\langle S_x\rangle_0 + \mathrm{i}\langle S_y\rangle_0\Big)\,\frac{\mathrm{e}^{\mathrm{i}\omega_n t}}{1+(\lambda_x^2+\lambda_y^2)\frac{\delta}{4}} \\ & + \Big(\lambda_y^2\langle S_x\rangle_0 + \mathrm{i}\lambda_x^2\langle S_y\rangle_0\Big)\,\delta\,\frac{\sin(t)}{t} \\ & - \mathrm{i}\Big(\lambda_x^2\langle S_x\rangle_0 + \mathrm{i}\lambda_y^2\langle S_y\rangle_0\Big)\,\delta\,p\,\frac{\cos(t)}{t}\,.\end{aligned} \tag{4.49}$$

4.5. Discussion and conclusion

According to Eq. (4.49), the overall dynamics of the electron spin components perpendicular to the external magnetic field is the same for any non-zero choice of the coupling constants λ_x, λ_y, and λ_z. They exhibit a dominant oscillating contribution, which describes a simple precession of the electron spin around the effective magnetic field $\omega_n = A^S_{\mathrm{ZE}} + \langle \hat{h}_z\rangle_n$ consisting of the external and nuclear magnetic fields. This contribution arises from the unitary part of the Nakajima-Zwanzig equation as described in Section 2.3. The conservation of the major part of $\langle \hat{S}_+(t)\rangle$ originates from the large Zeeman splitting A^S_{ZE}, which is expressed by the small parameter $\delta \propto (A^S_{\mathrm{ZE}})^{-2}$. Due to this large Zeeman splitting only virtual flip-flops are allowed effectively suppressing the action of the HI. However, a part of $\langle \hat{S}_+(t)\rangle$ is lost nevertheless, which is described by the second and third line of Eq. (4.49). The specific power-law decay found for this contribution originates from the non-Markovian corrections in Eq. (4.15), which take into account the flip-flop terms of

the HI. The term in the second line of Eq. (4.49) oscillates with a period given by the HI timescale $\tilde{\tau}^s_{\mathrm{HI}}$. Its amplitude exhibits a λ_x and λ_y weighted mixing of the initial values $\langle S_x\rangle_0$ and $\langle S_y\rangle_0$. This amplitude is proportional to the initial state $\langle\hat{S}_+\rangle_0 = \langle\hat{S}_x\rangle_0 + \mathrm{i}\langle\hat{S}_y\rangle_0$ if $\lambda_x = \lambda_y$, whereas it depends on the individual choices of $\langle\hat{S}_x\rangle_0$ and $\langle\hat{S}_y\rangle_0$ in the case of $\lambda_x \neq \lambda_y$. The property of the initial state reflects the broken rotational symmetry for different couplings within the x-y plane. The contribution to the non-Markovian dynamics in the last line of Eq. (4.49) exhibits qualitatively the same behavior as the former contribution. However, its amplitude shows a different mixing of the x- and y-components of the initial state, where λ_x and λ_y are interchanged. Furthermore, its amplitude depends on the polarization p of the nuclear spins, which quantifies the excess of one nuclear spin orientation over the other. For increasing p, one type of the HI-induced scattering processes, for instance $\hat{h}_+$, becomes more likely, while the other one is suppressed since its phase space is more and more limited. Probably, this can explain the polarization dependence of our result. However, within the Nakajima-Zwanzig formalism, it is not possible to single out microscopic processes explaining the specific form of the dependence on the anisotropy and the polarization demanding for successive studies using different techniques.

According to our findings, we can distinguish two classes of anisotropy. The first class is characterized by $\lambda_x = \lambda_y \neq \lambda_z$ for which Eq. (4.46) already describes the full dynamics of $\langle\hat{S}_+\rangle(t)$, since the off-diagonal elements $\Sigma^{(2)}_{\pm\mp}(s)$ are identically zero. In this case, this dynamics differ only quantitatively from the isotropic limit with $\lambda_x = \lambda_y = \lambda_z$. Analyzing our results in the isotropic case, we recover the initial power-law decay found in Refs. [61, 76], which is depicted in Fig. 4.1 in Section 4.1. The reason for the universal behavior for $\lambda_x = \lambda_y$ is the conserved rotational symmetry around the z-axis and the fact that the $\hat{S}_z$ and $\hat{S}_+$ subspaces are decoupled, cf. Eq. (4.22). This type of anisotropy is realized in graphene, if the external magnetic field is applied perpendicular to its plane and, hence, parallel to the symmetry axis of the $p_{2,z}$ orbital forming the conduction band. For more details on the role of this orbital, we refer to Section 1.3.1, in which we discuss the HI in graphene. Yet, there is another class of anisotropy, which is characterized by $\lambda_x \neq \lambda_y = \lambda_z$.[3] This class can also be realized in graphene if the external magnetic field is parallel to the graphene plane. For this choice of the coupling constants, the rotational symmetry around the z-axis is clearly broken. In this case, the individual initial values $\langle\hat{S}_x\rangle$ and $\langle\hat{S}_y\rangle$ are relevant rather than their superposition $\langle\hat{S}_+\rangle = \langle\hat{S}_x\rangle + \mathrm{i}\langle\hat{S}_y\rangle$ for $\lambda_x = \lambda_y$. The partial power-law decay of $\langle\hat{S}_+\rangle(t)$, however, is found for any (non-zero) choice of the constants λ_i.

All these results have been obtained for times $t \ll \min(\Delta^{-1}\tilde{\tau}^s_{\mathrm{HI}}, \tau^I_{\mathrm{ZE}})$, where the first timescale is determined by the ratio of the nuclear and external magnetic fields, $\Delta \propto A_{\mathrm{HI}}/A^S_{\mathrm{ZE}}$. For $\lambda_x = \lambda_y$, the HI is isotropic in the x-y plane and we can introduce a reference frame [76] rotating with a frequency given by the nuclear Zeeman energy A^I_{ZE}. In this reference frame, the nuclear Zeeman term is absent and, thus, the results hold always for times $t \ll \Delta^{-1}\tilde{\tau}^s_{\mathrm{HI}}$. For these times, the electron nuclear spin system is in a non-Markovian regime. Considering even longer times $t \gg \Delta^{-1}\tilde{\tau}^s_{\mathrm{HI}}$, which are not captured by our treatment, the system can, however, return to a Markovian regime again,

[3] As we have stated in Section 1.3.1, the specific choice of the x and y axis is arbitrary, such that this class can be likewise defined by $\lambda_y \neq \lambda_x = \lambda_z$.

as discussed in the beginning of this chapter. Our findings are qualitatively valid for other systems fulfilling the requirements of our model, where the most important demands are a Gaussian-like envelope function, slow dynamics of the nuclear spin environment and a sufficiently large Zeeman-splitting with respect to the HI energy scale. Besides the time-evolution of $\langle \hat{S}_+ \rangle(t)$, we have also analyzed the dynamics of the z-component of the electron spin. Due to the large external magnetic fields, most of its original amplitude is preserved, while we have found a small power-law decay for the remaining amplitude. These results have been published in Ref. [83].

5. Spin dynamics in a graphene quantum dot with few nuclear spins

In Chapter 4, we have investigated the behavior of the electron spin interacting with a large nuclear spin environment. Following an open system approach, we have used the Nakajima-Zwanzig equation to explore the non-Markovian dynamics of the electron spin. The present chapter can be regarded as complementary to this previous study. We consider the combined system formed by the electron and the nuclear spins as a closed quantum system. Moreover, we restrict ourselves to a small number of nuclear spins. While this choice is a rather strong approximation to the physics of the widely studied GaAs QDs, small nuclear spin environments can, in fact, be realized in graphene QDs. Due to the small size of our total system, we can analyze the dynamics of the electron spin using exact diagonalization, which allows us to study both its short time and long time dynamics. The presentation of our results closely follows our publication in Ref. [105].[1]

5.1. Model

We consider a graphene QD, whose properties we have discussed in detail in Section 1.3.1. Formally, this QD is described by a set of atomic sites $\{\boldsymbol{r}_k\}_{k=1}^{N_{sites}}$ defined by the cutoff relation in Eq. (1.25), where we use $C = 10^{-6}$ for the cutoff. The probability to find the electron at one of these sites is described by a Gaussian envelope function defined in Eq. (1.23), where we use a radius $R = 7\,a_{\mathrm{NN}}$ with a_{NN} being the distance between nearest neighbors. This corresponds to a dot with diameter $D \approx 7.2\,\mathrm{nm}$ containing $N_{sites} \approx 10^3$ carbon atoms, such that $K = 9$ atoms correspond to the natural abundance $n_I = 0.01$ of ^{13}C. Applying a spatial cutoff, we effectively ignore everything outside the barrier defined by the cut-off, which is justified by the vanishingly small probability to find the electron there. In order to find the electron with probability 1 inside of our QD, we impose the following normalization condition $\sum_{k=1}^{N_{sites}} v_0|\phi(\boldsymbol{r}_k)|^2 = 1$. A plot of a QD realized in this way is shown in Fig. 1.5. Since we do not have further knowledge about the distribution of ^{13}C within the dot, we randomly place the nuclear spins on the sites $\boldsymbol{r}_k$, where each site is chosen with equal probability. An example of a configuration of ten nuclear spins is shown in Fig. 1.5. Besides the HI, we also include an external magnetic field, which gives rise to a finite Zeeman interaction of the electron spin and the nuclear spin. In summary, the total Hamiltonian $\hat{H} = \hat{H}_{\mathrm{ZE}}^S + \sum_k \hat{H}_{\mathrm{ZE}}^k + \hat{H}_{\mathrm{HI}}$ is given by the electron Zeeman Hamiltonian $\hat{H}_{\mathrm{ZE}}^S = g^* \mu_B \boldsymbol{B}\hat{\boldsymbol{S}}$ in Eq. (1.9), all nuclear Zeeman terms $\hat{H}_{\mathrm{ZE}}^k = g_N \mu_N \boldsymbol{B}\hat{\boldsymbol{I}}_k$ defined in

[1]

Eq. (1.10), and the anisotropic HI in graphene

$$\hat{H}_{\mathrm{HI}} = \sum_{k=1}^{K} A_k \sum_{\mu,\nu} \overleftrightarrow{A}_{\mu\nu} \hat{S}_\mu \hat{I}_{k,\nu} \,, \tag{5.1}$$

where the sums run over spatial coordinates x, y, z and the tensor $\overleftrightarrow{A}_{\mu\nu}$ describing the anisotropy is defined in Eq. (1.29).

In the following, we aim to simulate a model experiment consisting of the preparation of the spins and the actual measurement of the spin dynamics. The electron spin can be well prepared[2] in experiments as we elaborately discuss in Section 1.3.3. There, we also describe schemes to prepare the nuclear spins in specific states. Since these schemes are, however, quite involved, we assume for this chapter, that no further efforts are undertaken to manipulate the nuclear spins. Since the energy scales of the nuclear spins are below the typical thermal energies found for such experiments [9, 24], the nuclear spins are assumed to be in a random, unpolarized state $\hat{\rho}_{\mathrm{nuc}}$ at the beginning of the actual experiment. The coefficients of this state are created by drawing random numbers $\mathrm{Re}[\alpha_p]$ and $\mathrm{Im}[\alpha_p]$ from $[-1, 1]$ with equal probability and normalizing them according to Eq. (5.8) below. A similar approach has been used in Refs. [54, 74].

We always choose the initial state of the electron to be $|-\frac{1}{2}\rangle$, such that the initial expectation value of its z-component is always $\langle \hat{S}_z \rangle(0) = -\frac{1}{2}$. Through this specific choice, we define a Cartesian coordinate system (x, y, z), which we will use for all calculations presented in this chapter. Yet, the geometry of the graphene sheet defines another coordinate system (x', y', z'), which is invariant under rotations around the z' axis perpendicular to the graphene plane. If we choose, without loss of generality, the y- and y'-axis to coincide, both coordinate systems are connected via a rotation matrix

$$\hat{D}(\beta) = \mathrm{e}^{-\mathrm{i}\frac{\beta}{2}(\hat{S}_y + \sum_k \hat{I}_{k,y})} \tag{5.2}$$

about this common axis as illustrated in Fig. 1.5. In this chapter, we investigate the time dependence of the z-component $\langle \hat{S}_z \rangle(t)$ of the electron spin, in contrast to $\langle \hat{S}_+ \rangle(t)$ analyzed in the previous chapter. However, in the specific setup considered in the present chapter, these two quantities are intimately related to each other. The time-dependent expectation value of the z-component of the electron spin is given by

$$\langle \hat{S}_z \rangle(t) = \mathrm{Tr}[\hat{S}_z \hat{U}(t) \hat{\rho}_0 \hat{U}^\dagger(t)] \,, \tag{5.3}$$

where

$$\hat{\rho}_0 = |-\tfrac{1}{2}\rangle\langle -\tfrac{1}{2}| \otimes \hat{\rho}_{\mathrm{nuc}} \tag{5.4}$$

describes the initial state of the total spin system and $\hat{U}(t) = \mathrm{e}^{-\mathrm{i}\hbar^{-1}\hat{H}t}$ is the time evolution operator determined by the total Hamiltonian. How is this expectation value connected

[2] Good control of the electron spin has been demonstrated for QDs build in group III-V materials. Up to now, the quality of graphene QDs hampers a comparable degree of control in these QDs. However, this is a problem of optimization of the processing techniques rather than a fundamental physical problem. Alternatively, one can also think of silicon based QDs, which are very promising with respect to the control of the electron spin.

with $\hat{S}_+$, which is an observable to detect (de)coherence? In Eq. (5.3), we have decided to measure the electron spin in a specific coordinate system. However, we are not at all limited to this choice, but we may, for instance, rotate all operators around the y-axis to find

$$\begin{aligned}\langle \hat{S}_z \rangle^{[\hat{\rho}_0,\hat{U}(t)]}(t) &= \mathrm{Tr}[\underbrace{\hat{D}(\beta)\hat{S}_z\hat{D}^\dagger(\beta)}_{\equiv\hat{S}(\beta)}\underbrace{\hat{D}(\beta)\hat{U}(t)\hat{D}^\dagger(\beta)}_{\equiv\hat{U}(\beta,t)}\underbrace{\hat{D}(\beta)\hat{\rho}_0\hat{D}^\dagger(\beta)}_{\equiv\hat{\rho}_0(\beta)}\underbrace{\hat{D}(\beta)\hat{U}^\dagger(t)\hat{D}^\dagger(\beta)}_{\equiv\hat{U}^\dagger(\beta,t)}] \\ &\equiv \langle \hat{S}(\beta) \rangle^{[\hat{\rho}_0(\beta),\hat{U}(\beta,t)]}(t)\,, \end{aligned} \tag{5.5}$$

where $\langle \ldots \rangle^{[\hat{\rho},\hat{U}(t)]}$ specifies with respect to which density matrix $\hat{\rho}$ and to which time evolution operator $\hat{U}(t)$ the expectation value is actually calculated. The time-evolution operator $\hat{U}(\beta,t) = \mathrm{e}^{\mathrm{i}\hbar^{-1}\hat{H}(\beta)t}$ is then determined by the transformed Hamiltonian $\hat{H}(\beta) = \hat{D}(\beta)\hat{H}\hat{D}^\dagger(\beta)$. Choosing $\beta = \frac{\pi}{2}$ yields $\hat{S}(\beta) = \hat{S}_x = \mathrm{Re}[\hat{S}_+]$ and $\hat{\rho}_0(\beta) = (|\frac{1}{2}\rangle + |-\frac{1}{2}\rangle)/\sqrt{2} \otimes \hat{\rho}_{\mathrm{nuc}}(\beta)$. Thus, the time-evolution of $\hat{S}_z$ with respect to $\hat{H}$ and $\hat{\rho}_0$ is equivalent to the dynamics of $\hat{S}_x$ with respect to $\hat{H}(\beta)$ and $\hat{\rho}_0(\beta)$. However, from the latter point of view, it is more apparent, that we are actually monitoring the fate of a coherent superposition of electron spin states. This observation illustrates the fact that the appearance of coherence and, thus, of decoherence depends on the specific choice of basis states [18].

5.2. Method

In order to analyze the time evolution of the electron spin, we apply exact diagonalization, which we have already introduced in Section 2.2.1. For this numerical procedure to work, we need a basis to represent the state of our system and the operators acting on it. A natural choice for $N = K + 1$ spins is given by the tensor product states of the electron spin and the nuclear spin eigenstates

$$|p\rangle = |m_S^p\rangle \otimes \bigotimes_{k=1}^{K} |m_k^p\rangle\,, \tag{5.6}$$

where the electron spin is represented by $|m_S^p\rangle$, $m_S^p = \Downarrow, \Uparrow$ and the nuclear spin states by $|m_k^p\rangle$, $m_k^p = \downarrow, \uparrow$. For convenience, we have ordered the nuclear spins $|m_S^p m_K^p m_{K-1}^p \ldots\rangle$ according to their coupling strength A_k to the electron spin:

$$A_K \geq A_{K-1} \geq \ldots \tag{5.7}$$

Within this basis, an arbitrary state is given by a linear superposition of these 2^N states

$$|\psi\rangle = \sum_{p=0}^{2^N-1} \alpha_p |p\rangle\,, \qquad \sum_{p=0}^{2^N-1} |\alpha_p|^2 = 1 \tag{5.8}$$

with complex coefficients α_p, which can be also written in terms of a density matrix $\hat{\rho} = |\psi\rangle\langle\psi|$. With the matrix representations of the Hamiltonian, H_{pq}, the electron spin

$(S_z)_{pq}$, and the initial state ρ_{pq}, we can use Eq. (2.26) in order calculate the time-evolution of the electron spin

$$\langle \hat{S}_z \rangle(t) = \mathrm{Tr}[\hat{S}_z \hat{\rho}(t)] = \sum_{\substack{n,m,p,q \\ \nu,\mu}} (S_z)_{nm} M^*_{m\nu} V_{\nu\nu}(t,t_0) M_{\nu p}\, \rho_{pq}(t_0)\, M^*_{q\mu} V^*_{\mu\mu}(t,t_0) M_{\mu n} \tag{5.9}$$

where the matrix elements of the time-evolution operator $V_{\nu\nu}(t,t_0) = e^{-\mathrm{i}\hbar^{-1}E_\nu t}$ are determined by the eigenvalues E_ν of the Hamiltonian $\hat{H}$. The numerical diagonalization to obtain these eigenvalues and the corresponding eigenstates forming the matrix $M_{n\nu}$ is performed using the EIGEN [169] package for C++.

5.3. Results

In this section, we present our findings for the model system defined above. As one can notice from the explanations above, we deal with a rather large parameter space in which we can analyze the outcome of Eq. (5.9). First, we control the shape of the dot by means of the envelope function $|\phi(r)|^2$, second the number of nuclear spins K is variable and finally these spins can have different positions or configurations c within the dot. All of these parameters change the HI Hamiltonian in Eq. (5.1). Moreover, we will investigate different initial states $|\psi_0\rangle$ of the electron and the nuclear spins affecting Eq. (5.9). Additionally, the eigenvector matrix $\hat{M}$, appearing in this equation is a function of the twisting angle β between the normal vector of the graphene plane and the orientation of the electron spin, which defines the z-direction. Note that the spectrum of eigenvalues E_ν is unaffected by a change of β. Finally, we can also modify the absolute value of the external magnetic field, which we will parametrize by the resulting Zeeman energy of the electron A^S_{ZE}.

In order to determine qualitatively and quantitatively the impacts of the parameters, we investigate the time dependent expectation value $\langle \hat{S}_z \rangle(t)$, which is calculated using Eq. (5.9). A typical time evolution of $\langle \hat{S}_z \rangle(t)$ is plotted in Fig. 5.1. Within the decoherence time T_D, the initial amplitude of the electron spin of $-\frac{1}{2}$ decays to its long-time average value, where still finite oscillations and beatings occur. This can be traced back to the finite size of the spin bath considered here. Its long-time average value is calculated by

$$\langle \hat{S}_z \rangle_T = \frac{1}{N_T} \sum_{n=0}^{N_T} \langle \hat{S}_z \rangle(T_{min} + n\,\Delta T)\,, \tag{5.10}$$

where we average over $N_T = (T_{max} - T_{min})/\Delta T$ time steps of width ΔT. In order to investigate the oscillations of $\langle \hat{S}_z \rangle(t)$ quantitatively, we consider the standard deviation

$$\sigma_{S_z} = \sqrt{\frac{1}{N_T} \sum_{n=0}^{N_T} \left(\langle \hat{S}_z \rangle(T_{min} + n\,\Delta T) - \langle \hat{S}_z \rangle_T \right)^2} \tag{5.11}$$

as well as the sample range

$$\Delta S_z = \max_{t \in [T_{min}, T_{max}]} [\langle \hat{S}_z \rangle(t)] - \min_{t \in [T_{min}, T_{max}]} [\langle \hat{S}_z \rangle(t)]\,. \tag{5.12}$$

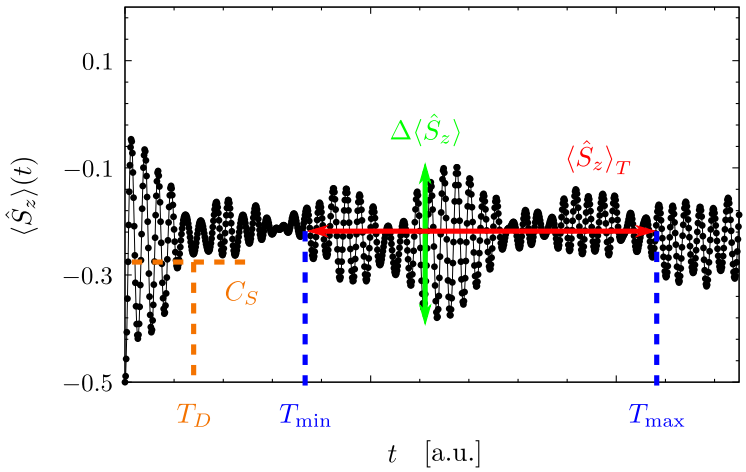

Figure 5.1. Exemplary time evolution of the electron spin component $\langle \hat{S}_z \rangle(t)$. For a certain range of time $[T_{min}, T_{max}]$, we calculate the long-time average $\langle \hat{S}_z \rangle_T$ and the standard deviation σ_{S_z} (not shown) using a a time resolution ΔT. Furthermore, we consider the maximal deviation ΔS_z of the signal within this time interval as explained in the text. The decoherence time T_D is determined by a constant threshold C_S. *Figure adapted with permission from [105].*

This sample range is sensitive to the occurrence of oscillations with a big amplitude which originate from either recurrences of the signal, an entire lack of decoherence or beatings. While for beatings one expects rather small sample ranges $\Delta S_z < \langle \hat{S}_z \rangle(0)$, the former two cases should give values on the order of the initial amplitude, $\Delta S_z \sim O(\langle \hat{S}_z \rangle(0))$ in the out-of-plane case $\beta = 0$ and $\Delta S_z \sim 2\,O(\langle \hat{S}_z \rangle(0))$ in the in-plane case $\beta = \frac{\pi}{2}$, cf. Fig. 1.5.

Besides these quantities characterizing the long time average of the electron spin, we are also interested in the amount of time it takes to decohere the system. In order to be independent from specific models of the decay, such as exponential or power-law decoherence, and to account for the characteristics of the numerics, we find this decoherence time T_D by the first minimum exceeding a certain threshold C_S. For clarity, C_S is also illustrated in Fig. 5.1. This approach is similar to the one used in Ref. [150] to find the decoherence times. Of course, the choice of this constant C_S changes the value of T_D. However, its order of magnitude and its dependence on the different parameters is rather independent from a specific choice as long as C_S is not too close to $\langle \hat{S}_z \rangle_T$, which we have confirmed for different values of C_S.

In the following, we analyze both the decoherence time and the long-time average of the z-component of the electron spin for different parameter sets. For each number of nuclear spins K, many initial states and configurations are created and labeled by numbers $0, 1, 2 \ldots$ for later comparison of the results. Note, that, for different nuclear spin numbers K, these labels describe different initial states and configurations. Moreover, we concentrate on two orientations of the quantization axis, namely out-of-plane orientation for $\beta = 0$ and in-plane orientation with $\beta = \frac{\pi}{2}$.

We have investigated the effect of finite magnetic fields for exemplary initial states, configurations and $K = 2, 4, 6$ nuclear spins, where we have varied the resulting Zeeman

constant from $A^S_{\mathrm{ZE}}/A_{\mathrm{HI}} \ll 1$ to $A^S_{\mathrm{ZE}}/A_{\mathrm{HI}} \gg 1$. For increasing A^S_{ZE}, we find a continuous crossover to a perfect alignment of the electron spin in the case of a very strong magnetic field. In the following, we set $B_z = 0$ because we would like to better understand the low-magnetic field behavior of the spin dynamics in the presence of the HI, which complements our high field analysis of Chapter 4.

5.3.1. The long-time average of the electron spin

First, we investigate the consequences of both different random complex (RC) initial states and different configurations of the nuclei within the dot. To this end, we have calculated $\langle \hat{S}_z \rangle_T$, σ_{S_z} and, ΔS_z for different parameter sets and found stable results for $T_{min} = 0.5 \times 10^9 \tau_{HI}$, $T_{max} = 1.5 \times 10^9 \tau_{HI}$, and $\Delta T = 10^4 \tau_{HI}$ with $\tau_{HI} = \hbar/A_{\mathrm{HI}} \approx 1\,\mathrm{ns}$. In Fig. 5.2 a), we plot the long-time average $\langle \hat{S}_z \rangle_T$ as a function of different RC states and configurations for $K = 3$ and $K = 6$, respectively, in out-of-plane orientation. The color map in Fig. 5.2 b) was created for the same parameters with in-plane orientation. For a small number of nuclear spins $K = 3$ and $\beta = 0$, we observe strong fluctuations for both different RC states and different configurations around an average value of $\langle \hat{S}_z \rangle_T \approx -0.22$ as depicted in the color map of Fig. 5.2 a). The horizontal stripes dominate over the vertical structures indicating, that the choice of the RC initial states has a greater influence on the results than the spatial configuration of the nuclear spins within the dot. Moreover, we find large oscillations around this long-time average value for many configurations and initial states. This results in both sizable sample ranges ΔS_z and standard deviations σ_{S_z}. By averaging over all 51×51 results, we find $\langle \langle \hat{S}_z \rangle_T \rangle = -0.22 \pm 0.06$, $\langle \sigma_{S_z} \rangle = (0.13 \pm 0.04)$, and $\langle \Delta S_z \rangle = 0.52 \pm 0.11$, which is also shown in Fig. 5.3. The large average value of the sample range $\langle \Delta S_z \rangle$ shows that for most cases analyzed, there is at least one big change in amplitude. However, no total spin flip with $\Delta S_z = 1$ is achieved. The occurrence of sizable standard deviations indicates that there are on average many of these events. Thus in the case of few nuclear spins, coherent oscillations of the electron spin are the dominant dynamics.

If we consider a larger environment of nuclear spins as presented in Fig. 5.2 a) with $K = 6$, the behavior of the long-time average changes. First of all, the result is much more uniform with respect to both the RC initial states and the configurations. In addition, the remaining differences in $\langle \hat{S}_z \rangle_T$ depend on the configurations rather than on the initial states, which is obvious from the vertical lines present in this color map. Averaging over all 51×51 results gives $\langle \langle \hat{S}_z \rangle_T \rangle = -0.22 \pm 0.02$, which is essentially the same as for $K = 3$. However, the standard deviation $\langle \sigma_{S_z} \rangle = 0.06 \pm 0.03$ and the sample range $\Delta S_z = 0.37 \pm 0.06$ clearly decrease. We confirmed this trend of decreasing fluctuations by repeating the above averaging procedure for other numbers of nuclear spins. These results are presented as a function of K in Fig. 5.3. While the long-time average value is constant, both the standard deviation and the sample range become smaller. Especially, the pronounced decay of the sample range clearly indicates that recurrences of $\langle \hat{S}_z \rangle(t)$ or an entire lack of decoherence occur much less. This behavior can be understood by

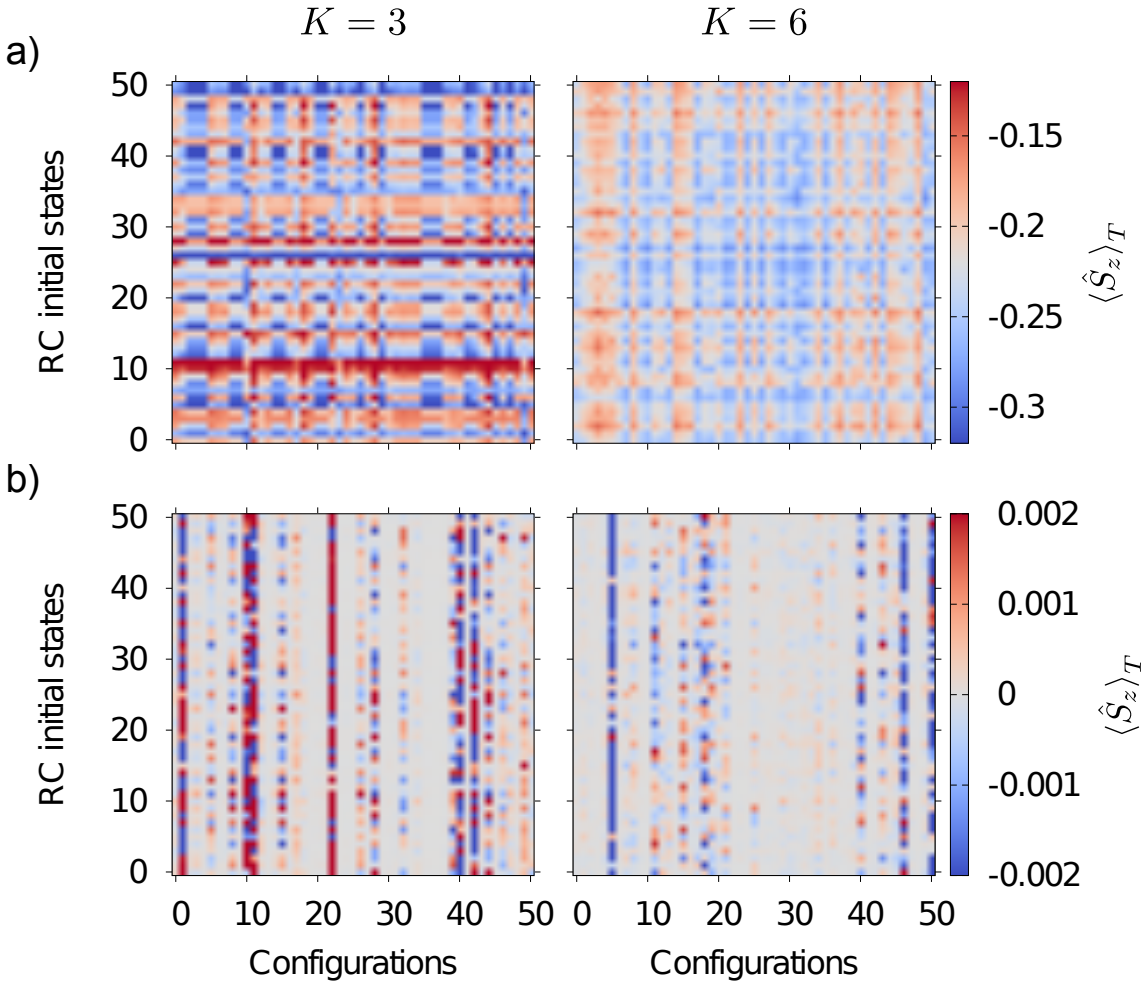

Figure 5.2. **a)**: Plot of the long-time average $\langle \hat{S}_z \rangle_T$ for out-of-plane orientation $\beta = 0$ and $K = 3$ and $K = 6$ nuclear spins without an external magnetic field. We have considered 51 different RC initial states and 51 random configurations. For both numbers of nuclear spins, the electron spin decays from its initial value $\langle \hat{S}_z \rangle(0) = -\frac{1}{2}$ to a finite long-time value $\langle \hat{S}_z \rangle_T$ around -0.22. **b)**: Same plot as in a) but for in-plane orientation with $\beta = \frac{\pi}{2}$. For all parameters the long-time average saturates around $\langle \hat{S}_z \rangle_T \approx 0$. *Figure adapted with permission from [105].*

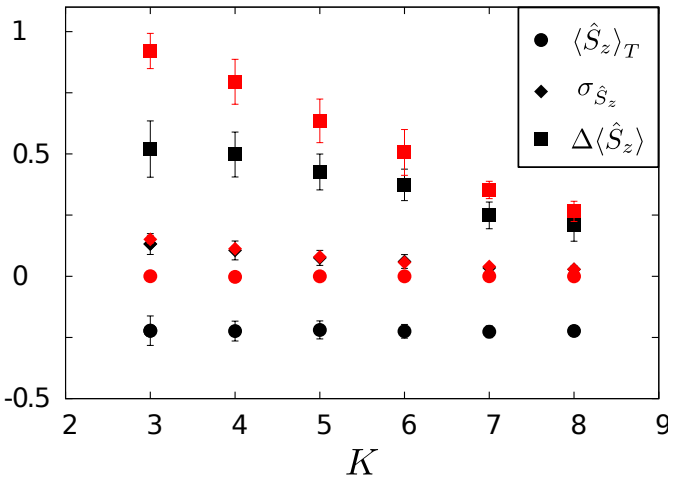

Figure 5.3. Plot of the long-time average $\langle \hat{S}_z \rangle_T$, the standard deviation σ_{S_z} and, the sample range ΔS_z as a function of the number of nuclear spins K for in-plane ($\beta = \frac{\pi}{2}$, red) and out-of-plane orientation ($\beta = 0$, black). The values are obtained by averaging over 51 RC initial states and 51 different configurations, see Figs. 5.2 a) and 5.2 b). Error bars are given by the standard deviation with respect to averaging over all 51×51 results. *Figure adapted with permission from [105].*

analyzing the impact of the nuclear spin number on the dimension of the Hilbert space and on the strength of the hyperfine interaction.

For a small number of nuclear spins, the dimension of the corresponding Hilbert space $D = 2^{K+1}$ is small and, hence, we draw our RC initial states from a rather limited set, where individual single product states $|p\rangle$ lead to very different dynamics of the electron spin. Due to the combination of only 2^K states $|p\rangle$ to a RC initial state, it is not unlikely that one of these states is occupied with a much larger probability than all other states leading to rather diverse results. By increasing K, the Hilbert space dimension grows with 2^{K+1}, which yields a different situation. Since the individual state of nuclear spins at the border of the dot is almost irrelevant due to a small $|\phi(\boldsymbol{r}_k)|^2$, groups of effectively equivalent states are superposed in this case. Thus, a more effective averaging is achieved suppressing the dependence on a specific initial state. As a consequence, it is very unlikely for a single state to dominate over the rest. A similar effect has been reported before in the context of quantum parallelism and amplitude averaging [54, 74].

The individual coupling strengths of the nuclear spins are the key in understanding the dependence of the results on the configuration. Its energy scale is proportional to the envelope function $|\phi(r_k)|^2$ at the respective sites of the nuclear spins. For a small number of spin carrying ^{13}C isotopes, the probability to find two or more nuclear spins, which couple almost equally with the electron spin, is low due to the large gradient of the envelope function. Hence, effectively only one nuclear spin strongly interacts with the electron leading to simple oscillations. This fact can be easily verified by diagonalizing the resulting, effective 4×4 matrix of the HI Hamiltonian, where we find a discrete spectrum

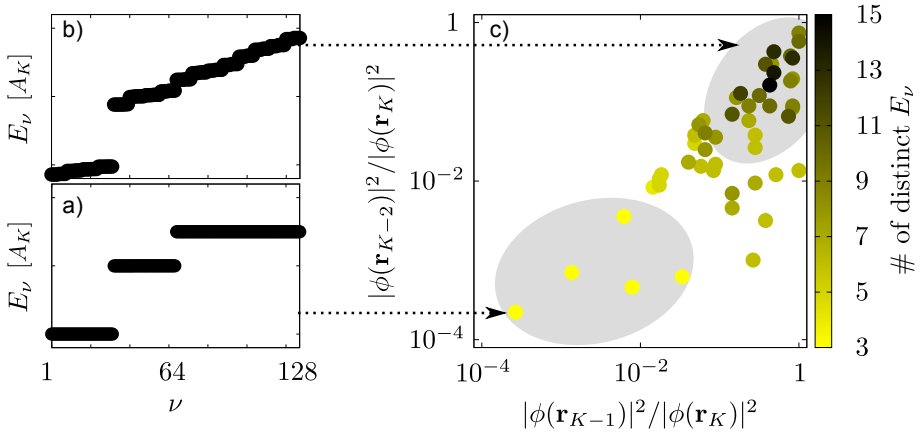

Figure 5.4. (a): Eigenvalues E_ν of the HI Hamiltonian for for $K = 6$ nuclear spins and configuration $c = 10$ in units of A_K. (b): Eigenvalues E_ν for $K = 6$ and $c = 3$. (c): Number of distinct eigenvalues E_ν as a function of the relative probabilities $|\phi(r_{K-1})|^2/|\phi(r_K)|^2$ and $|\phi(r_{K-2})|^2/|\phi(r_K)|^2$ for $K = 6$ nuclear spins. If both $|\phi(r_{K-1})|^2/\phi(r_K)|^2 \approx 1$ and $|\phi(r_{K-2})|^2/\phi(r_K)|^2 \approx 1$ at least three nuclear spins are strongly interacting with the electron spin causing a spectrum with many different eigenvalues as depicted in (b). If only the most central nuclear spin couples strongly to the electron spin (lower left part), the spectrum is highly degenerate showing only three different eigenvalues as shown in (a). The upper limit for the number of 15 has no deeper meaning besides distinguishing both types of spectra. *Figure adapted with permission from [105]. ©2013 American Physical Society. All rights reserved.*

of frequencies. These frequencies are given by the (highly) degenerate eigenvalues E_ν of the effective Hamiltonian $\{E_\nu\} = \{-\frac{1}{2}A_K, 0, \frac{1}{4}A_K, \frac{1}{4}A_K\}$. This limited amount of distinct frequencies is responsible for the rather uniform dynamics with respect to different configurations in a small K regime. This situation can of course also occur for larger nuclear spin environments, as shown in Fig. 5.4 (a) for $K = 6$. It is, however, rather the exception from the more probable case of several nuclei coupling comparably to the electron, where an almost continuous spectrum is found as depicted in Fig. 5.4 (b). If we characterize these spectra quantitatively by counting the number of distinct eigenvalues, i.e., eigenvalues which differ significantly, we can map the configuration of the nuclei to the spectra as depicted in Fig. 5.4 (c).

For the in-plane case, our findings are quite different from the former ones. The electron spin saturates around $\langle \hat{S}_z \rangle_T = 0$ for both $K = 3$ and $K = 6$ as shown in Fig. 5.2 b). Interestingly, we find already for $K = 3$, that this average is reached very precisely with smaller fluctuations than in the out-of-plane case. This fact becomes also clear from averaging the expectation value of the electron spin $\langle \langle \hat{S}_z \rangle_T \rangle = 0.000 \pm 0.004$ over all 51×51 results. Moreover, the results are independent from the choice of the RC initial state. Some single configurations, however, give rise to deviations from this, where also a dependence on the initial state is restored. It seems, that this is the case, whenever several nuclear spins couple comparably to the electron spin explaining the sensitivity on

the initial states. The size of the fluctuations is on average given by $\langle \sigma_{S_z} \rangle = 0.15 \pm 0.02$. The mean value of the sample range of $\langle \Delta S_z \rangle = 0.92 \pm 0.07$ close to 1 indicates, that in most cases, the electron spin is at least once almost completely flipped. The study for $K = 6$ exhibits qualitatively the same result with $\langle \langle \hat{S}_z \rangle_T \rangle = 0.000 \pm 0.001$, where the fluctuations $\langle \sigma_{S_z} \rangle = 0.057 \pm 0.004$ are further suppressed. Moreover, the appearance of recurrences and total spin flips is also strongly decreased for $K = 6$ as is clear from the sample range $\langle \Delta S_z \rangle = 0.51 \pm 0.09$. Analyzing this observable as a function of the number of nuclear spins, we observe again a prominent suppression of the fluctuations for growing K as is apparent in Fig. 5.3.

In order to understand the differences between the in-plane and out-of-plane dynamics of the electron spin in more detail, an analytic analysis of the dynamics in the case of only one nuclear spin is very useful. Calculating the long-time average analytically for $K = 1$ yields

$$\begin{aligned} \langle \hat{S}_z \rangle_T(\beta) &= \lim_{\Delta T \to \infty} \frac{1}{2\Delta T} \int_{T+\Delta T}^{T-\Delta T} \langle \hat{S}_z \rangle(t, \beta) \\ &= -\frac{1}{4} \cos(\beta) \Big[2\rho_{\downarrow\downarrow} \cos(\beta) + (\rho_{\uparrow\downarrow} + \rho_{\downarrow\uparrow}) \sin(\beta) \Big] , \end{aligned} \tag{5.13}$$

where the initial density matrix

$$\rho_0 = |\Downarrow\rangle\langle\Downarrow| \otimes \hat{\rho}_{\text{nuc}} \tag{5.14}$$

is a tensor product of the electron spin density matrix $\hat{\rho}_S = |\Downarrow\rangle\langle\Downarrow|$ and the nuclear spin density matrix

$$\hat{\rho}_{\text{nuc}} = \begin{pmatrix} \rho_{\downarrow\downarrow} & \rho_{\downarrow\uparrow} \\ \rho_{\uparrow\downarrow} & \rho_{\uparrow\uparrow} \end{pmatrix} . \tag{5.15}$$

For more nuclear spins involved, the resulting equations become much more complicated. However, for the special case of only one strongly coupling nuclear spin, the structure of the HI Hamiltonian remains the same and Eq. (5.13)) still holds. We have numerically investigated the dependence of the long-time average on β for some configurations and initial states and $K = 2, 4, 6$ and 9 nuclear spins, where we find good agreement of our results with $\langle \hat{S}_z \rangle_T(\beta) = \langle \hat{S}_z \rangle_T(0) \cos^2(\beta)$ with increasing K. Particularly, we observe this behavior also for configurations with several nuclear spins coupling almost equally to the electron spin. As an example, we plot the dependence of $\langle \hat{S}_z \rangle_T$ on β for $K = 6$ and configuration $C = 3$ in Fig. 5.5. Its spectrum is shown in Fig. 5.4 (b). This specific dependence on β is also supported by our results presented in Figs. 5.2 a) and 5.2 b), where we find on average $\langle \hat{S}_z \rangle_T \approx -0.22$ for $\beta = 0$ and $\langle \hat{S}_z \rangle_T \approx 0$ for $\beta = \frac{\pi}{2}$. The deviation of $\langle \hat{S}_z \rangle_T(\beta = 0)$ from $-\frac{1}{4}$ presumably originates from the finite time window $[T_{min}, T_{max}]$ used in the numerical calculations, which misses recurrences of the full initial value of $\langle \hat{S}_z \rangle(t = 0) = -\frac{1}{2}$. From these numerical findings and Eqs. (5.13) and (5.14), we suppose that contributions from the off diagonal parts cancel each other almost completely and that the elements of the diagonal parts of the density matrix $\rho_{\downarrow\downarrow}, \rho_{\uparrow\uparrow}$ have approximately equal weight of 2^{-K}, which seems reasonable for random complex initial states.

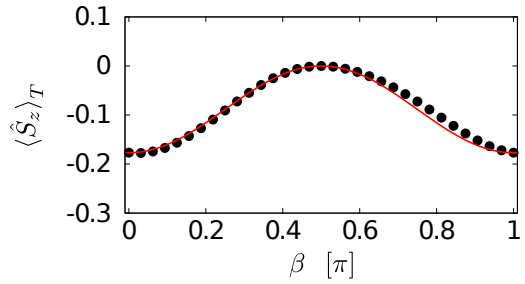

Figure 5.5. Dependence of the long-time average $\langle \hat{S}_z \rangle_T(\beta)$ on the angle β of the quantization axis with respect to the graphene plane for $K = 6$ nuclear spins. The example shown here has been calculated for a specific configuration, whose spectrum is presented in Fig. 5.4 (b). The only parameter used to fit the numerical values to the analytic curve $\langle \hat{S}_z \rangle_T(\beta) = \langle \hat{S}_z \rangle_T(0) \cos^2(\beta)$ is the longtime average value $\langle \hat{S}_z \rangle_T(0) = -0.22$. *Figure reprinted with permission from [105].*

5.3.2. Decoherence times of the electron spin

In this section, we want to investigate the decoherence times of the electron spin S_z for different initial states and different configurations. We have chosen the threshold to be always about 0.1 below the obtained long-time average, which gives $C_S = -0.325$ for the out-of-plane case $\beta = 0$ and $C_S = -0.1$ for the in-plane case $\beta = \frac{\pi}{2}$. Moreover, we used exactly the same initial states and configurations for all K as for the calculation of the long-time average. The decoherence times have been estimated for times up to $10^7\,\tau_{HI} \approx 10\,\text{ms}$ with a time resolution $\Delta T = 10^2\,\tau_{HI}$, which yields at least $P = 2\pi\hbar/(\Delta T A_K) \approx 20$ points per period.[3] By considering such long times, we make sure no to miss very slow decays with very long decoherence times.

As it turns out, the decoherence times obtained by this method are rather independent from the initial states. Several factors are important for this fact. First of all, for larger numbers of nuclei of course the same arguments concerning the Hilbert space dimensions as for the long-time average hold. However, we also find for small K only little dependence on the initial states. One reason for this is probably, that our method is robust against small changes of the electron spin caused by different initial states, since we measure when the minimum of the signal is above a certain threshold, but not how much. Finally, as we show below, the decoherence seems strongly related to the presence of many incommensurate frequencies. These frequencies are proportional to the eigenvalues of the hyperfine Hamiltonian and, hence, independent from the initial state.

Therefore, we focus in the following on the consequences of different configurations on the decoherence times for different numbers of nuclear spins. In principle, there are two relevant aspects concerning the positions of the nuclei, the absolute value of the envelope function $|\phi(\boldsymbol{r}_K)|^2$ at the site of the strongest coupling nuclear spin and the relative position of the nuclei with respect to each other. The importance of the former is obvious, since the envelope function sets the maximal energy scale A_K of the HI according to Eq. (1.24) and, consequently, rescales all times by a factor $|\phi(r_K)|^{-2}$. Therefore, if we want to analyze the

[3] For $K = 6$ we have extended the investigated time regime to $10^8\,\tau_{HI} \approx 100\,\text{ms}$ using the same time resolution ΔT in order to better understand the behavior of $\tilde{T}_D$ in Fig. 5.6.

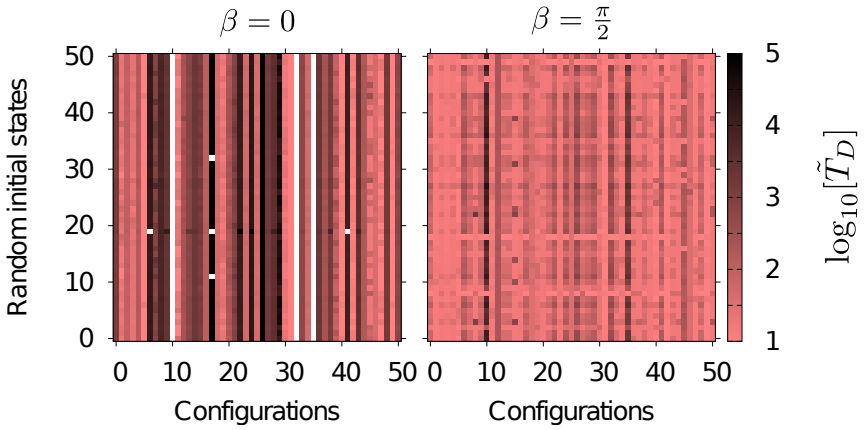

Figure 5.6. Normalized decoherence time $\tilde{T}_D$ as a function of 51 RC initial states and 51 random configurations for $K = 6$ nuclear spins in in-plane and out-of-plane orientation. Please note the logarithmic color scale of $\tilde{T}_D$. While the decoherence time is approximately the same for different initial states, it strongly depends on the configurations showing deviations over several orders of magnitude. White spaces indicate the total lack of decoherence up to absolute times of 0.1 s given a threshold of $C_S = -0.325$. For special configurations, $c = 10, 32$ and 35, and $\beta = 0$ there is no decoherence at all, but coherent oscillations of the electron spin. *Figure reprinted with permission from [105]. ©2013 American Physical Society. All rights reserved.*

influence of the relative positions, we have to measure the decoherence times T_D in units of $\tau_{\mathrm{HI}}^K = \hbar/A_K$, which yields dimensionless times $\tilde{T}_D = T_D/\tau_{\mathrm{HI}}^K$.

A color map of the normalized decoherence times for 51 initial states and 51 configurations is shown in Fig. 5.6. For the out-of-plane case, we find that the decoherence times are almost independent of the initial state, but vary over several orders of magnitude for different configurations. If we plot the normalized times as a function of the number of distinct eigenvalues, cf. Fig. 5.4, we find a direct connection between these times and the configuration of the nuclei in the dot shown in Fig. 5.7. As becomes clear from this figure, long decoherence times are only found for the discrete spectra, which are realized if only one nuclear spin strongly interacts with the electron. The configurations without any decoherence, which are indicated by white spaces in Fig. 5.6, exhibit discrete spectra with the minimal number of distinct eigenvalues of 3. An example of such a spectrum is shown in Fig. 5.4 (a). In this case, the dynamics of the electron spin are given by coherent oscillations. In contrast to this, short normalized decoherence times are a consequence of continuous spectra as presented in Fig. 5.4 (b). Thus, by the configurations studied, we can prove a direct relation between the relative positions of the nuclear spins and their relative coupling strengths, respectively, and the order of magnitude of the decoherence times. For the in-plane case, the qualitative picture is similar, however, with shorter normalized decoherence times over all, such that we find decoherence within the investigated times for all configurations. In contrast to the out-of-plane case, also discrete spectra can show rather short decoherence times for specific configurations. Altogether, this demonstrates a much faster decoherence due to the broken symmetry in the in-plane orientation.

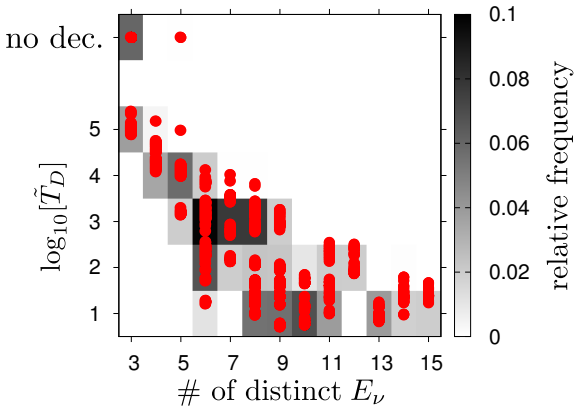

Figure 5.7. Normalized decoherence time $\tilde{T}_D$ as a function of the number of distinct eigenvalues E_ν of the HI Hamiltonian for $K = 6$ nuclear spins in out-of-plane orientation. For this plot all out-of-plane results presented in Fig. 5.6 are considered. Please note the logarithmic scale of $\tilde{T}_D$. The color scale encodes the relative frequency of the results within a rectangular determined by the decoherence time and the number of eigenvalues. For completeness, we plot cases exhibiting no decoherence within the investigated time interval at the top of this figure. *Figure adapted with permission from [105].*

Turning from normalized times to absolute decoherence times, the value of the envelope function $|\phi(r_K)|^2$ at the site of the strongest coupling nuclear spins additionally becomes relevant, since it sets the order of magnitude of all times. Putting a larger and larger number of nuclear spins on a QD of constant area increases the average value of $|\phi(r_K)|^2$, since it is more likely to find a spin very close to the center. Moreover, as we have discussed above, an increased number of nuclear spins K makes it much more likely to have several nuclear spins coupling almost equally to the electron spin. Altogether, this lets us generally expect a prominent decay of long decoherence times as a function of growing K, which is confirmed by Fig. 5.8. For $\beta = 0$ and very few nuclear spins $K = 3$, we find that the majority of decoherence times is longer than 10 ms, whereas very short T_D are almost completely irrelevant. For $K = 8$ this ratio of short and long times is inverse. In the in-plane orientation, long decoherence times make up only a small fraction even for few nuclear spins. Short decoherence times in the range of 5 μs to 500 μs are significantly increasing for more spins. Notably, ultra short times below 5 μs do not become much more important.

In summary, typical decoherence times are on the order of ms under ideal conditions of small nuclear spin numbers and out-of-plane orientation. In the case of such long decoherence times, of course, other effects like spin orbit coupling could become relevant. In the presence of acoustic phonons and small external magnetic fields, this spin orbit coupling [109, 170] can lead to spin relaxation times of $T_1 \sim 1$ ms below the decoherence times found here as discussed in Section 1.3.1. For larger numbers of nuclear spins and,

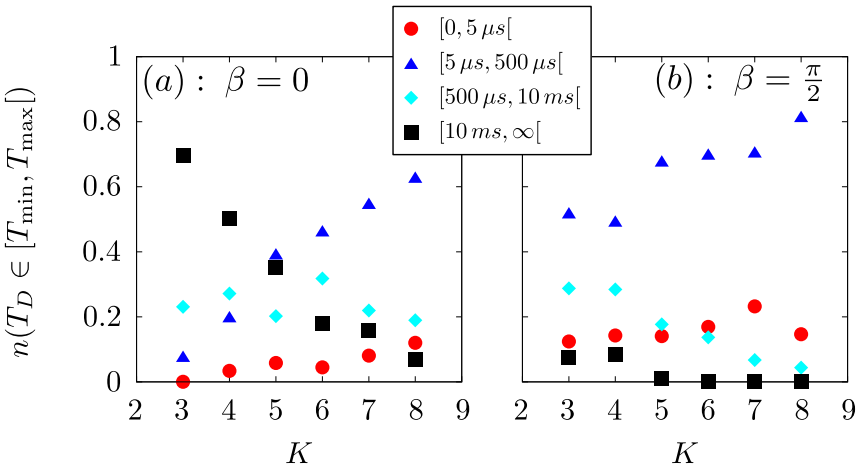

Figure 5.8. Relative number of absolute decoherence times T_D falling in a certain time interval $[T_{min}, T_{max}[$ for different numbers K of nuclei in in-plane and out-of-plane orientation. For each K 51 RC initial states and 51 configurations are considered leading to $N_{calc} = 2601$ calculations in total. (a): In the out-of-plane case, long decoherence times are clearly dominating for few nuclear spins. *Figure adapted with permission from [105]. ©2013 American Physical Society. All rights reserved.*

generally, for in-plane orientation, decoherence times are smaller, but still above 5 μs. Typical decoherence times of *GaAs* QDs under spin echo [171] lie in the $T_{2,echo} \sim 1\mu$s regime, whereas the current record of $T_{2,CPMG} \approx 200\,\mu$s was measured using the Carr-Purcell-Meiboom-Gill (CPMG) pulse sequence [172]. Pure dephasing times T_2^* are below 50 ns for *GaAs*. Although all our estimates for the decoherence times are done for a model without any effort to improve the coherence of the electron spin like pulse sequences or strong magnetic fields, in almost all considered cases, we are above the *GaAs* spin echo time $T_{2,echo}$. For smaller nuclear spin numbers, graphene even outperforms the CPMG time, which lets us expect very long decoherence times in graphene QDs when using pulse sequences.

5.4. Discussion and conclusion

Starting from a generic model of a graphene QD, we have studied the dynamics of the electron spin caused by the hyperfine interaction with the nuclear spins present in the dot. The number of nuclei has been varied from $K = 3$ to $K = 8$, where the upper limit corresponds to the natural abundance of spin carrying ^{13}C for the dot size considered in this work. Besides the role of the number of nuclei, we have also investigated the influence of the initial conditions as well as the impact of different configurations of the nuclei in the dot. Moreover, we have explored the consequences of the orientation of the spin quantization axis with respect to the graphene plane. In order to characterize and quantify these effects, we have analyzed both the long-time average $\langle \hat{S}_z \rangle_T$ of the z-component of electron spin and its decoherence time T_D.

Since nuclear spins are usually very hard to control in the envisioned experiments, we

have chosen the initial states to be random complex superpositions of single product states. For this class of initial states, we found an appreciable effect on the long-time average only in the case of very few nuclear spins. Upon increasing the number of nuclear spins, the effects of quantum parallelism and amplitude averaging [54, 74] reduce the differences between individual initial states more and more effectively. In this parameter regime, the results are dominated by the configuration of the nuclear spins within the dot, i.e., by their relative positions with respect to each other. For different configurations, the spectrum of eigenvalues of the hyperfine interaction varies from a highly discrete one with many degenerate eigenvalues to a continuous spectrum with many incommensurate frequencies.

For all K, a pronounced dependence of the long-time average on the orientation angle β between the spin quantization axis and the normal vector of the graphene plane was found. It saturates at approximately one-half of its initial value of $\langle \hat{S}_z \rangle_T \approx -\frac{1}{4}$ for $\beta = 0$ and at $\langle \hat{S}_z \rangle_T \approx 0$ in the in-plane case with $\beta = \frac{\pi}{2}$. While the long-time average of the electron spin is almost constant with respect to K, we have observed a strong reduction of fluctuations around it for larger nuclear spin baths. In contrast to the long-time average, the decoherence times T_D never exhibit a recognizable dependence on the initial states. Instead, the decoherence times depended decisively on the number of nuclear spins and their position in the QD. If only one nuclear spin is close to the center of the QD, long decoherence times have been observed, while a very fast decoherence results from several nuclei interacting equally strong with the electron spin. Moreover, the decoherence times show a strong dependence on the orientation of the quantization axis.

Although our results have been obtained for a specific model of the graphene quantum dot using a Gaussian envelope function, they can be generalized quite naturally. In our model, the QD was comparably small with a sharp boundary. This choice resulted in a steep envelope function. Physically, this situation corresponds approximately to an etched QD. Thinking of larger QDs with smoother boundaries, we expect a flatter envelope function which gives rise to more nuclear spins interacting comparably with the electron spin. Consequently, it becomes more likely to end up with rather low fluctuations around the long-time average and to find quite short decoherence times. In contrast, the realization of even smaller dots [53] with diameters of about 1 nm causes a very steep envelope function. This case should result in, at most, one nuclear spin interacting with the electron spin. Both scenarios seem experimentally interesting in order to engineer QDs for different applications. A ^{13}C enriched QD could potentially be used to prepare the electron spin very precisely in a certain superposition of spin up and down for subsequent experiments. A very small QD, in contrast, could serve as a storage for the electron spin where very long decoherence times are to be expected.

6. Equilibration in closed quantum systems: Applications to spin qubits

In the previous chapter, we have seen that the electron spin dynamics show a quasi-static behavior for long times, which is characterized by small fluctuations around a finite long-time average. Surprisingly, this long-time average shows no dependence on the number of nuclear spins in the investigated regime. The fluctuations, in contrast, clearly decrease with a larger size of the environment. From these observations, the question arises, in how far this behavior can be understood in terms of equilibration in closed quantum systems. The present chapter is dedicated to find an answer to this question. To this end, we consider a specific notion of equilibration in closed quantum systems and apply its predictions to numerical results, which have been obtained for a more general but related model as described in the previous chapter. The results presented in this chapter have been published in Ref. [173][1], whose text we closely follow.

6.1. Introduction

The theoretical understanding of the notion of equilibration in closed quantum systems has significantly developed in recent years [174, 175, 176, 177, 178, 179, 180, 181, 182]. In the absence of a thermal bath and the presence of quantum fluctuations, the classical concepts of the physical and mathematical description of equilibration do in general not work anymore [183]. Therefore, it is very important to first find a proper definition of equilibration in closed quantum systems. This difficult task is one of the driving forces of the research area of quantum thermodynamics. Useful concepts imply different definitions of equilibration. For instance, many authors identify equilibrium with the saturation of the expectation values of certain observables [178, 183, 184, 185, 186]. These ideas are appealing as they are intuitive and the relevant quantities are measurable. However, it is argued in Ref. [176], that this definition is not satisfying because the measurable probabilities of the outcomes of an observable may still be dynamical while its expectation values have saturated.

In this work, we start from a different concept [176, 177] of equilibration and link it to the above discussed idea of measuring expectation values. Doing so, we connect abstract definitions of quantum equilibration to spin dynamics in a QD. In our opinion, there are several aspects, which render solid state QDs a system suitable to study predictions related to quantum equilibration. First, as we discuss in Section 1.1, QDs offer a large variety of realizations, which differ, for instance, in their isotropic composition, the confinement of the electron spin and the number of nuclear spins in its environment. This flexibility

should allow us to investigate the influence of different parameters separately. Second, due to intensive experimental efforts over the past decade, there exists now a large set of methods to control both the electron and the nuclear spins. For further reading, we refer to Section 1.3.3, in which we discuss some of these means in more detail. Moreover, we also provide references to extensive review articles on further methods. These remarkable experimental achievements have been accompanied by intensive theoretical investigations, which should provide an excellent basis for the interpretation of future experiments. Some selected articles of the vast literature on these studies are presented at the beginning of Chapter 4. In summary, these properties of solid state QDs make us confident about their use to study quantum equilibration.

However, we first have to introduce a general theory of equilibration of a closed quantum system that fulfills all the requirements of the realization that we have in mind. This will be done on the basis of the *distinguishability* [176, 177] which is a measure to distinguish the actual state of a quantum system from its equilibrium state on the basis of a finite set of observables. If the values of the distinguishability are on average smaller than a given reference value ε we argue that the quantum system is ε-equilibrated. In order to connect our concept of equilibration with experimentally measurable predictions, we first relate the distinguishability with the *weak distinguishability*, [176, 178, 182] which offers an equivalent description of equilibration for two-outcome observables. The time-averaged weak distinguishability (TAWD), however, is capable to introduce an upper bound on the variances of expectation values. We have analytically derived certain limits for the TAWD, which depend on the Hamiltonian and the initial state of the quantum system. As a consequence, our analytical equilibration bounds for the TAWD should directly affect the experimentally determined variance of the measurement operator. Therefore, it should be possible to modify the system at hand such that the bounds are varied and to see the difference in a direct measurement of the variance. With this prediction at hand, we eventually try to better understand quantum equilibration by looking at our central spin model mentioned above. In order to calculate the TAWD, we treat very simple observables like the electron spin operator in direction parallel or perpendicular to an external magnetic field. Since we employ exact diagonalization for this calculation, we are limited to a finite number of nuclear spins. However, in state of the art QDs based on silicon or carbon host materials, such numbers of nuclear spins are within experimental reach as described in Section 1.1.

As a consequence of our approach to equilibration in closed quantum systems, this chapter is roughly divided into two major parts. First in Section 6.2, we explain the notion of equilibration employed in this work and introduce the (weak) distinguishability used to describe it. Subsequently, in Section 6.3, we will derive analytical results of equilibration bounds. Some derivations are presented in Appendix C. In Section 6.4, these general results are then compared to a central spin model of an electron spin in a QD coupled to a quantum environment of nuclear spins.

6.2. Basic concepts of equilibration

In this section, we briefly describe known concepts of quantum equilibration for future reference. We consider a closed quantum system whose state $\hat{\rho}(t)$ evolves according to the von Neumann equation $\dot{\hat{\rho}}(t) = \frac{\mathrm{i}}{\hbar}[\hat{\rho}(t), \hat{H}]$ where $\hat{H}$ is the d dimensional Hamiltonian of the total system $\mathcal{H}$. Due to the unitary time evolution, each finite quantum system obeys a recurrence time $T_R > 0$, at which the state of the system approaches within some accuracy its initial state. However, this time does not play a role in most experiments as it scales exponentially [144] with the dimension of $\mathcal{H}$ and is almost always much larger than the age of the universe. With the commonly used and well-defined time-averaged state [176, 178]

$$\hat{\omega} = \langle \hat{\rho} \rangle_\infty = \lim_{t\to\infty} \langle \hat{\rho} \rangle_t \tag{6.1}$$

one circumvents recurrence problems. Throughout this chapter, $\langle f \rangle_t = \frac{1}{t}\int_0^t \mathrm{d}t'\, f(t')$ is used to denote time averages. This time-averaged state can be considered as an equilibrium state for several reasons. First, it does not evolve in time as $[\hat{\omega}, \hat{H}] = 0$. More importantly, if the expectation value $O(t) := \mathrm{Tr}[\hat{O}\hat{\rho}(t)]$ of any observable $\hat{O}$ saturates at some value for long times, it can be calculated by $\langle O \rangle_\infty = \mathrm{Tr}[\langle \rho(t) \rangle_\infty \hat{O}] = \mathrm{Tr}[\hat{\omega}\hat{O}]$. In contrast to thermal states like the Gibbs state, $\hat{\omega}$ generally depends on the initial state.

Analogously to earlier works [176, 177, 178], we regard a quantum mechanical system to be in equilibrium if one cannot distinguish between the state $\hat{\rho}(t)$ of the full system and its equilibrium state $\hat{\omega}$ for most times by applying a finite set of measurements $\Omega = \{\hat{O}_i\}$. These measurements are not restricted to subspaces of the whole Hilbert space. Hence, this definition does not rely on the subdivision of the full quantum system into a small, measurable system and a large, not measurable environment. The restriction to a finite set reflects the conditions of realistic experiments. Let us consider an observable $\hat{O} = \sum_j o_j \hat{P}_j$, which is generally defined by its eigenvalues o_j and the projectors $\hat{P}_j$ onto the respective subspaces. Considering the above notion of equilibration and the limited number of measurements, Short [176] has introduced the distinguishability

$$d_\Omega(\hat{\rho}(t), \hat{\omega}) = \max_{\hat{O}\in\Omega} \frac{1}{2} \sum_j |\mathrm{Tr}[\hat{P}_j \hat{\rho}(t)] - \mathrm{Tr}[\hat{P}_j \hat{\omega}]| \,. \tag{6.2}$$

as a proper measure of distance between $\hat{\rho}(t)$ and $\hat{\omega}$. Mathematically, it is closely related to the trace distance, but considers the finite number of accessible measurement operators. In contrast to the trace distance, however, this measure is not a metric, but a semi-metric since $d_\Omega(\hat{\rho}(t), \hat{\omega}) = 0$ is possible for $\hat{\rho}(t) \neq \hat{\omega}$. This behavior is important, because it permits the desired property of equilibrated states: A sufficient condition for equilibrium is that one is not capable to distinguish the state of the system $\hat{\rho}(t)$ from $\hat{\omega}$ for most times by the set Ω of measurements.

In order to account for the fact that the state of the system must be indistinguishable for most times during the time evolution, one can demand the time-average of the positive quantity $d_\Omega(\hat{\rho}(t), \hat{\omega})$ to be small [176]. Consequently, we regard a system to be ε-equilibrated at time t if

$$\langle d_\Omega(\hat{\rho}(t), \hat{\omega}) \rangle_t < \varepsilon \,, \tag{6.3}$$

where ε is a small positive constant, which we are free to choose. A reasonable choice for this constant is, for instance, the precision of the measurement devices in an experiment. Further, we call systems equilibrating in a time interval I if the time-averaged distinguishability $\langle d_\Omega(\hat{\rho},\hat{\omega})\rangle_t$ decreases on average within I.

By introducing the distinguishability and its time average in Eq. (6.3), we achieved a suitable mathematical definition of our concept of equilibration. However, the distinguishability cannot be measured directly in an experiment. Yet, with a slight modification of the distinguishability, one can find the so-called weak distinguishability [176, 178, 180, 182]

$$D_{\hat{O}}(t) = \Big(\mathrm{Tr}[\hat{\rho}(t)\hat{O}] - \mathrm{Tr}[\hat{\omega}\hat{O}]\Big)^2 . \tag{6.4}$$

This quantity is unlike the distinguishability $d_\Omega(\hat{\rho}(t),\hat{\omega})$ only given by the expectation values of $\hat{O}^2$ with respect to both $\hat{\rho}$ and $\hat{\omega}$, but does not depend on the probabilities to measure individual eigenvalues. Hence, the weak distinguishability carries the same unit as the squared measurement operator and takes values between 0 and $4\|\hat{O}\|^2$, where $\|\hat{O}\|$ is the spectral norm[3] of $\hat{O}$. As we will show below, the long-time average of the weak distinguishability can be identified with the variances of the observable, which can be determined in an experiment. A small time-averaged weak distinguishability (TAWD) $\langle D_{\hat{O}}\rangle_t < \varepsilon' \ll \|\hat{O}\|^2$ is a necessary condition for $\langle d_{\hat{O}}(\hat{\rho}(t),\hat{\omega})\rangle_t < \varepsilon \ll 1$ and, hence, according to Eq. (6.3) for the system to be in equilibrium. If two-outcome measurements $\hat{O} = o_1\hat{P}_1 + o_2\hat{P}_2$ with $o_1 \neq o_2$ and $\hat{P}_1 + \hat{P}_2 = \mathbb{1}_d$ are considered, both quantities are even equivalent as they are then related to each other by

$$D_{\hat{O}}(t) = (o_1 - o_2)^2[d_{\hat{O}}(\hat{\rho}(t),\hat{\omega})]^2. \tag{6.5}$$

However, for general measurements, it is not sufficient that the expectation value of a observable saturates, since $\rho(t)$ and ω can still be distinguished by the (experimentally) measurable probabilities $\mathrm{Tr}[\hat{\rho}(t)\hat{P}_j]$ of its eigenvalue o_j. Rather each of these time-depend probabilities has to saturate in order to guarantee indistinguishability, which is taken into account by the distinguishability $d_{\hat{O}}(\hat{\rho}(t),\hat{\omega})$. In Fig. 6.1, we summarize these dependencies and the connection to equilibrium. As a last property of the TAWD, we show in Appendix C.1 that the TAWD

$$\langle D_{\hat{O}}\rangle_t = \Delta_{\hat{O}} + \delta_{\hat{O}}(t) \tag{6.6}$$

is separable in a time-independent part $\Delta_{\hat{O}}$ and a time-dependent part $\delta_{\hat{O}}(t)$, which decreases at least with $\delta_{\hat{O}}(t) = \mathcal{O}(t^{-1})$ for $t \to \infty$. This behavior will play an important role for relating the TAWD to measurable quantities in the next section.

[2] As the distinguishability can only become small if $\hat{\rho}$ and $\hat{\omega}$ cannot be distinguished by any $\hat{O} \in \Omega$, we will study the contribution a single but arbitrary observable $\hat{O}$

[3] For a Hermitian operator such as an observable $\hat{O}$, the spectral norm $\|\hat{O}\| = \max_j(|o_j|)$ is equal to the largest absolute value of its eigenvalues λ_j.

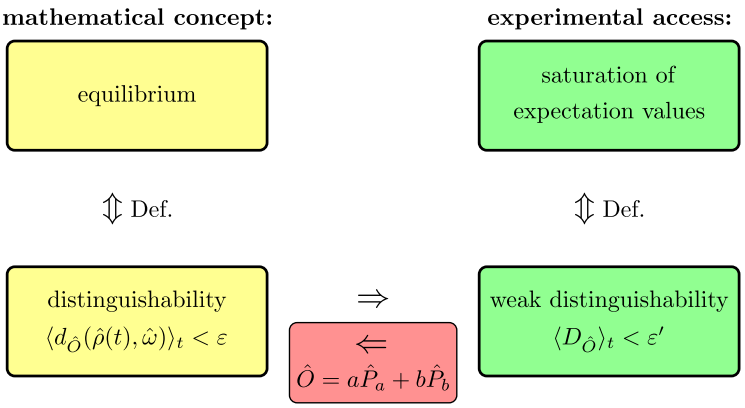

Figure 6.1. Relation between equilibrium, distinguishability, weak distinguishability, and expectation values. For clarity within this figure, we assume that only one observable $\hat{O}$ is measurable, i. e., $\Omega = \{\hat{O}\}$. If $\hat{O}$ is a measurement with only two possible outcomes $a \neq b$, the weak distinguishability is equivalent to the distinguishability. Therefore, saturated expectation values are then a necessary and sufficient condition for equilibrium. *Figure reprinted with permission from [173].*

6.3. Equilibration bounds

Weak distinguishability *vs.* variance

As argued above, the TAWD is a useful quantity to describe equilibration in closed quantum systems. Moreover, it is directly related to measurable properties of the system under consideration. As we explicitly derive in Appendix C.2, the variance $\mathrm{Var}_{\hat{O}}(t,\Delta t)$ of expectation values $O(t')$ in a time interval $t' \in I = [t, t+\Delta t]$ is bounded by

$$\mathrm{Var}_{\hat{O}}(t,\Delta t) \leq \langle D_{\hat{O}}\rangle_t, \tag{6.7}$$

where the size Δt of the time interval I needs to be sufficiently large. More precisely, Δt must be of such a size, that $\langle D_{\hat{O}}\rangle_t$ does not increase on average within I. The above estimate turns into an equality if $\langle D_{\hat{O}}\rangle_t$ is constant within I. According to Eq. (6.6), this is the case for each system and all observables at long times because the TAWD converges. Consequently, its infinite-time limit

$$\Delta_{\hat{O}} = \lim_{t\to\infty} \langle D_{\hat{O}}\rangle_t = \lim_{t\to\infty} \mathrm{Var}_{\hat{O}}(t,\Delta t) \tag{6.8}$$

equals the variance of expectation values in any time interval I at long times. Since the time-dependent part $\delta_{\hat{O}}(t)$ can decay much faster than $\mathcal{O}(t^{-1})$, this saturation will be already reached within finite times for many systems. The quantity $\Delta_{\hat{O}}$ describes the variance of expectation values of $\hat{O}$ arising from the fluctuations within the finite quantum system. It is, however, not related to possible measurement errors. Hence, $\Delta_{\hat{O}}$ also quantifies the capability of the system to equilibrate with respect to $\hat{O}$. The smaller $\Delta_{\hat{O}}$, the less fluctuations of the expectation values of $\hat{O}(t)$ around $\mathrm{Tr}[\hat{\omega}\hat{O}]$ are present.

Useful equilibration bounds at large times

As we elaborately show in Appendix C.3, the long-time values of the TAWD can be estimated in different manners giving rise to the bounds

$$\Delta_{\hat{O}} \leq \widetilde{\Delta}^1_{\hat{O}} := N_{\mathrm{G}} \|\hat{\rho}\|^2 \mathrm{Tr}[\hat{O}^2]\,, \tag{6.9}$$

$$\Delta_{\hat{O}} \leq \widetilde{\Delta}^2_{\hat{O}} := N_{\mathrm{G}} \|\hat{O}\|^2 \mathrm{Tr}[\hat{\rho}^2]\,, \tag{6.10}$$

$$\Delta_{\hat{O}} \leq \widetilde{\Delta}^3_{\hat{O}} := N_{\mathrm{G}} \frac{\|\hat{O}\|^2}{d_{\mathrm{eff}}}\,. \tag{6.11}$$

Before we discuss and compare these findings, let us explain the quantities they depend on. First, in all bounds the maximum degeneracy N_{G} of gaps in the energy spectrum of the Hamiltonian enters, whose size is, hence, crucial for them to be of reasonable magnitude. Note that it is not sufficient to have a non-degenerate spectrum of eigenvalues in order to reach $N_{\mathrm{G}} = 1$.[4] The properties of the observable enter the equations via $\|\hat{O}\|$ and $\mathrm{Tr}[\hat{O}^2]$, which are related to each other by $\|\hat{O}\|^2 \leq \mathrm{Tr}[\hat{O}^2] \leq \|\hat{O}\|^2 \operatorname{rank} \hat{O}$.[5] The bounds also take into account different initial states $\hat{\rho}$. Explicitly, $\mathrm{Tr}[\hat{\rho}^2]$ is its purity and $\|\hat{\rho}\|$ is the maximum eigenvalue of the initial state, where $\mathrm{Tr}[\hat{\rho}^2], \|\hat{\rho}\| \geq d^{-1}$ are bounded from below by the inverse of the dimension. Moreover, the initial state also determines the size of the so-called effective dimension [176] d_{eff}, which is defined by $d_{\mathrm{eff}}^{-1} = \sum_j (\mathrm{Tr}[\hat{E}_j \hat{\rho}])^2$ with $\hat{E}_j$ being the projector onto the eigenspace of energy E_j. Vividly, d_{eff} quantifies the dimension of the Hilbert space that is actually reached during the time evolution. It takes values between 1 and d. The latter is the case for the totally mixed state $\hat{\rho} = \frac{1}{d}\mathbb{1}$ or for pure states such as $|\psi\rangle = \frac{1}{\sqrt{d}} \sum_j |E_j\rangle$.

Due to the last property of d_{eff}, the third estimate $\widetilde{\Delta}^3_{\hat{O}}$, which has previously been found in Ref. [177] with a different approach, is the most restrictive bound if pure initial states are considered. The other two estimates are useful for mixed states as both $\|\hat{\rho}\|$ and $\mathrm{Tr}[\hat{\rho}^2]$ become small if the state $\hat{\rho}$ is mixed. The advantage of $\widetilde{\Delta}^2_{\hat{O}}$ is that the quantity $\mathrm{Tr}[\hat{\rho}^2]$ is independent of the basis whereas one needs to know all eigenstates and eigenvalues of $\hat{H}$ in order to calculate d_{eff}. The bound $\widetilde{\Delta}^1_{\hat{O}}$ is more restrictive than $\widetilde{\Delta}^2_{\hat{O}}$, $\widetilde{\Delta}^3_{\hat{O}}$, and previously found estimates [176, 178], if

$$d_{\mathrm{eff}} \, \|\hat{\rho}\|^2 \operatorname{rank} \hat{O} \leq 1\,. \tag{6.12}$$

This is the case if the rank of $\hat{O}$ is small while the mixture of the initial state $\hat{\rho}$ is high, since d_{eff} scales as d for very mixed states while $\|\hat{\rho}\|^2$ scales as d^{-2}.

Generalization to finite times

So far we have focused on the behavior of the TAWD for long times. However, according to Eqs. (6.6) and (6.7), we can even give estimates for finite times provided that one can bound the time-dependent part $\delta_{\hat{O}}(t)$. As we have discussed, $\delta_{\hat{O}}(t)$ is at least decaying as t^{-1} in the long-time limit. In a recent analysis, L. P. García-Pintos and coworkers [182]

[4] For instance, although each eigenvalue $E_n = \hbar\omega(n + \frac{1}{2})$ of a one-dimensional harmonic oscillator is non-degenerate, the gap $\hbar\omega$ is infinite-times degenerate.

[5] The rank of a hermitian matrix equals the number of its non-zero eigenvalues.

have derived many interesting properties of the TAWD. Among other things, the authors have bounded the time dependent part of the TAWD by $\delta_{\hat{O}}(t) \leq \frac{L}{t}$ for all times, where L is a constant that dependents on $\hat{\rho}$, $\hat{H}$, and $\hat{O}$. Thus, we can estimate the variance of expectation values around the long-time average $\mathrm{Tr}[\hat{\omega}\hat{O}]$ within any time interval $[t, t+\Delta t]$ by

$$\mathrm{Var}_{\hat{O}}(t, \Delta t) \leq \langle D_{\hat{O}} \rangle_t \leq \frac{L}{t} + \min_i \widetilde{\Delta}^i_{\hat{O}}. \tag{6.13}$$

The infinite-time bounds $\widetilde{\Delta}^i_{\hat{O}}$ are given in Eqs. (6.9) to (6.11). If one of the $\widetilde{\Delta}^i_{\hat{O}}$ is a small number and $\hat{O}$ is a two-outcome measurement, then the system will equilibrate in the way defined in Section 6.2. In that sense, $\widetilde{\Delta}^i_{\hat{O}}$ gives an estimate for the ability of a closed quantum system to equilibrate. Regardless of a specific notion of equilibration, the above bounds always estimate the variances of observables in any closed system.

6.4. Application to spin models

6.4.1. Definition of the model

In this section, we apply the general concepts of equilibration explained above to the dynamics of an electron spin in a QD. This allows us to show the physical significance of the above ideas for experiments. Besides the hyperfine interaction (HI) defined in Eq. (1.28) between the electron spin and the nuclear spins, we consider an external magnetic field, which is commonly used to split the Zeeman levels of the spins according to Eqs. (1.9) and (1.10). For convenience, we measure all spin operators in the reference frame defined by the graphene plane such that $\beta = 0$ and (x, y, z) coincides with (x', y', z') in Fig. 1.5. By means of isotopic purification, it is possible to manipulate the number of nuclear spins present in the QD, which in turn allows to probe the influence of the system size on our bounds in Eqs. (6.9) to (6.11). In the following, we are especially interested in how the nuclear spins will equilibrate the electron spin. Since the observables of the electron spin $\hat{S}_{x,y,z}$ all have two outcomes, the distinguishability and the weak distinguishability are equivalent according to Eq. (6.5). The saturation of the expectation values of spin operators, hence, corresponds to the equilibration of the full system—given that they are the only accessible measurements.

After these general considerations, let us introduce the total Hamiltonian $\hat{H} = \hat{H}_{\mathrm{HI}} + \hat{H}_{\mathrm{ZE}}$ describing our model in more detail. Although our qualitative results are independent of this choice, we choose a graphene QD as a reference in order to benefit from the results of Chapter 5. Then, the HI Hamiltonian is given by

$$\hat{H}_{\mathrm{HI}} = \sum_{k=1}^{K} A_k \left[\hat{S}_z \hat{I}_{k,z} - \frac{1}{4}(\hat{S}_+ \hat{I}_{k,-} + \hat{S}_- \hat{I}_{k,+})\right] \tag{6.14}$$

according to Eq. (1.28), where the coupling constants are defined in Eq. (1.24). The strongest HI coupling A_K defines the characteristic time $\tau^K_{\mathrm{HI}} = \hbar/A_K$. Whenever we average over different initial conditions, we maintain a maximum ratio of $A_k/A_j < 100$ for all k, j. For qualitative results, we present the results for an exemplary set of coupling constants as we have found similar results for many randomly generated sets of coupling

constants. The effect of an external magnetic field B_z is described by the Zeeman Hamiltonian

$$\hat{H}_{\mathrm{ZE}} = A^S_{\mathrm{ZE}}\hat{S}_z + A^I_{\mathrm{ZE}}\sum_{k=1}^{K}\hat{I}_{k,z} = b\,A_K\,(\hat{S}_z - \frac{1}{\kappa}\sum_{k=1}^{K}\hat{I}_{k,z})\,, \tag{6.15}$$

where $b = A^S_{\mathrm{ZE}}/A_K$ is the electron Zeeman splitting in units of the strongest HI coupling and $\kappa = A^S_{\mathrm{ZE}}/A^I_{\mathrm{ZE}}$ is the ratio of the electron and nuclear Zeeman energies, which is $\kappa \approx 2.5 \times 10^3$ for graphene.

Besides the Hamiltonian, the time evolution of observables depends on the initial state $\hat{\rho}$. In the following, we choose a product state $\hat{\rho} = \hat{\rho}_S \otimes \hat{\rho}_{\mathrm{nuc}}$, where $\hat{\rho}_S = |\psi_S\rangle\langle\psi_S|$ and $\hat{\rho}_{\mathrm{nuc}}$ describe the initial states of the electron and nuclear spins, respectively. The absence of entanglement between the electron spin and the nuclear spins is plausible since the initial state of the electron spin can be experimentally well prepared in a pure (polarized) state as described in Section 1.3.3. The nuclear spins, however, will on average be in an unpolarized state if no further efforts are undertaken in an experiment. Since experimentally relevant temperatures are on the order of mK to K [9, 24], the thermal energy exceeds all other energy scales of the nuclear spins by far. In order to follow the time evolution of the electron spin, however, many repetitions of the experiment are needed. Since each of these runs start with a different initial state due to the thermal fluctuations, the nuclear spin state can be described by a totally mixed state $\hat{\rho}_{\mathrm{nuc}} = \mathbb{1}/2^K$ on average. However, the nuclear spin state can be also manipulated by means of dynamical nuclear polarization (DNP) and state narrowing (SN), cf. Section 1.3.3, which allow to significantly polarize the nuclear spins and to change the composition of their initial state. Motivated by these experimental possibilities, we additionally investigate the effect of polarized initial states of the nuclear spins.

With both, the Hamiltonian and the initial state given, the time evolution of the density matrix and, hence, of every observable in the system can be calculated by exact diagonalization as described in Section 2.2.1, which is performed using the EIGEN [169] package for C++.

6.4.2. Spin dynamics

Once the time evolution of an observable is known, its variance, the weak distinguishability and the TAWD defined in Sec. 6.2 are readily calculated. This enables us to demonstrate, that the TAWD indeed bounds the variances of an observable. As an example, we show the evolution of $\langle\hat{S}_x\rangle(t)$ in Fig. 6.2. At times $t \sim \tau^K_{\mathrm{HI}}$, the initially polarized electron spin begins to oscillate with decreasing amplitude around its long-time average $\langle S_x\rangle_\infty \approx 0$. The square root of the weak distinguishability $\sqrt{\langle D_{\hat{S}_x}\rangle_t}$ bounds the standard deviation of $\langle\hat{S}_x\rangle(t)$ as predicted at all times. At large times, the TAWD $\langle D_{\hat{S}_x}\rangle_t$ saturates at a finite value whose size corresponds to the quantum fluctuations in our finite model. As explained above, the TAWD in turn can be bounded itself by the analytical expression given in Eq. (6.13). For finite times, this bound decays with $\mathcal{O}(t^{-1})$, while it saturates at $\widetilde{\Delta}^2_{\hat{S}_x}$ given in Eq. (6.10) for large times. For the parameters chosen in Fig. 6.2, we find $\widetilde{\Delta}^2_{\hat{S}_x} = 2^{-(K+1)}$, where we have used Eq. (6.10) with $N_G = 1$, $\mathrm{Tr}[\hat{\rho}^2] = \frac{d}{2}(\frac{2}{d})^2$, $\|\hat{S}_x\|^2 = \frac{1}{4}$, and $d = 2^K$. Remarkably, already for $K = 6$ nuclear spins, this long-time estimate yields

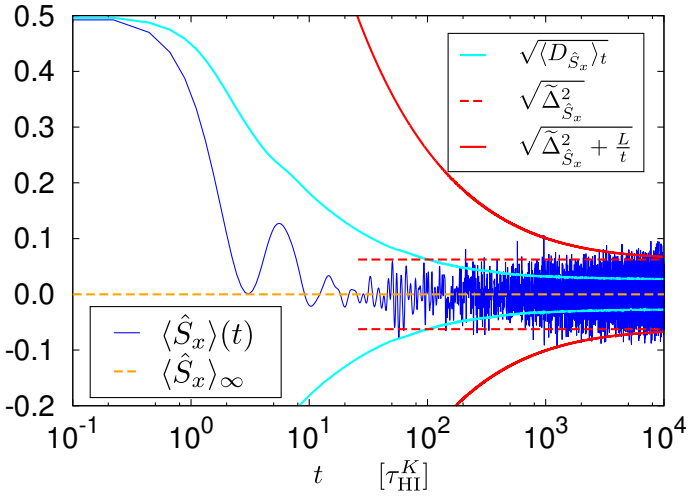

Figure 6.2. The time evolution of the electron spin component $\langle \hat{S}_x \rangle(t)$ and its long-time average $\langle \hat{S}_x \rangle_\infty$. We use a magnetic field $b = \frac{1}{4}$ and $K = 6$ nuclear spins with random coupling constants. Initially, the electron spin is maximally polarized in x-direction while the nuclear spins are in the totally mixed state. The square root of the TAWD $\sqrt{\langle D_{\hat{S}_x} \rangle_t}$ bounds the standard deviation of $\langle \hat{S}_x \rangle(t)$ for all times and converges to it for large times. The apparent increase of the fluctuations is a consequence of the logarithmic presentation of the data, which highlights large spikes. For comparison, we plot the analytically derived bounds given in Eq. (6.13) and Eq. (6.10). All quantities are dimensionless. *Figure adapted with permission from Ref. [173].*

a very sharp upper bound on the standard deviation of fluctuations of the signal.

As explained above, the properties of the TAWD and its bounds depend on the Hamiltonian of the system. Thus, one should test how different Hamiltonians alter the equilibration. In a QD, the easiest way to change the Hamiltonian is to modify the external magnetic field. By varying b over approximately two orders of magnitude, we sweep from a situation in which the electron spin couples most strongly to the nuclear spins to a scenario where the Zeeman coupling is dominant. In Fig. 6.3, we compare the TAWDs of $\hat{S}_x$ and $\hat{S}_z$ for different b. For both spin components, we observe that equilibration sets in approximately at the time τ_{HI}^{K} and reduces the initial values of the TAWDs roughly by two orders of magnitude for all values of b. As we discuss later, the size of this reduction depends on the number of nuclear spins. In fact, even high values of b cause only Lamor oscillations of $\hat{S}_x$ at small times $\tau_{\mathrm{ZE}}^{S} \propto b$, but do not change the overall equilibration behavior. Besides this, the only effect of large magnetic fields is a reduced initial value of the TAWD for $\hat{S}_z$. This can be understood as follows. As the electron spin is initially fully polarized parallel to a strong magnetic field, its initial state is almost fully preserved, since the flip-flop terms of the HI are suppressed due to the large Zeeman splitting of the electron spin states. In other words, the electron is initially approximately in an eigenstate of the total Hamiltonian for strong external magnetic fields. Hence, $\hat{\rho}$ is already initially close to $\hat{\omega}$ and, as a consequence, indistinguishable from $\hat{\omega}$ by means of $\hat{S}_z$. Similar effects can be found for polarized states, which we approximate by a Gaussian distribution of states characterized by a mean polarization $\bar{p}$ and a standard deviation σ_p. First, we

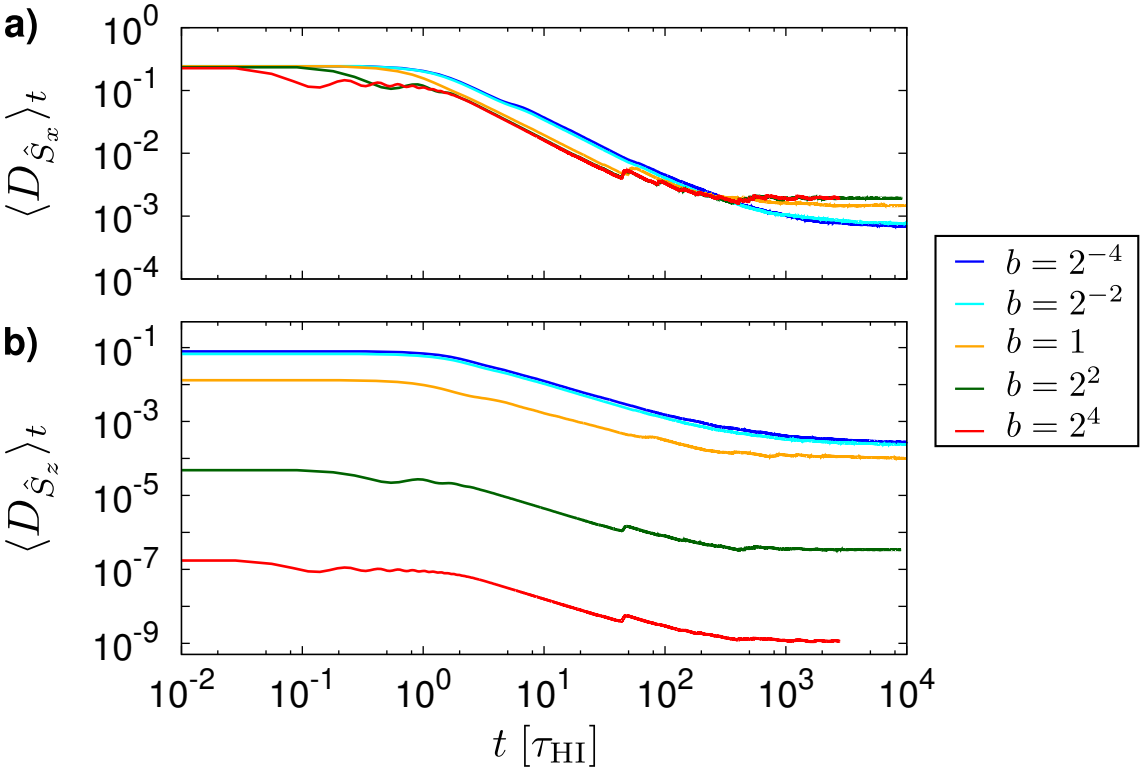

Figure 6.3. The TAWD as a function of time for different external magnetic fields b in z-direction for **a)** $\hat{S}_x$ and **b)** $\hat{S}_z$. The electron spin is initially polarized in x- and z-direction, respectively. Apart from that, the same parameters as in Fig. 6.2 have been used. **a)** All TAWDs start with the same value and show oscillations on a timescale $\tau^S_{\mathrm{ZE}} \propto b$. The actual equilibration starts at τ^K_{HI}. **b)** The TAWDs start with a different value for different b. The equilibration due to the HI also starts at τ^K_{HI}. *Figure reprinted with permission from [173].*

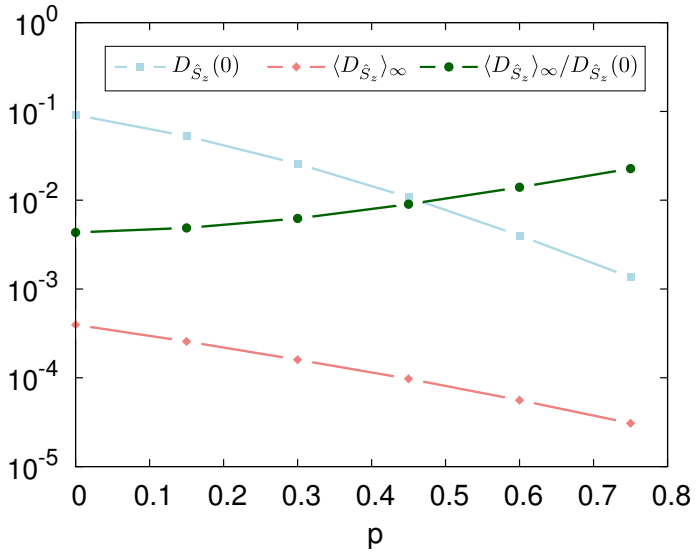

Figure 6.4. Dependence of the weak distinguishability on the mean polarization $\bar{p}$ of the nuclear spin bath for a distribution of states with standard deviation $\sigma_p = 0.3$. Both the initial weak distinguishability $D_{\hat{S}_z}(0)$ and its long-time average $\langle D_{\hat{S}_z}\rangle_\infty$ decrease for a larger polarization. However, their ratio $\langle D_{\hat{S}_z}\rangle_\infty / D_{\hat{S}_z}(0)$ increases as a function of p.

have fixed $\sigma_p = 0.3$ and varied the mean polarization between $p = 0$ and $p = 0.75$ for a system containing $K = 6$ nuclear spins as shown in Fig. 6.4. Since the initial states approach eigenstates of the total Hamiltonian for increasing polarization, we observe a decreasing initial distinguishability $D_{\hat{S}_z}(0)$. Due to the HI, the TAWD $\langle D_{\hat{S}_z}\rangle_\infty$ saturates again around a value, which is about two orders of magnitude smaller than its initial size. For larger polarizations this reduction becomes smaller, since the HI spin flip-flops become less effective. These findings are consistent with a smaller effective dimension d_{eff} of polarized initial states in Eq. (6.11). Analogous simulations with standard deviations in an interval $0.15 < \sigma_p < 0.75$ show no significant differences to these observations.

6.4.3. Dependence on the size of the nuclear spin environment

We finally want to address the question how many nuclear spins are required in order to treat them effectively as a large environment. By adding more and more nuclear spins, no sudden change is observed but the fluctuation of spin components of the electron decrease exponentially with the number of nuclear spins, cf. Fig. 6.5.

The numerically obtained values of the long-time TAWD are about one order of magnitude smaller than the presented bound $\widetilde{\Delta}^2_{\hat{S}_z}$. Fig. 6.5 also suggests that quantum fluctuations may decrease even faster with increasing system size than our analytic bounds require. Note that this K-dependence of the equilibration properties is not limited to mixed states only. Reconsidering the data obtained in Chapter 5, we have calculated the effective dimension for these randomly chosen pure initial states. For these states, it scales approximately with $d_{\text{eff}} \sim d/2 = 2^K$. According to $\widetilde{\Delta}^3_{\hat{S}_z} \propto d_{\text{eff}}^{-1} = 2^{-K}$ given in Eq. (6.11), this dependence also gives rise to an exponential decay of $\langle D_{\hat{S}_z}\rangle_\infty$, which is confirmed

by the results of Chapter 5. As discussed by Reimann [178], the effective dimension of almost all states grows exponentially with the size of the system. Hence, such a decay is a rather generic result, which can be understood as follows. If we add a nuclear spin to the system, we double both the size of the Hilbert space and the number of energies driving the dynamics of the electron spin, which finally leads to the observed reduction of fluctuations.

We can indeed generalize these findings to other quantum systems that differ from our model, e.g., a central spin model with isotropic hyperfine interaction or even more distinct models like spin chains. Assuming that the effective dimension $d_{\text{eff}} \sim d$ scales exponentially with the number K of nuclear spins, we can use Eq. (6.11) to find the number $\tilde{K}$ of nuclear spins that is sufficient to reduce the fluctuations of the electron spin below resolution of the measurement apparatus. If we set $d_{\text{eff}} = c\,d$, this number is given by

$$\tilde{K} \geq \log_2 \left(N_G \|O\|^2 \frac{1}{c} \frac{1}{r^2} \right) , \tag{6.16}$$

where $c \in \mathbb{R}$. Interestingly, it increases only logarithmically with the inverse resolution $1/r$. For instance, assuming a resolution $r = 0.01$ of the measurement of the electron spin and an initial state far away from an energy eigenstate ($c \to 1$), the electron spin components equilibrate in any quantum model with (almost) non-degenerate gaps ($N_G = O(1)$) if the electron is coupled to more than 11 bath spins. As our model demonstrates, even less bath spins $\tilde{K} \approx 7$ are capable of equilibrating the electron spin components below this resolution in experimentally relevant scenarios.

6.5. Discussion and conclusion

In summary, we have shown how a general theory on equilibration can be applied to a realistic closed quantum system. We have introduced a specific understanding of equilibration relevant for our system under consideration and analyzed its properties by analytical calculations. Afterwards, we have applied this concept to a model of electron and nuclear spins in a solid state QD, which we have investigated by numerical simulations.

A system is assumed to be in equilibrium, if an observer cannot distinguish, for most times, between the actual state of the system and its equilibrium state using a finite set of measurements. Notably, two observers with different measurement sets could come to different conclusions. This equilibrium state is not necessarily a thermal state since it can, for instance, depend on the initial state of the system. The distinguishability between the state of the system and its equilibrium state can be quantified by a suitable "measure of distance". We consider the so-called weak distinguishability which vanishes whenever the system is in equilibrium. For two-outcome measurements, we have been able to show that a saturation of the corresponding expectation values is equivalent to equilibration. Furthermore, we have demonstrated how the variance of a time-dependent observable can be bounded by this weak distinguishability, which has allowed us to connect this abstract mathematical function to an experimentally measurable quantity. We have also derived three different bounds for the time-averaged weak distinguishability and thereby recovered one previously known bound by means of a new method [176]. We have therefore been able to predict upper limits to the size of fluctuations in small closed quantum systems.

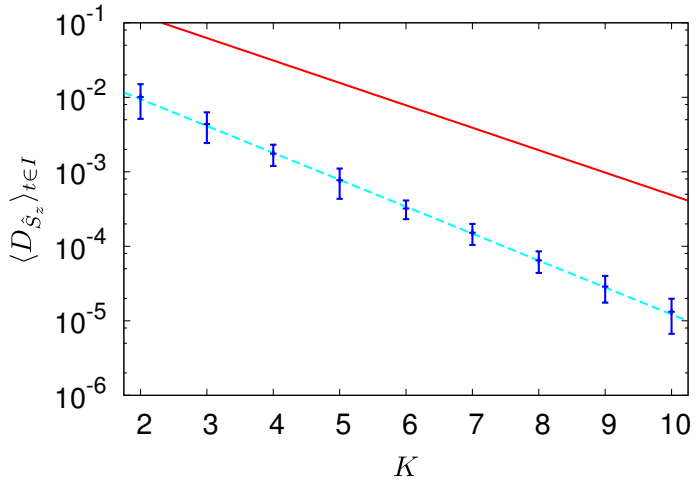

Figure 6.5. Dependence of the long-time TAWD for the observable $\hat{S}_z$ on the number of nuclear spins K. We approximate $\langle D_{\hat{S}_z} \rangle_\infty$ by $\langle D_{\hat{S}_z} \rangle_{t \in I}$, where $I = [\tau, \tau + \Delta\tau]$ is a time interval with $\tau \gg \Delta\tau \gg \tau_{\mathrm{HI}}^K$. The numerical data is compared to the analytical bound $\widetilde{\Delta}^2_{\hat{S}_z}$ (solid line) given in Eq. (6.10). The fit (dashed line) suggests a $\langle D_{\hat{S}_z} \rangle_\infty \sim 2^{-1.2K}$ dependence. We average over at least 100 (40 for $K = 10$) sets of random coupling constants $|\phi_k|^2$ and show the mean value with the standard deviation as blue points. Besides a magnetic field of $b = 0.05$, we use the totally mixed state for nuclear spins but polarize the electron spin in z direction. *Figure reprinted with permission from [173].*

Applying our analytical results to a QD setup in which an electron spin is coupled to nuclear spins of the host material through the hyperfine interaction enables us to make precise predictions. Since this spin system is typically well isolated from its environment, QDs can be considered as a closed quantum system for sufficiently short timescales. We have simulated the time evolution of the total spin system and have analyzed its dependence on experimentally accessible parameters such as the strength of an external magnetic field and the polarization of the initial state of the nuclear spins. Intriguingly, we have discovered cases in which strong magnetic fields do not prevent the electron spin from equilibration, while polarized nuclear spins always diminishes the equilibration capability. Finally, we have also investigated the importance of the number of nuclear spins on equilibration properties. We show both analytically and numerically that very small amounts of nuclear spins are sufficient to fully equilibrate the electron spin in our model. The analytical results even hold for a wider class of spin models, and, thus are not limited to our specific model.

Conclusion

The investigation of the physics of the electron spins hosted in solid state QDs is a very active and promising field of physics. While its long-term goal is beyond doubt the realization of a working quantum computer, the findings reported in this Thesis also suggest that it may be beneficial to broaden our view to the interesting developments made aside from this main route.

Our first discovery is a thermally induced flip of the electron spin in a QD. This intriguing effect arises from an interesting interplay between the HI of the electron spin with the nuclear spins of the host material and the Zeeman interaction of these spins with an external magnetic field. Starting from the system's ground-state, the electron spin suddenly flips upon increasing the temperature. The specific temperature of this spin flip is a constant, which depends on material-specific properties. Relevant materials include group III-V based structures, which all exhibit a negative effective g-factor g^*. Since the spin flip temperatures lie in the mK regime for these materials, we are confident about a detection of our predictions in the near future. While this result has been obtained in the framework of statistical equilibrium physics, all of our other results have been realized analyzing the dynamics of the spins.

As we have explained in detail in the first part of this Thesis, group IV based materials such as graphene feature several specific properties in comparison to the widely used GaAs heterostructures. In particular, graphene allows for the realization of a variable number of nuclear spins within the QD and, thus, for a change of the relevance of the HI, which is, oftentimes, the major source of decoherence of the electron spin. Moreover, this HI is anisotropic in graphene arising from the peculiarities of its electronic bandstructure. Motivated by these possibilities, we have studied the dynamics of the electron spin in different setups, which are characterized by the number of involved nuclear spins and the presence and strength of an external magnetic field. In our first project on spin dynamics, we have analyzed the consequences of this anisotropy on the coherence of the electron spin in the limit of large external magnetic fields and a large number of nuclear spins. This choice generalizes previous results considering an isotropic HI to the case of an anisotropic HI. Due to the slow internal dynamics of the nuclear spins, the system is non-Markovian, which can be analyzed using the Nakajima-Zwanzig master equation. Following this scheme, we have recovered the power-law decay of the coherence reported before arising from this non-Markovian dynamics. In contrast to the isotropic case, however, we have revealed a strong dependence of the details of this decay on the orientation of the external magnetic field with respect to the plane of graphene. In a subsequent project, we have investigated a contrary regime characterized by a very small number of nuclear spins and small or even absent external magnetic fields. Due to the small size of the total spin system, we have been able to exploit exact diagonalization, which has provided us additional insights into the microscopic processes dominating the dynamics of the electron

spin. In particular, it has been possible to study the importance of initial states and the coupling of individual nuclear spins to the electron spin. In this context, we have also observed a strong tendency of the electron spin to exhibit a quasi stationary behavior characterized by small fluctuations around its long-time average value. This equilibration has been reached in most cases by a fast decay of its amplitude. This observation has been the starting point for our last project. Extending the numerical investigations to a more general setup including finite magnetic fields and thermal initial states of the nuclear spins, we have obtained a more complete picture of this quasi equilibration. Furthermore, we have achieved the formulation of analytical bounds for the size of the fluctuations of the electron spin in the framework of quantum thermodynamics. Interestingly, already a comparably small number of nuclear spins is sufficient to induce this equilibration, as we have verified by a comparison of our numerical and analytical results. By this procedure, we have successfully applied a rather abstract concept from quantum thermodynamics to a realistic system.

With these theoretical findings in mind, let us briefly comment on the current experimental situation of graphene based QDs. While certain steps towards graphene QDs competing with GaAs QDs have been taken, there remain major problems yet to be solved, which hamper further progress. Most importantly, neither single electron occupation nor the Pauli blockade regime have been achieved so far. While the single electron regime is essential to study the effects of the HI on the electron spin dynamics, the Pauli blockade regime provides one of the best tools to actually measure the electron spin. Hopefully, these challenges will be overcome in the next years, but, nonetheless, other materials should also be considered in the future. Fortunately, other elements of the fourth group of the periodic table are available to create QDs with a variable number of nuclear spins. In our opinion, the most promising material is silicon, which offers a large variety of different realizations of QDs and the (dis)advantage of an isotropic HI. Most importantly, the occupation of QDs with a single electron and the readout of its spin via Pauli blockade have already been successfully demonstrated. In summary, the realization of QDs featuring a single electron spin in contact with a variable nuclear spin environment can in fact be experimentally realized. However, it is certainly beneficial to consider the peculiarities of other materials than just graphene, e.g., silicon.

Based on these experimental possibilities, it would be most interesting to study the evolution of the electron spin dynamics under a continuous change of the number of nuclear spins. To this end, the regime of nuclear spin environments of intermediate size should be additionally studied. For this task, a twofold strategy seems most promising, which includes an extension of the numerical analysis to larger spin systems. Since the computational effort of the exact diagonalization grows exponentially with the number of nuclear spins, other numerical methods such as the Suzuki-Trotter approach and the Chebyshev expansion could be considered. Moreover, these numerical studies have to be accompanied by further analytical work. As a starting point, it should be investigated how our analytical results can be extended to an intermediate number of nuclear spins. However, the Nakajima-Zwanzig master equation is mathematically demanding due to the convolution in its non-unitary part. Further, this master equation does not allow for an expansion in terms of simple diagrams representing important microscopic processes. Hence, other analytic methods such as the time-convolutionless master equation [145] or cluster expan-

sions [187, 188] could, for instance, be considered. These additional tools would most likely also allow us to better explore the long-time behavior of the electron spin interacting with many nuclear spins. In the case of GaAs, theory predicts the restoration of Markovian dynamics on longer timescales. Analytical results on the long-time dynamics of the electron spin would also certainly promote the formulation of time-dependent bounds on the fluctuation of the electron spin, which is the next step towards a deeper understanding of these dynamics in terms of quantum thermodynamics.

In addition to the electron spin dynamics, future research might also consider the nuclear spins as a resource rather than an obstacle. In parts, the community interested in GaAs based QDs has already undergone such a change of paradigm. However, with the reduction of the environment to only few nuclear spins, a more directed manipulation of the nuclear spin states becomes possible [113, 189]. With the additional possibility to control the strength of the HI via the probability density of the electron spin, at least to some extent, group IV based QDs seem very promising in this regard. In this sense also other spin related physics such as many body localization could be explored in QDs in the future.

A. Thermal electron spin flip for the extended Hamiltonian

A.1. Properties of the extended Hamiltonian

In this section, we briefly discuss the properties of the extended Hamiltonian $H_\alpha \equiv \hat{H}(\sigma, \nu, \alpha)$ given in Eq. (3.7). Since all nuclear spins couple with the same strength to both the electron spin and the external magnetic field, the Hamiltonian is invariant under an exchange of two nuclear spins

$$\hat{X}_{i,j}|m_S, m_K, \ldots, m_i, \ldots, m_j, \ldots, m_1\rangle = |m_S, m_K, \ldots, m_j, \ldots, m_i, \ldots, m_1\rangle\,, \tag{A.1}$$

where $\hat{X}_{i,j} = \hat{X}_{j,i}$, $\hat{X}_{i,j} = \hat{X}_{i,j}^\dagger$ and $\hat{X}_{i,j}^2 = \mathbb{1}$. This invariance is formally described by the vanishing commutator

$$[\hat{H}, \hat{X}_{i,j}] = 0 \;\; \forall \;\; i, j \in \{1, 2, \ldots, K\}\,. \tag{A.2}$$

Moreover, we want to analyze how the Hamiltonian behaves under a total flip of all spins

$$\hat{F}|m_S, m_K, \ldots, m_1\rangle = |-m_S, -m_K, \ldots, -m_1\rangle\,, \tag{A.3}$$

where $\hat{F}^2 = \mathbb{1}$ and $\hat{F}^\dagger = \hat{F}$. Applying this operator to the Hamiltonian yields

$$\hat{F}\hat{H}(\sigma, \nu, \alpha)\hat{F}^\dagger = \hat{H}(-\sigma, -\nu, \alpha)\,, \tag{A.4}$$

since the Zeeman part of the Hamiltonian changes its sign and the HI interaction is invariant under a total flip of all spins. Finally, the Hamiltonian commutes with the z-component of the total spin $\hat{S}_z + \sum_k \hat{I}_{k,z} \equiv \hat{S}_z + \hat{J}_z$, where we have introduced the total nuclear spin $\hat{\boldsymbol{J}} = \sum_k \hat{\boldsymbol{I}}_k$. Due to this last property, it is convenient to represent the extended Hamiltonian in the basis of product states between the electron spin and the total nuclear spin $|m_S\rangle \otimes |J, M_J, \{q_i\}\rangle = |m_S, J, M_J, \{q_i\}\rangle$, in which it has a simple block-diagonal structure. The additional quantum numbers $\{q_i\}$ are related to the corresponding Clebsch-Gordon coefficients. These quantum numbers $q_i = q_i(\{I_k\}_{k=1}^K)$ depend on the quantum numbers I_k of the original states $|I_k, m_k\rangle$. Thus, these states form an orthonormal basis with

$$\langle m_S, J, M_J, \{q_i\}\,|\,m_S', J', M_J', \{q_i'\}\rangle = \delta_{m_S, m_S'}\delta_{J,J'}\delta_{M_J, M_J'}\delta_{\{q_i\},\{q_i'\}}\;\;, \tag{A.5}$$

where both sets of quantum numbers $\{q_i\}$ and $\{q_i'\}$, respectively, have to be equal in all elements as indicated by the "δ" symbol. Since the Hamiltonian is degenerate in these quantum numbers, we will use the shorthand notation $|J, M_J\rangle$ for the nuclear spin state whenever it is appropriate.

A.2. Diagonalization of the extended Hamiltonian

In this section, we show how the extended Hamiltonian $H_\alpha \equiv \hat{H}(\sigma,\nu,\alpha)$ in Eq. (3.7) can be diagonalized [154, 155, 156, 157]. Ordering the product states $|m_S, J, M_J\rangle$ defined in the previous section properly,

$$\begin{aligned}
&|\tfrac{1}{2},\tfrac{K}{2},\tfrac{K}{2}\rangle, |-\tfrac{1}{2},\tfrac{K}{2},\tfrac{K}{2}\rangle, |\tfrac{1}{2},\tfrac{K}{2},\tfrac{K}{2}-1\rangle, |-\tfrac{1}{2},\tfrac{K}{2},\tfrac{K}{2}-1\rangle, \dots, |-\tfrac{1}{2},\tfrac{K}{2},-\tfrac{K}{2}\rangle,\\
&|\tfrac{1}{2},\tfrac{K}{2}-1,\tfrac{K}{2}-1\rangle, |-\tfrac{1}{2},\tfrac{K}{2}-1,\tfrac{K}{2}-1\rangle, \dots, |-\tfrac{1}{2},\tfrac{K}{2}-1,-\tfrac{K}{2}+1\rangle,\\
&\vdots\\
&|\tfrac{1}{2},\tfrac{K \bmod 2}{2},-\tfrac{K \bmod 2}{2}\rangle, |-\tfrac{1}{2},\tfrac{K \bmod 2}{2},-\tfrac{K \bmod 2}{2}\rangle,
\end{aligned} \tag{A.6}$$

this yields a block-diagonal representation of the Hamiltonian, where the blocks are of dimension 1 or 2. In this basis, all diagonal entries of the Hamiltonian are formed by the energies

$$\begin{aligned}
E_1(\sigma,\nu,M_J,m_S) &= \langle m_S, J, M_J|H(\sigma,\nu,\alpha)|m_S, J, M_J\rangle\\
&= -\sigma m_S - \nu M_J + 2 m_S M_J\,,
\end{aligned} \tag{A.7}$$

where $m_S = 1/2, -1/2$. The states $|1/2, J, J\rangle$ and $|-1/2, J, -J\rangle$ are already eigenstates of the Hamiltonian, and, hence the corresponding energies constitute the one-dimensional blocks. The off-diagonal parts of the two-dimensional blocks are given by

$$\begin{aligned}
F(J,M_J) &= \langle -\frac{1}{2}, J, M_J|H(\sigma,\nu,\alpha)|\frac{1}{2}, J, M_J-1\rangle\\
&= \sqrt{J(J+1) - M_J(M_J-1)}
\end{aligned} \tag{A.8}$$

Thus, the eigenenergies and eigenstates of the two-dimensional blocks are obtained by diagonalizing the 2×2 matrices

$$\begin{aligned}
&H_2(\sigma,\nu,\alpha,J,M_J) =\\
&\begin{pmatrix} E_1(\sigma,\nu,M_J,-\frac{1}{2}) & \alpha F(J,M_J)\\ \alpha F(J,M_J) & E_1(\sigma,\nu,M_J-1,\frac{1}{2}) \end{pmatrix}.
\end{aligned} \tag{A.9}$$

The eigenenergies of the 2×2 matrix in Eq. (A.9) are, then, given by

$$\begin{aligned}
&E_{2,\pm}(\sigma,\nu,\alpha,J,M_J)\\
=&\frac{1}{2}\Big[E_1(\sigma,\nu,M_J,-\frac{1}{2}) + E_1(\sigma,\nu,M_J-1,\frac{1}{2})\Big]\\
&\pm\left\{\Big[E_1(\sigma,\nu,M_J,-\frac{1}{2}) - E_1(\sigma,\nu,M_J-1,\frac{1}{2})\Big]^2 + 4\alpha^2 F(J,M_J)^2\right\}^{\frac{1}{2}}
\end{aligned} \tag{A.10}$$

The eigenstates of this matrix are given by

$$\begin{aligned}
|E_{2,\pm}(\sigma,\nu,\alpha,J,M_J)\rangle &= \eta_\pm^{\frac{1}{2}}(\sigma,\nu,\alpha,J,M_J)|\frac{1}{2}, J, M_J-1\rangle\\
&\quad + \eta_\pm^{-\frac{1}{2}}(\sigma,\nu,\alpha,J,M_J)|-\frac{1}{2}, J, M_J\rangle\,,
\end{aligned} \tag{A.11}$$

where all coefficients $\eta_{\pm}^{m_S}$ are real. With this relation, we know all eigenenergies and eigenstates of the total Hamiltonian. For later convenience, we invert the above relation in order to obtain a representation of the total spin basis states in terms of energy eigenstates:

$$\begin{aligned}|-\frac{1}{2}, J, M_J\rangle = \quad & \gamma_{+}^{-\frac{1}{2}}(\sigma,\nu,\alpha,J,M_J))|E_{2,+}(\sigma,\nu,\alpha,J,M_J)\rangle \\ & +\gamma_{-}^{-\frac{1}{2}}(\sigma,\nu,\alpha,J,M_J))|E_{2,-}(\sigma,\nu,\alpha,J,M_J)\rangle \end{aligned} \tag{A.12}$$

and

$$\begin{aligned}|\frac{1}{2}, J, M_J\rangle = \quad & \gamma_{+}^{\frac{1}{2}}(\sigma,\nu,\alpha,J,M_J+1))|E_{2,+}(\sigma,\nu,\alpha,J,M_J+1)\rangle \\ & +\gamma_{-}^{\frac{1}{2}}(\sigma,\nu,\alpha,J,M_J+1))|E_{2,-}(\sigma,\nu,\alpha,J,M_J+1)\rangle\,, \end{aligned} \tag{A.13}$$

respectively.

A.3. Calculation of the partition function

In this section, we calculate the partition function $Z = \mathrm{Tr}[e^{-\beta\hat{H}_\alpha}]$ of the extended Hamiltonian $\hat{H}_\alpha \equiv \hat{H}(\sigma,\nu,\alpha)$ in Eq. (3.7). Since the Hamiltonian is invariant under an exchange of two nuclear spins, the trace can be written as

$$Z = \sum_{m_S} \sum_{M_J=-\frac{K}{2}}^{\frac{K}{2}} N_{M_J}^K \langle m_S, \Psi_{M_J}|e^{-\beta\hat{H}_\alpha}|m_S,\Psi_{M_J}\rangle\,, \tag{A.14}$$

where the nuclear spin state is given by

$$|\Psi_{M_J}\rangle = |\underbrace{-\frac{1}{2},\ldots,-\frac{1}{2}}_{\frac{K}{2}-M_J},\underbrace{\frac{1}{2},\ldots,\frac{1}{2}}_{\frac{K}{2}+M_J}\rangle \tag{A.15}$$

and $N_{M_J}^K$ is defined in Eq. (3.18). In order to benefit from previous results [156, 157], which have been obtained for $M_J \geq 0$, we additionally use the effect of a total flip of all spins $\hat{F}|m_S,\Psi_{M_J}\rangle = |-m_S,\Psi_{-M_J}\rangle$ and $\hat{F}\hat{H}(\sigma,\nu,\alpha)\hat{F}^\dagger = \hat{H}(-\sigma,-\nu,\alpha)$. Thus, the partition function can be expressed by

$$\begin{aligned} Z = \sum_{m_S} \Bigg[& \sum_{M_J=\frac{K \bmod 2}{2}}^{\frac{K}{2}} N_{M_J}^K \langle m_S,\Psi_{M_J}|e^{-\beta\hat{H}(\sigma,\nu,\alpha)}|m_S,\Psi_{M_J}\rangle \\ & + \sum_{M_J=\frac{1-K \bmod 2}{2}}^{\frac{K}{2}} N_{M_J}^K \langle m_S,\Psi_{M_J}|e^{-\beta\hat{H}(-\sigma,-\nu,\alpha)}|m_S,\Psi_{M_J}\rangle \Bigg]. \end{aligned} \tag{A.16}$$

Next, we replace the states $|m_S,\Psi_{M_J}\rangle$ by the states $|m_S,J,M_J\rangle$. For spin one-half particles, this replacement [156, 157] is given by

$$|m_S,\Psi_{M_J}\rangle = \sum_{k=0}^{\frac{K}{2}-M_J} \sum_{\{q_i\}} c_k^{\{q_i\}} |m_S, \frac{K}{2}-k, M_J, \{q_i\}\rangle \tag{A.17}$$

where the coefficients $c_k^{\{q_i\}}$ obey the following relation

$$\sum_{\{q_i\}} |c_k^{\{q_i\}}|^2 = \frac{(\frac{K}{2} - M_J)!\,(\frac{K}{2} + M_J)!\,(K - 2k + 1)}{(K-k)!\,k!\,(K-k+1)} \equiv d_k \tag{A.18}$$

The states $|1/2, M_J, M_J, \{q_i\}\rangle$ are already eigenstates of the Hamiltonian. Moreover, the state $|-1/2, 0, 0, \{q_i\}\rangle$ is also an eigenstate. All other remaining states can be expressed in terms of eigenstates of the Hamiltonian according to Eqs. (A.12) and (A.13). With this, we have calculated the partition function $Z = Z(\sigma, \nu, \alpha, K)$, which allows us to find the thermal expectation value of the electron spin according to Eq. (3.12). In order to confirm that there is still a spin flip in the presence of the flip-flop terms, we have calculated this thermal expectation value for up to $K = 60$ nuclear spins. In Fig. 3.3 a), we show the electron spin at zero temperature. Clearly, the flip-flop terms reduce the polarization of the electron spin for small system sizes. For larger K, the thermal expectation value $\langle \hat{S}_z \rangle_0$, however, tends to the same value as without the flip-flop terms. In the next section, we analytically show, that $\langle \hat{S}_z \rangle_0 = -\frac{1}{2}$ is exactly reached for large system sizes. Moreover, we have analyzed the maximum value of the electron spin $\langle \hat{S}_z \rangle_{2/\rho}$, which is approximately found at $\tau = \frac{2}{\rho}$, cf. Fig. 3.1. As is clear from Fig. 3.3 b), this quantity tends to $\langle \hat{S}_z \rangle_{2/\rho} = \frac{1}{2}$ for a large number of nuclear spins K. Note, that also for $\alpha = 0$, this quantity is a function of K. Since the quantum fluctuations due to the flip-flop terms are already at zero temperature irrelevant for large system sizes, it is evident that they are also unimportant at higher temperatures.

A.4. Ground state of the Hamiltonian

In this section, we want to find the ground state of the extended Hamiltonian with $\alpha = 1$. To this end, we first find the minimum of the energies $E_{2,-}(\sigma, \nu, 1, J, M_J)$ for a fixed J with respect to M_J. From this set of minima, we then find the smallest energy with respect to J. Finally, we compare this minimum to the energies $E_1(\sigma, \nu, J, m_S)$ resulting from the one-dimensional sub-spaces of the Hamiltonian.

The minimum with respect to M_J for fixed J can be found by investigating the derivative

$$\begin{aligned} &\frac{\mathrm{d}}{\mathrm{d}M_J} E_{2,-}(\sigma, \nu, 1, J, M_J) \\ =& -\nu - \frac{\sigma - \nu}{[4J(J+1) - 4M_J(M_j - 1) + (1 - 2M_J - \nu + \sigma)^2]^{\frac{1}{2}}}\,, \end{aligned} \tag{A.19}$$

which is always negative for $\sigma > \nu > 0$. Hence, the energy is a decreasing function of M_J with its "local" minimum at $M_J = J$. In order to find the absolute minimum of $E_{2,-}(\sigma, \nu, 1, J, J)$, we analyze the derivative with respect to J, which is

$$\frac{\mathrm{d}}{\mathrm{d}J} E_{2,-}(\sigma, \nu, 1, J, J) = -\nu - \frac{2 - (1 - 2J - \nu + \sigma)}{[8J + (1 - 2J - \nu + \sigma)^2]^{\frac{1}{2}}}\,. \tag{A.20}$$

For a nuclear Zeeman energy $\nu > 1$, this derivative is negative for all values of J within $(K \bmod 2)/2 \leq J \leq K/2$. As a consequence, the absolute minimum of $E_{2,-}(\sigma, \nu, 1, J, J)$

is then given by

$$E_{2,-}(\sigma,\nu,1,\frac{K}{2},\frac{K}{2}) = \frac{1}{2}[\nu - 1 - K\nu - \sqrt{4K + (1 - K - \nu\sigma)}] \tag{A.21}$$

This minimum has to be compared to the minimum of the energies $E_1(\sigma,\nu,J,m_S)$ given in Eq. (A.7). For $\sigma > \nu > 1$, the minimum energy is found for $m_S = \frac{1}{2}$ and $J = K/2$ with

$$E_1(\sigma,\nu,\frac{K}{2},\frac{1}{2}) = \frac{1}{2}[-\sigma - K\nu + K]\,, \tag{A.22}$$

As we have shown in the main text, the spin-flip occurs if $\sigma = K\rho\nu$ with $\rho\nu < 1$ and $\rho < 1$. In this case, the minimum of the $E_{2,-}$ energies is given by

$$\begin{aligned} E_{2,-}(\sigma,\nu,1,\frac{K}{2},\frac{K}{2}) &= \frac{1}{2}[\nu - 1 - K\nu - \sqrt{4K + (1 - K - \nu\sigma)}] \\ &\leq -\frac{K}{2}[\nu + 1 - \rho\nu] \\ &< -\frac{K}{2}[\nu - 1 + \rho\nu] = E_1(K\rho\nu,\nu,\frac{K}{2},\frac{1}{2}) \end{aligned} \tag{A.23}$$

Thus, the ground state energy is given by $E_{2,-}(\sigma,\nu,1,\frac{K}{2},\frac{K}{2})$. In order to find the thermal expectation value of the electron spin at zero temperature, we have to calculate the coefficients

$$\eta_-^{-\frac{1}{2}}(K\rho\nu,\nu,1,\frac{K}{2},\frac{K}{2}) = \frac{r-s}{t}\frac{1}{\left[(\frac{r-s}{t})^2+1\right]^{\frac{1}{2}}} \tag{A.24}$$

and

$$\eta_-^{\frac{1}{2}}(K\rho\nu,\nu,1,\frac{K}{2},\frac{K}{2}) = \frac{1}{\left[(\frac{r-s}{t})^2+1\right]^{\frac{1}{2}}}\,, \tag{A.25}$$

where $r = 1 - K - \nu + K\rho\nu$, $t = 2K^{\frac{1}{2}}$, and $s = (r^2 + t^2)^{\frac{1}{2}}$. In the limit of large K, $\eta_-^{-\frac{1}{2}}(K\rho\nu,\nu,1,\frac{K}{2},\frac{K}{2}) = 1$ and $\eta_-^{\frac{1}{2}}(K\rho\nu,\nu,1,\frac{K}{2},\frac{K}{2}) = 0$ and, hence, also for $\alpha = 1$ the ground state exhibits $\langle\hat{S}_z\rangle_0 = -\frac{1}{2}$.

B. Matrix elements of the self-energy of the Nakajima-Zwanzig equation

In this appendix, we discuss the computation of the self-energy matrix-elements given in Eqs. (4.28) to (4.31) in more detail. We assume, that the nuclear magnetic field operators $\hat{g}_\pm = \frac{1}{2}\left[\lambda_\pm \hat{h}_+ + \lambda_\mp \hat{h}_-\right]$ defined in Eq. (4.12) have already been inserted. Thus, all matrix elements of the self-energy are linear combinations with prefactors depending on the couplings λ_i. The respective summands always contain one super-operator $\mathcal{G}_{\uparrow,\downarrow}$, two bare nuclear magnetic field operators $\hat{h}_\pm$, and the nuclear density matrix $\hat{\rho}_I = |n\rangle\langle n|$. Calculating expectation values with respect to the nuclear state $|n\rangle$, all summands featuring squared operators $\hat{h}_\pm^2$ vanish identically, which reduces the number of contributions. In the following, we will present, how the remaining expressions can be evaluated in a general approach. For simplicity, we will neglect the prefactors in the following presentation.

Due to the linearity and the cyclicity of the trace, all self-energy parts in second order can be written as a linear combination of terms of the form

$$\mathrm{Tr}_I\left(\_\,\_\,\_\,\hat{\rho}_I\right), \tag{B.1}$$

where the free spots can be filled with one raising operator $\hat{h}_+$, one lowering operator $\hat{h}_-$, and one of the two super-operators $\mathcal{G}_{\uparrow,\downarrow}(\mathcal{L}_-)$ given in Eq. (4.32). Altogether, this leads to $3 \times 2 \times 2 = 12$ possible combinations. This number can be reduced by using the relation [147] of Liouvillian-like operators:

$$\mathrm{Tr}_I\left(f[\mathcal{L}_\pm]\hat{O}_1\hat{O}_2\right) = \mathrm{Tr}_I\left(\hat{O}_1 f[\pm\mathcal{L}_\pm]\hat{O}_2\right) \tag{B.2}$$

for arbitrary operators $\hat{O}_{1,2}$ and a function $f[\mathcal{L}_\pm]$, which can be expanded in powers of (anti-)commutators $\mathcal{L}_-$ ($\mathcal{L}_+$). Therefore, moving $\mathcal{G}_{\uparrow,\downarrow}(\mathcal{L}_-)$ to a neighboring position involves a change of sign of its argument $\mathcal{L}_- \to -\mathcal{L}_-$. As a consequence of this, it is sufficient to calculate the following trace $\mathrm{Tr}_I(\mathcal{G}_{\uparrow,\downarrow}\hat{h}_\pm\hat{h}_\mp\hat{\rho}_I)$, which gives rise to sums over expectation values with respect to nuclear eigenstates $|q\rangle = \bigotimes_k |m_k^q\rangle$:

$$\begin{aligned}
\mathrm{Tr}_I\left(\mathcal{G}_i\hat{h}_\pm\hat{h}_\mp\hat{\rho}_I\right) &= \sum_{p,q,r}\langle p|\mathcal{G}_i\Big\{|q\rangle\langle q|\hat{h}_\pm|r\rangle\langle r|\Big\}\hat{h}_\mp|n\rangle\langle n\,|\,p\rangle \\
&= \sum_{q,r}\langle n|\mathcal{G}_i\Big\{|q\rangle\langle r|\Big\}\langle q|\hat{h}_\pm|r\rangle\hat{h}_\mp|n\rangle \\
&= \sum_{q,r}\Big[\mathcal{G}_i\Big]_{qr}\langle q|\hat{h}_\pm|r\rangle\langle n\,|\,q\rangle\langle r|\hat{h}_\mp|n\rangle \\
&\equiv \sum_r \Big[\mathcal{G}_i\Big]_{nr}\Big[\hat{h}_\pm\Big]_{nr}\Big[\hat{h}_\mp\Big]_{rn},
\end{aligned} \tag{B.3}$$

As we explain in the main text, we assume the nuclear Zeeman energy to be sufficiently small such that we can neglect A^I_{ZE} from now on. Using Eq. (4.32), one can calculate the expectation values of these super-operators:

$$\left[\mathcal{G}_{\uparrow,\downarrow}\left(\beta\mathcal{L}_{-}\right)\right]_{nr} = \left\{s + \mathrm{i}\alpha_{\uparrow,\downarrow}\beta\,\frac{\lambda_z}{2}\sum_k A_k\left(m_k^n - m_k^r\right)\right\}^{-1}, \tag{B.4}$$

where $\alpha_{\uparrow,\downarrow} = \pm 1$ and $\beta = \pm 1$. The factor λ_z is the anisotropy coefficient in z-direction. Next, we calculate the magnetic field expectation values, where we begin with the action of a local operator $\hat{I}_{k,\pm}$ at an arbitrary site k in order to simplify later steps:

$$\begin{aligned}\hat{I}_{k,\pm}\bigotimes_l |m_l^q\rangle &= \sqrt{I(I+1) - m_k^q(m_k^q \pm 1)}|m_k^q \pm 1\rangle \otimes \bigotimes_{l\neq k}|m_l^q\rangle \\ &\equiv M_{\pm}(m_k^q)\ \ |m_k^q \pm 1\rangle \bigotimes_{l\neq k}|m_l^q\rangle\,,\end{aligned} \tag{B.5}$$

We introduced the shorthand notation $M_{\pm}(m_k^q)$, which obeys the relation $M_{\pm}(m_k^q \mp 1) = M_{\mp}(m_k^q)$. Note, that only one single nuclear spin state was changed by the action of $\hat{I}_{k,\pm}$ while all other states remain unchanged. Using the above equation, one can calculate the expectation value of the nuclear magnetic field operators $\hat{h}_{\pm}$ with respect to eigenstates $|p\rangle$, $|q\rangle$ of the $\hat{h}_z$-component:

$$\begin{aligned}\langle p|\hat{h}_{\pm}|q\rangle = \left[\hat{h}_{+}\right]_{pq} &= \langle p|\sum_k A_k \hat{I}_{k,\pm}\bigotimes_p |m_p^q\rangle \\ &= \sum_k A_k M_{\pm}(m_k^q)\ \langle p|\Big\{|m_k^q \pm 1\rangle \otimes \bigotimes_{p\neq k}|m_p^q\rangle\Big\} \\ &= \sum_k A_k M_{\pm}(m_k^q)\ \Big\{\bigotimes_{l'}\langle m_{l'}^p|\Big\}\Big\{|m_k^q \pm 1\rangle \otimes \bigotimes_{l\neq k}|m_l^q\rangle\Big\} \\ &= \sum_k A_k M_{\pm}(m_k^q)\ \delta_{m_k^p, m_k^q \pm 1}\prod_{l,l'\neq k}\delta_{m_{l'}^p, m_l^q}\,.\end{aligned} \tag{B.6}$$

This equation completely sets the relation between the two sets of product states $\left\{m_l^{p/q}\right\}$ with $l \in \{1,\ldots,K\}$. Inserting this result in Eq. (B.3), we find:

$$\begin{aligned}\sum_r \left[\mathcal{G}_{\uparrow,\downarrow}\left(\beta\mathcal{L}_{-}\right)\right]_{nr}\left[\hat{h}_{\pm}\right]_{nr}\left[\hat{h}_{\mp}\right]_{rn} &= \left\{s + \mathrm{i}\alpha_{\uparrow\downarrow}\beta\frac{\lambda_z}{2}\sum_{k_1} A_{k_1}\left(m_{k_1}^n - m_{k_1}^r\right)\right\}^{-1} \\ &\quad\times\Big\{\sum_{k_2} A_{k_2}M_{\pm}(m_{k_2}^r)\ \delta_{m_{k_2}^n, m_{k_2}^r \pm 1}\prod_{l,l'\neq k_1}\delta_{m_{l'}^n, m_l^r}\Big\} \\ &\quad\times\Big\{\sum_{k_3} A_{k_3}M_{\mp}(m_{k_3}^n)\ \delta_{m_{k_3}^r, m_{k_3}^n \mp 1}\prod_{\tilde{l},\tilde{l}'\neq k_3}\delta_{m_{\tilde{l}'}^r, m_{\tilde{l}}^n}\Big\} \\ &= \sum_{k_2}\frac{A_{k_2}^2 M_{\mp}^2(m_{k_2}^n)}{s \pm \mathrm{i}\alpha_{\uparrow\downarrow}\beta\frac{\lambda_z}{2}A_{k_2}}\,.\end{aligned} \tag{B.7}$$

The functions $M_{\pm}^2(m_k^n)$ defined in Eq. (B.5) can be replaced by their average assuming a nuclear state which is highly degenerate [76, 152]:

$$\langle\langle M_{\pm}^2(m_k^n)\rangle\rangle = c_{\pm}\,. \tag{B.8}$$

Finally, for a large nuclear spin system with $K \gg 1$, the remaining sums in Eq. (B.7) can be replaced by integrals in the continuum limit. Changing to dimensionless units by measuring energies in units of $\epsilon_{HI} = |\lambda_z| n_I A_{\mathrm{HI}}/2K$, one finds up to small corrections [76]:

$$\mathrm{Tr}_I \left(\mathcal{G}_{\uparrow,\downarrow} (\beta \mathcal{L}_-) \, \hat{h}_\pm \hat{h}_\mp \hat{\rho}_I \right) = \frac{4K}{\lambda_z^2} c_\mp I_{\mp\{\alpha_{\uparrow\downarrow} \beta \tilde{\lambda}_z\}}(s) \,, \tag{B.9}$$

where $\tilde{\lambda}_z = \lambda_z/|\lambda_z|$ and

$$I_\pm (s) = s \left[\log (s \mp \mathrm{i}) - \log (s) \right] \pm \mathrm{i} \,. \tag{B.10}$$

Applying this continuum limit, however, sets an upper bound $t \ll \sqrt{\frac{K}{2}} \tau_{HI}$ as discussed in the main text. Knowing the four basic terms given in Eq. (B.9), respectively, all other remaining possible summands to the self-energy are readily obtained using Eq. (B.2).

C. Properties of the weak distinguishability and its bounds

C.1. Saturation of variances

In this appendix, we show that the TAWD $\langle D_{\hat{O}} \rangle_t = \delta_{\hat{O}}(t) + \Delta_{\hat{O}}$ defined in Eq. (6.4) is separable in a time dependent part $\delta_{\hat{O}}(t)$ that vanishes at large times and a time independent part $\Delta_{\hat{O}}$. To do so, we follow a previous analysis [182] and use the fact that the matrix elements $\omega_{ij} = \langle E_i | \hat{\omega} | E_j \rangle$ of $\hat{\omega}$ in energy space are given by

$$\omega_{ij} = \begin{cases} \rho_{ij} & E_i = E_j \\ 0 & \text{else} \end{cases} , \tag{C.1}$$

where E_i is the energy of the i-th eigenvector $|E_i\rangle$ of $\hat{H}$. Now, we can rewrite the TAWD by

$$\begin{aligned} \langle D_{\hat{O}} \rangle_t &= \frac{1}{t} \int_0^t \mathrm{d}t' \, \left(\mathrm{Tr}[\hat{\rho}(t') \hat{O}] - \mathrm{Tr}[\hat{\omega} \hat{O}] \right)^2 \\ &= \frac{1}{t} \int_0^t \mathrm{d}t' \, |\sum_{n,m} (\rho_{nm} e^{-\mathrm{i}\hbar^{-1}(E_n - E_m)t'} - \omega_{nm}) O_{mn}|^2 \\ &= \frac{1}{t} \int_0^t \mathrm{d}t' \, |\sum_{n,m} (\rho_{nm} - \omega_{nm}) e^{-\mathrm{i}\hbar^{-1}(E_n - E_m)t'} O_{mn}|^2 . \end{aligned} \tag{C.2}$$

The last step is possible, because for all n, m with $\omega_{nm} \neq 0$ follows $E_n = E_m$ according to Eq. (C.1). Therefore, $\omega_{nm} e^{-\mathrm{i}\hbar^{-1}(E_n - E_m)t'} = \omega_{nm}$ is time independent. We define $v_\alpha = (\rho_{nm} - \omega_{nm}) O_{mn}$ and gaps $G_\alpha = E_n - E_m$. Note that α is an abbreviation for a double index, running over all d^2 gaps. We then find

$$\begin{aligned} \langle D_{\hat{O}} \rangle_t &= \frac{1}{t} \int_0^t \mathrm{d}t' \, |\sum_{\alpha} v_\alpha e^{-\mathrm{i}\hbar^{-1} G_\alpha t'}|^2 \\ &= \frac{1}{t} \int_0^t \mathrm{d}t' \, \sum_{\alpha,\beta} v_\alpha v_\beta^* e^{-\mathrm{i}\hbar^{-1}(G_\alpha - G_\beta)t'} \\ &= \frac{1}{t} \int_0^t \mathrm{d}t' \, \Big(\sum_{\substack{\alpha,\beta \\ G_\alpha = G_\beta}} + \sum_{\substack{\alpha,\beta \\ G_\alpha \neq G_\beta}} \Big) v_\alpha v_\beta^* e^{-\mathrm{i}\hbar^{-1}(G_\alpha - G_\beta)t'} \\ &= \underbrace{\frac{1}{t} \sum_{\substack{\alpha,\beta \\ G_\alpha \neq G_\beta}} v_\alpha v_\beta^* \int_0^t \mathrm{d}t' \, e^{-\mathrm{i}\hbar^{-1}(G_\alpha - G_\beta)t'}}_{=\delta_{\hat{O}}(t)} + \underbrace{\sum_{\substack{\alpha,\beta \\ G_\alpha = G_\beta \neq 0}} v_\alpha v_\beta^*}_{=\Delta_{\hat{O}}} . \end{aligned} \tag{C.3}$$

We can exclude the cases $G_\alpha = G_\beta = 0$ in the second term because $G_\alpha = 0$ implies $v_\alpha = 0$. Note that $\delta_{\hat{O}}(t)$ vanishes at least with $\frac{1}{t}$ in the limit of infinite times, because the sum in $\delta_{\hat{O}}(t)$ is upper-bounded by $\sum_{\{\alpha,\beta\,|\,G_\alpha \neq G_\beta\}} |v_\alpha v_\beta^*|$, which yields

$$\lim_{t\to\infty} \langle D_{\hat{O}} \rangle_t = \Delta_{\hat{O}}\,. \tag{C.4}$$

C.2. Relation between distinguishability and variance

Defining $s(t) := \frac{\mathrm{d}}{\mathrm{d}\ln t} \ln \langle D_{\hat{O}} \rangle_t$, one can rewrite the definition of $\langle D_{\hat{O}} \rangle_t$ (see Eq. (6.4)) by

$$D_{\hat{O}}(t) = [s(t)+1] \langle D_{\hat{O}} \rangle_t\,. \tag{C.5}$$

An average over the time interval $I = [t, t+\Delta t]$ yields

$$\int_I \mathrm{d}t'\; D_{\hat{O}}(t') \leq \max_{t'\in I} \langle D_O \rangle_{t'} \int_I \mathrm{d}t'\; [s(t')+1]\,. \tag{C.6}$$

With $D_{\hat{O}}(t) = (\mathrm{Tr}[\hat{\rho}(t)\hat{O}] - \mathrm{Tr}[\hat{\omega}\hat{O}])^2$, the left hand side of the latter equation represents the variance of expectation values of $\hat{O}$ around the value $\mathrm{Tr}[\hat{\omega}\hat{O}]$ within the time interval I. Defining $\bar{s}(t)$ to be the average slope $s(t)$ within I, we derive

$$\mathrm{Var}_{\hat{O}}(t, \Delta t) \leq [\bar{s}(t)+1] \langle D_{\hat{O}} \rangle_t\,, \tag{C.7}$$

where we assume that $\max_{t'\in I} \langle D_{\hat{O}} \rangle_{t'} = \langle D_{\hat{O}} \rangle_t$. This assumption is correct if the system is on average approaching its equilibrium state. The value of $\bar{s}(t)$ is then negative, however, $s(t) \geq -1$ holds strictly. This follows from both the semi-positive values of $D_{\hat{O}}(t)$ and the $\frac{1}{t}$ in the definition of $\langle D_{\hat{O}} \rangle_t$. Therefore, we prove that

$$\mathrm{Var}_{\hat{O}}(t, \Delta t) \leq \langle D_{\hat{O}} \rangle_t\,. \tag{C.8}$$

The latter bound holds for all systems that approach equilibrium in the sense defined in Section 6.2. If a system is already equilibrated, the TAWD $\langle D_{\hat{O}} \rangle_t$ is no longer decreasing such that $\bar{s}(t) = 0$. Note that in this limit, the estimate for the variance becomes exact. This is also the case at large times, where $\langle D_{\hat{O}} \rangle_t$ of each system saturates as we explain above in App. C.1.

C.3. Infinite time estimates

In the following, we show how to estimate $\Delta_{\hat{O}}$ using only basic information about the system. For this purpose, we start with the long-time limit of C.3

$$\Delta_{\hat{O}} = \sum_{\substack{\alpha,\beta \\ G_\alpha = G_\beta \neq 0}} v_\alpha v_\beta^* = \sum_j \sum_{a,b}^{n_j} v_a^j v_b^{j\,*}\,, \tag{C.9}$$

where the sum in the last step is symmetrized by defining a parameter j to run over all distinct values of energy gaps, while a and b run over all n_j gaps of size G_j. Therefore, v_a^j belongs to the a-th gap of size $G_j \neq 0$. We estimate the symmetric double sum by

$$\begin{aligned}\sum_{i,j}^{N} x_i x_j^* &= \sum_{i}^{N} |x_i|^2 + \frac{1}{2}\sum_{i\neq j}^{N}\left(x_i x_j^* + x_j x_i^*\right) \\ &\leq \sum_{i}^{N}|x_i|^2 + \frac{1}{2}\sum_{i\neq j}^{N}\left(|x_i|^2 + |x_j|^2\right) = N\sum_{i}^{N}|x_i|^2, \end{aligned} \tag{C.10}$$

where $\{x_i\}$ is a set of N arbitrary complex numbers. Applying this relation to Eq. (C.9), we obtain

$$\Delta_{\hat{O}} \leq \sum_j n_j \sum_a^{n_j} |v_a^j|^2, \tag{C.11}$$

which even is an equality as long as all gaps are not degenerate, i.e., $n_j = 1\ \forall j$. With the maximum degeneracy of energy gaps $N_\mathrm{G} = \max_j n_j$, we find

$$\Delta_{\hat{O}} \leq N_\mathrm{G} \sum_j \sum_a^{n_j} |v_a^j|^2, \tag{C.12}$$

where both sums combined run over all d^2 gaps in the energy spectrum. In the previous notation, this reads

$$\widetilde{\Delta}_{\hat{O}} \leq N_\mathrm{G} \sum_\alpha |v_\alpha|^2. \tag{C.13}$$

We now insert the definition of v_α and use $|\rho_{nm} - \omega_{nm}| \leq |\rho_{nm}|$, which follows from Eq. (C.1). Thus, we find

$$\widetilde{\Delta}_{\hat{O}} \leq N_\mathrm{G} \sum_{n,m} |\rho_{nm} O_{mn}|^2. \tag{C.14}$$

First and second estimate

For the first estimate $\widetilde{\Delta}^1_{\hat{O}}$, we use that $|\rho_{nm}O_{mn}| = |\rho_{nm}||O_{mn}|$ and $|\rho_{nm}| \leq \|\hat{\rho}\|$, where $\|\hat{\rho}\|$ is the spectral norm of $\hat{\rho}$. Using this and $\hat{O} = \hat{O}^\dagger$, this yields

$$\Delta_{\hat{O}} \leq N_\mathrm{G}\|\hat{\rho}\|^2 \sum_{nm} O_{nm}O_{nm}^* = N_\mathrm{G}||\hat{\rho}||^2\,\mathrm{Tr}[\hat{O}^2] =: \widetilde{\Delta}^1_{\hat{O}} \tag{C.15}$$

The same steps but $\hat{\rho}$ and $\hat{O}$ interchanged yields

$$\Delta_{\hat{O}} \leq \widetilde{\Delta}^2_{\hat{O}} := N_\mathrm{G}\|\hat{O}\|^2 \mathrm{Tr}[\hat{\rho}^2]. \tag{C.16}$$

Third estimate

We derive estimate $\widetilde{\Delta}^3_{\hat{O}}$ by following an approach along the lines of Ref. [177]. We can then estimate Eq. (C.14) by

$$\Delta_{\hat{O}} \leq N_{\mathrm{G}} \sum_{n,m} \rho_{nn}\rho_{mm}O_{mn}O_{nm} = N_{\mathrm{G}}\,\mathrm{Tr}[\hat{\rho}_{\mathrm{diag}}\hat{O}\hat{\rho}_{\mathrm{diag}}\hat{O}], \tag{C.17}$$

where $|\rho_{nm}|^2 \leq \rho_{nn}\rho_{mm}$ because $\hat{\rho}$ is positive and $(\hat{\rho}_{\mathrm{diag}})_{nm} = \rho_{nm}\delta_{nm}$. With the Cauchy-Schwarz inequality and $\mathrm{Tr}[AB] \leq \|A\|\mathrm{Tr}[B]$ for positive A and B follows

$$\begin{aligned}\Delta_{\hat{O}} &\leq N_{\mathrm{G}}\,\mathrm{Tr}[\hat{O}^2\hat{\rho}^2_{\mathrm{diag}}] \\ &\leq N_{\mathrm{G}}\|\hat{O}\|^2\mathrm{Tr}[\hat{\rho}^2_{\mathrm{diag}}] \\ &\leq N_{\mathrm{G}}\|\hat{O}\|^2\mathrm{Tr}[\hat{\omega}^2] = N_{\mathrm{G}}\frac{\|\hat{O}\|^2}{d_{\mathrm{eff}}} =: \widetilde{\Delta}^3_{\hat{O}}\end{aligned} \tag{C.18}$$

This bound has previously been obtained in Ref. [177] on the basis of an analysis with pure initial states that have been expanded to mixed states afterwards.

Acronyms

2DEG	two-dimensional electron gas
CNT	carbon nanotube
EFA	envelope function approximation
EDSR	electron-dipole spin resonance
EPC	electron-phonon coupling
ESR	electron spin resonance
DNP	dynamical nuclear polarization
FID	free induction decay
HI	hyperfine interaction
NMR	nuclear magnetic resonance
QD	quantum dot
RC	random complex
SN	state narrowing
SOI	spin-orbit interaction
TAWD	time-averaged weak distinguishability

Bibliography

[1] R. S. Westfall. *The life of Isaac Newton*. Cambridge University Press, New York (1994). [p. 1]

[2] Wikipedia. "Zwerge auf den Schultern von Riesen — Wikipedia, Die freie Enzyklopädie" (2015). URL `https://de.wikipedia.org/w/index.php?title=Zwerge_auf_den_Schultern_von_Riesen&oldid=145161107`. [pp. 1, 3]

[3] W. H. Zurek. "Decoherence and the Transition from Quantum to Classical - Revisited". *Los Alamos Sci.* 86–109 (2002). [pp. 1, 41]

[4] K. Hornberger, S. Gerlich, P. Haslinger, S. Nimmrichter, and M. Arndt. "Colloquium : Quantum interference of clusters and molecules". *Rev. Mod. Phys.* **84**, 157 (2012). [pp. 1, 42]

[5] A. Van Dormael. "The "French" transistor". In "Proc. 2004 IEEE Conf. Hist. Electron. Bletchley Park", (2004). [p. 1]

[6] J. Bardeen and W. H. Brattain. "The Transistor, A Semi-Conductor Triode". *Phys. Rev.* **74**, 230 (1948). [p. 1]

[7] G. E. Moore. "Cramming more components onto integrated circuits". *Electronics* **38**, 114 (1965). [p. 1]

[8] L. P. Kouwenhoven, D. G. Austing, and S. Tarucha. "Few-electron quantum dots". *Reports Prog. Phys.* **64**, 701 (2001). [p. 1]

[9] R. Hanson, L. P. Kouwenhoven, J. R. Petta, S. Tarucha, and L. M. K. Vandersypen. "Spins in few-electron quantum dots". *Rev. Mod. Phys.* **79**, 1217 (2007). [pp. 1, 7, 8, 13, 18, 21, 22, 29, 30, 31, 32, 35, 94, 116]

[10] M. A. Nielsen and I. L. Chuang. *Quantum Computation and Quantum Information*. Cambridge University Press, Cambridge (2010). ISBN 9780511976667. [pp. 1, 33, 35, 41, 49, 75]

[11] L. K. Grover. "A fast quantum mechanical algorithm for database search". In "Proc. twenty-eighth Annu. ACM Symp. Theory Comput. - STOC '96", 212–219. ACM Press, New York, New York, USA (1996). ISBN 0897917855. [p. 1]

[12] P. W. Shor. "Polynomial-Time Algorithms for Prime Factorization and Discrete Logarithms on a Quantum Computer". *SIAM J. Comput.* **26**, 1484 (1997). [p. 1]

[13] D. Loss and D. P. DiVincenzo. "Quantum computation with quantum dots". *Phys. Rev. A* **57**, 120 (1998). [pp. 1, 7, 30]

[14] H. D. Zeh. "On the interpretation of measurement in quantum theory". *Found. Phys.* **1**, 69 (1970). [p. 2]

[15] W. H. Zurek. "Pointer basis of quantum apparatus: Into what mixture does the wave packet collapse?" *Phys. Rev. D* **24**, 1516 (1981). [p. 2]

[16] W. H. Zurek. "Environment induced superselection rules". *Phys. Rev. D* **26**, 1862 (1982). [pp. 2, 43]

[17] E. Joos and H. D. Zeh. "The emergence of classical properties through interaction with the environment". *Zeitschrift für Phys. B Condens. Matter* **59**, 223 (1985). [p. 2]

[18] M. Schlosshauer. *Decoherence and the Quantum-To-Classical Transition.* Frontiers Collection. Springer-Verlag, Berlin, Heidelberg, New York (2007). ISBN 9783540357735. [pp. 2, 41, 42, 43, 44, 46, 47, 49, 51, 56, 57, 58, 95]

[19] W. H. Zurek. "Decoherence and the Transition from Quantum to Classical". *Phys. Today* **44**, 36 (1991). [p. 2]

[20] D. P. DiVincenzo. "Topics in Quantum Computers". In L. L. Sohn, L. P. Kouwenhoven, and G. Schön (eds.), "Mesoscopic Electron Transp.", Nato Science Series E, chapter 2, 657–677. Springer Netherlands, Dordrecht (1997). ISBN 9780792347378. [p. 7]

[21] G. Burkard and D. Loss. "Electron Spins in Quantum Dots as Qubits for Quantum Information Processing". In D. D. Awschalom, D. Loss, and N. Samarth (eds.), "Semicond. Spintron. Quantum Comput.", NanoScience and Technology, chapter 8, 229–276. Springer-Verlag, Berlin, Heidelberg, New York (2002). ISBN 9783642075773. [p. 7]

[22] C. Kloeffel and D. Loss. "Prospects for Spin-Based Quantum Computing in Quantum Dots". *Annu. Rev. Condens. Matter Phys.* **4**, 51 (2013). [pp. 7, 8, 9, 19, 22, 29, 36, 76, 77]

[23] P. Recher and B. Trauzettel. "Quantum dots and spin qubits in graphene." *Nanotechnology* **21**, 302001 (2010). [pp. 7, 9, 22, 25, 27]

[24] B. Urbaszek, X. Marie, T. Amand, O. Krebs, P. Voisin, P. Maletinsky, A. Högele, and A. Imamoğlu. "Nuclear spin physics in quantum dots: An optical investigation". *Rev. Mod. Phys.* **85**, 79 (2013). [pp. 7, 8, 13, 18, 22, 37, 38, 94, 116]

[25] A. Pfund, I. Shorubalko, R. Leturcq, and K. Ensslin. "Pauli spin-blockade in an InAs nanowire double quantum dot". *Phys. E Low-dimensional Syst. Nanostructures* **40**, 1279 (2008). [p. 8]

[26] X. L. Liu, D. Hug, and L. M. K. Vandersypen. "Gate-defined graphene double quantum dot and excited state spectroscopy." *Nano Lett.* **10**, 1623 (2010). [p. 8]

[27] C. H. Yang, W. H. Lim, F. A. Zwanenburg, and A. S. Dzurak. "Dynamically controlled charge sensing of a few-electron silicon quantum dot". *AIP Adv.* **1**, 42111 (2011). [p. 8]

[28] J. Yoneda, T. Otsuka, T. Nakajima, T. Takakura, T. Obata, M. Pioro-Ladrière, H. Lu, C. J. Palmstrøm, A. C. Gossard, and S. Tarucha. "Fast Electrical Control of Single Electron Spins in Quantum Dots with Vanishing Influence from Nuclear Spins". *Phys. Rev. Lett.* **113**, 267601 (2014). [p. 8]

[29] Y. Hu, H. O. H. Churchill, D. J. Reilly, J. Xiang, C. M. Lieber, and C. M. Marcus. "A Ge/Si heterostructure nanowire-based double quantum dot with integrated charge sensor." *Nat. Nanotechnol.* **2**, 622 (2007). [p. 8]

[30] H. O. H. Churchill, A. J. Bestwick, J. W. Harlow, F. Kuemmeth, D. Marcos, C. H. Stwertka, S. K. Watson, and C. M. Marcus. "Electron-nuclear interaction in ^{13}C nanotube double quantum dots". *Nat. Phys.* **5**, 321 (2009). [p. 8]

[31] J. G. Keizer, J. Bocquel, P. M. Koenraad, T. Mano, T. Noda, and K. Sakoda. "Atomic scale analysis of self assembled GaAs/AlGaAs quantum dots grown by droplet epitaxy". *Appl. Phys. Lett.* **96**, 062101 (2010). [p. 8]

[32] V. Cerletti, W. A. Coish, O. Gywat, and D. Loss. "Recipes for spin-based quantum computing". *Nanotechnology* **16**, R27 (2005). [p. 8]

[33] A. M. Tyryshkin, S. A. Lyon, A. V. Astashkin, and A. M. Raitsimring. "Electron spin relaxation times of phosphorus donors in silicon". *Phys. Rev. B* **68**, 193207 (2003). [pp. 9, 13]

[34] G. Balasubramanian, P. Neumann, D. J. Twitchen, M. L. Markham, R. Kolesov, N. Mizuochi, J. Isoya, J. Achard, J. Beck, J. Tissler, V. Jacques, P. R. Hemmer, F. Jelezko, and J. Wrachtrup. "Ultralong spin coherence time in isotopically engineered diamond." *Nat. Mater.* **8**, 383 (2009). [pp. 9, 13]

[35] E. Abe, A. M. Tyryshkin, S. Tojo, J. J. L. Morton, W. M. Witzel, A. Fujimoto, J. W. Ager, E. E. Haller, J. Isoya, S. A. Lyon, M. L. W. Thewalt, and K. M. Itoh. "Electron spin coherence of phosphorus donors in silicon: Effect of environmental nuclei". *Phys. Rev. B* **82**, 121201 (2010). [pp. 9, 13]

[36] T. Ishikawa, K.-M. C. Fu, C. Santori, V. M. Acosta, R. G. Beausoleil, H. Watanabe, S. Shikata, and K. M. Itoh. "Optical and spin coherence properties of nitrogen-vacancy centers placed in a 100 nm thick isotopically purified diamond layer." *Nano Lett.* **12**, 2083 (2012). [pp. 9, 13]

[37] M. Steger, K. Saeedi, M. L. W. Thewalt, J. J. L. Morton, H. Riemann, N. V. Abrosimov, P. Becker, and H.-J. Pohl. "Quantum Information Storage for over 180s using Donor Spins in a ^{28}Si "Semiconductor Vacuum"". *Science* **336**, 1280 (2012). [p. 9]

[38] A. V. Rozhkov, G. Giavaras, Y. P. Bliokh, V. Freilikher, and F. Nori. "Electronic properties of mesoscopic graphene structures: Charge confinement and control of spin and charge transport". *Phys. Rep.* **503**, 77 (2011). [pp. 9, 11, 25]

[39] J. Güttinger, F. Molitor, C. Stampfer, S. Schnez, A. Jacobsen, S. Dröscher, T. Ihn, and K. Ensslin. "Transport through graphene quantum dots." *Rep. Prog. Phys.* **75**, 126502 (2012). [pp. 9, 22, 25]

[40] E. A. Laird, F. Kuemmeth, G. A. Steele, K. Grove-Rasmussen, J. Nygård, K. Flensberg, and L. P. Kouwenhoven. "Quantum transport in carbon nanotubes". *Rev. Mod. Phys.* **87**, 703 (2015). [pp. 9, 22, 36]

[41] M. W. Doherty, N. B. Manson, P. Delaney, F. Jelezko, J. Wrachtrup, and L. C. L. Hollenberg. "The nitrogen-vacancy colour centre in diamond". *Phys. Rep.* **528**, 1 (2013). [p. 9]

[42] F. A. Zwanenburg, A. S. Dzurak, A. Morello, M. Y. Simmons, L. C. L. Hollenberg, G. Klimeck, S. Rogge, S. N. Coppersmith, and M. A. Eriksson. "Silicon quantum electronics". *Rev. Mod. Phys.* **85**, 961 (2013). [pp. 9, 11, 18, 36]

[43] W. A. Coish and J. Baugh. "Nuclear spins in nanostructures". *Phys. Status Solidi (B)* **246**, 2203 (2009). [pp. 10, 13, 15, 18, 20, 23, 37, 39, 72, 73]

[44] R. Winkler. *Spin-orbit coupling effects in two-dimensional electron and hole systems.* Springer-Verlag, Berlin, Heidelberg, New York (2003). ISBN 9783540011873. [pp. 10, 11, 13, 14, 73]

[45] D. A. Abanin, P. A. Lee, and L. S. Levitov. "Charge and spin transport at the quantum Hall edge of graphene". *Solid State Commun.* **143**, 77 (2007). [p. 11]

[46] P. Recher, B. Trauzettel, A. Rycerz, Y. M. Blanter, C. W. J. Beenakker, and A. F. Morpurgo. "Aharonov-Bohm effect and broken valley degeneracy in graphene rings". *Phys. Rev. B* **76**, 235404 (2007). [pp. 11, 25]

[47] P. Recher, J. Nilsson, G. Burkard, and B. Trauzettel. "Bound states and magnetic field induced valley splitting in gate-tunable graphene quantum dots". *Phys. Rev. B* **79**, 085407 (2009). [pp. 11, 25, 27]

[48] W. Greiner. *Relativistische Quantenmechanik.* Verlag Harri Deutsch, Thun und Frankfurt am Main (1987). ISBN 3817110227. [p. 12]

[49] F. Schwabl. *Quantenmechanik für Fortgeschrittene.* Springer-Verlag, Berlin, Heidelberg, New York (2005). ISBN 9783540259046. [p. 12]

[50] J. J. Sakurai. *Advanced Quantum Mechincs.* Addison-Wesley, Reading, Mass. (1967). ISBN 0201067102. [pp. 12, 15]

[51] A. M. Stoneham. *Theory of Defects in Solids.* Oxford University Press, Oxford (1985). ISBN 019851378X. [pp. 12, 15]

[52] W. Pauli. "Zur Quantenmechanik des magnetischen Elektrons". *Zeitschrift für Phys.* **43**, 601 (1927). [p. 12]

[53] A. Barreiro, H. S. J. van der Zant, and L. M. K. Vandersypen. "Quantum dots at room temperature carved out from few-layer graphene." *Nano Lett.* **12**, 6096 (2012). [pp. 13, 25, 107]

[54] J. Schliemann, A. V. Khaetskii, and D. Loss. "Electron spin dynamics in quantum dots and related nanostructures due to hyperfine interaction with nuclei". *J. Phys. Condens. Matter* **15**, R1809 (2003). [pp. 13, 14, 15, 20, 73, 94, 100, 107]

[55] L. M. Roth, B. Lax, and S. Zwerdling. "Theory of Optical Magneto-Absorption Effects in Semiconductors". *Phys. Rev.* **114**, 90 (1959). [p. 14]

[56] C. E. Soliverez. "The contact hyperfine interaction: an ill-defined problem". *J. Phys. C Solid State Phys.* **13**, L1017 (1980). [p. 16]

[57] J. Fischer, W. A. Coish, D. V. Bulaev, and D. Loss. "Spin decoherence of a heavy hole coupled to nuclear spins in a quantum dot". *Phys. Rev. B* **78**, 155329 (2008). [pp. 16, 76, 77]

[58] J. Fischer, B. Trauzettel, and D. Loss. "Hyperfine interaction and electron-spin decoherence in graphene and carbon nanotube quantum dots". *Phys. Rev. B* **80**, 155401 (2009). [pp. 16, 25, 26, 27, 73]

[59] Y. Yafet. "Hyperfine interaction due to orbital magnetic moment of electrons with large g factors". *J. Phys. Chem. Solids* **21**, 99 (1961). [p. 16]

[60] C. Ramanathan. "Dynamic nuclear polarization and spin diffusion in nonconducting solids". *Appl. Magn. Reson.* **34**, 409 (2008). [p. 18]

[61] W. A. Coish, J. Fischer, and D. Loss. "Free-induction decay and envelope modulations in a narrowed nuclear spin bath". *Phys. Rev. B* **81**, 165315 (2010). [pp. 18, 23, 37, 77, 81, 91]

[62] C. P. Slichter. *Principles of Magnetic Resonance.* Springer-Verlag, Berlin, Heidelberg, New York (1980). ISBN 3540084762. [p. 18]

[63] A. Abragam. *The Principles of Nuclear Magnetism.* Oxford University Press, New York (1989). ISBN 019852014X. [p. 18]

[64] A. V. Khaetskii and Y. V. Nazarov. "Spin relaxation in semiconductor quantum dots". *Phys. Rev. B* **61**, 12639 (2000). [pp. 18, 23]

[65] A. V. Khaetskii and Y. V. Nazarov. "Spin-flip transitions between Zeeman sublevels in semiconductor quantum dots". *Phys. Rev. B* **64**, 125316 (2001). [pp. 18, 23]

[66] M. Schreiner, H. Pascher, G. Denninger, S. Studenikin, G. Weimann, and R. Lösch. "Nuclear spin relaxation in heterostructures observed via optically detected magnetic resonance (ODMR) experiments". *Solid State Commun.* **102**, 715 (1997). [p. 19]

[67] A. M. Panich and G. B. Furman. "Nuclear spin-lattice relaxation and paramagnetic defects in carbon nanomaterials". *Diam. Relat. Mater.* **23**, 157 (2012). [p. 19]

[68] P. Barthelemy and L. M. K. Vandersypen. "Quantum Dot Systems: A versatile platform for quantum simulations". *Ann. Phys.* **525**, 808 (2013). [pp. 20, 21]

[69] R. Brunner, Y.-S. Shin, T. Obata, M. Pioro-Ladrière, T. Kubo, K. Yoshida, T. Taniyama, Y. Tokura, and S. Tarucha. "Two-Qubit Gate of Combined Single-Spin Rotation and Interdot Spin Exchange in a Double Quantum Dot". *Phys. Rev. Lett.* **107**, 146801 (2011). [pp. 20, 31, 33, 34]

[70] E. A. Chekhovich, M. N. Makhonin, A. I. Tartakovskii, A. Yacoby, H. Bluhm, K. C. Nowack, and L. M. K. Vandersypen. "Nuclear spin effects in semiconductor quantum dots". *Nat. Mater.* **12**, 494 (2013). [pp. 21, 32, 36, 37, 38]

[71] F. R. Braakman, P. Barthelemy, C. Reichl, W. Wegscheider, and L. M. K. Vandersypen. "Long-distance coherent coupling in a quantum dot array". *Nat. Nanotechnol.* **8**, 432 (2013). [p. 21]

[72] J. M. Taylor, J. R. Petta, A. C. Johnson, A. Yacoby, C. M. Marcus, and M. D. Lukin. "Relaxation, dephasing, and quantum control of electron spins in double quantum dots". *Phys. Rev. B* **76**, 035315 (2007). [pp. 22, 23, 35]

[73] A. V. Khaetskii, D. Loss, and L. Glazman. "Electron Spin Decoherence in Quantum Dots due to Interaction with Nuclei". *Phys. Rev. Lett.* **88**, 186802 (2002). [pp. 22, 23, 76, 77]

[74] J. Schliemann, A. V. Khaetskii, and D. Loss. "Spin decay and quantum parallelism". *Phys. Rev. B* **66**, 245303 (2002). [pp. 22, 23, 48, 94, 100, 107]

[75] A. V. Khaetskii, D. Loss, and L. Glazman. "Electron spin evolution induced by interaction with nuclei in a quantum dot". *Phys. Rev. B* **67**, 195329 (2003). [pp. 22, 23, 76, 77]

[76] W. A. Coish and D. Loss. "Hyperfine interaction in a quantum dot: Non-Markovian electron spin dynamics". *Phys. Rev. B* **70**, 195340 (2004). [pp. 22, 23, 37, 59, 76, 77, 78, 79, 81, 85, 91, 134, 135]

[77] V. N. Golovach, A. V. Khaetskii, and D. Loss. "Phonon-Induced Decay of the Electron Spin in Quantum Dots". *Phys. Rev. Lett.* **93**, 016601 (2004). [p. 23]

[78] W. A. Coish, J. Fischer, and D. Loss. "Exponential decay in a spin bath". *Phys. Rev. B* **77**, 125329 (2008). [pp. 23, 37, 76, 77]

[79] J. Güttinger, C. Stampfer, S. Hellmüller, F. Molitor, T. Ihn, and K. Ensslin. "Charge detection in graphene quantum dots". *Appl. Phys. Lett.* **93**, 212102 (2008). [p. 24]

[80] S. Fringes, C. Volk, B. Terrés, J. Dauber, S. Engels, S. Trellenkamp, and C. Stampfer. "Tunable capacitive inter-dot coupling in a bilayer graphene double quantum dot". *Phys. Status Solidi (C)* **9**, 169 (2012). [p. 24]

[81] S. Schnez, J. Güttinger, M. Huefner, C. Stampfer, K. Ensslin, and T. Ihn. "Imaging localized states in graphene nanostructures". *Phys. Rev. B* **82**, 165445 (2010). [p. 24]

[82] F. Molitor, H. Knowles, S. Dröscher, U. Gasser, T. Choi, P. Roulleau, J. Güttinger, A. Jacobsen, C. Stampfer, K. Ensslin, and T. Ihn. "Observation of excited states in a graphene double quantum dot". *Europhys. Lett.* **89**, 67005 (2010). [p. 24]

[83] M. Fuchs, V. Rychkov, and B. Trauzettel. "Spin decoherence in graphene quantum dots due to hyperfine interaction". *Phys. Rev. B* **86**, 085301 (2012). [pp. 24, 75, 79, 82, 84, 85, 86, 87, 89, 92]

[84] K. S. Novoselov, A. K. Geim, S. V. Morozov, D. Jiang, Y. Zhang, S. V. Dubonos, I. V. Grigorieva, and A. A. Firsov. "Electric Field Effect in Atomically Thin Carbon Films". *Science* **306**, 666 (2004). [p. 23]

[85] T. Ando. "Theory of Electronic States and Transport in Carbon Nanotubes". *J. Phys. Soc. Japan* **74**, 777 (2005). [p. 23]

[86] A. H. Castro Neto, F. Guinea, N. M. R. Peres, K. S. Novoselov, and A. K. Geim. "The electronic properties of graphene". *Rev. Mod. Phys.* **81**, 109 (2009). [pp. 23, 25]

[87] M. Braun, P. Struck, and G. Burkard. "Spin exchange interaction with tunable range between graphene quantum dots". *Phys. Rev. B* **84**, 115445 (2011). [p. 25]

[88] M. I. Katsnelson, K. S. Novoselov, and A. K. Geim. "Chiral tunnelling and the Klein paradox in graphene". *Nat. Phys.* **2**, 620 (2006). [p. 25]

[89] A. Pályi and G. Burkard. "Hyperfine-induced valley mixing and the spin-valley blockade in carbon-based quantum dots". *Phys. Rev. B* **80**, 201404 (2009). [pp. 25, 27]

[90] B. Trauzettel, D. V. Bulaev, D. Loss, and G. Burkard. "Spin qubits in graphene quantum dots". *Nat. Phys.* **3**, 192 (2007). [p. 25]

[91] S. Schnez, K. Ensslin, M. Sigrist, and T. Ihn. "Analytic model of the energy spectrum of a graphene quantum dot in a perpendicular magnetic field". *Phys. Rev. B* **78**, 195427 (2008). [p. 25]

[92] G. Giovannetti, P. A. Khomyakov, G. Brocks, P. J. Kelly, and J. van den Brink. "Substrate-induced band gap in graphene on hexagonal boron nitride: Ab initio density functional calculations". *Phys. Rev. B* **76**, 073103 (2007). [p. 25]

[93] S. Y. Zhou, G.-H. Gweon, A. V. Fedorov, P. N. First, W. A. de Heer, D.-H. Lee, F. Guinea, A. H. Castro Neto, and A. Lanzara. "Substrate-induced bandgap opening in epitaxial graphene". *Nat. Mater.* **6**, 770 (2007). [p. 25]

[94] T. Ohta, A. Bostwick, T. Seyller, K. Horn, and E. Rotenberg. "Controlling the electronic structure of bilayer graphene." *Science* **313**, 951 (2006). [p. 25]

[95] E. V. Castro, K. S. Novoselov, S. V. Morozov, N. M. R. Peres, J. M. B. L. dos Santos, J. Nilsson, F. Guinea, A. K. Geim, and A. H. Castro Neto. "Biased Bilayer Graphene: Semiconductor with a Gap Tunable by the Electric Field Effect". *Phys. Rev. Lett.* **99**, 216802 (2007). [p. 25]

[96] Y. Zhang, T.-T. Tang, C. Girit, Z. Hao, M. C. Martin, A. Zettl, M. F. Crommie, Y. R. Shen, and F. Wang. "Direct observation of a widely tunable bandgap in bilayer graphene." *Nature* **459**, 820 (2009). [p. 25]

[97] B. N. Szafranek, D. Schall, M. Otto, D. Neumaier, and H. Kurz. "Electrical observation of a tunable band gap in bilayer graphene nanoribbons at room temperature". *Appl. Phys. Lett.* **96**, 112103 (2010). [p. 25]

[98] S. Engels, A. Epping, C. Volk, S. Korte, B. Voigtländer, K. Watanabe, T. Taniguchi, S. Trellenkamp, and C. Stampfer. "Etched graphene quantum dots on hexagonal boron nitride". *Appl. Phys. Lett.* **103**, 073113 (2013). [p. 25]

[99] C. Neumann, C. Volk, S. Engels, and C. Stampfer. "Graphene-based charge sensors." *Nanotechnology* **24**, 444001 (2013). [p. 25]

[100] A. Epping, S. Engels, C. Volk, K. Watanabe, T. Taniguchi, S. Trellenkamp, and C. Stampfer. "Etched graphene single electron transistors on hexagonal boron nitride in high magnetic fields". *Phys. Status Solidi (B)* **250**, 2692 (2013). [p. 25]

[101] M. Drögeler, F. Volmer, M. Wolter, B. Terrés, K. Watanabe, T. Taniguchi, G. Güntherodt, C. Stampfer, and B. Beschoten. "Nanosecond spin lifetimes in single-and few-layer graphene-hBN heterostructures at room temperature". *Nano Lett.* **14**, 6050 (2014). [p. 25]

[102] N. J. G. Couto, D. Costanzo, S. Engels, D.-K. Ki, K. Watanabe, T. Taniguchi, C. Stampfer, F. Guinea, and A. F. Morpurgo. "Random Strain Fluctuations as Dominant Disorder Source for High-Quality On-Substrate Graphene Devices". *Phys. Rev. X* **4**, 041019 (2014). [p. 25]

[103] A. Jacobsen, P. Simonet, K. Ensslin, and T. Ihn. "Finite-bias spectroscopy of a three-terminal graphene quantum dot in the multilevel regime". *Phys. Rev. B* **89**, 165413 (2014). [p. 25]

[104] J. J. Sakurai. *Modern Quantum Mechanics*. Addison-Wesley, Reading, Mass. (1994). ISBN 0201539292. [pp. 26, 34, 35]

[105] M. Fuchs, J. Schliemann, and B. Trauzettel. "Ultralong spin decoherence times in graphene quantum dots with a small number of nuclear spins". *Phys. Rev. B* **88**, 245441 (2013). [pp. 27, 93, 97, 99, 100, 101, 103, 104, 105, 106]

[106] D. Subramaniam, F. Libisch, Y. Li, C. Pauly, V. Geringer, R. Reiter, T. Mashoff, M. Liebmann, J. Burgdörfer, C. Busse, T. Michely, R. Mazzarello, M. Pratzer, and M. Morgenstern. "Wave-Function Mapping of Graphene Quantum Dots with Soft Confinement". *Phys. Rev. Lett.* **108**, 046801 (2012). [p. 26]

[107] M. Droth and G. Burkard. "Acoustic phonons and spin relaxation in graphene nanoribbons". *Phys. Rev. B* **84**, 155404 (2011). [p. 28]

[108] M. Droth and G. Burkard. "Electron spin relaxation in graphene nanoribbon quantum dots". *Phys. Rev. B* **87**, 205432 (2013). [p. 28]

[109] M. O. Hachiya, G. Burkard, and J. C. Egues. "Nonmonotonic spin relaxation and decoherence in graphene quantum dots with spin-orbit interactions". *Phys. Rev. B* **89**, 115427 (2014). [pp. 28, 105]

[110] J. Güttinger, T. Frey, C. Stampfer, T. Ihn, and K. Ensslin. "Spin States in Graphene Quantum Dots". *Phys. Rev. Lett.* **105**, 116801 (2010). [p. 28]

[111] J. M. Elzerman, R. Hanson, J. S. Greidanus, L. H. Willems van Beveren, S. De Franceschi, L. M. K. Vandersypen, S. Tarucha, and L. P. Kouwenhoven. "Few-electron quantum dot circuit with integrated charge read out". *Phys. Rev. B* **67**, 161308 (2003). [p. 29]

[112] J. R. Petta, A. C. Johnson, J. M. Taylor, E. A. Laird, A. Yacoby, M. D. Lukin, C. M. Marcus, M. P. Hanson, and A. C. Gossard. "Coherent manipulation of coupled electron spins in semiconductor quantum dots." *Science* **309**, 2180 (2005). [pp. 29, 36]

[113] R. Hanson and D. D. Awschalom. "Coherent manipulation of single spins in semiconductors". *Nature* **453**, 1043 (2008). [pp. 29, 125]

[114] J. M. Elzerman, R. Hanson, L. H. Willems van Beveren, B. Witkamp, L. M. K. Vandersypen, and L. P. Kouwenhoven. "Single-shot read-out of an individual electron spin in a quantum dot". *Nature* **430**, 431 (2004). [p. 29]

[115] B. Bertrand, H. Flentje, S. Takada, M. Yamamoto, S. Tarucha, A. Ludwig, A. D. Wieck, C. Bäuerle, and T. Meunier. "Quantum Manipulation of Two-Electron Spin States in Isolated Double Quantum Dots". *Phys. Rev. Lett.* **115**, 096801 (2015). [p. 30]

[116] W. G. van der Wiel, S. De Franceschi, J. M. Elzerman, T. Fujisawa, S. Tarucha, and L. P. Kouwenhoven. "Electron transport through double quantum dots". *Rev. Mod. Phys.* **75**, 1 (2002). [p. 30]

[117] F. H. L. Koppens, C. Buizert, K. J. Tielrooij, I. T. Vink, K. C. Nowack, T. Meunier, L. P. Kouwenhoven, and L. M. K. Vandersypen. "Driven coherent oscillations of a single electron spin in a quantum dot." *Nature* **442**, 766 (2006). [p. 34]

[118] K. C. Nowack, F. H. L. Koppens, Y. V. Nazarov, and L. M. K. Vandersypen. "Coherent control of a single electron spin with electric fields." *Science* **318**, 1430 (2007). [p. 35]

[119] E. A. Laird, C. Barthel, E. I. Rashba, C. M. Marcus, M. P. Hanson, and A. C. Gossard. "Hyperfine-Mediated Gate-Driven Electron Spin Resonance". *Phys. Rev. Lett.* **99**, 246601 (2007). [pp. 35, 36]

[120] G. Burkard, D. Loss, and D. P. DiVincenzo. "Coupled quantum dots as quantum gates". *Phys. Rev. B* **59**, 2070 (1999). [p. 35]

[121] R.-B. Liu, W. Yao, and L. J. Sham. "Quantum computing by optical control of electron spins". *Adv. Phys.* **59**, 703 (2010). [p. 36]

[122] X. Hao, R. Ruskov, M. Xiao, C. Tahan, and H. Jiang. "Electron spin resonance and spin-valley physics in a silicon double quantum dot". *Nat. Commun.* **5**, 1 (2014). [p. 36]

[123] D. D. Awschalom, L. C. Bassett, A. S. Dzurak, E. L. Hu, and J. R. Petta. "Quantum Spintronics : Engineering". *Science* **339**, 1174 (2013). [p. 36]

[124] I. T. Vink, K. C. Nowack, F. H. L. Koppens, J. Danon, Y. V. Nazarov, and L. M. K. Vandersypen. "Locking electron spins into magnetic resonance by electron-nuclear feedback". *Nat. Phys.* **5**, 764 (2009). [p. 36]

[125] J. R. Petta, J. M. Taylor, A. C. Johnson, A. Yacoby, M. D. Lukin, C. M. Marcus, M. P. Hanson, and A. C. Gossard. "Dynamic Nuclear Polarization with Single Electron Spins". *Phys. Rev. Lett.* **100**, 67601 (2008). [pp. 36, 37]

[126] S. Foletti, H. Bluhm, D. Mahalu, V. Umansky, and A. Yacoby. "Universal quantum control of two-electron spin quantum bits using dynamic nuclear polarization". *Nat. Phys.* **5**, 903 (2009). [p. 37]

[127] R. M. Ribeiro, N. M. R. Peres, J. Coutinho, and P. R. Briddon. "Inducing energy gaps in monolayer and bilayer graphene: Local density approximation calculations". *Phys. Rev. B* **78**, 075442 (2008). [p. 37]

[128] J. Baugh, Y. Kitamura, K. Ono, and S. Tarucha. "Large Nuclear Overhauser Fields Detected in Vertically Coupled Double Quantum Dots". *Phys. Rev. Lett.* **99**, 096804 (2007). [p. 37]

[129] G. Giedke, J. M. Taylor, D. D'Alessandro, M. D. Lukin, and A. Imamoğlu. "Quantum measurement of a mesoscopic spin ensemble". *Phys. Rev. A* **74**, 032316 (2006). [p. 37]

[130] D. Klauser, W. A. Coish, and D. Loss. "Nuclear spin state narrowing via gate-controlled Rabi oscillations in a double quantum dot". *Phys. Rev. B* **73**, 205302 (2006). [p. 37]

[131] D. Stepanenko, G. Burkard, G. Giedke, and A. Imamoglu. "Enhancement of Electron Spin Coherence by Optical Preparation of Nuclear Spins". *Phys. Rev. Lett.* **96**, 136401 (2006). [p. 37]

[132] H. Bluhm, S. Foletti, D. Mahalu, V. Umansky, and A. Yacoby. "Enhancing the Coherence of a Spin Qubit by Operating it as a Feedback Loop That Controls its Nuclear Spin Bath". *Phys. Rev. Lett.* **105**, 216803 (2010). [p. 38]

[133] M. N. Makhonin, K. V. Kavokin, P. Senellart, A. Lemaître, A. J. Ramsay, M. S. Skolnick, and A. I. Tartakovskii. "Fast control of nuclear spin polarization in an optically pumped single quantum dot." *Nat. Mater.* **10**, 844 (2011). [p. 39]

[134] H. Fröhlich and F. R. N. Nabarro. "Orientation of Nuclear Spins in Metals". *Proc. R. Soc. A Math. Phys. Eng. Sci.* **175**, 382 (1940). [p. 39]

[135] P. Simon and D. Loss. "Nuclear Spin Ferromagnetic Phase Transition in an Interacting Two Dimensional Electron Gas". *Phys. Rev. Lett.* **98**, 156401 (2007). [p. 39]

[136] P. Simon, B. Braunecker, and D. Loss. "Magnetic ordering of nuclear spins in an interacting two-dimensional electron gas". *Phys. Rev. B* **77**, 045108 (2008). [p. 39]

[137] B. Braunecker, P. Simon, and D. Loss. "Nuclear Magnetism and Electronic Order in C13 Nanotubes". *Phys. Rev. Lett.* **102**, 116403 (2009). [p. 39]

[138] E. Joos, H. D. Zeh, C. Kiefer, D. Giulini, J. Kupsch, and I.-O. Stamatescu. *Decoherence and the Appearance of a Classical World in Quantum Theory.* Springer-Verlag, Berlin, Heidelberg, New York (2003). ISBN 9783642055768. [pp. 41, 44]

[139] W. H. Zurek. "Quantum Darwinism". *Nat. Phys.* **5**, 181 (2009). [p. 41]

[140] D. P. DiVincenzo. "Fault-tolerant architectures for superconducting qubits". *Phys. Scr.* **T137**, 014020 (2009). [pp. 41, 75]

[141] L. Chirolli and G. Burkard. "Decoherence in solid-state qubits". *Adv. Phys.* **57**, 225 (2008). [pp. 41, 42]

[142] J. Klafter and I. M. Sokolov. *First Steps in Random Walks.* Oxford University Press, Oxford (2011). ISBN 9780199234868. [p. 43]

[143] F. M. Cucchietti, J. P. Paz, and W. H. Zurek. "Decoherence from spin environments". *Phys. Rev. A* **72**, 052113 (2005). [p. 43]

[144] W. Thirring. *Quantum Mathematical Physics.* Springer Berlin Heidelberg, Berlin, Heidelberg, New York (2002). ISBN 978-3-642-07711-1. [pp. 43, 58, 111]

[145] H.-P. Breuer and F. Petruccione. *The Theory of Open Quantum Systems.* Oxford University Press, Oxford (2002). ISBN 9780199213900. [pp. 45, 47, 50, 51, 124]

[146] F. Schwabl. *Statistische Mechanik.* Springer-Verlag, Berlin, Heidelberg, New York (2006). ISBN 3540310959. [p. 45]

[147] E. Fick and G. Sauermann. *The Quantum Statistics of Dynamic Processes.* Springer-Verlag, Berlin, Heidelberg, New York (1990). ISBN 3-540-50824-4. [pp. 47, 50, 51, 52, 56, 133]

[148] N. Shenvi, R. de Sousa, and K. B. Whaley. "Universal scaling of hyperfine-induced electron spin echo decay". *Phys. Rev. B* **71**, 224411 (2005). [p. 48]

[149] J. Särkkä and A. Harju. "Spin dynamics in a double quantum dot: Exact diagonalization study". *Phys. Rev. B* **77**, 245315 (2008). [p. 48]

[150] B. Erbe and J. Schliemann. "Perturbative regimes in central spin models". *Phys. Rev. B* **85**, 235423 (2012). [pp. 48, 97]

[151] J. Fischer and H.-P. Breuer. "Correlated projection operator approach to non-Markovian dynamics in spin baths". *Phys. Rev. A* **76**, 052119 (2007). [pp. 51, 55, 57]

[152] E. Barnes, Ł. Cywiński, and S. Das Sarma. "Master equation approach to the central spin decoherence problem: Uniform coupling model and role of projection operators". *Phys. Rev. B* **84**, 155315 (2011). [pp. 55, 57, 76, 83, 85, 134]

[153] M. Fuchs, F. Krauß, D. Hetterich, and B. Trauzettel. "Thermal electron spin flip in quantum dots". *Phys. Rev. B* **92**, 035310 (2015). [pp. 63, 67, 70, 72, 73]

[154] W. Zhang, V. V. Dobrovitski, K. A. Al-Hassanieh, E. Dagotto, and B. N. Harmon. "Hyperfine interaction induced decoherence of electron spins in quantum dots". *Phys. Rev. B* **74**, 205313 (2006). [pp. 69, 128]

[155] W. A. Coish, D. Loss, E. A. Yuzbashyan, and B. L. Altshuler. "Quantum versus classical hyperfine-induced dynamics in a quantum dot". *J. Appl. Phys.* **101**, 081715 (2007). [pp. 69, 128]

[156] M. Bortz and J. Stolze. "Spin- and entanglement-dynamics in the central spin model with homogeneous couplings". *J. Stat. Mech. Theory Exp.* P06018 (2006). [pp. 69, 128, 129]

[157] B. Erbe and J. Schliemann. "Hyperfine induced spin and entanglement dynamics in double quantum dots: A homogeneous coupling approach". *Phys. Rev. B* **81**, 235324 (2010). [pp. 69, 128, 129]

[158] C. Testelin, B. Eble, F. Bernardot, G. Karczewski, and M. Chamarro. "Signature of the Overhauser field on the coherent spin dynamics of donor-bound electrons in a single CdTe quantum well". *Phys. Rev. B* **77**, 235306 (2008). [p. 73]

[159] B. M. Terhal. "Quantum error correction for quantum memories". *Rev. Mod. Phys.* **87**, 307 (2015). [p. 76]

[160] I. A. Merkulov, A. L. Efros, and M. Rosen. "Electron spin relaxation by nuclei in semiconductor quantum dots". *Phys. Rev. B* **65**, 205309 (2002). [p. 76]

[161] R. de Sousa and S. Das Sarma. "Theory of nuclear-induced spectral diffusion: Spin decoherence of phosphorus donors in Si and GaAs quantum dots". *Phys. Rev. B* **68**, 115322 (2003). [pp. 76, 77]

[162] W. Yao, R.-B. Liu, and L. J. Sham. "Theory of electron spin decoherence by interacting nuclear spins in a quantum dot". *Phys. Rev. B* **74**, 195301 (2006). [pp. 76, 77]

[163] C. Deng and X. Hu. "Analytical solution of electron spin decoherence through hyperfine interaction in a quantum dot". *Phys. Rev. B* **73**, 241303 (2006). [pp. 76, 77]

[164] C. Deng and X. Hu. "Electron-spin dephasing via hyperfine interaction in a quantum dot: An equation-of-motion calculation of electron-spin correlation functions". *Phys. Rev. B* **78**, 245301 (2008). [p. 76]

[165] Ł. Cywiński, W. M. Witzel, and S. Das Sarma. "Electron Spin Dephasing due to Hyperfine Interactions with a Nuclear Spin Bath". *Phys. Rev. Lett.* **102**, 057601 (2009). [p. 76]

[166] E. Barnes, Ł. Cywiński, and S. Das Sarma. "Nonperturbative Master Equation Solution of Central Spin Dephasing Dynamics". *Phys. Rev. Lett.* **109**, 140403 (2012). [p. 76]

[167] J. Fischer and D. Loss. "Dealing with Decoherence". *Science* **324**, 1277 (2009). [p. 77]

[168] Ł. Cywiński, W. M. Witzel, and S. Das Sarma. "Pure quantum dephasing of a solid-state electron spin qubit in a large nuclear spin bath coupled by long-range hyperfine-mediated interactions". *Phys. Rev. B* **79**, 245314 (2009). [p. 77]

[169] G. Guennebaud, B. Jacob, and Others. "Eigen v3" (2010). URL `http://eigen.tuxfamily.org`. [pp. 96, 116]

[170] P. R. Struck and G. Burkard. "Effective time-reversal symmetry breaking in the spin relaxation in a graphene quantum dot". *Phys. Rev. B* **82**, 125401 (2010). [p. 105]

[171] F. H. L. Koppens, K. C. Nowack, and L. M. K. Vandersypen. "Spin Echo of a Single Electron Spin in a Quantum Dot". *Phys. Rev. Lett.* **100**, 236802 (2008). [p. 106]

[172] H. Bluhm, S. Foletti, I. Neder, M. S. Rudner, D. Mahalu, V. Umansky, and A. Yacoby. "Dephasing time of GaAs electron-spin qubits coupled to a nuclear bath exceeding 200 μs". *Nat. Phys.* **7**, 109 (2011). [p. 106]

[173] D. Hetterich, M. Fuchs, and B. Trauzettel. "Equilibration in closed quantum systems: Application to spin qubits". *Phys. Rev. B* **92**, 155314 (2015). [pp. 109, 113, 117, 118, 121]

[174] J. M. Deutsch. "Quantum statistical mechanics in a closed system". *Phys. Rev. A* **43**, 2046 (1991). [p. 109]

[175] M. Srednicki. "Chaos and quantum thermalization". *Phys. Rev. E* **50**, 888 (1994). [p. 109]

[176] A. J. Short. "Equilibration of quantum systems and subsystems". *New J. Phys.* **13**, 053009 (2011). [pp. 109, 110, 111, 112, 114, 120]

[177] A. J. Short and T. C. Farrelly. "Quantum equilibration in finite time". *New J. Phys.* **14**, 013063 (2012). [pp. 109, 110, 111, 114, 140]

[178] P. Reimann. "Foundation of Statistical Mechanics under Experimentally Realistic Conditions". *Phys. Rev. Lett.* **101**, 190403 (2008). [pp. 109, 110, 111, 112, 114, 120]

[179] A. Polkovnikov, K. Sengupta, A. Silva, and M. Vengalattore. "Colloquium : Nonequilibrium dynamics of closed interacting quantum systems". *Rev. Mod. Phys.* **83**, 863 (2011). [p. 109]

[180] P. Reimann and M. Kastner. "Equilibration of isolated macroscopic quantum systems". *New J. Phys.* **14**, 043020 (2012). [pp. 109, 112]

[181] L. del Rio, A. Hutter, R. Renner, and S. Wehner. "Relative Thermalization". *arXiv eprint [quant-ph]* (2014). arXiv:1401.7997. [p. 109]

[182] L. P. García-Pintos, N. Linden, A. S. L. Malabarba, A. J. Short, and A. Winter. "Equilibration time scales of physically relevant observables". *arXiv eprint [quant-ph]* (2015). arXiv:1509.05732. [pp. 109, 110, 112, 114, 137]

[183] M. Srednicki. "The approach to thermal equilibrium in quantized chaotic systems". *J. Phys. A. Math. Gen.* **32**, 1163 (1999). [p. 109]

[184] V. I. Yukalov. "Equilibration and thermalization in finite quantum systems". *Laser Phys. Lett.* **8**, 485 (2011). [p. 109]

[185] J. Eisert, M. Friesdorf, and C. Gogolin. "Quantum many-body systems out of equilibrium". *Nat. Phys.* **11**, 124 (2015). [p. 109]

[186] C. Gogolin and J. Eisert. "Equilibration, thermalisation, and the emergence of statistical mechanics in closed quantum systems". *arXiv eprint [quant-ph]* (2015). arXiv:1503.07538. [p. 109]

[187] W. Yang and R.-B. Liu. "Quantum many-body theory of qubit decoherence in a finite-size spin bath". *Phys. Rev. B* **78**, 085315 (2008). [p. 125]

[188] W. Yang and R.-B. Liu. "Quantum many-body theory of qubit decoherence in a finite-size spin bath. II. Ensemble dynamics". *Phys. Rev. B* **79**, 115320 (2009). [p. 125]

[189] J. J. Pla, K. Y. Tan, J. P. Dehollain, W. H. Lim, J. J. L. Morton, F. A. Zwanenburg, D. N. Jamieson, A. S. Dzurak, and A. Morello. "High-fidelity readout and control of a nuclear spin qubit in silicon." *Nature* **496**, 334 (2013). [p. 125]

Acknowledgments

During my PhD studies, I have enjoyed the support from many different people to whom I want to express my sincere gratitude. First, I would like to thank all past and present members of TP4 for the stimulating and cooperative atmosphere in our group. I especially enjoyed the numerous discussions on various fields of physics and the willingness of everyone to help each other with any kind of problem. Let me especially thank Dietrich, Stefan, Rolf, and Thore for their efforts. Besides this supportive professional environment, I am also very grateful for all the social activities of our group, which made my PhD studies also a very pleasant personal experience. I very much appreciate my office mates from "downstairs", Florian, Sebastian, Stefan, and Anselm, as well as François, with whom Florian and I shared the "French" office. Moreover, I was delighted by the international character of our group with many colleagues and guests from different countries, which broadened my view on the world. Further, I want to specially thank Daniel for the very productive collaboration on the spin physics in quantum dots. With him, I finally got a very motivated and talented coworker on the central spin problem. I would also like to thank Luis-Pedro García Pintos, with whom Daniel and I had many interesting discussions on equilibration in quantum systems. Further, I would like to thank John Schliemann, who introduced me to the numerical investigation of spin dynamics. Many thanks are also due to Nelly Meyer, who took care of all the administrative matters in a friendly and cordial manner.

I am very grateful to my advisor Björn Trauzettel for his excellent guidance. He always managed to have time for discussions, in which I could profit from his physical intuition and expertise. In his patient and deliberate leadership, I found great support. I also benefited a lot from the opportunities he gave me to attend to various conferences and workshops.

Finally, I would like to thank my parents and my brother for their support during all my studies. I am especially grateful to Erika for her permanent support and encouragement. With her taking care of our children Anton and Nora, I could spend all the time needed to finish this thesis.